High-temperature superconductors in high-field magnets

Huub Weijers

The work in this thesis was performed at the Magnet Science and Technology division of the National High Magnetic Field Laboratory, Florida State University, Tallahassee, Florida, United States of America.

H.W. Weijers
High-temperature superconductors in high-field magnets
PhD. thesis, University of Twente, The Netherlands

ISBN 978-90-365-2849-8
DOI: 10.3990/1.9789036528498

Cover: Image of the 5T insert coil

Printed by Ipskamp drukkers

HIGH-TEMPERATURE SUPERCONDUCTORS IN HIGH-FIELD MAGNETS

PROEFSCHRIFT

ter verkrijging van
de graad van doctor aan de Universiteit Twente,
op gezag van rector magnificus,
prof. dr. H. Brinksma,
volgens besluit van het College voor Promoties
in het openbaar te verdedigen
op 24 juni 2009 om 16.45 uur

door

Hubertus Wilhelmus Weijers
geboren op 29 maart 1965
te Montferland

Dit proefschrift is goedgekeurd door de promotor

Prof. dr. ir. H.H.J. ten Kate

**The only reliable and useful way to determine a safe operational limit,
is to exceed it carefully and observe the consequences.**

Preface and acknowledgement

This thesis deals with selected topics out of a wide research and development effort on HTS insert coil technology. Its origin goes back to the founding charter of the NHMFL in the year 1988 which listed the goal of realizing a 25 T superconducting magnet as one of the milestones the NHMFL was to achieve. High-temperature superconductors had only just been discovered and the required technology was non-existent. The path to where we are now has been eventful and a real learning experience. From the early days in the mid-1990-ies of the 'Wind and Pray" approach when coil testing relentlessly pointed out the shortcomings of both conductor and coil technologies at the time to the first successful "mini-coils" (around coil number 70) to the successive 1 T, 3 T and 5 T inserts (the latter reaching 25 T and bringing the total of numbered coils over 300 a decade later) to the promise of 30^{+}T superconducting user magnets with coated conductors in the not-too-distant future.

Lacking the funds to buy the very expensive conductors, a collaboration was established with industry. This approach has served us well and resulted in a wide assortment of conductors to work with. New superconductors were donated in exchange for feedback on its performance as observed in our magnet technology development program. We also tested complete coils built by ourselves or by partners, in background magnetic field, a task for which the NHMFL facilities are well suited.

This work is centered on the 5T insert coil for a total magnetic field of 25 T, but the research and development effort is interwoven with and inseparable from the broader HTS insert coil technology development program. Therefore discussions on a wider range of conductors and coils in line with the broader scope of this thesis are presented.

While I take full responsibility for the described NHMFL insert coil designs, analysis and interpretation of the data on coils and conductors, having executed or been directly involved with all experiments described and having wound many a coil, this work has had the benefit of many direct and indirect contributions of a large number of people inside and outside the NHMFL. In contrast, developing this thesis itself has been the loneliest work I have ever done, but ultimately just as rewarding. There are many people that I would like to thank for their contributions to the HTS insert program in general and this thesis in particular.

First people from the University of Twente and Saxion Hogeschool in Enschede, many of whom spent time at the NHMFL. In no particular order: Bennie ten Haken, Arno Godeke, Maarten Meinesz, Danko van der Laan, Hans van Eck, Anne-Freerk de Jager, Marc Dhallé, Andries en Ouden and of course Herman ten Kate. At the NHMFL in Tallahassee: Steven Van Sciver, Hans Schneider-Muntau, David Hilton, Yusuf Hascicek, Ibrahim Mutlu, Sastry Pamidi, Yehia Eyssa, Youri Viouchkov, the late Abdallah Umbaruku, Hill Thompson, Frederic Trillaud, Bob Walsh, Bianca and Ulf Trociewitz, David Larbalestier, Justin Schwartz and many more. Ken Marken, Drew Hazelton, Juan Farré, Michia Okada, Jaimoo Yoo and others in industry. The late Wendy Crook, friends, family and above all Annet Forkink: I could not have done this without you! Thank you all.

Huub Weijers

Table of Contents

Symbols and Acronyms

	Description	unit
//	Parallel orientation of magnetic field to the wide side of a tape	
⊥	Perpendicular orientation of magnetic field to the wide side of a tape	
a	Strain sensitivity parameter	[-]
ab-plane	Base plane of BSCCO grains	
area	Cross-sectional area	[m^2]
$\boldsymbol{B}$	Magnetic induction vector (also referred to as magnetic field)	[T]
B	Magnetic field value	[T]
$B_{//}$	Component of B_A parallel to the wide side of the tape	[T]
$B_{//ab}$	Component of B parallel to the *ab*-plane of a grain	[T]
$B_{\perp}$	Component of B_A perpendicular to the wide side of the tape	[T]
$B_{\perp ab}$	Component of B perpendicular to the *ab*-plane of a grain	[T]
B_{∞}	Central magnetic field generated by an infinitely long coil	[T]
B_0	Scaling magnetic field for weakly linked current paths	[T]
B_A	Applied magnetic field	[T]
B_{CF}	Magnetic field at Field Center	[T]
B_{eff}	Effective magnetic field	[T]
B_r	Component of $\boldsymbol{B}$ in the radial direction of a magnet	[T]
B_{sc}	Scaling magnetic field for strongly linked current paths	[T]
B_{total}	Magnetic field value	[T]
B_z	Component of $\boldsymbol{B}$ in the axial direction of a magnet	[T]
Bi-2212	$Bi_2Sr_2Ca_1Cu_2O_x$	
Bi-2223	$Bi_2Sr_2Ca_2Cu_3O_x$	
c-axis	Direction perpendicular to the *ab*-plane in BSCCO grains	
DP	Double Pancake	
e	Degree of plasticity	[-]
e	Base of the natural logarithm	[-]
E	Electrical field	[V/m]
E_c	Critical electric field (criterion)	[V/m]
E_i	Initial slope of the stress-strain curve	[GPa]
E_p	Slope of the stress-strain curve in the plastic regime	[GPa]
f	Scaling function for magnetic field	[-]
f_{CC}	Ratio between the distance from the neutral line to the ReBCO layer to the distance from the neutral line to the conductor surface	[-]
f_{fil}	Ratio of filament zone thickness to conductor thickness	[-]
g	Scaling function for magnetic field	[-]
G	Distribution function of the grain misalignment angle	[-]
h	Axial dimension of a coil	[m]
HTS	High-Temperature Superconductor	
I	Current	[A]

Continued on next page

	Description	unit
I_c	Critical current	[A]
I_{op}	Operating current	[A]
ID	Inner Diameter of windings	[m]
IR	Inner Radius of windings	[m]
J_{ew}	Critical current density of a network of weakly linked current paths	[A/mm^2]
J_{es}	Critical current density of a network of strongly linked current paths	[A/mm^2]
J_e	Critical current density in the conductor	[A/mm^2]
j_e	Critical current density normalized to the self-field value	[-]
J_e(self)	Engineering critical current density at self field (measured)	[A/mm^2]
$J_e^{calc}(self)$	Engineering critical current density in conductor at self field (calculated)	[A/mm^2]
J_{ave}	Average critical current density in the windings	[A/mm^2]
J_{op}	Operating current density	[A/mm^2]
J_q	Quench current density	[A/mm^2]
L	Self-inductance	[H]
LBRM	Large Bore Resistive Magnet	
LTS	Low Temperature Superconductor	
LW	Layer Wound	
min	Minimum (subscript)	
max	Maximum (subscript)	
n	*n*-value, index of transition	[-]
N	Number of turns	[-]
OR	Outer Radius of windings	[m]
OD	Outer Diameter of windings	[m]
p	Plasticity parameter	[-]
r	Radius or radial direction	[m]
r_b	Bend radius	[m]
r_f	Final radius	[m]
r_i	Initial radius	[m]
ReBCO	Rare-earth-Barium-Copper-Oxide	
SS	Stainless steel	
t	Conductor thickness	[m]
T	Temperature	[K]
T_c	Upper critical temperature	[K]
UTS	Ultimate Tensile Strength	[MPa]
x	Magnetic field dependence parameter for J_e	[-]
z	Axial dimension	[m]
Greek symbols		
α	Grain misalignment angle	[°]
α^*	Average grain misalignment angle	[°]
α^{**}	Anisotropy parameter that is only valid for a limited range of ϕ	[°]
α	Ratio of winding outer and inner diameter	[-]
β	Ratio of winding height and inner diameter	[-]

Continued on next page

	Description	**unit**
β	Geometric parameter reflecting the geometry of weak links	[-]
Δ	Increment	
ε	Strain	[-]
ε_{crit}	Critical strain	[-]
ε_{p}	Strain at the onset of the plastic regime	[-]
ϕ	Magnetic field angle	[°]
λ	Fill factor	[-]
μ_0	Magnetic permeability of vacuum	[H/m]
σ	Standard deviation (chapter 3)	[-]
σ	Stress (chapter 6)	[MPa]
σ_L	Hoop stress (chapter 6)	[MPa]
σ_{OD}	Hoop stress at outer diameter of windings (chapter 6)	[MPa]
σ_p	Tensile stress from fit to plastic regime (chapter 6)	[MPa]

1 Introduction

This chapter provides an introduction to superconducting high-field magnets, their design considerations and specific features of high-temperature superconductors (HTS) that distinguish them from low-temperature superconductors (LTS) in the context of magnet technology. Generic benchmark numbers for the target current carrying capacity and stress tolerance of HTS conductors are presented. An overview is presented of significant HTS insert coils developed so far and their remarkable features. The design brief of the so-called 5T insert coil that represents the core of this thesis is shown. The chapter is concluded with the scope of this thesis.

1.1 High-field magnets

1.1.1 Applications

Superconducting magnets are in use and under development for a large variety of applications including fundamental research, medical diagnostics and therapy, electrical utility, military purpose and magnetically levitated trains. Magnetic Resonance Imaging (MRI) magnets used in hospitals are the most widespread and commercially successful application of superconducting magnet technology. At present, the largest super-conducting magnet system is the Large Hadron Collider (LHC) and with a 27 km circumference consisting of some 9000 superconducting magnets and used for fundamental particle physics research [1].

This work targets the development of technology for the strongest fully superconducting magnets operating in a steady state, i.e. in DC mode, using the current generation of commercially available superconductors. Strong in this case refers to the height of the magnetic field generated in the bore of the magnet. The obvious target for researchers at the NHMFL was 25 T, if only because one of the charges to the NHMFL, dating back to the time of its founding [2], is the development of a 25 T superconducting magnet for Nuclear Magnetic Resonance (NMR). The two main applications for 25 T class magnets are high-frequency NMR and use as general purpose research magnets.

NMR systems allow the analysis of complex chemical substances in terms of chemical composition and molecular structure. The pharmaceutical industry and national health organizations see NMR as a crucial tool in cancer research. Imaging capabilities (MRI) can be added to NMR systems as demonstrated with the NHMFL 21.1 T NMR system, although the volume available will likely be the size of grapes, oranges or small animals at best, not humans. Research magnets are used for a wide array of research areas including condensed matter physics, study of quantum effects, semi-conductors, super-conductors and magnetic processing. Commercial state-of the-art NMR and research magnets feature maximum magnetic field values around 22 T. For a number of reasons, including increased range, increased resolution and reduced data acquisition times, there is constantly a demand for stronger magnets hence the target of 25 T.

1.1.2 25 T magnet development

The relevance of the number 25 in this context is that it requires the development of magnet technology for High-Temperature Superconductors (HTS). Of this class of mate-rials two are currently most relevant for high-field magnets: the BiSrCaCu oxides and

Rare-Earth-BaCu oxides. Commercial or near-commercial HTS conductors include $Bi_2Sr_2Ca_2Cu_3O_x$, $Bi_2Sr_2Ca_1Cu_2O_x$, $Y_1Ba_2Cu_3O_x$ and $Gd_1Ba_2Cu_3O_x$, commonly abbreviated to Bi-2223, Bi-2212, YBCO and GdBCO. The HTS conductors relevant in this work are further introduced in section 2.1. However, a discussion of the fundamentals of superconductivity is outside the scope of this work.

The current carrying capacity at 4.2 K of the Low-Temperature Superconductors (LTS) NbTi and Nb_3Sn decrease sharply in magnetic fields over 10 and 20 T respectively, unlike HTS conductors. For some time PbMS was developed as this material with its critical field of up to 30-35 T [3][1] could in principle reach 25 T. Practical conductors of long length could, however, not be made and the issues mentioned in [3] have not been resolved. Ten years ago the target of 25 T was considered out of reach with LTS conductors only. Continued improvements in Nb_3Sn conductors incrementally increase its reach, but never passed 22.3 T, the highest record magnetic field in this type of magnets [5]. Since the target magnetic field strength for future generations of superconducting magnets shifts to 30 T and even beyond, as it recently has, the development of practical HTS magnet technology is crucial. LTS magnet technology remains relevant for high-field magnet technology as the current carrying capacity of LTS conductors for magnetic fields well below 20 T exceeds those in current HTS conductors and at a much lower cost. A 25 T magnet is therefore typically foreseen as a set of nested coils with NbTi, Nb_3Sn and HTS conductor sections. A conceptual sketch of a 25 T NMR magnet is presented in Figure 1-1 and a more specific description is given in section 4.4.

The research and development project that lead to the first HTS coil to reach 25 T forms the main thrust of this thesis. A close collaboration between Oxford Superconducting Technology (OST) and the NHMFL made this project possible and provided us with the Bi-2212[2] tape conductor used in this magnet. Collaborations with OST and other partners in industry and research provided the opportunity to study various Bi-2223 tapes, Bi-2212 wire and YBCO coated conductor[3] for their applicability in high-field magnets and allow the scope of this work to be wider than the development of one particular magnet.

1.1.3 Magnet technology issues

Common factors in the design of high-field superconducting magnets are well established and understood and several reference books on LTS magnets exist including [6, 7, 8]. A brief sampling of topics applicable to both HTS and LTS follows.

Current density

Every magnet design starts with consideration of current density. For a coil with given dimensions the generated magnetic field is proportional to the current density, which in itself is magnetic field dependent. A large current carrying ability at the magnetic field levels present in the windings is a pre-requisite.

Conductor stress-strain management in normal operation

All superconductors have a maximum strain level beyond which irreversible degradation of its current carrying properties occurs. The current carrying capacity is reversibly affected for strains below the irreversibility threshold. While the specifics vary for different superconductors, all have a specific strain state or range of strain states that is

[1] Based on screening current measurements. Measurements based on resistivity suggest upper critical magnetic field of 50-60 T [4].
[2] Terminology for high temperature superconductors is introduced in section 2-1.
[3] An overview of conductors is given in section 2-1.

desirable. It is a critical part of magnet design to manage the strain state of the superconductor from manufacturing through operation. The strain state of the superconductor depends on many factors including the stress-strain characteristics of the superconductor, the electro-magnetic or Lorentz force acting on the conductor and strain resulting from differences in thermal contraction between the superconductor and other materials in the coil. Two primary tools to limit the peak strain on the superconductor are reinforcement, either in the form of co-wound materials or overbanding, and radial sectioning of the windings.

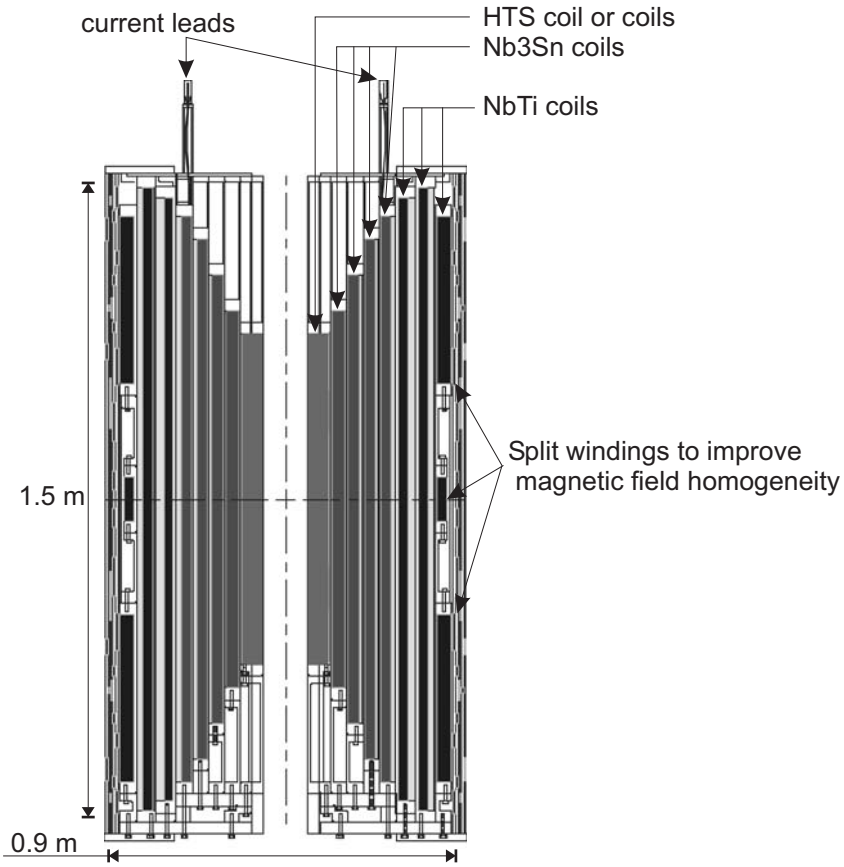

Figure 1-1. Cross sectional schematic of a 25 T NMR magnet. Overall dimensions are 1.5 m length, 0.9 m outer diameter and a useful bore of 105 mm. The superconducting coils are indicated in shades of grey. Reinforcement in the form of overbanding is present in some coils and is indicated with a lighter shade of grey than the windings.

Stability against thermal disturbance

The current carrying capacity in superconductors is strongly temperature dependent and a small temperature rise in a small section of superconductor can lead to a propagation of the zone of elevated temperature and loss of superconductivity: the process known as thermal runaway or quench. Cooling of the superconductor is required, typically either through direct contact with liquid helium, conduction cooling or a mix of those strategies.

Quench protection

Quenches can occur for a number of reasons including events that are hard to foresee or impossible to prevent. It is generally accepted that superconducting coils should be protected against possible damage from the stored energy in the coil that is released

during a quench, if the stored energy is large enough to locally heat the coil to dangerous levels. Large voltages can occur during quenches requiring adequate measures to prevent breakdown of insulation and risk to personnel.

Fault conditions

Fault conditions that do not originate in a quench of the superconducting magnet, but may very well lead to one, include large forces and induced currents resulting from misaligned coils, electrical shorts or rapid de-energization of only a part of a magnet system.

AC-loss

AC-loss in superconductors is a widely studied topic for applications of superconductors in the power utility industry and for magnets whose operation requires fast ramping of the current such that transient effects become performance limiting. The magnets under consideration here are DC magnets although they still require ramping to reach the operating condition. The maximum ramp rate may be limited by the AC loss properties of the superconductor in combination with the chosen cooling strategy.

Magnetic field quality

Magnetic field quality refers to the spatial and temporal variation of the magnetic field vector over a specific volume around the geometric center of the coil known as center field or CF.

Joints

Low-resistance joints are typically required at coil terminals. Conductor splices occur if the available uninterrupted conductor length is insufficient to wind a single coil.

Reliability

Magnet performance should meet its specifications under routine operation over a large number of years.

1.1.4 Demonstration magnets

A magnet that is developed taking all relevant design aspects into account, that is built and routinely operated for multiple years is known as a user magnet at facilities like the NHMFL and a commercial system in industry. Magnets that are solely built to develop and demonstrate new magnet technology during a brief test on the other hand are demonstration magnets[4]. Most HTS coils developed in the field of high-field magnet technology so far, including the ones discussed here, are demonstration magnets[5]. Mature magnet technology for user magnet and commercial magnets is commonly developed through a succession of demonstration coils with increasingly demanding specifications and increased sophistication.

Emphasis in this work is on current density and conductor strain management in normal operation. Protection against fault conditions and quench protection required gradually more attention during the course of the work described here, while stability, AC loss, magnetic field quality, joints and reliability are considered but not subject of a significant development effort within the framework of this thesis. A general review of demonstration coils built by industry and research institutions follows in section 1.4.

[4] The term model coil is also used, especially for large scale magnets.
[5] Insert built by Hitachi and installed at NIMS has operated as user magnet for 1.5 years [44].

During the development the understanding of desirable and undesirable aspects of the superconducting wire or tape is improved. An essential part of magnet technology development if feed-back of this understanding to the manufacturers of the superconductor. In an ideal world, magnet technology and conductor development would go hand in hand. This is a reality in projects with multi-million dollar conductor budgets like ITER and LHC. Smaller projects like the one described here are usually limited to requesting minor variations within established production parameters. In fact, there was no budget to purchase the expensive conductors. All conductors described here were donated with the understanding that the manufacturer would receive detailed feedback on the applicability of their conductor for high-field magnets and usually inclusion of the main observations in a publication. Most conductors are off-the-shelf and came with various levels of documentation, although it should be noted that our collaboration with OST was uncommonly open and allowed us some customization of the conductor.

To assess the properties of a demonstration coil, and the validity of the physics that lead to the prediction of its properties, a test should be carried out by operating the coil in a background magnetic field that mimics the conditions of its intended application as closely as possible. Word-wide there are only a few magnets capable of generating about 20 T with suitably large bores [8, 9, 10]. Some of those are resistive magnets, which brings practical advantages as well as additional complications compared to a superconducting background magnet, which is discussed in section 2.1.6. Usually the background magnet is powered separately from the demonstration coil, in which case the former is known as an outsert and the latter as the insert coil.

1.1.5 State of the art LTS high-field magnets

NMR magnets

State of the art in high-field NMR magnets is represented by magnets like the 22.3 T system at the National Institute of Material Science (NIMS) in Japan [11], the NHMFL 21.1 T NMR magnet with its wide-bore and unique imaging capabilities, and the commercial 22.3 T NMR systems sold by Bruker and formerly by Oxford Instruments. See Figure 1-2 for pictures of these magnets. Complete NMR systems consisting of magnet, cryostat and instrumentation are commonly referred to by their proton resonance frequency. At 44.7 MHz/T, 21.1 T corresponds to 900 MHz and 25 T to 1066 MHz.

Research magnets

State of the art in narrow bore research magnets is represented by a 21 T system from Bruker [12] (see Figure 1-3). An older 21 T system at NIMS [13, 14] is no longer in active use [15]. The 20 T HOMER II magnet [9] with a 185 mm bore is state of the art for large bore magnets.

1.1.6 Magnetic field homogeneity

Research magnets often feature homogeneity specifications of 10^{-3} to 10^{-4} relative variation in magnetic field strength over a spherical volume with a diameter of a few centimeters. Such homogeneity can generally be obtained using simple concentric solenoid coils of moderate height[6]. NMR magnets on the other hand require extreme magnetic field homogeneity in space and time to fully realize the potential frequency resolution of the NMR signals: in the order of 10^{-6} for solid state NMR and around 10^{-9} for solution NMR.

[6] Beta values of 2-3, as introduced in section 1-4.

Figure 1-2. (left) A 22.3 T/950 MHz NMR system of 3.3 m radial and 4.6 m axial dimension by Bruker; (middle) the 21.6 T/930 MHz NMR system at the Tsukuba Magnet Lab of NIMS; (right) the NHMFL 21.1 T/900 MHz Ultra Wide Bore NMR system.

Figure 1-3. (left) Research magnet capable of generating 21 T in a 64 mm cold bore at 2.2 K and 19 T at 4.2K; (right) 20 T research magnet hanging above its 1.4 m diameter cryostat.

Thus NMR magnets typically feature a collection of very tall solenoid coils, split coils and smaller compensation coils, as shown in Figure 1-1, plus sets of copper shim coils. NMR magnets require operation in persistent mode with nearly-superconducting joints or the use of sophisticated magnet power supplies using sensitive feedback circuits to maintain a 0.1-1 ppm level stable current in the magnet [16]. In either case it is desirable for the current distribution within the windings to be as homogeneous as possible. Layer wound coils using round or rectangular conductors with low aspect ratios are therefore strongly preferred in NMR magnets.

1.2 Premise and problems of high-temperature superconductors

The ability to carry significant current density at 4.2 K to much higher magnetic field and temperature than LTS conductors [17] create the prospect of fully superconducting magnets with central field values far beyond those of LTS conductors. This may best be illustrated with a graph of current density versus applied magnetic field as in Figure 1-4. Not only is the value of the current carrying capacity generally larger at magnetic fields above 20 T, the magnetic field dependence is also fairly weak. This implies that the current carrying capacity itself is not likely to be a limiting factor in the design of magnets with magnetic field strengths in the 25-50 T range. As opposed to the incremental increases in the peak magnetic field that have characterized LTS magnets over the past decade or so [18], large increases appear feasible with HTS conductors based on its current density. One can conceive conceptual designs of superconducting magnets of 30 T [19, 20], and science drivers have been identified for 30 T superconducting NMR magnets [21]. This National Academy of Sciences report also acknowledges the significance of reaching 25 T with the 5T insert.

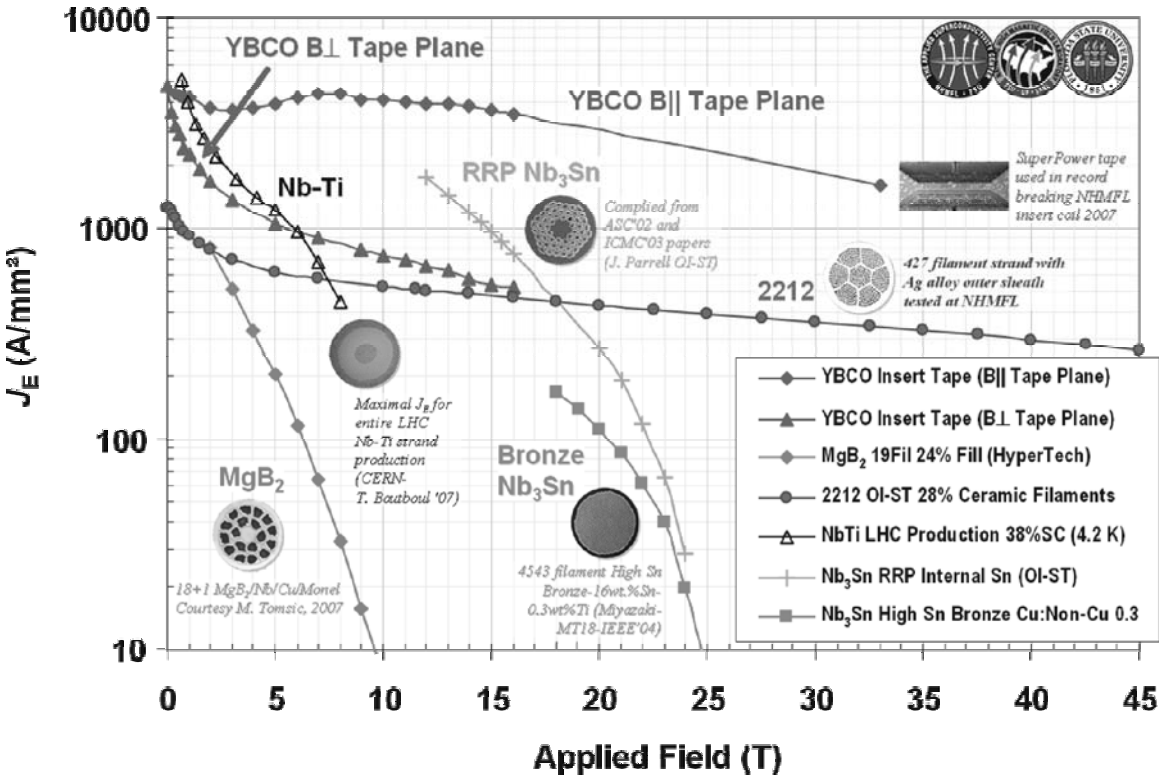

Figure 1-4. Engineering critical current density in HTS and LTS conductors. Image courtesy of Peter Lee, http://magnet.fsu.edu/~lee/plot/plot.htm (October 2008).

The weak field dependence for magnetic field down to a few tesla also means that the current carrying capacity of an HTS coil in stand-alone condition, i.e. without a background magnetic field, is in the same order of magnitude as in the operating condition. This allows measurement of the current carrying properties in stand-alone, or self-field, condition without undue worry that the stored energy may damage the coil in the case of a quench. Concern about damage is often quoted as the argument to not test Nb_3Sn coils at self field. The ability to relatively easily test HTS coils at self-field will prove a useful tool in the investigation of the effect that the magnetic field angle

dependence, or anisotropy, of the current carrying ability of HTS conductors, as observed in small samples, has on the current carrying capacity of HTS coils.

Although HTS conductors remain superconducting to higher temperatures than LTS conductors, its current carrying capacity also decreases with temperature. To maximize the performance of HTS coils it is a natural choice to operate them at or near the same temperature as their LTS counterparts: 4.2 K in the case of atmospheric bath cooled magnets or between 1.8 and 2.2 K in sub-atmospheric helium baths.

To state the obvious: a high current carrying capacity at high magnetic field is a necessary but not sufficient condition for the successful application of HTS conductors in high-field magnets. The magnet technology must be drastically adapted to the specific material properties HTS conductors.

Specific challenges with BSCCO conductors originate in the thermo-mechanical treatment required to form the desired ceramic phase. This heat treatment can be performed before winding the coil, i.e. React & Wind, or after coil winding: Wind & React. A uniform heat treatment in pure O_2 with peak temperatures between 800 and 900 °C is required that requires tight control of temperature. The number of materials that can tolerate such a corrosive atmosphere is limited. Material selection is further reduced as the presence of even small amounts of many materials is associated with degradation of the superconductor [22, 23]. Most BSCCO conductors produced are composites consisting of poly-crystalline filaments inside an Ag or Ag-alloy matrix. The superconducting ceramic is brittle after heat treatment and susceptible to handling damage, while the strength of the matrix is typically below that of the matrix in LTS conductors. This is problematic as the hoop stress in HTS coils is larger than in LTS coils of comparable radii and current density on account of the higher magnetic field. Others at the NHMFL and OST have focused on the heat treatment itself [24, 25], while most of the work described here concentrates on the resulting mechanical and current carrying properties of BSCCO conductors in the context of application in high-field superconducting magnets.

Over the last two years ReBCO conductors from various manufacturers have approached or reached the status of commercial[7] product. These conductors feature thin-film technology on relatively strong substrates to form robust conductors. Scalability of the process and reduced material costs make ReBCO conductors potentially much less expensive than BSCCO conductors. The current carrying capacity is now large enough to make its measurement at self-field challenging; all promising factors. However, funding of ReBCO conductor development is mostly driven by applications in the power industry, which lead to a focus on applications at or some 10-30 K below 77 K and in AC applications. Conductor availability has been limited and relatively little systematic work relating to ReBCO conductor and coil characteristics at 4.2 K is published, despite inspiring results from the few small coils that were built and tested at 4.2 K [26, 27, 28]. ReBCO conductors are considered in this work as their availability allowed.

Anisotropy of the current carrying capacity of HTS conductors, briefly mentioned in the previous section, is not a problem in itself but a feature that requires a thorough understanding before an accurate prediction of the current carrying capacity of a coil can be made. The degree of anisotropy varies significantly between conductors depending on details of the production process.

[7] Commercial implies a reliable and practical product with a technologically relevant current carrying capacity, with homogeneous properties over its length and availability in quantities large enough for applications, in this case magnets.

1.3 Benchmark parameters

The intent of this paragraph is to outline a realistic range of dimensions for HTS insert coils in user magnets, identify relevant current density levels and present a first order estimate of the average stress in the HTS coil windings.

1.3.1 Magnetic field and current density

The magnetic field generated by a constant current density solenoid as sketched in Figure 1-5 is fully determined by the average current density[8] J_{ave} in the windings plus radial and axial dimensions of the windings. It is conventional to define the ratios:

$$\alpha = \frac{OR}{IR} \text{ and } \beta = \frac{0.5 \cdot height}{IR}, \tag{1-1}$$

in which *IR* is the inner radius of the windings, *OR* is the outer radius and *height* is the axial dimension of the windings. The magnetic field generated by such a solenoid is [29]:

$$B = \mu_0 \cdot J_{ave} \cdot IR \cdot \beta \cdot \left(a\sinh\left(\frac{\alpha}{\beta}\right) - a\sinh\left(\frac{1}{\beta}\right)\right), \tag{1-2}$$

with $\mu_0 = 4 \cdot \pi \cdot 10^{-7}$. Dimensions are in units of meters in equation 1-2.

For an infinitely long solenoid one has:

$$B_\infty = \mu_0 \cdot J_{ave} \cdot (OR - IR). \tag{1-3}$$

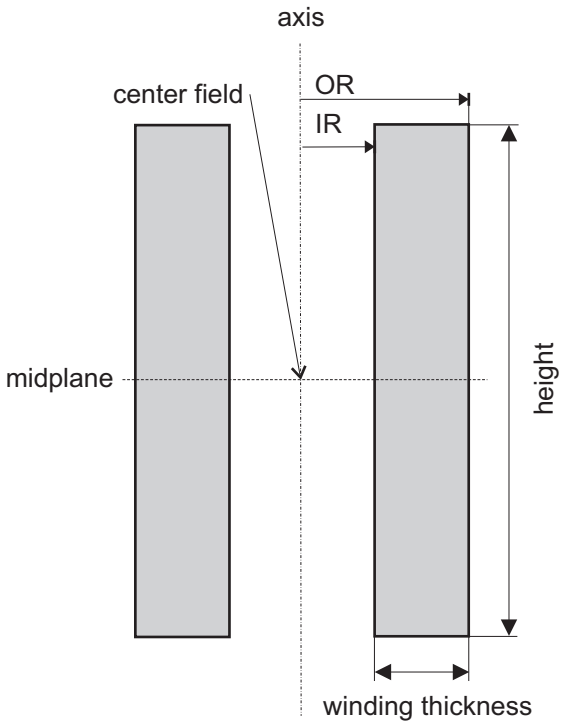

Figure 1-5. Sketch of a solenoid in cross section. The windings are indicated in grey.

An infinitely long solenoid operating at an average winding current density of 100 A/mm^2 thus generates 1.26 tesla per cm winding thickness, regardless of inner diameter. Most

[8] J_{ave} is explicitly defined in equation 2-3, section 2.2.

HTS insert coils built to date are tall relative to minimum volume coils [29] with a β value of about 3 and generating about 85% of B_∞ [9]. So one arrives at a convenient rule-of-thumb that a typical coil generates about 1 tesla per centimeter winding thickness if the average winding current density is 100 A/mm^2. This current density value is used as the benchmark value for HTS insert coils at the NHMFL [30][10]. Accordingly a total winding thickness of about 5 cm is foreseen for an HTS insert generating 5 T.

1.3.2 Diameters and stress

Superconducting research magnets are generally preferred to have a warm bore of at least 30 mm corresponding to a cold bore of at least 50 mm. To arrive at a useable bore size and allow for the NMR hardware typically required inside the bore, one arrives at a desirable warm bore of at least 50 mm and a cold bore above 90 mm in NMR magnets.

To estimate the outer diameter of HTS insert coils a hypothetical 25 T NMR magnet is considered. Taking the NHMFL 21.1 T NMR magnet without its inner Nb_3Sn coil, an outer diameter of 180 mm for a 5 T HTS insert remains[11]. Similarly, ForschungsZentrum Karlsruhe in Germany is developing a 25 T 50 mm cold bore magnet based on a 20 T, 180 mm bore LTS magnet [8][12]. In general, the windings of NMR magnets are expected to have larger radii than the windings of research magnets generating the same central field value. Also, the NHMFL Large Bore Resistive magnet and its cryostat are thus found to have a relevant cold bore and background magnetic field at 168 mm diameter and 20 T central magnetic field, which makes it a suitable system for testing of HTS demonstration coils.

In order to establish the order of magnitude of the hoop stress one can expect, a generic categorization of small, medium and large size coils is made for research and NMR magnets as presented in Figure 1-6. This categorization will prove a frame of reference when discussing observed current density and tolerance to hoop stress of HTS coils in chapter 6. The range of radii is taken slightly larger than discussed above. Inserts to research magnets are presumed to have one or more coils with radii in the small to medium range, while inserts to NMR magnets are presumed to consist of one or more coils with radii in the medium to large range. A hypothetical insert coil whose radial dimension would cover two ranges would generate 5 T if the average winding current density were 100 A/mm^2.

The hoop stress in each *turn* can be estimated as the product of radius, current density and axial magnetic field using equation 6-1. As shown in Figure 1-6, one can expect a hoop stress range of 45 to 160 MPa in 5 T insert coils in 25 T research magnets and 100 to 215 MPa in 25 T NMR magnets. Listing the lower end of the stress range as 45 MPa is somewhat misleading. Taking for example an imaginary coil with the minimum practical inner radius of 20 mm and assuming a minimum practical winding thickness of 13 mm, the estimated maximum hoop stress is 77 MPa. Thus the conductor used in such a coil should tolerate at least 77 MPa, not 45 MPa, to be considered a possible candidate conductor. So the maximum stress in each insert *coil* can be estimated as 77 to 160 MPa in insert coils of 25 T research magnets and 122 to 215 MPa in insert coils of 25 T NMR magnets.

---

[9] The average β of all coils in Table 1-2 is 3.1, generating 85% of B_∞ on average. See also section 4.3.
[10] NIMS targets 70 A/mm^2 for their 23.5 T NMR magnet program [31].
[11] See section 4.4.
[12] NIMS targets a lower total field (23.5 T) and smaller field increment of 2.4 T from an HTS insert in a smaller, 130 mm-21.1 T outsert [31].

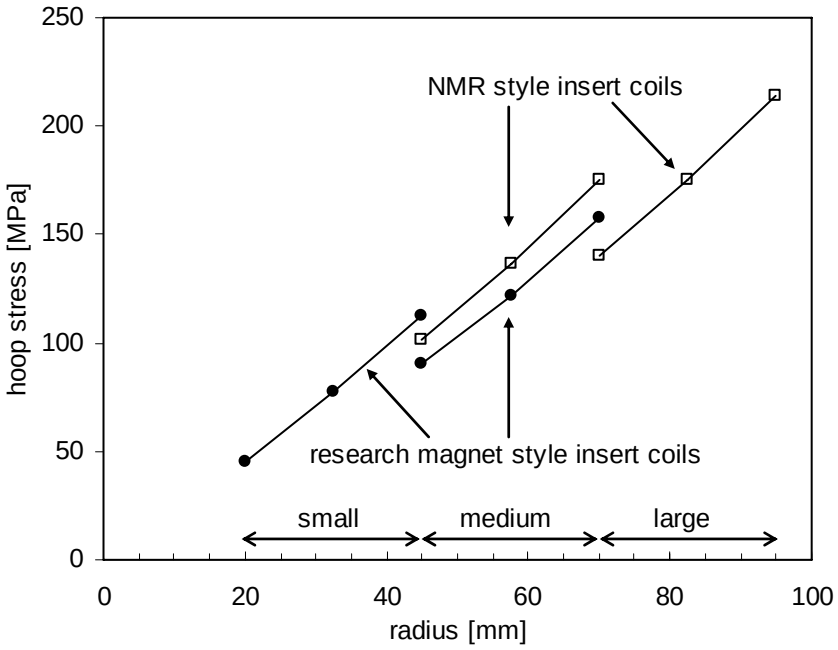

Figure 1-6. Generic estimation of the hoop stress in insert coils to 25 T magnets. The average current density in the windings is taken as 100 A/mm^2.

The quoted stress values are averaged over the windings, so including conductor, insulation, epoxy and reinforcement materials. Peak stress in the conductor can be higher or lower depending on the mechanical properties and relative amounts of the conductor, insulation and reinforcement in the windings. The turns are also not mechanically independent in a typical epoxy impregnated coil, leading to a redistribution of local stress and strain in the windings and typically higher peak values.

To compare the stress levels in different coils, the hoop stress at the outer diameter is used. This stress value is not intended as an accurate representation of the maximum conductor stress in each coil, although it is a reasonable approximation, but it serves as an unambiguous measure of stress to create a relative ranking of coils from low to high stress. The hoop stress value at the outer diameter, explicitly defined in equations 6-7 and 6-8, is also calculated for all actual coils discussed in this work. The results for nearly all BSCCO and ReBCO coils fall in the range of ~ 30 to 215 MPa, so the classification appears relevant. The highest value of 245 MPa is observed in a ReBCO insert. All values are either tabulated in Table 1-1 or presented graphically in Figure 6-9.

30 T magnets

An insert generating 5 T operating at J_{ave} = 100 A/mm^2 in a 20 T background magnetic field would hypothetically generate a field increment of 10 T for a total of 30 T if J_{ave} = 200 A/mm^2. The Lorentz-force induced stress would be a factor of 2 to 2.4 higher as the magnetic field in the coil is up to 20% higher at a given radius and the winding current density is doubled. The amount of conductor reinforcement would also have to be doubled, requiring an increase in conductor J_e to compensate for the reduced packing factor. Thus one can state that to upgrade a 5 T insert to 10 T requires a conductor that carries at least twice the current density and is more than twice as strong. A more elaborate discussion follows in section 6-7.

1.4 Brief history of insert coils

To place this work in context, a survey of HTS insert coils is given. Almost all coils are demonstration coils and exceptions are noted in the text. Key parameters of the coils are presented in Table 1-1 and a chronology of central magnetic field and average current density in the windings is given in Figure 1-7.

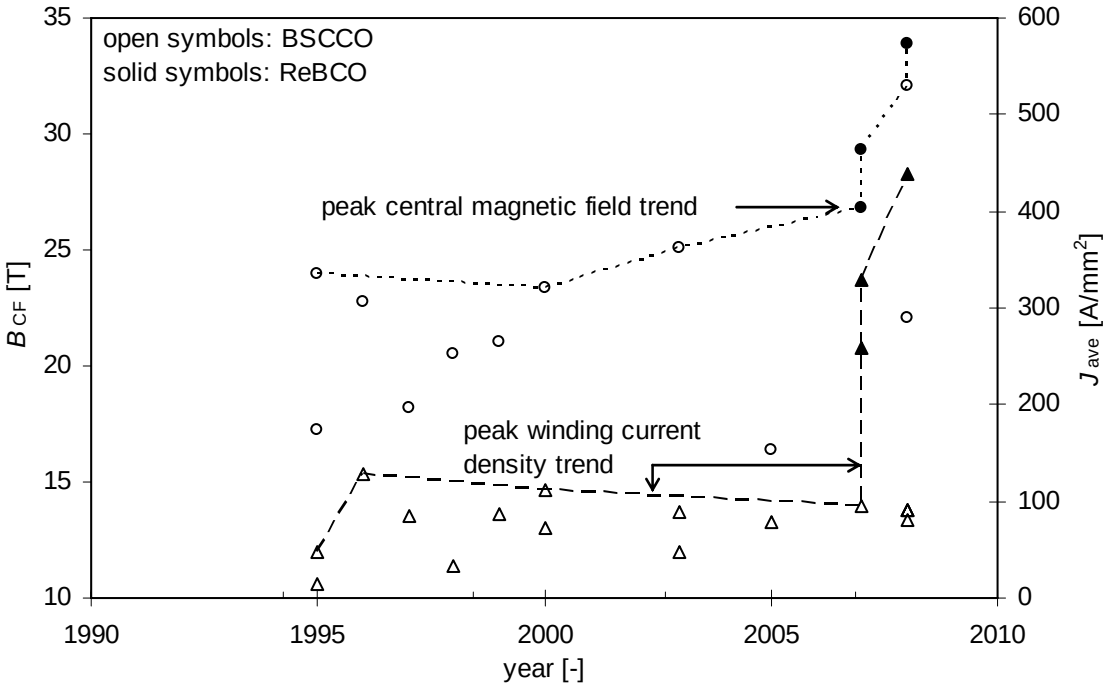

Figure 1-7. Chronology of peak central magnetic field (circles) and average current density in the windings (triangles) in HTS insert coils. The years with a downward trend in peak B_{CF} and J_{ave} generally coincide with increasing coil size and increasing field increment generated. The rapid increase in peak B_{CF} and J_{ave} in the last 2 years is attributed to small ReBCO coils complemented by a Bi-2212 wire wound coil that achieved the second-highest central field value to date.

After the discovery of high-temperature superconductors in 1986 [32], their potential application in high-field magnets was generally recognized, including by NSF Panel on Large Magnetic Fields [2]. The founding charter of the NHMFL [33] was in part based on this document. It included a charge to expand resistive and pulse magnet technology, create a 21.1 T superconducting LTS NMR magnet and a follow-up 25 T LTS-HTS NMR magnet. Since then a program under various names has been in place at the NHMFL to characterize HTS conductors and later to develop HTS magnet technology.

The first significant HTS insert coil was developed by Sumitomo, tested at the Francis Bitter National Magnet Lab at MIT and published in 1995 [34]. This sizeable coil with a useable bore size generated 1.5 T in a background magnet for a central field of 24 T, a value that would not be exceeded until 2003 with the 5T insert. The current density in the windings is about half the benchmark value, although this is likely the first HTS insert requiring reinforcement to prevent strain degradation on account of the relatively weak

pure Ag matrix. The first HTS insert tested at the NHMFL was developed by Intermagnetics General Corporation. (IGC)[13] [35].

The Japanese national magnet lab, now part of NIMS[14], embarked on a program towards a 23.5 T LTS/HTS NMR magnet, in collaboration with industry. Several small coils were tested in the 21.1 T, 50-mm bore superconducting magnet of the Tsukuba Magnet Lab [36]. One of the noteworthy coils was developed by Hitachi [37], exceeding the 100 A/mm^2 benchmark for the average winding current density. A comparably sized coil of similar construction built at the NHMFL in collaboration with OST approached that benchmark [38, 39]. Both coils could use unreinforced pure-Ag matrix conductor as the outer diameter is small and the hoop stress relatively low. Their bore sizes are considered too small though to be useful for applications.

In 1998 the NHMFL Large Bore Resistive Magnet plus a cryostat with a 168 mm cold bore became available at the NHMFL. The first HTS insert tested in this system was developed by IGC and targeted at a field increment of 2.5 T in a 19 T background magnetic field [40]. This is the first sizeable HTS coil to use layer wound tapes and radial sectioning to limit hoop stress. Relatively low-cost dip-coated tape conductor is used instead of the more common Powder-In-Tube material. However, in-field testing revealed degraded performance in a section, presumably resulting from exceeding the bend strain tolerance of the conductor. Later tests using separate power supplies for the sections [41] indicated that this coil could have generated about 2.2 T in the absence of this degradation. A year later an NHMFL/OST developed HTS insert achieved its intended field increment of 3 T, although winding current densities are still below 100 A/mm^2 and electrical shorts resulting from the ceramic interacting with the insulation during heat treatment resulted in a high rejection ratio of double pancake units [42]. Also, the free bore size is not technologically useful. Conductor strain is effectively managed through radial sectioning and employing dispersion hardened AgMg alloy in the matrix of the conductor in the two sections with the largest radii.

By 2000 Hitachi had developed the first and possibly the only HTS coil that became part of a high-field user magnet [43]. It replaced the inner Nb_3Sn section of the NIMS 21.1 T superconducting magnet to create a new 50 mm bore 21.1 T LTS/HTS high-field magnet that was operated for 1.5 years[15]. This HTS coil meets the NRIM average current density target of 70 A/mm^2 in the windings for a 23.45 T NMR magnet. The maximum hoop stress is estimated at 100 MPa requiring the use of co-wound AgMg tape to reinforce the superconductor. Slight degradation of the coil performance is observed due to thermal cycling after operation at 2 K [44]. Another Hitachi-developed HTS insert reminiscent of their 1996 coil is operated in this 21.1 T background field creating a field increment of almost 2 T for a record central field of 23.42 T [43, 14].

Meanwhile Hitachi also developed round Bi-2212 conductor by extrusion of their Bi-2212 tapes restacked in Ag or AgMg alloy tubes. These conductors showed relevant current density levels and little anisotropy. Layer wound solenoids equipped with persistent current switches were tested [43]. However, Hitachi ended their Bi-2212 activities before any round-wire solenoids were tested in background magnetic field, terminating the most promising HTS magnet technology development activity at the time.

---

[13] Now SuperPower Inc., a company owned by Philips Nederland BV.
[14] National Institute for Material Science, at the time named National Research Institute for Metals (NRIM).
[15] Nb_3Al and Nb_3Sn inserts were successively installed, illustrating the concurrent use of this user magnet as test bed for insert coil testing.

Table 1-1. Properties of HTS demonstration magnets.

Section	**Material**	**Technique**	**Reinforcement**	**Conductor length**	***ID-OD*× winding height**	$B_{outsert}+\Delta B_{insert}=B_{center\ field}$	I_{op}, J_e, J_{ave}	σ_{OD}
unit				m	mm, mm, mm	T,T,T	A, A/mm^2, A/mm^2	MPa
1995, Sumitomo/MIT [34]								
	Bi-2223	R&W, DP 3 in-hand	co-wound SS tape	1200	40-108×113	22.5+1.5=24.0	117, 194, 48	58
1995, IGC 5 Double Pancakes [35]								
	Bi-2223	W&R, DP 2 in-hand	-	100	26-46×72	17.0+0.2=17.2	56, 42, 14	5
1996, Hitachi **[37]**								
	Bi-2212	W&R, DP		28	17-45×45	21.0+1.8=22.8	281, 225, 128	60
1997, NHMFL/OST 1T insert [38, 39]								
	Bi-2212	W&R, DP	-	74	16-46×40	17.0+1.2=18.2	67, 110, 85	33
1998, IGC/NHMFL 2.5 T insert [40]								
A	Bi-2212	W&R, LW 3 in-hand	glass fiber	528	54-82×200	19.0+1.5=20.5	112, 68, 33	26
B				858	89-121×200		112, 68, 31	36
C				924	127-152×200		112, 68, 32	46
1999, NHMFL/OST 3T insert [42]								
A	Bi-2212	W&R, DP	-	184	16-46×96	19.0+3.0=21.0	66, 110, 86	38
B	Bi-2212	W&R, DP	-	383	57-87×98		49, 79, 57	47
C	Bi-2212	W&R, DP	-	467	97-127×75		44, 70, 51	62
2000, Hitachi/NIMS [14, 43]								
A	Bi-2212	W&R, DP	co-wound AgMg tape	1000	64-147×220	18.0+5.4=23.4	217, 128, 73	97
B	Bi-2212	W&R, DP 2 in-hand	co-wound AgMg tape	34	17-48×63		334, 145, 112	48
2003, NHMFL/OST 5T insert [45, 46]								
A	Bi-2212	R&W, DP	co-wound SS tape	801	41-96×185	19.9+5.1=25.1	120, 120, 89	85
B				1034	106-146×185		120, 120, 86	125
C		R&W, LW		269	156-165×209		120, 120, 69	114
2003, MIT360 [47]								
	Bi-2223	R&W, DP	3-ply, SS tapes	2130	82-119×325	7.5+1.3=8.7	51, 82, 48	21
2004, HOMER II [48]								
	Bi-2223	R&W, DP	3-ply, SS tapes	2037	60-90×150	11.5+5.4=16.9	151, 137, 91	94
2005-2007, MIT700 [49, 57]								
	Bi-2223	R&W, DP	3-ply, SS tapes	2192	78-127×416	14.1+2.4=16.5	116, 139, 79	70
2006, ISTEC [27]								
	GdBCO	R&W, LW	-	54	30-71×44	0.0+5.7=5.7	895, 558, 328	-
2007, SuperPower **(SP-YBCO)** [28]								
	YBCO	R&W, DP	-	430	19-87×52	19.0+7.8=26.8	175, 458, 259	215

Continued on next page

Table 1-1. Continued. Properties of HTS demonstration magnets.

Section	Material	Technique	Reinforcement	Conductor length	*ID-OD*× winding height	$B_{outsert}+\Delta B_{insert}=B_{center\ field}$	I_{op}, J_e, J_{ave}	σ_{OD}
unit				m	mm, mm, mm	T,T,T	A, A/mm^2, A/mm^2	MPa
2007, ISTEC [53]								
	GdBCO	R&W, LW	-	12	18-36×84	28.3+1.0=29.3	115, 128, 96	49
2008, Oxford instruments [56]*								
	Bi-2212	R&W, LW	-	50	25-45×100	20+2.1=22.1	257, 145, 92	41
	Bi-2212	R&W, LW	-	94	55-75×100		257, 145, 92	69
2008, NHMFL (NHMFL-YBCO) [55]								
	YBCO	R&W, DP	-	36	24-36×46	31.0+2.8=33.8	325, 580, 460	245
2008, NHMFL-Bi2212 [55]								
	Bi-2212	R&W, LW		66	15-38×100	31.0+1.1=32.1	120, 153, 80	47

* Most parameters for this entry are estimated due to limited published information.
Abbreviations and terminology: *ID* is the inner diameter, *OD* is the outer diameter, I_{op} is the transport current, J_e is the conductor current density, J_{ave} is the average current density in the windings (see also section 2.1.1), σ_{OD} is the hoop stress at the outer diameter as introduced in section 6.4 and calculated using equations 6-7 and 6-8, W&R is Wind-and-React, R&W is React-and-Wind, *n*-in hand refers to the numbers of co-wound conductors that form a single turn, DP is double pancake, LW is layer wound, SS is stainless steel, 3-ply is a 3-layer sandwich of reinforcement, conductor and reinforcement.

In 2003 the NHMFL/OST 5T insert is the first to reach the 25 T central field benchmark, with the Large Bore resistive magnet providing 20 T background magnetic field [45, 46]. The current density in the conductor is moderate compared to some other conductors, requiring efficient strain management and a thorough understanding of the anisotropy in the current density in order to realize the target field increment in the available volume. However, this insert is intended to operate at or near its critical current density, unlike the next two inserts, and its outer diameter is larger than that of any other insert. Consequently, the hoop stress levels at the outer radius in two of its three sections are significantly higher than in any other insert coil. Strain management is based on radial sectioning and co-wound stainless steel reinforcement tapes. The peak stress in the reinforced conductor exceeds 200 MPa. Initial plans to avoid bending strain by using the Wind&React process were abandoned as electrical shorts resulting from the ceramic interacting with the insulation during heat treatment could not be solved at the time. Increased understanding of the conductor properties under bending stain allowed the use of the React&Wind technique to diameters previously considered too small for the conductor thickness. At 38 mm the bore is the smallest size considered reasonable for a research magnet.

The same year the first NMR spectrum is obtained, albeit of poor quality and at a relatively low central field of 7.5 T, at MIT using an LTS/HTS superconducting magnet [47]. Bi-2223 conductor is now a commercial product. The conductor used in the above magnet is produced by the market leader at this time, American Superconductor Corporation, and has proven potential for high-field applications[16]. It consists of a Bi-2223 tape sandwiched between two stainless steel tapes through a soldering process. This provides both reinforcement against hoop stress and unprecedented protection against handing damage of the conductor. It does not protect against penetrating superfluid

[16] This product is represented by conductor A in this work.

helium however, as is observed by the HOMER II team, as they destroyed a 5 T insert intended to be part of a 25 T superconducting user magnet [48]. This mishap highlights the necessity to test as realistically as possible at a small scale, like operating at 1.8 K instead of 4.2 K, before moving to a larger scale in the process of technology development.

From 2005 to 2007 the MIT team built a near replica of the above mentioned coil and operated it at 4.2 K in a 14.1 T background NMR magnet with the intent to quantify field homogeneity rather than achieving maximum central field [49]. Magnetization currents in the HTS tape conductor were found to be limiting [49, 50, 51]. In a similar effort, a layer wound Bi-2223 coil with brass laminated tape from Sumitomo was installed in a 500 MHz /14.1 T NMR system and approached solid-state NMR suitable field quality in a driven mode with a highly stabilized power supply and NMR feedback after allowing 2 weeks for the magnetization currents to recede [15].

Where four out of the last five insert coils each contained more than 2 km of BSCCO conductor, the first ReBCO coils generate comparable or larger magnetic field increments with far less conductor [27, 28, 52]. These coils feature winding current densities at least double the highest values observed in BSCCO coils despite a nearly non-existent development activity specific to ReBCO coils. Even the most basic data with which to reasonably predict the coil current density are lacking, as well as reliable and tested procedures for coil construction. It is noteworthy that the coil built at ISTEC [27] is not operated in a background magnetic field, so strain levels are low. This coil is not impregnated with epoxy and turns are observed to have shifted during testing. This is both a testament to the resilience of the conductor, as BSCCO and Nb_3Sn conductors would likely have failed under these circumstances, as to the lack of ReBCO coil technology development. Furthermore, the current carrying capacity of the coil built by SuperPower [28] is degraded due to conductor damage during coil construction but it still exceeds by far the highest winding current density observed in BSCCO insert coils.

No coil technology development is reported for the latest ISTEC ReBCO insert [53] which, operated in a narrow bore 28.3 T Hybrid magnet, brings the maximum central field inside an HTS insert to 29.3 T. This is tantalizingly close to 30 T, although the winding current density appears to be modest at just below 100 A/mm^2 compared to the two ReBCO insert mentioned above. The coil performance is reportedly well below short sample performance and limited by conductor damage near the terminals [54]. A comparably sized YBCO insert is constructed at the NHMFL and operated in a 31 T resistive magnet. Thus an HTS insert coil is operated above 30 T for the first time. More remarkable is the winding current density of 460 A/mm^2 at 33.8 T, which is nearly double the winding current density in the previous record value demonstrated in ReBCO insert coils and four times that of the best BSCCO insert coil, while this insert operates in significantly higher magnetic field [55]. Cryogenic complications[17] caused an elevated coil temperature, limiting the coil performance to well below projections based on short sample performance at 4.2 K. The potential of ReBCO conductors to lead to strong, compact superconducting magnets is however clearly established while research and development specific to ReBCO insert has barely started.

ReBCO coated conductors are inherently strong, greatly alleviating the strain management task in coil design as discussed in section 1.1.3. Coated conductors tend to be thin, highly aspected tapes. No clear path presents itself to develop the round or rectangular conduc-

[17] Discussed in detail in section 2.1.4.

tors preferred for reasons of field quality in NMR magnets for example. Most required technology aspects, outside current density and strength, remain to be proven. The first of two successful layer wound HTS inserts with round wire was recently announced [56] and seems to indicate that the problem of ceramic leakage during heat treatment of Bi-2212 Wind&React coils can be solved. The average current density in the windings is close to 100 A/mm^2 and the free bore size of the larger of the two coils is useful. Although the peak field is no record for an all-superconducting system, it does clearly present Bi-2212 round wire as the only HTS candidate conductor with the desired low-aspect-ratio cross section for high field-quality magnets. A second Bi-2212 wire-wound Wind&React coil, built at the NHMFL, achieved a similar current density in a 31 T background field of a resistive magnet for a total of 32.1 T. The latter coil operated at ~ 70% of the projected current density based on short sample properties, which is a large fraction compared to previous Wind&React Bi-2212 wire and tape coils, further illustrating the progress in development and potential for application in high-field magnets of Bi-2212 wire [55].

1.5 The 5T insert

The goal of the "5T" project is the design, construction and testing of an insert coil using OST Bi-2212 tape conductor with a target field increment of 5 T. The intent of this project is to advance BSCCO magnet technology and demonstrate the potential of this conductor for magnet applications. To maximize the technology development, early concepts of the design encompassed three concentric sections: a Wind&React inner section, a React&Wind middle section with reinforced conductor and a layer wound outer section. However, the React&Wind approach proved not feasible as described above in the history section (1.4). Therefore, the React&Wind approach is chosen for the inner section as well. The free bore is set to the smallest value that seems reasonable for a possible future 25 T research magnet. The design brief is summarized in Table 1-2. A picture and a schematic cross-section of the 5T coil is given in Figure 1-8.

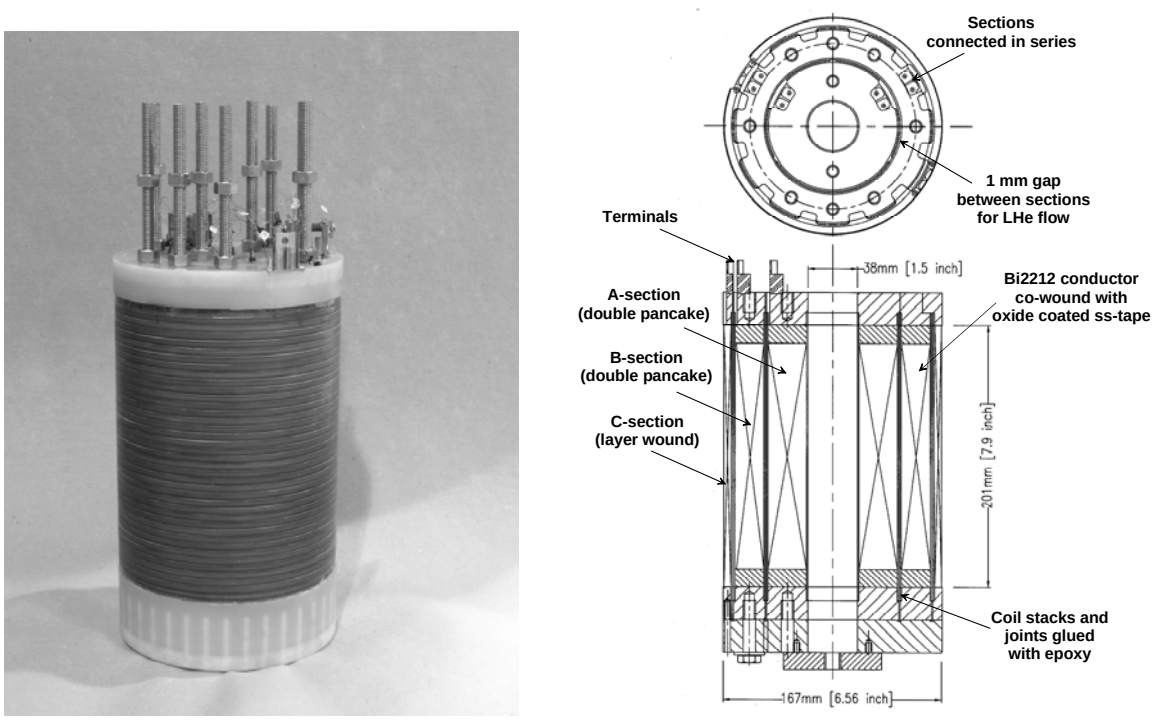

Figure 1-8. Picture of the 5T insert (left) and cross-sectional schematic (right). Pictures of the A and B sections individually are presented in Figure 5-5.

Table 1-2. Design brief of the 5T insert coil.

Parameter	Value	Comment
Field increment	5 T	In a background of 19 or 20 T
Free bore	39.1 mm	1 mm larger than 38.1 mm (1.5 inch)
Outer diameter	< 168 mm	Determined by the cryostat for the background magnet
Maximum conductor strain	0.36%	Critical strain = 0.4%
Number of radial sections	3	Mechanically independent, electrically in series
Reinforcement	Co-wound 28 μm thick stainless steel tape	Commercial product, nominally 25.4 μm (0.001 inch thick)
Turn-turn insulation	MgO-ZrO_2	Applied to reinforcement
A and B section	React&Wind, double pancakes with co-wound reinforcement	Winding thickness as large as strain tolerance allows
C section	React&Wind, layer wound with co-wound reinforcement	Minimal winding thickness to reduce risk
Background magnet	NHMFL Large Bore Resistive Magnet at 19 T	Later set up to operate at 20 T

Design aspects

A conductor cross section of 0.2 by 5 mm was selected as the standard for this project based on the properties of an early production run of a batch with 19 filaments and a mixed Ag and AgMg matrix rolled to different widths. The resulting difference in microstructure is shown in [24].

The process to determine the coil geometry, achievable current density and stress-strain distribution is iterative. Calculations are periodically updated as more data become available. The final radial dimensions are listed in Table 5-2. The number of double pancakes and their stacking order is determined shortly before assembly of the stacks, based on the measured properties of all available units, as described in chapter 5.

The initial design is based on an average current density in the winding of 89 A/mm^2, and a packing factor of 71%. The corresponding operating current density in the conductor for a field increment of 5 T is 126 A/mm^2. Thus this insert is intended for operation at a relevant magnetic field and current density levels and therefore at realistic stress levels for high-field HTS inserts, with a realistic bore size. Achieving the benchmark central field of 25 T with this bore size would be unprecedented[18]. Strain management is required as the hoop stress would otherwise irreversibly degrade unreinforced conductor. The specified conductor current density is slightly above the levels routinely observed in the conductor from the supplier at the outset of the 5T project, thus requiring conductor improvement as well as efficient strain management and operation at small safety margins in order to meet the target field increment and central field value.

1.6 Scope of the thesis

Characterize available conductor considering the primary properties that are relevant to application in 25 T class superconducting magnets and beyond, specifically the limits that magnetic field and strain place on the current carrying capacity of HTS conductors. The conductor selection includes but is not limited to reacted Bi-2212 tape conductor from

[18] To date no insert with comparable or larger bore size has achieved a higher central field value.

Oxford Superconducting Technology (OST). Most of the conductors studied in this work are BSCCO tapes, reflecting the state of the art at the onset. Bi-2212 round wire and ReBCO coated conductors are considered as their availability allowed.

Verify the suitability of a model based on the average grain misalignment to describe the anisotropy in the magnetic field dependence of the current carrying ability.

Correlate the conductor limits to the current carrying limits of small coils in a background magnetic field, carefully separating the reversible magnetic field effects from the irreversible strain effects. The intent of developing this correlation is twofold. The first intent to develop the ability to accurately predict the current carrying ability of larger coils in general and specifically a Bi-2212 tape insert intended to generate 5 T in a 20 T background magnetic field for a central field of 25 T. The second intent is to study the behavior of HTS inserts beyond the irreversible strain limit in general and predict the onset of strain induced irreversible degradation in the 5T insert to determine if the radial dimensions and conductor reinforcement chosen in the baseline design are adequate and efficient.

Determine in general the effect of the degree of anisotropy in the magnetic field dependence of the current carrying capacity on the design optimization process of HTS inserts to 25 T magnets.

Build and test inserts, using the developed technology, and demonstrate the proof of principle for 25 T class insert coils.

Chapter 2 introduces terminology, equations and experimental methods for determining the critical current density, stress and strain in short samples and coils. The conductors used are described and key properties tabulated.

Chapter 3 deals with the magnetic field dependence and anisotropy of the critical current density and *n*-value in short samples at 4.2 K from self-field to peak values between 30 and 45 T.

Chapter 4 discusses the effect that various degrees of anisotropy in the magnetic field dependence of the critical current have on the design process. The degree of anisotropy varies from conductor to conductor and determines which parameters are important and unimportant in the optimization of an HTS insert in a 25 T magnet.

Chapter 5 deals with the insights gained in chapter 3 when applied to model the magnetic field dependence of the critical current density of two small coils. Also the relation between the critical current density of conductors at self-field and coils at self-field made from this conductor is investigated. This leads to qualification criteria for candidate conductors and coils for the 5T insert and a prediction of the magnetic field dependence of the critical current density of the 5T insert based on the known properties of its constituent coils. The prediction is then compared with measured properties of the 5T insert coil.

C*hapter 6* presents the effect of stress and strain on the critical current density. The effects of bending strain and uni-axial tension on short samples are studied separately, leading to estimations of the maximum bending strain in the conductor versus bending radius and determination of the critical tensile strain values for a set of conductors. Seven mostly small coils from these conductors are subjected to increasingly larger hoop stress to observe the onset and propagation of strain induced critical current density degradation. The observed behavior is compared with short sample behavior using calculated bending strain values and a simulation model to calculate hoop stress and strain, to assess the

predictability of strain induced degradation. Four out of these seven coils are prototype or candidate coils for the 5T insert and their strain tolerance is compared to the 5T qualification criteria. Finally the measured critical current density in the 5T coil at high strain levels is compared to the predictions.

Chapter 7 provides the conclusions.

A *Summary* of the thesis and an *outlook* on 30 T superconducting magnets form the final section.

2 Experimental methods

This chapter covers the definitions used and experimental methods applicable to the experiments in this work; specifically those related to critical current density, stress and strain in short samples and coils. A list and description of the superconductor samples is given.

2.1 Conductors investigated

Nine conductors are introduced: three Bi-2223 tapes, three Bi-2212 tapes, a Bi-2212 round wire and two YBCO coated conductors. Most of these are candidates for high-field magnet applications. For two additional YBCO coated conductors data were taken from the literature. Key parameters of the conductors are listed in *Table 2-1*.

2.1.1 BSCCO powder-in-tube conductors

All BSCCO conductors considered here are produced by the so-called powder-in-tube method. The ceramic starting powder is packed in a silver tube, drawn and shaped to a hexagonal cross-section. These tubes are cut and the desired number is stacked inside a silver or silver-alloy[19] tube for a second round of drawing steps to reduce the cross-sectional area to the desired size. The tubes fuse together during these deformation steps and the resulting structure which surrounds the ceramic filaments is referred to as the matrix. Examples of the resulting structures can be seen in several of the images below. Bi-2212 wires are drawn to size, while a switch is made from drawing to rolling at a certain diameter for BSCCO tape conductors. Bi-2223 conductors require intermediate heat treatments precluding the option of using the conductor in Wind&React applications. Bi-2212 conductors require a partial-melt heat treatment that can be executed either before of after coil winding (React&Wind and Wind&React respectively). However, all coils considered in this work are React&Wind. A more detailed description of BSCCO conductor production and conductor properties is given in [58].

Whereas the ceramic carries the current when superconducting, the matrix provides strength to the conductor, stability in the case the current carrying capacity[20] J_e is exceeded and environmental protection for the ceramic. Oxygen diffuses through the matrix during heat treatment and thereby allows the formation of the desired superconducting phases. Some of the oxygen reacts with the alloying elements in the silver matrix to form nanometer sized oxide particles that strengthen the matrix in a process referred to as oxide dispersion hardening. If a pure silver matrix is used, it will be soft and fully annealed after heat treatment. Such conductor will certainly require reinforcement if it is considered for application in high-field magnets, whereas conductors with a strengthened matrix require less or no reinforcement.

The ceramic filaments form a poly-crystalline structure with a three-dimensional distribution of plate-like grains. Grain connectivity can be limiting J_e, leading to a magnetic field dependence of J_e that is partially determined by inter-grain properties and partially by intra-grain properties. Small-angle grain boundaries are the least limiting, so the preferred microstructure is one with aligned grains. Intra-grain current density is

[19] Mn, Zr and Au are commonly used.
[20] Definitions of J_e and I_c are given in section 2.2.

largest within the plane of the platelets and flux pinning is optimized if the flux lines are within the same plane [59]. Considering that the magnetic flux lines penetrating the conductor in an HTS insert magnet is predominantly parallel to the tape we arrive at a desired microstructure in which all grains are parallel to the flat surface of the tape. The degree in which conductor manufacturers are able to achieve this goal varies, and grain misalignment, porosity and undesirable ceramic phases can readily be recognized in cross sectional images of even the best available conductor. While the ceramic content can range from ~ 15-50% of the conductor cross section, only a small fraction of the grains carry significant current, as evidenced by the fact that the current density averaged over the filaments is significantly below current carrying capacity of single grains. The transport current tends to follow a meandering path which can be unambiguously observed with magnet-optical imaging.

Conductor A

Conductor A, see Figure 2-1, is a commercial product of the American Superconductor Corporation Inc. (AmSC). In the year 1999 this conductor represented the state-of-the-art in BSCCO conductor technology with a specified I_c at 77 K of at least 110 A and excellent uniformity. It was sold with thin stainless steel reinforcement strips soldered to the flat sides, which is referred to as the three-ply geometry. These strips protect the superconductor against handling damage and forces exerted on the conductor during operation. These are important practical aspects for candidate conductors to HTS insert magnets although this conductor was not specifically targeted for high magnetic field applications. The strips are removed before J_e measurements on short samples and not considered part of the cross-section of the conductor but a form of external reinforcement. Coils are wound with the conductor as-received. This conductor has the highest critical current density, fill factor and *n*-values of the BSCCO tape conductors investigated in this work.

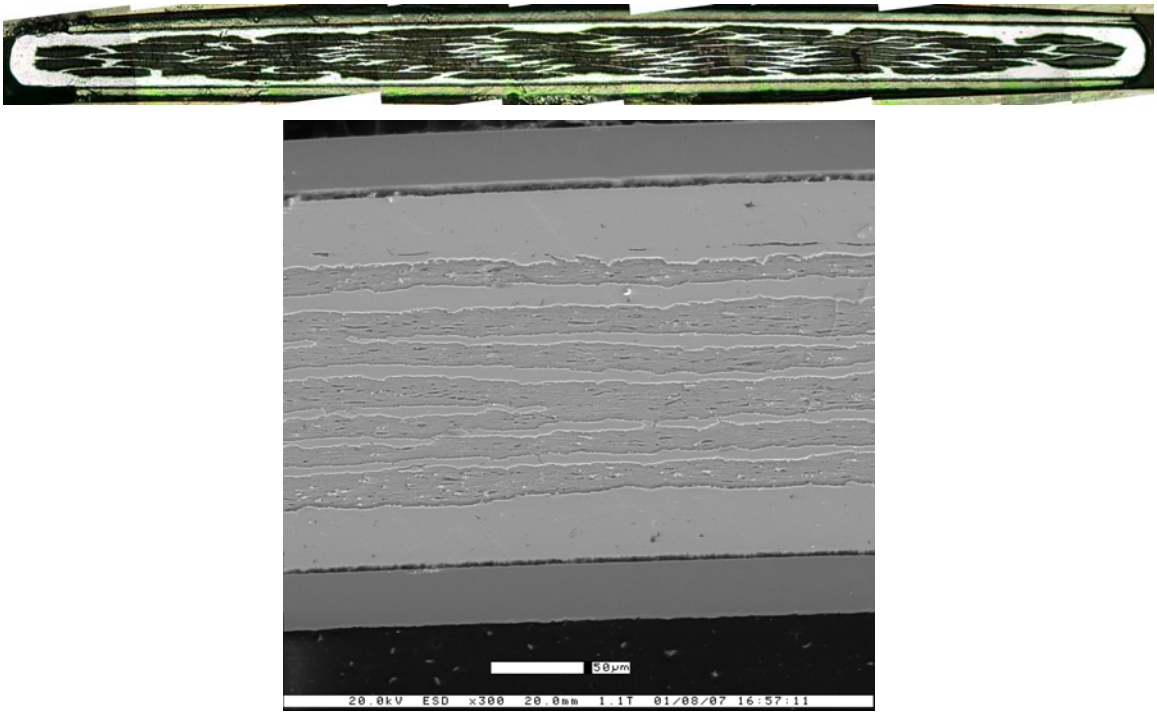

Figure 2-1. Transverse (above) and longitudinal (below) cross-section of conductor A (4.1 by 0.3 mm).

Conductors B and C

Conductors B and C, see Figure 2-2, each represent one batch of conductors specifically produced for the 5T insert magnet project, a joint research and development effort of the NHMFL and Oxford Superconducting Technology (OST) [60]. This Bi-2212 conductor, produced by OST, can be applied in both React&Wind and Wind&React applications. Batch to batch variations occur with this conductor and appear to be mostly related to carbon content in the ceramic powder before heat treatment. Carbon content measurements, all performed by third parties, range from 200 to 500 ppm but lack reliability and reproducibility. The exact source of batch-to-batch variations therefore remains elusive.

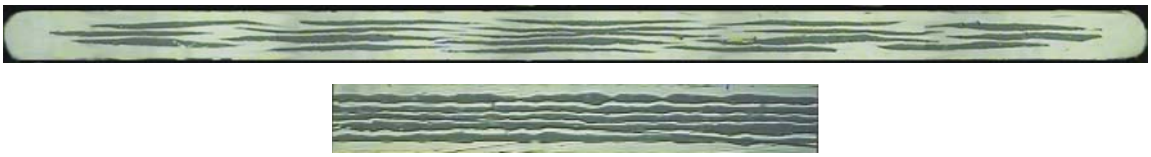

Figure 2-2. Transverse (above) and longitudinal cross-section (below) of conductors B and C (5.0 by 0.2 mm).

Conductor D

Conductor D, also produced by OST, is similar to conductors B and C in geometry and details of the production process [25]. The ceramic starting powder however is slightly different and produced by a different company (Nexans instead of SCI).

Conductor E

Conductor E is a Bi-2212 round wire produced by OST [61]. Its 7×85 filament architecture makes it the only double-stacked conductor and results in a fine filamentary structure with ~ 14 μm diameter filaments before heat treatment, as shown in Figure 2-3. Significant bridging occurs between the filaments during heat treatment. While thus lacking the grain alignment generally associated with high current density in Bi-2212 and Bi-2223 tapes [62, 63, 64], it shows a surprisingly high current density at high magnetic field after a very limited conductor development effort as compared to BSCCO tapes.

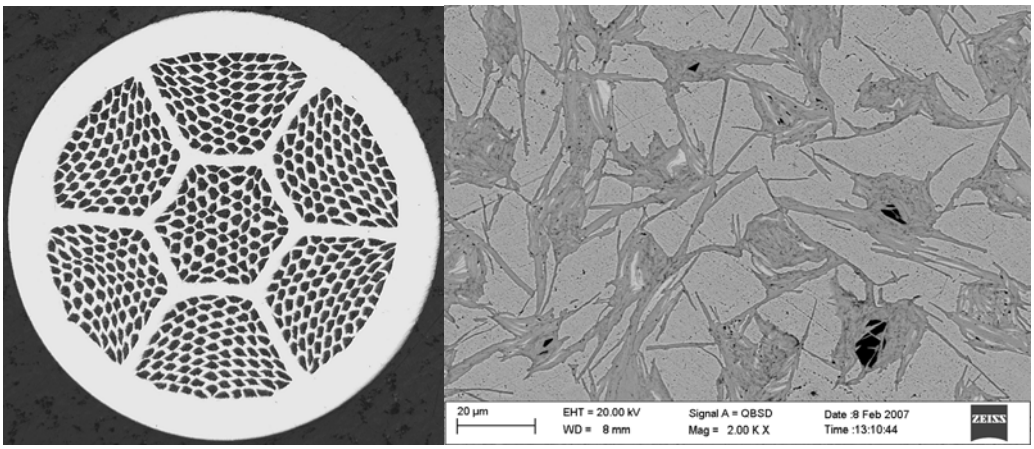

Figure 2-3. (left) Transverse cross section of conductor E (0.8 mm diameter) before heat treatment;(right) Detail of the cross section after heat treatment. The scale bar on the lower left represents 20 μm.

Bi-2212 wire is among the few HTS conductors worldwide that is predominantly developed for high magnetic field applications. The absence of large anisotropy and the ability of making low-aspect ratio wires and conventional cable technology to arrive at multi-kA conductors are essential features and justifies further development.

Conductor H

Conductor H, see Figure 2-4, is a commercial grade "Zerome Hercules" Bi-2223 conductor from the former Nordic Superconductor Technologies A/S (NST) [58].

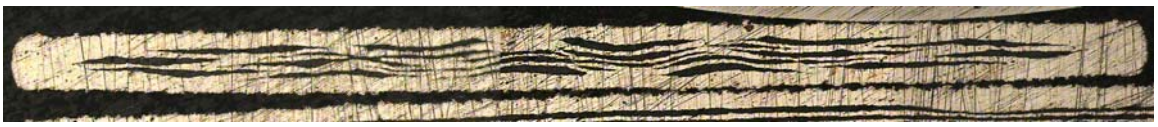

Figure 2-4. Transverse cross-section of conductor H (3.0 by 0.18 mm).

It was produced in 1998 under manufacturer's batch number 81214 NHM and targeted for application in the electrical utility industry. Its strength and current carrying capacity are sufficient to consider it a candidate conductor for high-magnetic field applications.

Conductor I

Conductor I, see Figure 2-5, is a Bi-2223 tape conductor from an early phase (1998-1999) of conductor development at the Korea Institute of Machinery and Materials (KIMM) [65]. Characteristic features are a relatively low fill-factor, relatively low current density and a pure Ag matrix resulting in a soft and weak conductor. While this conductor is not suitable for applications in insert magnets, it is interesting to study as its characteristics allow the operating current in coils to exceed the critical current density by a much larger factor than for any other conductor considered here.

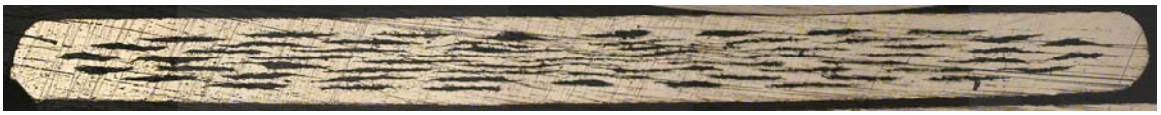

Figure 2-5. Transverse cross-section of conductor I (4.1 by 0.32 mm).

2.1.2 ReBCO conductors

The superconducting ceramic in coated conductors is often YBCO, but Y can be partially or completely substituted with Gd, Sm, Eu, Dy or Nd, so the more generic expression ReBCO (Re refers to the Rare earth elements) is used here. Many alternate production processes are in use and under development, which is reported on extensively in the literature but is outside the scope of this work. The resulting conductor architecture generically features a metallic buffer layer of 50-150 μm thickness, at most a few μm of ceramic buffer layers, one or a few μm of ReBCO, and a protective Ag cap layer of several μm. The tensile mechanical properties of the conductor are mostly determined by the properties of the substrate. Environmental protection of the superconducting ceramic is provided by the buffer layers below and the Ag cap layer on top[21]. The cap layer is neither adequate as stabilizer nor suitable as contact layer for soldering, which makes J_e measurements on pre-commercial conductor at low temperatures challenging. More recent

[21] Top and below refer to the conductor orientation as in Figure . In coils the conductor is often wound with the superconducting layer on the inside.

commercial conductors feature additional Cu layers that provide stability and a suitable contact surface.

ReBCO conductors typically have a fill factor in the order of 1% whereas 13 to 46% of the cross section of BSCCO conductors consists of ceramic, as can be observed in Table 2-1. Thus the current density in the ReBCO layer must be at least an order of magnitude higher than the current density in the ceramic filaments of BSCCO conductors to arrive at a similar or higher engineering critical current density. A bi-axial texture of the ReBCO layer is a pre-requisite to high current density which is typically obtained by growing the ReBCO layer on a suitably textured substrate. Substrate texture is often obtained by either ion beam assisted deposition of the buffer layer or by depositing the buffer layer on a suitably textured substrate. Intrinsic flux pinning is poor in ReBCO compared to BSCCO, so artificial pinning sites are required to obtain technically relevant engineering critical current density levels. J_e is determined by flux pinning on defects in the ReBCO crystal structure. Defects can be layered, columnar and spherical. The type and orientation of such defects largely affect the magnetic field dependence and anisotropy of the current carrying ability of these conductors.

Conductor F

Conductor F, see Figure 2-6, is YBCO coated conductor formed by Metallo-Organic-Deposition (MOD) of the YBCO superconductor on a textured NiW substrate. Substrate texture is induced using rolling, leading to the MOD/RABiTS acronym in which the latter term stands for Rolling Assisted Biaxially Textured Substrates. This conductor is produced by American Superconductor (AmSC). Representing the pre-commercial state of conductor development in late 2003, it has a relatively thick substrate and lacks a Cu stabilizer. It is the first coated conductor for which the field dependence of J_e is measured to 45 T at 4.2 K.

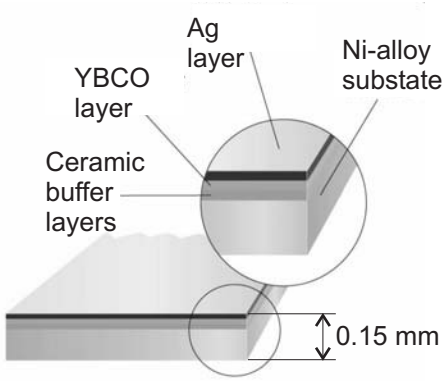

Figure 2-6. Architecture of conductor F.

Conductor G

Conductor G, see Figure 2-7, is a commercial YBCO coated conductor produced in 2007 by SuperPower Inc. [66]. It is formed by Ion Beam Assisted Deposition (IBAD) of an MgO buffer layer on a Hastelloy C276 substrate and Metallo-Organic Chemical Vapor Deposition of YBCO. A Cu stabilizing layer is added via a plating process. The use of IBAD for the buffer layer results in a textured template for the YBCO layer, thus no specific substrate texture is required. This allows a non-magnetic, relatively thin and strong Hastelloy substrate to be used. Although not specifically developed for magnet applications, the features of this conductor are well suited for insert coil application.

Conductor G is used in the SP-YBCO and NHMFL-YBCO inserts[22], the first HTS inserts to significantly exceed the 25 T and 30 T central field values respectively when operated with an outsert.

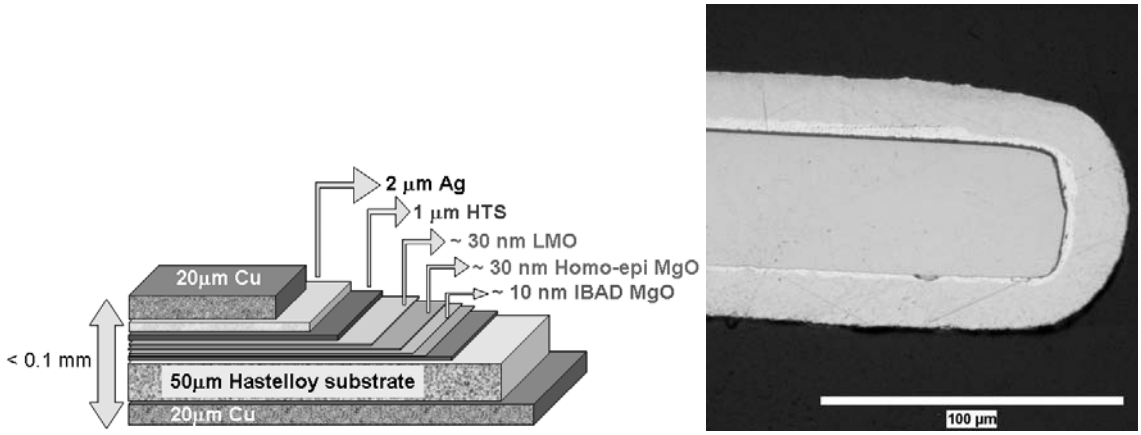

Figure 2-7. Architecture of conductor G (left); Cross section of part of conductor G (right).

Conductors K and L

Conductors K and L are commercial YBCO conductors produced in 2006 by the American Superconductor Corporation (AmSC) using the afore mentioned MOD/ RABiTS process, and are in that sense successors to conductor F. Details of the production process evolved and the substrate thickness is reduced to 75 μm but the general architecture is unchanged. Copper stabilizer and stainless steel reinforcement strips can be added through a soldering step after the superconductor and Ag cap layers are deposited. The observed critical current density and anisotropy of the standard conductor, represented by conductor K, is in part attributed to pinning on 124-type stacking faults. Stacking faults are more effective in pinning magnetic field lines parallel to the tape surface, which is the predominant magnetic field component in insert magnets, than in pinning perpendicular field components. The latter correspond to the radial magnetic field component. To improve the critical current density and reduce its anisotropic dependence on magnetic field angle a modified conductor is produced as well. Two YBCO layers are deposited on top of each other, the first a YBCO layer featuring non-superconducting nano-particles as artificial pinning centers, the second layer a standard YBCO layer [67, 68]. The nano-particles provide random pinning as opposed to the *ab*-plane pinning provided by the 124 intergrowths. No experiments are performed on this conductor as part of this work, but its published properties are used as an example to illustrate the effect of varying degrees of anisotropy on the design of HTS insert coils based on ReBCO coated conductor.

[22] See Table 1-2 and Figure 6-8.

Table 2-1, part 1.[#] Properties of the conductors studied.

Conductor	**Unit**	**A**	**B**	**C**	**D**	**E**	**F**
Manufacturer		AmSC	OST	OST	OST	OST	AmSC
NHMFL Batch identification		AmSC01	OST 38	OST 43	OST 71		
Superconducting phase		Bi-2223	Bi-2212	Bi-2212	Bi-2212	Bi-2212	YBCO
Tape width	mm	4.1	5.0	5.0	5.0		4.05
Tape thickness	mm	0.22*	0.20	0.20	0.20		0.15
Wire diameter	mm					0.8	
Number of filaments		54	19	19	19	595	1
Fill factor		0.46	~0.3	~0.3	~0.3	~0.3	~0.01
Matrix/Substrate		Ag alloy	Ag alloy	Ag alloy	Ag alloy	Ag alloy	Ni-5at%W
I_c(self, 77 K)	A	110[+]					
J_e(self, 77 K)	A/mm^2	122					
J_e (self, 4.2 K) sample 1	A/mm^2	694 //	573 //	562 //	562 //	1172	711 //, ⊥
J_e (self, 4.2 K) sample 2	A/mm^2	733 ⊥	573 ⊥	554 //	554 //		
J_e (self, 4.2 K) sample 3	A/mm^2			562 ⊥	562 ⊥		

Part 1 contains the conductors for which $J_e(B_A)$ is measured to at least 25 T and the analyzed data presented in chapter 3.

***** As received 0.3 mm thick with reinforcement strips.

+ I_c according to company specifications.

//, ⊥ Indicates the orientation of the field applied to this sample after self field measurements.

Table 2-1, part 2. Properties of the conductors studied.

Conductor	**Unit**	**G**	**H**	**I**	**K**	**L**
Manufacturer		SuperPower	NST	KIMM	AmSC	AmSC
NHMFL Batch identification			NST 01	KIMM01	-	-
Superconducting phase		YBCO	Bi-2223	Bi-2223	YBCO	Y(Dy)BCO/ YBCO
Tape width	mm	4.0	3.0	4.1	4.0	4.0
Tape thickness	mm	0.095	0.18	0.32	0.075[*]	0.075[*]
Number of filaments or layers		1	55	61	1	2
Fill factor		0.01	0.3	~0.2	0.01	0.015
Matrix/Substrate		Hastelloy-C276	Ag alloy	Ag	Ni-5at%W	Ni-5at%W
I_c(self, 77 K)	A	72 to 82	29	~20	~95	145
J_e(self, 4.2 K)	A/mm^2		155	87-106	~320	480

[*] without stabilizer strips

2.2 Critical current density

2.2.1 Definitions

The operating current density J_{op} in a conductor is calculated by dividing the transport current I by the transverse conductor cross-sectional area:

$$J_{op} = \frac{I}{area}. \tag{2-1}$$

When the voltage drop per meter E across a section of conductor equals the critical electrical field E_c, the current is by definition equal to the critical current I_c and the operating current density J_{op} is equal to the conductor engineering critical current density J_e:

$$I \equiv I_c \text{ and } J_{op} \equiv J_e \text{ for } E = E_c. \tag{2-2}$$

The usual 1 μV/cm criterion is used to determine the critical voltage and is further discussed below. Equations 2-1 and 2-2 are also used to calculate the critical current density of the conductor in a coil, in which *area* represents only the bare conductor cross section.

The average current density is a definition specific to coils which takes all materials in the windings into account, including conductor, insulation, epoxy and co-wound reinforcement as applicable. For a coil with inner radius *IR*, outer radius *OR* and height *h* containing *N* turns we have

$$J_{ave} = \frac{I \cdot N}{h \cdot (OR - IR)}. \tag{2-3}$$

2.2.2 Critical current density measurement

All measurements of the engineering critical current density J_e in this work refer to the transport current density[23] and are in essence 4-point measurements of the DC voltage-current characteristics of the conductor. All data presented in this work are taken at 4.2 K on conductors submerged in liquid helium under atmospheric pressure, unless otherwise noted. The following discussion of measurement techniques is augmented by [69].

Ramping the current

Typically the voltage across a section of conductor is measured while increasing the operating current from zero to above the value where a voltage rise exceeding the criterion E_c is measured. Two methods of increasing the operating current are used.

1. The step-wise or “staircase” ramp, which allows for extensive averaging of data and can yield very accurate data.
2. The fixed-rate ramp. This method provides the fastest measurements of J_e with reasonable accuracy, provided that inductive voltages are subtracted and the current and voltage measurement are synchronized.

Most short samples in this work are characterized using a fixed-rate current ramp whereas coil measurements are generally done using the staircase method except where noted otherwise.

[23] As opposed to magnetization based measurements.

Critical current density criterion

In the literature the criterion of 1 μV/cm is commonly used for HTS short samples. In this work, section lengths over which the voltage is measured range from 6 mm for some of the shorter samples to 2 km for the largest coil, which has implications for the criteria that can be used. A single value for the coil J_e is calculated by applying the electric field criterion to the total coil voltage. However, there is likely to be some variation in J_e within a coil. Thus, strictly speaking, there is no single J_e value for a coil as the superconducting properties of the conductor itself may vary along its length. Also, the local magnetic field varies due to coil self-field effects and slight inhomogeneity in the background magnetic field. These effects are moderated by the relatively low *n*-value and weak magnetic field dependence at high magnetic fields in HTS conductors, such that the electric field distribution in a coil is relatively wide compared to LTS coils. An example is given in section 2.2.5. Larger J_e variations occur when bending and hoop strain, both strongly dependent on radius, degrade the superconducting properties. This is addressed by measuring the voltage drop across multiple sections to determine J_e per section, in addition to determining the overall J_e, before interpreting the results.

For the shortest conductor sections tested in the relatively noisy background of resistive magnets, the choice of criterion is limited by noise. The lowest criteria that can be directly applied to the data and yield a J_e value with an accuracy of 1% or better range from 5 μV/cm to 10 μV/cm. Coils on the other hand can often only be operated up to 2 μV/cm for some of the medium-sized coils down to a maximum of 0.3 μV/cm for the largest coils before the heat generated causes thermal runaway. These ranges do not overlap, thus no single criterion can directly be applied to all data to allow a direct comparison between the properties of short samples and coils. Therefore, curve fitting of the E-J_{op} data and scaling of J_e between criteria are used if necessary to determine J_e at he standard criterion of 1 μV/cm so a comparison of conductor and coil properties can be made.

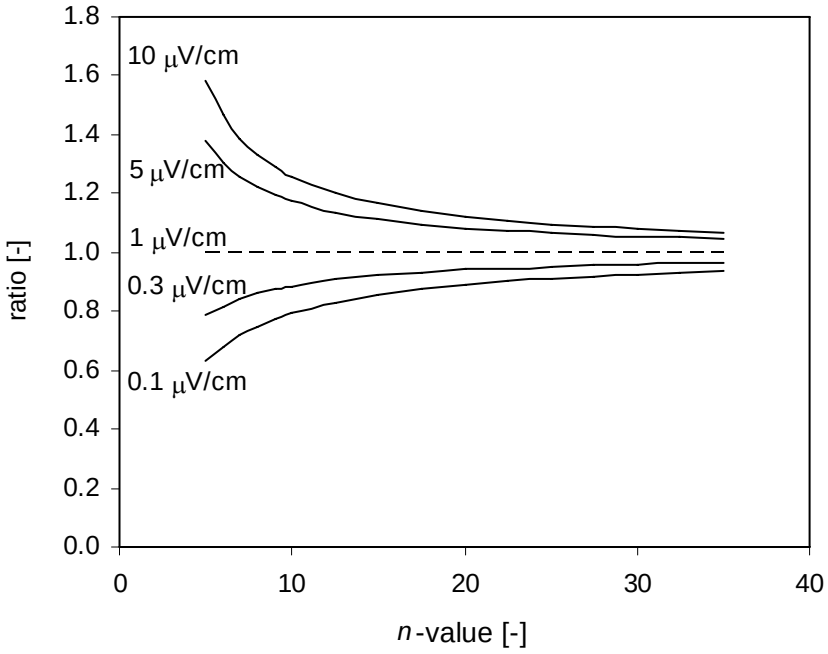

Figure 2-8. Ratio between J_e at various criteria and J_e at the 1 μV/cm criterion for ideal power law type E-J_{op} curves. These ratios are used to convert J_e values obtained at those criteria to the standard 1 μV/cm criterion. The dashed line indicates unity.

J_e can be scaled between criteria if the data closely follow the power law of equation 2-4, which is usually the case over a limited range. The scale factor depends on the *n*-value as illustrated in Figure 2-8. Scale factors used for the data presented in this work range from 0.84 to 1.25.

For the size of conductors used in this work, the 1 μV/cm criterion yields comparable J_e values as the 10^{-11} Ω.m criterion. Criteria like 0.01 μV/cm and 10^{-14} Ω.m respectively are generally more appropriate in the design of insert coils as the heat dissipated in larger coils operating at 1 μV/cm and the associated load on the cryogenic system is prohibitively high for long term operation. However, the 1 μV/cm criterion serves well to compare the properties of the developmental coils in this work with the properties of short samples of their constituent conductor.

Description of the characteristics

The shape of the E-J_{op} curve is presumed to follow the power law as expressed in equation 2-4:

$$\frac{E - E_{offset}}{E_c} = \left(\frac{J_{op}}{J_e} \right)^n , \qquad (2\text{-}4)$$

in which the exponent is known as the *n*-value, E_c is the critical electric field criterion and $J_e \equiv J_{op}$ for $E = E_c$ after correcting E for the offset. The electric field offset is determined from the intercept of a linear fit to the E-J_{op} data up to the current value where a significant increase in voltage is observed. Both inductive voltages proportional to the ramp rate and thermal e.m.f. in the voltage measurement circuit contribute to the offset electric field. A typical data set for a short sample in a resistive magnet and data analysis following equation 2-4 is presented in Figure 2-9. For a number of runs, voltages are also measured during the down ramp of the current using the same ramp rate to verify that sample remains at a constant temperature during the measurement. If the sample remains at the same temperature throughout the run, the voltage for decreasing current must be equal or slightly lower than for increasing current, at every current density level. A higher voltage, and therefore higher electric field, for decreasing current implies a temperature rise and thereby invalidates the data set. Corrective action is then required either by adjusting the measurement procedure or improving the sample holder.

***n*-value**

Measured data can not always be fitted with a single *n*-value as the *n*-value is often observed to decrease as the voltage increases [70]. To reduce ambiguity, the *n*-value is defined here as the parameter providing the best fit to the data in the range between 0.5 and 5 μV/cm. The *n*-value is sensitive to noise in the voltage measurement and uncertainty in the offset voltage as well if the tap length is in the order of a few centimeters or less. There are numerous valid mathematical approaches to determine the *n*-value [69] that yield comparable but not identical results. Here the *n*-value is determined from a direct fit to the E-J_{op} data using equation 2-4. Minimizing the sum of the absolute errors between measurement and fit tends to give the best fit, judged by visual inspection of the data and resulting fit in one graph. Considering the typical noise levels and ambiguity in the *n*-value determination, a minimum error bar of ± 1 is assigned to all *n*-values below 20 and ± 2 for $20 < n < 40$.

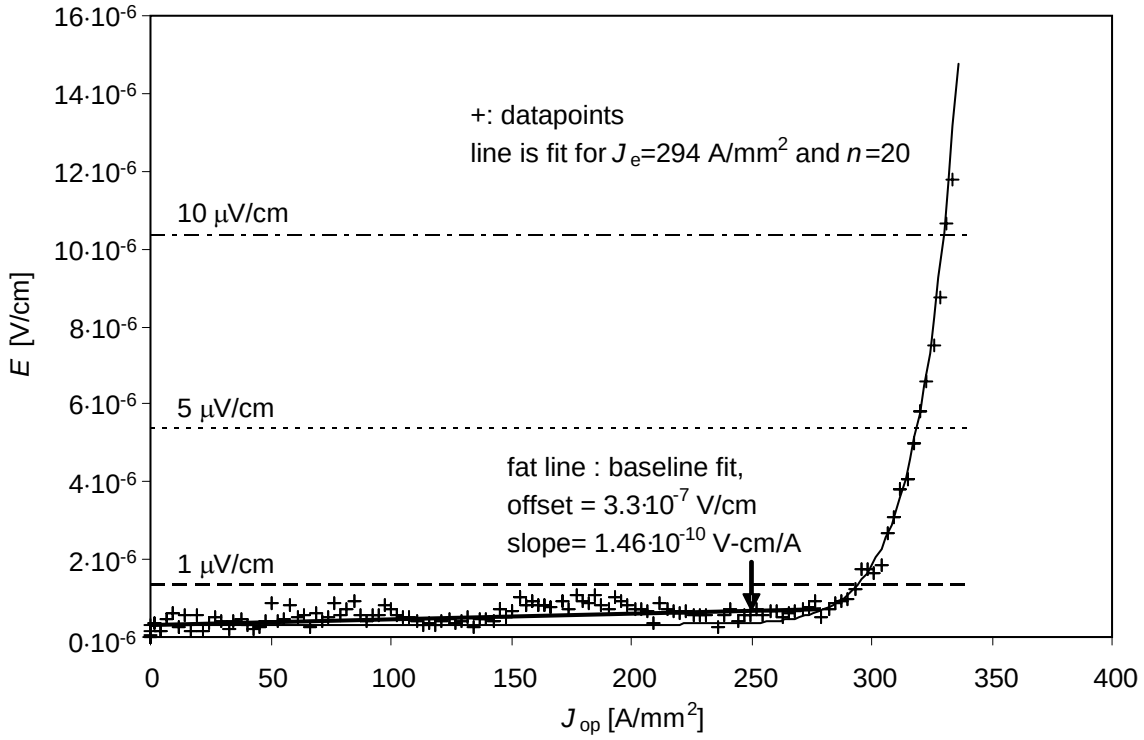

Figure 2-9. Example of characteristic E-J_{op} data for short samples in high magnetic field. These data are for conductor A, sample 1 (see Table 2-1) at 4.2 K and 25 T magnetic field applied parallel to the flat side of the conductor. This $J_e(B_{//})$ data point is included in Figure 3-2. Oscillations in the baseline voltage are associated with sample motion and flexing of the sample support under Lorentz-force at a ramp rate of 11 A/s (13 A/mm^2-s). Data are taken at a rate of 5 points/second and the total data-acquisition time is 39 seconds, including the down ramp (not shown). The dashed horizontal lines represent the critical electric field for the 6-mm tap length relative to the offset electric field.

2.2.3 Devices for short sample measurements

Critical current density measurement at self-field

The device used for J_e determination in self-field conditions (MSP-2) holds 6 samples that can be measured sequentially using a built-in room temperature switch. The lower end of this probe is shown in Figure 2-10. It is mostly operated below 670 A with ramp rates of 56 A/s or below, although operation to 1000 A is possible at 100 A/s. For HTS tape conductors up to 6 mm wide, this device generally complies with the IEC/VAMAS standard [71] on critical current measurements: the contact length between the sample and current lead is at least equal to the conductor width, the voltage taps are positioned at least one conductor width away from the solder connection to the current lead and the voltage tap separation is at least two conductor widths. Indium is used as solder because of its low melting point. The total sample length is 50 mm allowing a voltage tap length of 25 to 30 mm, which is adequate for J_e measurements at 100 A/s using the 1 μV/cm criterion with an accuracy of better than 1%. The base material is G-10 with the cloth oriented parallel to the plane of the sample to minimize the thermal strain on the conductor after cooling to 4.2 K. A self-field measurement of J_e on 6 samples including mounting, careful thermal cycling, removal and documentation takes about 3 hours. Most or all of the data in Table 5-5, Figure 5-16 and 5-17, Figures 6-5 through 6-7 are obtained using this device.

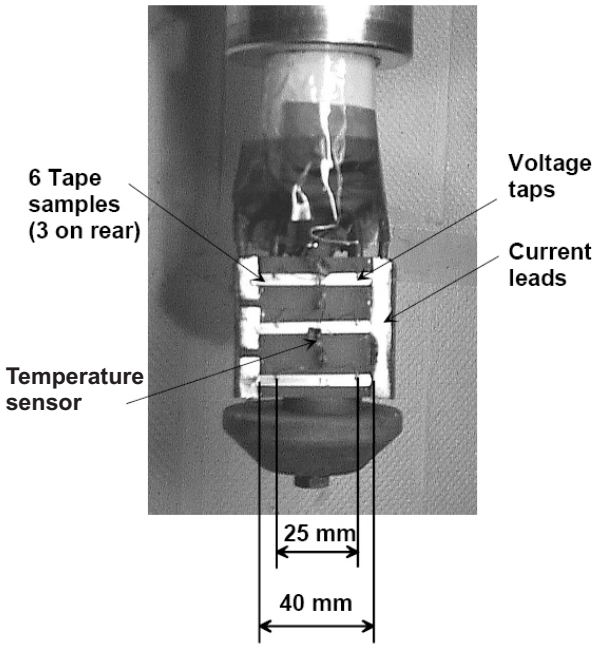

Figure 2-10. Picture of the Multi-Sample Probe2 (MSP2) used for routine characterization of conductors at self-field.

Critical current density measurement in a background magnetic field

The limited space available in cryostats that fit the NHMFL resistive magnets capable of at least 25 T does not allow sample holders built following the geometric guidelines outlined above. Considering a dewar inner diameter of 24.6-mm and the space needed to electrically insulate the sample holder from the dewars while remaining a loose fit between sample holder and dewar, a maximum sample holder diameter and maximum sample length of ~ 22 mm follows. This leaves a voltage tap length of 6 mm, taking 4 mm per side for contact to the current lead (4×4 mm in cross section) and 4 mm spacing between leads and voltage taps. This current transfer length is acceptable for samples up to 4 mm wide but is marginal for the 5 mm wide Bi-2212 tapes, leading to minor distortion of the baseline however without significantly affecting J_e at the criterion used.

To determine the anisotropy in the magnetic field dependence of J_e it is desirable to measure J_e for both the parallel and perpendicular magnetic field orientation on the same sample. Two devices are constructed with this additional feature in mind. Both devices are routinely used to 675 A and can be operated to 1000 A at sufficiently high ramp rates.

The first device allows each sample to be soldered in either the parallel or perpendicular orientation and is shown in Figure 2-11. In the perpendicular orientation the sample width is limited to 5 mm. To change the orientation, the sample must be unsoldered and re-soldered using a soldering iron and rosin-core Sn60Pb40. The current polarity relative to the magnetic field is such that the Lorentz-force is pointed into the sample holder. The sample is mounted using vacuum grease which becomes solid at cryogenic temperatures to provide seamless support against these forces. Despite careful handling, J_e degradation of 10% or more is observed after a thermal cycle and remounting, which is more then desirable.

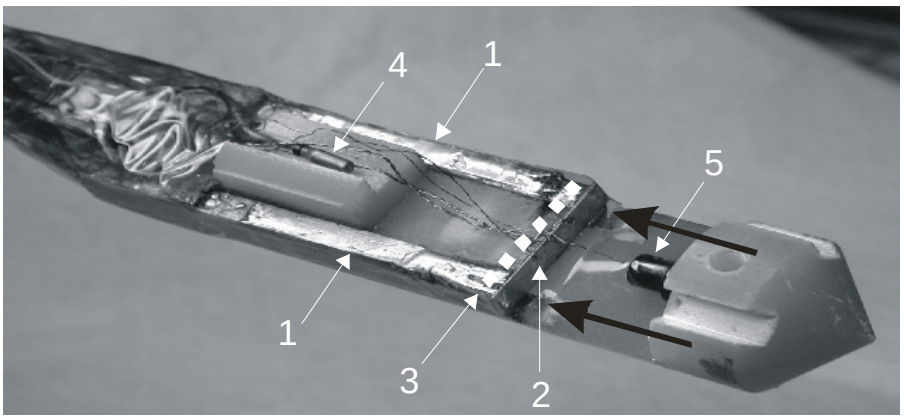

Figure 2-11. Sample holder used for characterization of conductors A, B, C and D. Visible are (1) copper current leads traced with BSCCO tape to reduce ohmic heating, (2) sample mounted for magnetic field perpendicular to the flat face, (3) sample alternate position for the parallel field orientation, (4) temperature sensor, (5) magnetic field sensor. The black arrows indicate the direction of the magnetic field.

The second device features a G-10 and Cu sample holder that can be mounted using screws to the rest of the device in two orientations, corresponding the parallel and perpendicular orientations of the conductor. Conductors, which can be up to 10 mm wide, are soldered to the Cu terminals and embedded in STYCAST 2850 epoxy where it contacts the G-10. This assembly is clamped to the current leads with brass screws. Figure 2-12 presents pictures of the sample holder mounted to the lower end of the device showing a sample in the perpendicular orientation. Careful thermal cycling is still required but the sample orientation can be changed without soldering.

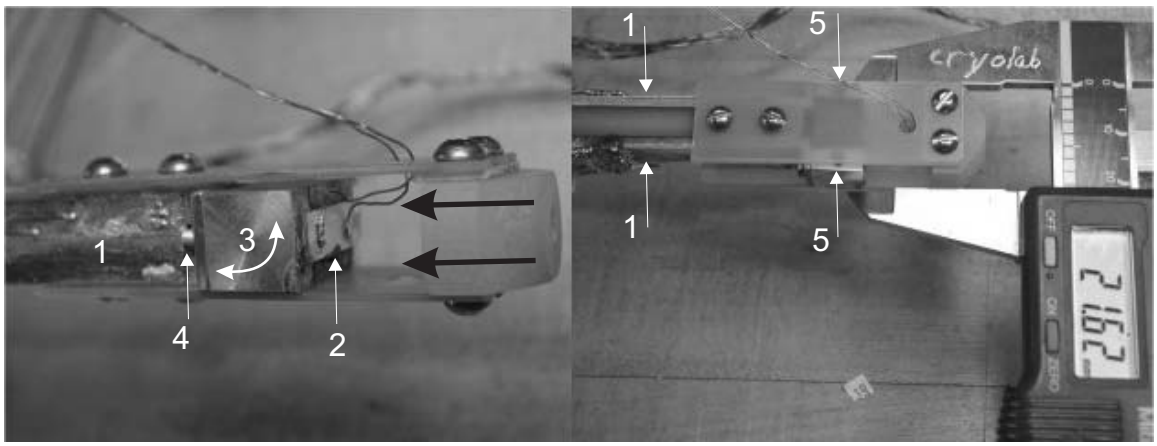

Figure 2-12. Sample holder and part of the device used for characterization of conductors E and F. Visible are (1) copper current leads traced with BSCCO conductor, (2) sample with voltage taps oriented perpendicular to the magnetic field (black arrows), (3) sample mount that can be attached to the leads in two orthogonal orientations as indicated, (4) brass screws; (5) threaded holes that are used when the sample is oriented parallel to the magnetic field.

2.2.4 Procedures for short sample measurements in high magnetic field

Several issues determine the measurement procedure:

1. The tolerance for Ohmic heating is limited; especially when the applied field is above 20 T. This is caused by the magnetic properties of helium gas in combination with the limited helium volume around the sample holder in the tail of the dewar. Above center field there exists a zone where the product of magnetic field and magnetic field gradient, representing the local magnetic force, exceeds 2100 T^2/m, as shown in Figure 2-13. Helium is diamagnetic and the repulsive force acting on liquid is larger than on gas on account of their difference in density, resulting in a downward force on helium gas bubbles that exceed their buoyancy [72]. The helium bubbles are in effect trapped. A larger gas bubble will form and expand with continued helium boil off until the sample itself is enveloped. Without bath cooling, ohmic heating in the sample, current leads and their connections will cause a temperature rise in the sample. This invalidates the measurement as J_e will be below its 4.2 K value. Thus Ohmic heating should be minimized through design of the sample holder and procedures should be implemented to remove the trapped helium gas. $J_e(B)$ curves that are distorted for magnetic field above about 20 T occur in the absence of such measures [26].
2. J_e is not only determined by the magnetic field and its orientation but is also affected by the recent history of magnetic field changes. These hysteresis effects are reversible. An example of observed differences in $J_e(B)$ for increasing versus decreasing magnetic field values is presented in Figure 3-2.
3. Irreversible degradation of J_e can occur in a sample as a result of the Lorentz-force at high magnetic field and current. Such degradation is observed in some samples when J_e is measured in applied magnetic fields above 25 T. Only data taken in the absence of such irreversible degradation are considered here. Therefore repeated verification of J_e at a reference magnetic field is required. The sequence of magnetic field changes before such verification must be standardized to prevent the above mentioned magnetic field history effects on J_e.

The procedures for changes in applied field is therefore as follows:

1. After cooling each sample to 4.2 K and before starting the reported measurements, the background field is ramped to its maximum value and back to zero. This ensures a repeatable magnetization state of the sample for all self-field measurements, in the absence of irreversible degradation.
2. After each measurement in the 33 T magnet with an applied field above 17.5 T, the background field is reduced to 17.5 T, allowing trapped helium gas to rise to the liquid helium surface.
3. In a measurement sequence for increasing fields above 17.5 T, the field is then ramped directly from 17.5 T to the next relevant field value.
4. In a sequence of measurements with decreasing background fields above 17.5 T, the field is ramped from 17.5 T to the maximum field value and then down to the magnetic field value for an J_e measurement. The same patterns are followed using the 20 T magnetic field value when operating in the 45 T Hybrid.
5. The magnetic field value chosen for a repeated J_e measurement to verify the absence of irreversible J_e degradation is always approached from beneath.

Different J_e criteria and linear current ramps with varying rates are used, depending on the specific configuration of the sample holder and properties of the sample. The choice of ramp rate is a compromise, since low rates improve accuracy but tolerance for ohmic

heating is limited. All ramp rates are between 11 A/s and 60 A/s, a range in which little (< 1%) or no ramp rate dependence of J_e is observed. The criterion is chosen such that J_e can be determined with a repeatability of better than 0.5%. For most samples discussed here this corresponds to the 5 μV/cm criterion, and 10 μV/cm for the remainder.

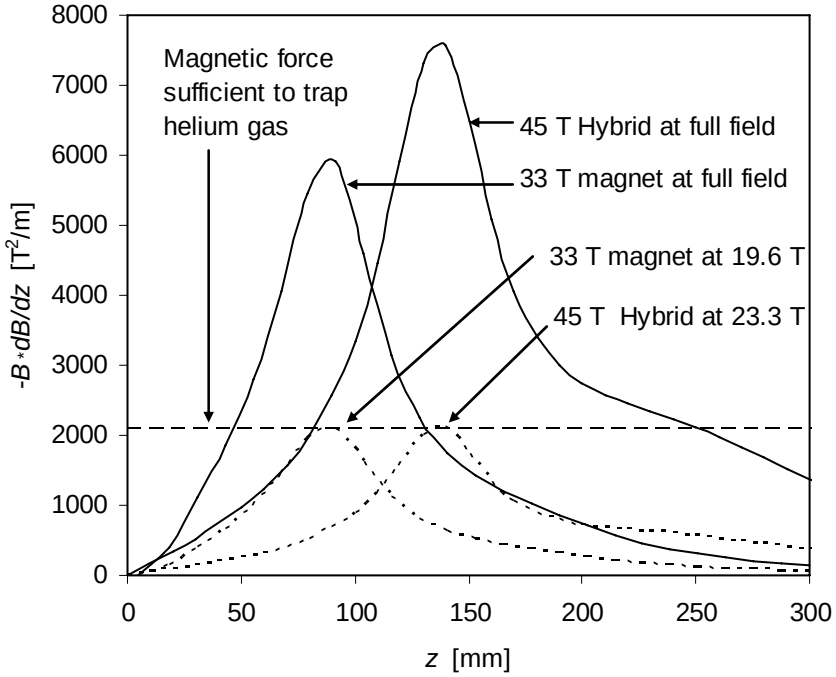

Figure 2-13. Magnetic force represented by the product of magnetic field and magnetic field gradient versus position on the vertical axis of the NHMFL 45 T Hybrid magnet and a 33 T resistive magnet.

2.2.5 Engineering critical current density in coils

Additional factors play a role when measuring the critical current density of coils. Voltage and current ripple of the power supply output have an effect on the coil voltage proportional to the self-inductance of the coil. Additional AC noise is induced when a background magnetic field is present proportional to the current ripple in that magnet and the mutual inductance with the coil being tested. A superconducting magnet with large self-inductance is preferable as background magnet in this respect, but the only magnet available with sufficiently large bore and magnetic field range is the NHMFL Large Bore Resistive Magnet. However, the noise level is manageable as outlined below.

The self-inductance of a 0.02 m section of tape is about 0.01μH, and the noise level in a voltage measurement over one power line cycle (17 ms) is typically in the order of a few-tenths of a microvolt. In contrast, double pancake coils have a self-inductance in the order of a few mH while the self-inductance of the 5 T insert with 2 km of conductor is 1.2 H. So the range of self-inductance for the samples and coils considered here spans eight orders of magnitude. Ten to twenty voltage readings with 17 ms integration time are averaged to reduce the effect of AC noise to levels that are small compared to the J_e criterion. Coils typically have multiple voltage taps that are measured sequentially using a multiplexer, so the total time required per data point is 15 to 30 seconds and 5 to 20 minutes for a complete E-J_{op} curve. Included in the time per data point is a delay of typically 5 seconds between a change in current and the start of the voltage measurement

to allow the power supply to stabilize again. Thus the critical current density of a coil and smaller sections of that coil are determined with an accuracy of better than 1 %.

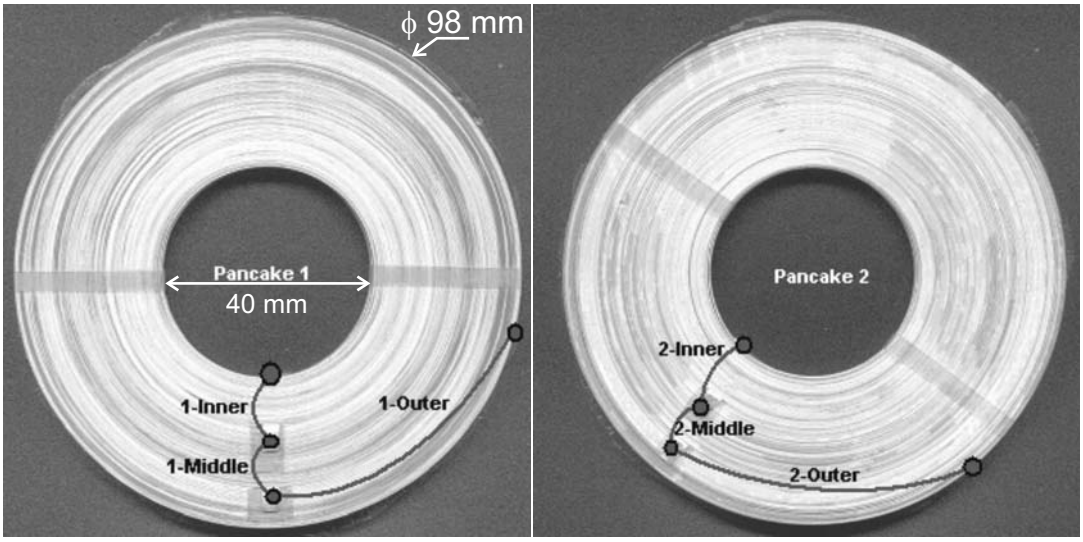

Figure 2-14. Images of a double pancake coil indicating the voltage tap positions. "Whole coil" spans from 1-Outer to 2-Outer. This coil is known as A12 within the 5 T project, and Coil 4 in chapter 6. A graph of a critical current density measurement on this coil is shown in Figure 2-15.

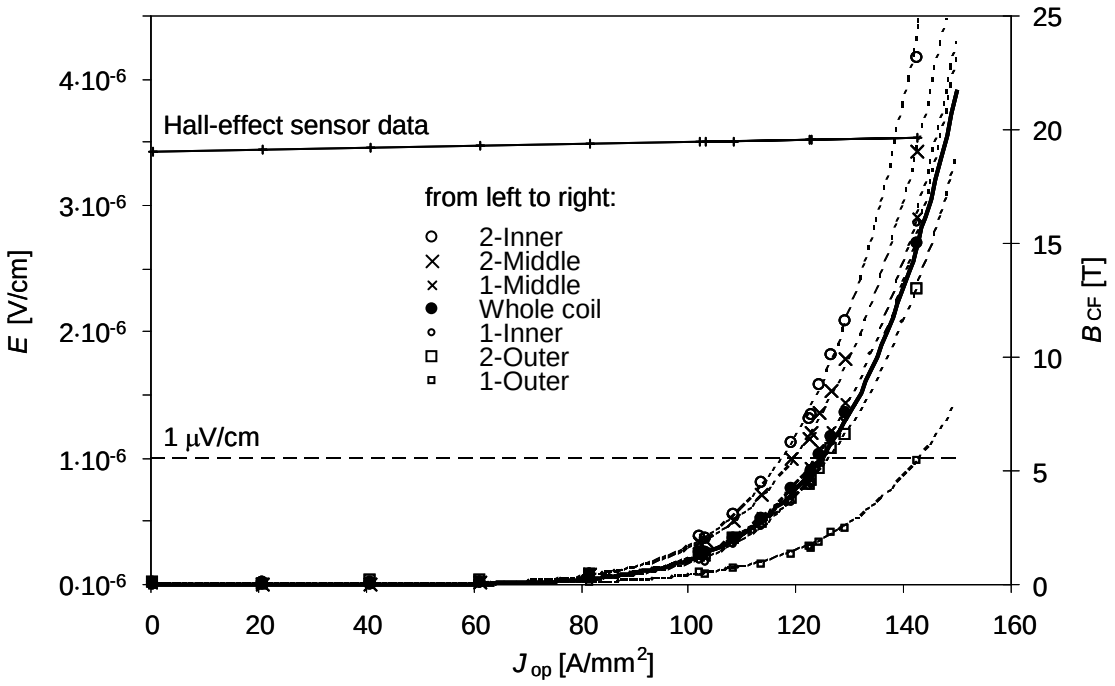

Figure 2-15. Example of E-J_{op} data on a double pancake coil (Coil 4) plus the readings of a Hall-effect sensor placed at the magnetic field center. The background magnetic field is 19 T. Curves through data points represent power law fits, except for the Hall-effect sensor data that are linearly interpolated. The voltage offset is negligible. The voltage tap definitions are introduced in Figure 2-14. The critical current density of a coil or a coil section is determined by the J_{op} value for which a curve representing the data intersects with the criterion.

An example of voltage tap locations that allow the properties of different sections of a coil to be determined is given in Figure 2-14, and a plot of the critical current density measurement of the same coil in a 19 T background magnetic field is shown in Figure 2-15. A Hall-effect sensor is placed at field center to monitor the magnetic field generated by the background magnet and the HTS coil. Usually there is a distribution of J_e and n-values across the different sections of a coil, as shown in Figure 2-15 and Figure 2-16. No clear pattern can be discerned in Figure 2-16, other than that the outer sections have a higher J_e. This, however, is not consistently found in other coils. One might expect a gradient in J_e related to the local magnetic field. The axial magnetic field varies about 0.6 T in the coil due to self-field effects and inhomogeneity in the background magnetic field. This corresponds to a variation of less than 1% in J_e. Considering the gradient in the effective perpendicular magnetic field, a concept that will be introduced in chapter 3 and applied to coil data in chapter 5, results in a gradient of 1% in J_e, with J_e again lowest at the inner radius. Magnetic field variation can therefore not explain the observed J_e variation of 20%. The J_e variation in the coil is likely related to variations in the superconducting properties along the length of the conductor, as ±10% variations in J_e are routinely observed (see Figure 6-5 for example) between short samples taken from a single batch of this conductor (conductor B).

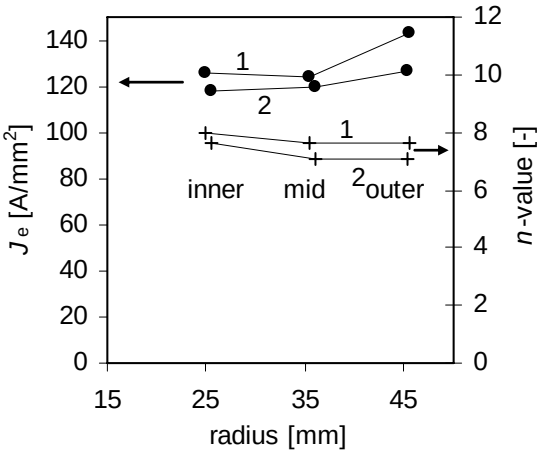

Figure 2-16. Variation in J_e and n-value plotted versus the median radius of each section of Coil 4 in an applied magnetic field of 19 T.

2.2.6 Quench protection and safety

Protection of coils is required to prevent degradation of properties from quenches, trips of the background magnet, and shorts in the background magnet. The forces and voltages involved are a potential danger to personnel and equipment as well. Regarding protection and safety, a distinction is made between large coils on one hand and short samples plus small coils on the other. Short samples and small coils like double pancake coils are adequately protected from overheating after a transition to the normal state by shutting the power supply down when the total voltage exceeds a certain value. This can be done in multiple ways: manually, using the overvoltage protection feature of the power supply or using a digital signal generated by either the data acquisition software or a dedicated electronic circuit. Additional risk factors exist for larger coils, especially when operated in the background magnetic field of a resistive magnet. The majority of the stored energy in the coil should be dumped elsewhere to prevent the possibility of burning out a small

section of the coil. Here we use the example of the 5T insert, which represents the case with the highest potential fault forces and induced voltages of insert coils tested so far at the NHMFL, to introduce the protection and safety measures taken.

Trip of the resistive magnet

A common occurrence when operating resistive magnets is the event of a *trip*, in which the resistive magnet is rapidly de-energized in response to a fault detected by its protection system or much less frequently through activation of an emergency shut-down button or a general power failure. The time constant of the field decay in the case of a trip of the Large Bore Resistive Magnet (LBRM)[24] is 1.4 seconds, resulting in an induced voltage of ~ 1 kV in the circuit of the 5T insert. Without protection the insert current would rise faster than the background magnetic field can decrease, resulting in a temporary increase in the Lorentz-force experienced by the insert coil. The induced current may also cause a quench of the insert. The impact of a trip on an insert is at its highest when both the resistive magnet and insert are at maximum field. Several small HTS insert coils have been damaged or destroyed as a result of resistive magnet trips in the period before the protection system was developed.

Insert quench protection is provided using the over-voltage protection feature of the power supply for the insert current and a dump resistor mounted between the current leads. The over-voltage threshold is set just above the voltage required to power the insert at design current. The supply output becomes an open circuit when the overvoltage protection circuit engages, forcing a safe discharge of the 5T insert over the dump resistor.

A set of circuit breakers in the current leads between the dump resistor and the power supply are implemented as shown in Figure 2-17 to protect the 5T insert from the consequences of a trip of the LBRM. They are activated by a trip detection system consisting of a pick-up coil bolted to the bottom of the resistive magnet housing and an electronic trigger circuit. The maximum induced voltage in the pick-up coil during normal ramping[25] of the LBRM is 108 mV, and the trigger level is set at 150 mV for a high sensitivity to trips but low risk of a false trigger during normal operation.

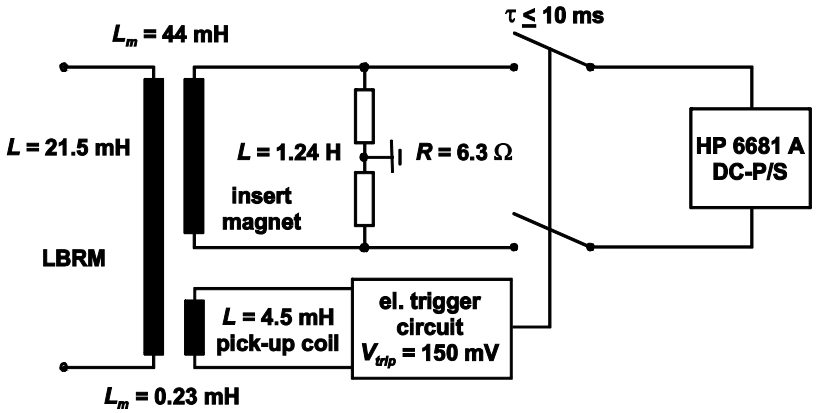

Figure 2-17. Schematic of the system used to protect the 5T insert from trips of the Large Bore Resistive Magnet (LBRM).

[24] See Table 4-1 and Figure 4-1.
[25] The maximum rate during normal operation is 600 A/s, compared to a maximum of ~27 kA/s during a trip.

The current decay in the LBRM in the event of a trip increases the current in the insert, resulting in higher hoop stress and higher voltage across the insert coil the longer it takes to open the contactors. The delay between the onset of the trip and the opening of the contactors is a critical parameter, as well as the resistance of the dump resistor. The stress in the insert coil increases with delay in opening the contactors as shown in Figure 2-18 (left). The margin between design stress and the onset of degradation in the 5T coil is not exactly known but is expected to be in the range from zero to 20%.[26] Thus the delay should be as short as practical as no value above zero is safe with the insert at design current and the LBRM at 20 T. A delay above 40 ms is likely to result in strain induced degradation of the critical current density. The time delay from the onset of an LBRM trip to discharge of the insert over the dump resistor is approximately 10 ms for the protection system as implemented and limits the stress increase in the insert to 3-4% of the stress at the moment of the resistive magnet discharge. This also keeps the voltage at the opening of the contactors below 900 V.

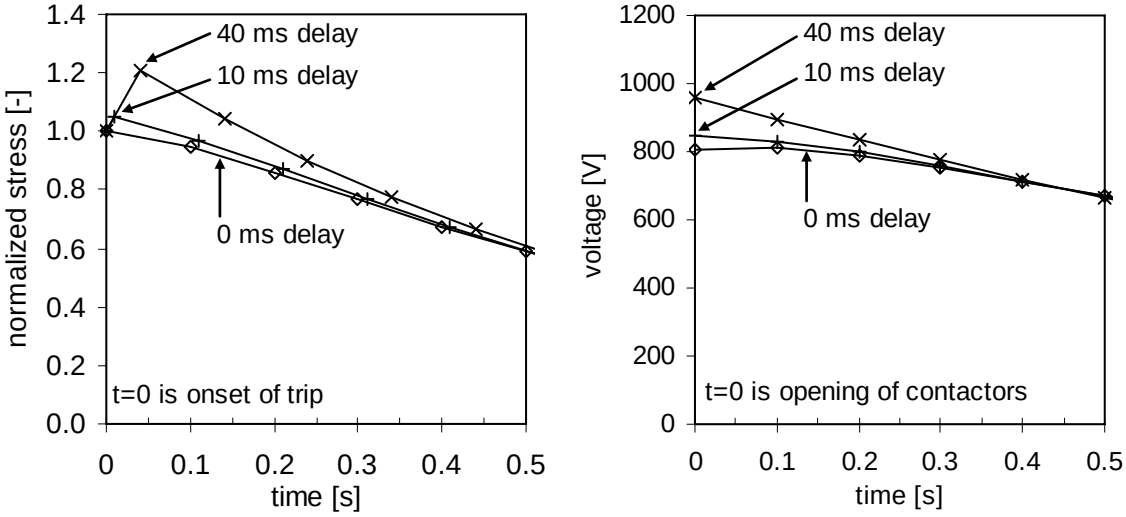

Figure 2-18. (left) Dependence of the hoop stress in the 5T insert on the delay time in opening the breakers if the Large Bore Resistive Magnet were to trip at 20 T with the insert at design current. (right) Dependence of the voltage across the insert coil on the delay time for the same scenario.

The dump resistor value must be large enough (> 6 Ω) to ensure that the insert current, and therefore stress, decrease as soon as the contactors open. A resistance value larger than about 7 Ω is problematic as the voltage drop over the resistor would exceed 1 kV, and thereby exceed the specifications for the maximum input voltage of the digital multimeters used to measure the voltage across sections of the insert. The breakers chosen have a specified maximum of voltage of 900 V across their terminals when breaking a load and are thus slightly more limiting. Hence a resistance value of 6.3 Ω is selected. The circuit of the insert is grounded in the middle of the dump resistor to keep the maximum possible voltage-to-ground for any point of the insert below 500 V from ground, again to satisfy the specifications of the multimeters.

[26] This is discussed in detail in Chapter 6.

Figure 2-19. View of Cell 4 at the NHMFL. (1) 5T insert, (2) coil support structure hanging from the crane, (3) dewar stand, (4) dewar, (5) dewar tail that fits the bore of the (6) resistive magnet, (7) structure to react fault forces on the insert support structure to the resistive magnet housing.

The dump resistor can absorb 100 kJ and is thus capable to absorb both the stored energy of the insert (~ 10 kJ) and the additional energy transferred from the LBRM to the insert during the LBRM discharge. This additional energy is small compared to the stored

energy of the resistive magnet (16 MJ at 20 T), so the insert has a negligible effect on the resistive magnet during discharge. The dump resistor housing contains a number of additional resistors that can be series or parallel connected to customize the resistance for other insert coils.

Shorting of the resistive magnet

A scenario with low probability but with potentially hazardous consequences for equipment and personnel is the development of a short in the resistive magnet. The worst possible case would be shorting at the midplane between all sections of the resistive magnet. This results in an axial shift of the peak magnetic field of the background magnet. The minimum energy state for two co-axial solenoid magnets with the same polarity occurs when their field centers coincide, thus an attractive force between insert and current carrying part of the background magnet develops. This force exists only for a short time, as the short should trigger a trip of the resistive magnet, but the magnitude of the force is large enough to severely damage or destroy the coil support structure and the cryostat if these are not specifically designed to handle such forces. The worst-case fault load, which can be pointed either upwards or downwards, for the 5T insert is 270 kN. Fault loads are reacted to the resistive magnet housing via the dewar top flange which is integrated with a structure of I-beams that is bolted to the housing. The body of the dewar is suspended from these I-beams and is thus not in the load path. This hardware can be recognized in a picture taken during disassembly of the test setup as presented in Figure 2-19.

Misalignment

Forces form axial misalignment between the insert and background magnet in the order of a few mm are insignificant (< 1 kN) compared to the forces during a worst-case scenario of resistive magnet shorting and the capacity of the structure to transmit axial forces to the resistive magnet housing. To keep forces from radial displacement in the order of a kN or less the insert should be centered to within 5 mm. This is ensured by the small radial margin of ~ 1 mm between the insert and the dewar wall.

2.3 Tensile stress and strain

2.3.1 Definitions

Expressions used to describe the mechanical properties of superconductors and reinforcement materials under uni-axial loads are introduced in this section. Stress is defined as the force on a section of material divided by the transverse cross sectional area of that material. Strain is the elongation of that section of material divided by the original length. Both definitions follow common conventions. The initial slope of a stress-strain curve is taken as the modulus of elasticity. Determination of the initial slope is however not trivial for the curves of the HTS conductors measured as part of this work as there is no clearly identifiable linear part of the stress-strain curve for low strain values[27]. Yielding appears to be partially plastic from the onset, as illustrated in Figure 2-20. The word elasticity is therefore somewhat of a misnomer. The initial slope is referred to as E_i. Typically the slope of the stress-strain curve of a superconductor gradually decreases from its initial value in the range of 30 to 80 GPa to a final value E_p around 1 GPa. The ultimate tensile strength or *UTS* is defined as the stress at ε_p, the strain value at which this final slope is reached. The conductor deformation is considered to be fully plastic for $\varepsilon \geq \varepsilon_p$, i.e.

[27] This is discussed in more detail in section 6.2

the plastic regime. Below ε_p the deformation is partially plastic, partially elastic. The stress-strain data obtained when reducing the stress back to zero are referred to as the return line. Figure 2-20 illustrates the latter definitions.

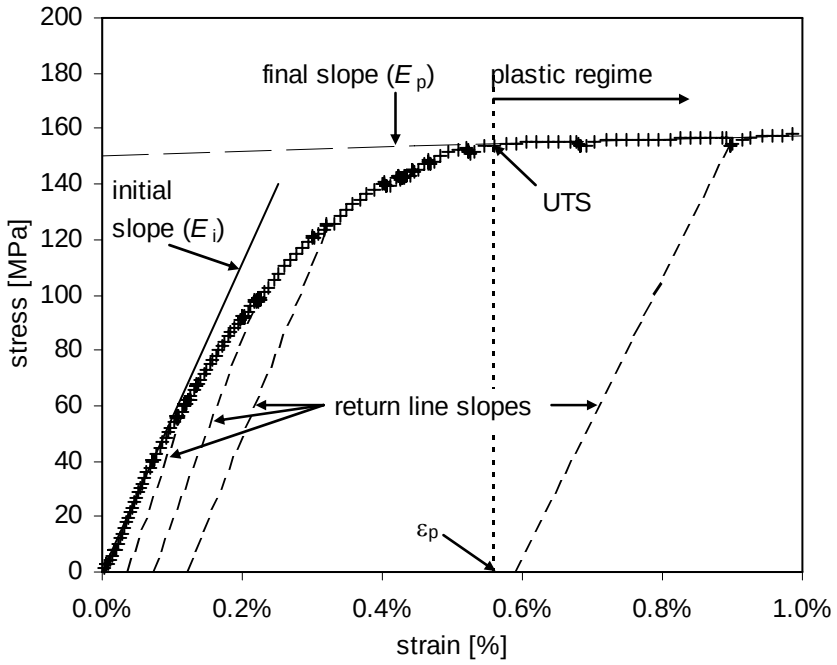

Figure 2-20. Stress-strain data (+) of conductor B at 77 K on which the initial slope (E_i), final slope (E_p), ultimate tensile strength (UTS) and the plastic regime ($\varepsilon \geq \varepsilon_p$) are indicated. The initial slope is determined using the linear term of a second order polynomial fit to the data as discussed in section 6.2.2. The average slope of the measured return lines are indicated; the actual return line data points are omitted for clarity. With load cycling the conductor behavior will closely follow the return line, not the virgin stress-strain curve.

2.3.2 Measurement device

Most stress-strain measurements are performed using a tensile tester that was developed in-house. The structure of the tensile tester is conventional: a stepping motor is mounted to a rigid frame. The horizontally oriented sample is clamped by two grips: one grip is connected to the frame, the other connected to the moving part of the stepping motor. The force on the conductor is measured through a load cell with 400 N capacity placed between the stepping motor and the moving grip. The displacement of the moving grip is determined using a linear variable displacement transducer mounted on the frame and connected to the moving grip. A picture of the tester is shown in Figure 2-21.

A G-10 enclosure allows the sample and grips to be cooled by liquid nitrogen (LN_2). The lower half of this chamber is integrated with the mount for the fixed grip. The upper half is installed after positioning the sample and tightening the moving grip. A trickle flow of nitrogen is supplied via a tube connected to a fitting on the upper half of the chamber and is vented through a gap between the chamber and the moving grip mount.

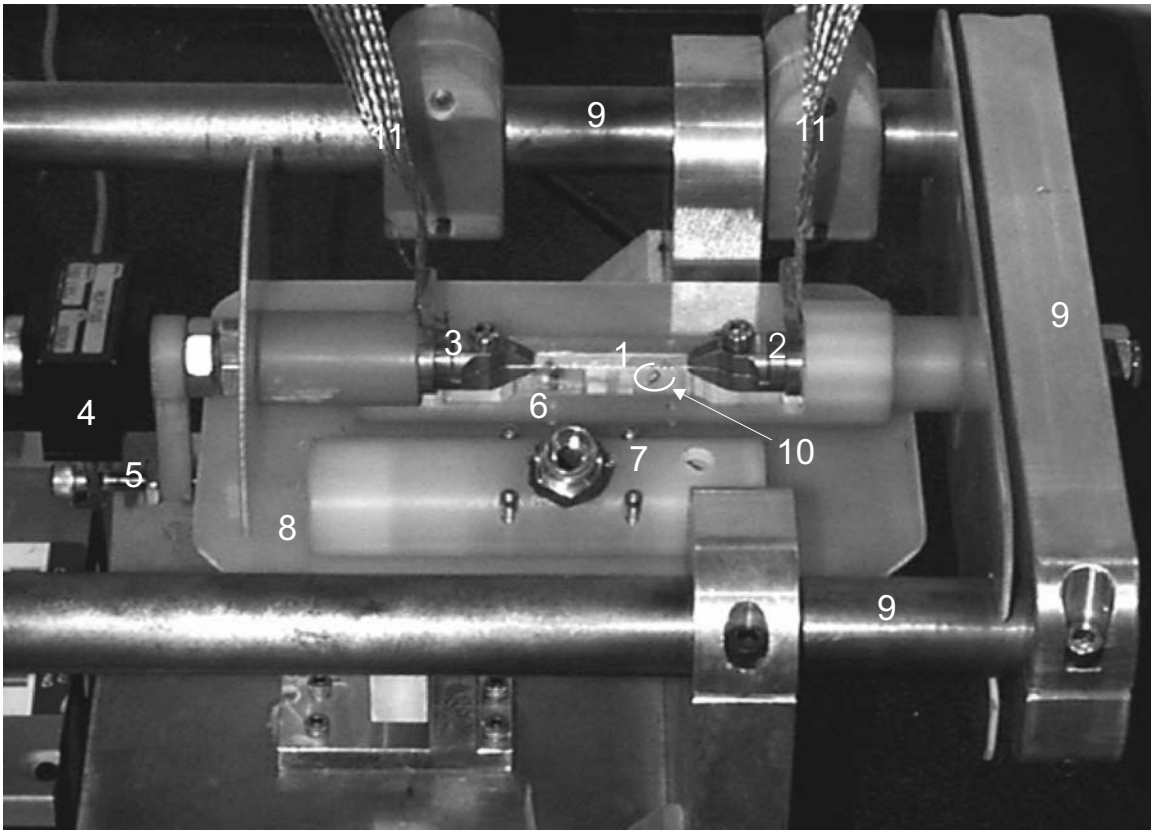

Figure 2-21. Picture of the linear tensile tester used for stress-strain measurements on HTS conductors at 295 and 77 K. Visible are: (1) sample, (2) fixed grip, (3) moving grip, (4) load cell, (5) connection between the moving segment and the displacement transducer, (6) lower half of the LN_2 chamber, (7) upper half of the LN_2 chamber which is disconnected and placed on the (8) shield plate that directs the N_2 exhaust of the sample chamber away from the displacement transducer. Visible features on the (7) upper chamber half are a fitting for a nitrogen supply tube, four screws for mounting to the lower chamber half and an opening for an Allen wrench to tighten the fixed grip when the upper chamber is in place. Also visible are (9) elements of the frame. The displacement transducer is obscured by the shield plate and the stepping motor is to the left, outside the frame of the picture, (10) temperature sensor used to monitor the temperature in the chamber, (11) optional current leads and voltage taps can be installed to allow measurements of J_e in situ.

Standard flat-plate grips were found to be inadequate as they lead to stress concentrations near the grips and premature rupture of the conductors at the grips. Therefore multiple sets of custom grips were used, one set for each size of conductor tested [73]. These custom grips hold the conductor without undue stress concentrations, are more compact and can be tightened with a single screw. The latter is convenient as the fixed grip is only tightened after the sample is cooled down, using an Allen wrench through a port in the upper half of the chamber.

While the frame of the tester is very rigid compared to the sample, the assembly of parts between the tensile testers moving part and the frame is somewhat compliant. This compliance is determined using a piece of stainless steel with known tensile properties and dimensions. The magnitude of the correction required to compensate for this compliance is typically in the order of a few percent of the strain signal.

2.3.3 Procedures

Preparation of straight samples

To understand the mechanical properties of BSCCO tape conductors, the stress-strain measurements are preferably performed on straight samples with no strain history. However, most superconductors are heat treated while curved or spooled after heat treatment. Mechanically straightening reacted conductor from a curved state after un-spooling by placing the conductor on a flat surface and rubbing the convex side until the sample is straight induces work hardening and can affect the stress-strain characteristics. Preferably, samples should be heat treated straight or otherwise annealed above 300 °C to release work hardening of the matrix due to straightening. This procedure is used for all conductors investigated here except conductor A. The latter is a sandwich of super-conductor and pre-strained steel tapes held together by solder with a melting point well below 300 ºC. However, since this conductor shows almost perfect elasticity for the relatively low bending strains involved in straightening, the effect of mechanical straightening on the uni-axial stress-strain curve is expected to be negligible. Thus preparation procedures to straighten initially curved samples without significantly affecting the measured stress-strain curve are described for conductors A-F.

Measurement protocol

The measurement protocol is fairly straightforward:

1. Grips customized to the sample dimensions are installed.
2. Grips spacing is determined and sample cut to length.
3. Sample is placed between grips and the moving grip is tightened.
4. Upper half of the LN_2 chamber is mounted and connected to LN_2 source.
5. Sample and chamber are cooled with LN_2.
6. The fixed grip is tightened when the displacement transducer indicates that thermal equilibrium is reached.
7. Reading of the displacement transducer is reset to zero.
8. Strain is applied at a rate of typically 2%/minute.
9. Sample is unloaded at various strain levels before further loading until the conductor fails.

The average slope of an un-loading curve, also known as return loop, can be used as a measure of the modulus of the conductor at the peak strain level of the loop. Here return loops are primarily used to verify that strain errors resulting from changes in the temperature distribution in the tensile tester are insignificant.

2.4 Combining tensile stress-strain and critical current density measurements

It is well established that the critical current density in HTS conductors is strain dependent and that significant and irreversible degradation occurs above certain strain levels. In the design process of insert coils it is therefore essential that

1. the J_e-strain relation is known to determine the maximum design strain and,
2. the conductor stress-strain relation is known, as well as the mechanical properties of all other materials in the windings, to calculate the conductor strain.

There are two principal approaches to combining such stress-strain measurements with critical current density measurements. One approach is to measure J_e in situ while the single sample is strained step by step. The other approach is to strain multiple samples each to a single specific strain state followed by J_e measurement using a separate device.

Both approaches are used here and are described in more detail below. The data thus obtained are used in chapter 6 to correlate the observed strain induced J_e degradation in coils with the stress-strain-J_e properties of their constituent conductor.

Using a single sample in multiple strain states

The relation between J_e and tensile strain can be determined by incremental changes in the strain state of a single sample in a cryogenic environment alternated with J_e measurements. Implementations of this technique have taken the form of linear tensile testers, U-shaped bending springs [74] and spirals [75] which are designed or modified to perform critical current measurements as well [76, 73]. These methods offer the possibility to precisely monitor changes in the electrical performance of a single sample relative to its initial properties. As these experiments are generally time consuming, usually one or at most a few samples per conductor batch are investigated. Then little or no insight is gained on possible sample-to-sample variations within a conductor batch. In this work, a tensile tester is used to determine the relation between strain, J_e and n-value for conductor H, a Bi-2223 conductor.

Using a unique sample per strain state

Processing that is optimized to maximize J_e of Bi-2212 conductors at 4.2 K typically results in T_c values close to or below 77 K, as is the case for conductors B, C and D. The method of measuring J_e in-situ at 77 K is therefore not useful. Instead, the following approach is used:

1. Using the same tensile tester, samples are strained to a specific value of stress or strain at 77 K. The strain values range from 0 to values that cause large J_e - degradation.
2. The strain is released, and the sample is warmed to room temperature.
3. J_e is measured at 4.2 K in a separate facility.

Since some inhomogeneity in J_e exists along the length of each conductor, it is necessary to use multiple samples per strain level to obtain a useful average J_e. At the same time, this approach yields insights in the sample-to-sample variations of conductor properties.

2.5 Bending strain

2.5.1 Definitions

The maximum tensile surface strain in the case of fully elastic bending of initially straight and thin conductor is:

$$\varepsilon_{\max,surface,elastic}^{bend} = \frac{t}{2r_b}, \tag{2-5}$$

in which t is the thickness of the conductor and r_b the bending radius. This strain value occurs on the outside of the bent conductor. Outside, inside and other geometric aspects of bent HTS conductors are defined in Figure 2-22.

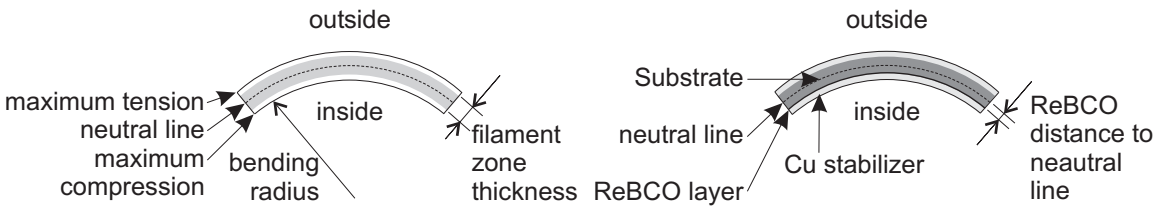

Figure 2-22. Schematic longitudinal cross section of a bent BSCCO conductor (left) and a ReBCO coated conductor (right).

The conductor is usually heat treated while spooled in a pancake shape or layer wound on a cylinder, which results in a corresponding curvature for the strain-free state. The expression for the maximum surface strain then becomes:

$$\varepsilon^{bend}_{\max,surface,elastic} = abs\ t\cdot\left(\frac{1}{2r_b}-\frac{1}{2r_i}\right), \tag{2-6}$$

with the subscripts *b* and *i* denoting the bend radius and initial strain free radius respectively. Note that the bending radius can be larger than the initial radius, in which case the peak tensile strain is on the inside of the conductor.

Plasticity in the mechanical properties of the conductors must be taken into account as well. We assume that, for deformations that do not result in significant J_e degradation, the matrix exhibits some plastic yield, thereby releasing some of the bending strain in the filaments. To quantify this, several pieces of conductor are wound to one turn at a specific smaller radius and released. This process is the equivalent of a loading and unloading sequence in a linear tensile test and is referred to as the *bend-and-release* procedure. Upon release, the conductor assumes a shape characterized by radius r_f, and is considered strain-free. The strain retained in the conductor corresponds to the difference in strain between the as-bend and final state

$$\varepsilon^{bend}_{\max,surface} = abs\ t\cdot\left(\frac{1}{2r_b}-\frac{1}{2r_f}\right). \tag{2-7}$$

Bending is perfectly elastic if $r_f = r_i$, and completely plastic if $r_f = r_b$. The degree of elasticity varies between conductors. If the degree of elasticity *e* is constant, then $\varepsilon^{bend}_{\max,surface}$ can also be described as a percentage of $\varepsilon^{bend}_{\max,surface,elastic}$.

$$\varepsilon^{bend}_{\max,surface} = abs\ e\cdot t\cdot\left(\frac{1}{2r_b}-\frac{1}{2r_i}\right) with\ 0 \le e \le 1. \tag{2-8}$$

However, the filaments are not on the surface for any of conductors considered here, as is evident in Figures 2-1 through 2-7. BSCCO conductors differ from ReBCO coated conductors in architecture and in cross-sectional composition. Therefore BSCCO and ReBCO conductors are considered separately to calculate the strain on the superconducting filament(s).

BSCCO conductors

Maintaining the assumption of a linear gradient in strain between the inner and outer surface of the conductor, the maximum strain in the filaments is calculated using

$$\varepsilon^{bend}_{\max,filament} = abs\ f_{fil}\cdot e\cdot t\cdot\left(\frac{1}{2r_b}-\frac{1}{2r_i}\right), \tag{2-9}$$

where f_{fil} is the ratio of the filament zone thickness to conductor thickness. This maximum is on the outside if the bend diameter is smaller than the heat treatment diameter and on the inside if the reverse is the case.

ReBCO conductors

As opposed to BSCCO conductors which typically feature a symmetric arrangement of filaments on either side of the neutral line, ReBCO conductor are typically asymmetric with a single thin filament that is not at the neutral line. Bending places the single filament

either in tension or compression at, for all practical purposes, a single value of strain. Insert coils like SP-YBCO and NHMFL-YBCO (see Table 1-1) are wound with the superconducting filament on the inside, such that the compressive bending strain will negate some of the tensile strain resulting from Lorentz-forces during coil operation in high magnetic field. In that case the bending strain in the filament is:

$$\varepsilon_{filament}^{bend} = - f_{CC} \cdot e \cdot t \cdot \left(\frac{1}{2r_b} - \frac{1}{2r_i} \right), \qquad (2\text{-}10)$$

in which f_{CC} is the ratio between the distance from the neutral line to the ReBCO layer to the distance from the neutral line to the conductor surface. The sign in equation 2-10 is obviously positive if the superconducting filament is on the outside.

2.5.2 Procedure

The bending procedure is not trivial. Measurements of J_e versus bending diameter for BSCCO conductor often show poor reproducibility, especially when the conductor is "finger pressed" to the desired radius. Therefore the following bending procedure is used:

1. A cylinder with a diameter conform the desired bending diameter is mounted on a coil winder.
2. The end of a conductor section is attached with adhesive tape to this cylinder.
3. The conductor is bent by winding a thin steel tape over the conductor with a low winding tension, as used for winding the 5T insert coils.
4. The steel tape is un-wound and the conductor detached from the cylinder.
5. The unconstrained diameter of curvature is determined.
6. J_e is measured.

This bend-and-release process is repeated with a new sample for each radius. While the procedure does not conform to a standard, it is systematic, minimizes touching of the conductor and closely mimics the coil winding process.

2.6 Conclusion

The conductors, equipment, methods and definitions used in this work are introduced. The conductors include BSCCO tapes and round wire, either with pure Ag matrix, Ag-alloy matrix or reinforced with stainless steel strips and ReBCO tapes; all produced in industry within the past 10 years. The key properties of interest are magnetic field dependence of the engineering critical current density, stress-strain curves and the effect of both bending and uni-axial tension on the engineering critical current density in conductors and coils. The conductor properties cover a wide range of current density and mechanical properties.

Methods, hardware and repeatable procedures are described to measure accurately and safely the engineering critical current density in both short samples of superconductor and in coils, at self-field and in background magnetic fields. Examples of measured data are given such that the noise level can be assessed.

The device and the procedure used to measure stress-strain properties of conductors at 77 K are introduced. Equations to calculate the maximum bending strain on the superconducting ceramic are derived separately for BSCCO and ReBCO conductors; and the procedure used to bend conductors is described as well.

Combining the above allows a comparison between the measured engineering critical current density of coils at high strain levels and predictions following from calculations based on the measured properties of the constituent conductor.

3 Magnetic field dependence of the engineering critical current density

This chapter covers the effect of magnetic field on the superconducting properties of BSCCO and ReBCO superconductors, specifically the engineering critical current density and n-value. Short, straight samples of Bi-2223 tape, Bi-2212 tape and wire, and YBCO coated conductors are investigated in external DC magnetic field. The magnetic field is always oriented perpendicular to the transport current. For magnetic fields within this plane, the dependence of the engineering critical current density of the tape conductors is anisotropic with respect to the field angle. The engineering critical current density is most sensitive to magnetic field perpendicular to the flat side of the tape. The relation between this anisotropy and grain misalignment as it applies to BSCCO tapes is explored. Measured data of the engineering critical current versus magnetic field are compared with a model expressed as the sum of the critical currents of strongly and weakly linked networks. Measurements are presented that relate the n-value to applied magnetic field and the role of anisotropy therein. The ultimate goal is to find a description of the anisotropic conductor properties that is a suitable base for prediction of the magnetic field dependence of the engineering critical current density of coils and magnets.

3.1 Introduction

Knowledge of the transport properties of the superconductor at the temperature and in the magnetic field range where in it is applied is an obvious requirement in the design and construction of superconducting magnets. The required knowledge encompasses primarily the field dependence of the current carrying capacity, and secondarily the shape of the transition between the superconducting and normal state. The engineering critical current density J_e, defined as the critical current divided by the transverse conductor cross section, is used as the quantity expressing the current carrying capacity of a conductor, consistent with the focus of this work on magnets. Conductors do not make up the entire cross section of magnet windings. Insulation, reinforcement and epoxy typically form the remaining components, reducing the average winding current density to a value considerably below the engineering critical current density depending on the superconductor fill factor. Where the average current density in the windings is one of the prime parameters in magnet design, the focus of this chapter is on the engineering critical current density of the constituent conductor.

The investigations described in chapters 3 and 5 focus primarily on Bi-2212 and Bi-2223 tape conductors [25, 77]. These BSCCO tape conductors undergo similar deformation steps during production, wire drawing followed by rolling, resulting in flat filaments that are parallel to the wide surface of the tape. Micaceous deformation of the ceramic occurs during deformation and grain growth during heat treatment is anisotropic. This results in a microstructure that is dominated by colonies of grains that are often not uniquely distinct but share a common *c*-axis direction. The colonies are macroscopically anisotropic; large in the directions of the *ab*-plane and thinner in the *c*-axis direction. Due to interactions with the Ag or Ag-alloy sheathing material, the *ab*-planes of the colonies are aligned with the surface of the conductor but not perfectly. The superconducting properties are also anisotropic. On a microscopic level, the component of *B* perpendicular to the *ab*-plane of

each grain, determines the J_c of that grain [78]. This results in anisotropy on the scale of a conductor, in which a given magnetic field oriented perpendicular to a tape has a stronger reducing effect on the critical current than in parallel orientation. Anisotropic J_e is a relatively new element in high magnetic field superconducting magnet technology, as the traditional conductors NbTi and Nb_3Sn are considered isotropic for practical purposes.

The critical current density in BSCCO tapes is commonly expressed as the sum of the contributions of two parallel networks. The characteristics of the "strongly linked" network are determined by the intra-grain properties, exhibiting significant critical current density to magnetic fields well beyond the reach of state-of-the-art magnets. However, connectivity between grains can be a bottleneck and magnetic fields in the order of a tesla reduce the current density in the network of "weakly-linked" grains to nearly zero[28]. When $J_e(B)$ of a conductor sample is measured there are generally two contributions to the magnetic field: the conductor self-field resulting from its transport current and the applied magnetic field B_A, also known as the background magnetic field. The $J_e(B_A)$ properties thus have three consecutive regimes with increasing B_A. First is the self-field regime, where the conductor self-field determines J_e, and J_e is thus nearly insensitive to the applied field. Second is the weak-links regime characterized by a sharp reduction in J_e, a clear "step down", followed by gradual rate of reduction upon entry in the strong-links regime. The current density in the strongly linked network is reduced to zero as well, the second "step", at sufficiently high magnetic field. A schematic representation of such "double step" behavior [79] is shown in Figure 3-1. The transition between the strong-links and weak-links regime is not sharply defined in reality and the available range of magnetic fields is hardly sufficient to see the second step in J_e at 4.2 K, although it is more easily observed at higher temperatures. However, the parallel network model with corresponding "double-step" behavior is well suited to describe the experimental results.

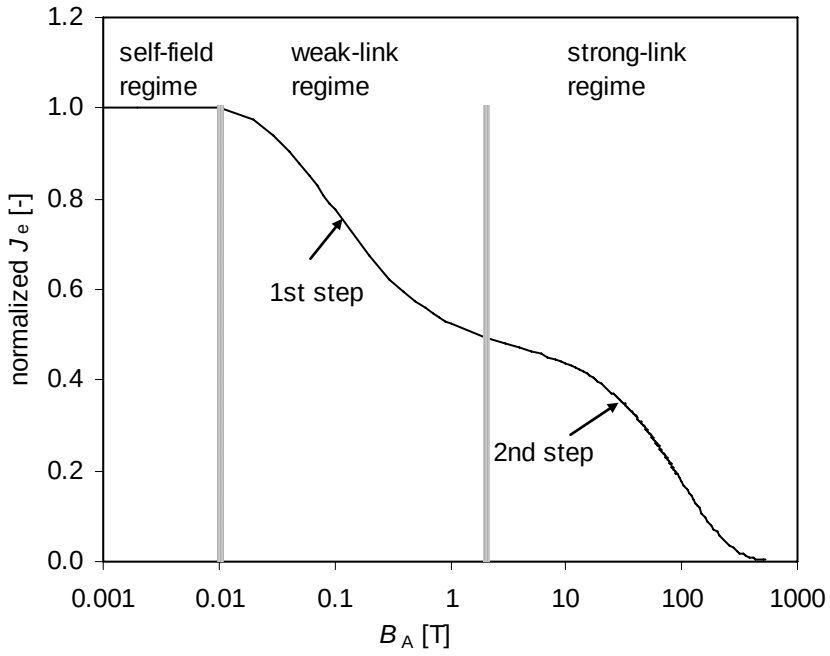

Figure 3-1. Schematic representation of the "double step" behavior in the magnetic field dependence of the critical current density.

[28] This generalization applies to commercial BSCCO tape conductors at 4.2 K in magnetic fields applied perpendicular to both the flat side and the current.

The first challenge, which will be addressed in this chapter, is to correlate grain properties to conductor anisotropy in the critical current density and develop a mathematical expression using the parallel network approach to describe the current carrying properties of those conductors at a temperature and over a magnetic field range that is relevant to Bi-2212 and Bi-2223 sections in 25 T magnets. The average grain misalignment angle α^* is used here as the single parameter determining the link between microscopic and conductor level anisotropy. The second challenge, and a logical next step, is to determine the link between coil properties and their constituent conductors. Again, α^* plays a key role in this relation, which is presented in chapter 5.

For comparison, two other types of conductor are investigated that can be considered extreme cases of grain misalignment: Bi-2212 round wire [61] and YBCO coated conductor [80]. This provides an opportunity to determine to what degree equations and parameters that describe the magnetic field dependence and anisotropy of the critical current density in BSCCO tapes are applicable to HTS conductors with a different architecture.

Production of the Bi-2212 wire considered here shares much in terms of materials and procedures with the Bi-2212 tapes, as they are both produced by the same company. However, the final rolling steps as used for tapes are replaced by additional drawing steps, resulting in a microstructure with some degree of axial alignment of the *ab*-planes but without preferential *c*-axis alignment of the grain colonies in the plane perpendicular to the conductor. This leads to isotropic magnetic field dependence of J_e. For wires to be considered equivalent to tapes with maximum grain misalignment, the magnetic field dependence of J_e should then exhibit the "double step" behavior typical of parallel networks of strong and weak links. Measurements of $J_e(B_A)$ will clarify if the above equivalency statement holds.

The production process for YBCO coated conductor is entirely different to that of the BSCCO conductors and results in a thin-film microstructure that is two-dimensional, as opposed to the three-dimensional poly-crystalline nature of the BSCCO conductors considered here. The grain orientation in this thin-film geometry approaches the limit of zero grain misalignment. Analysis of measured $J_e(B_A)$ properties will clarify if these tapes exhibit the double step behavior as observed in BSCCO tapes and YBCO bulk [79], and also if the anisotropy in $J_e(B_A)$ can be modeled with the same grain-misalignment based mathematical formalism as used for BSCCO.

3.2 Measurements of the critical current versus magnetic field

The samples described in this chapter are from batches A through F, as introduced in chapter 2. The samples within each batch were heat-treated simultaneously in order to create samples that are as near to identical as possible. Each tape sample is measured at 4.2 K; the magnetic field is applied either perpendicular or parallel to the flat surface of the tape and always perpendicular to the current. These orientations correspond to radial respectively axial magnetic field components in a double pancake magnet. In layer wound solenoids there is an axial pitch per turn of conductor introducing a small magnetic field component parallel to the transport current. This applies to the transition turns of double pancake coils as well but this effect is ignored as it is not expected to have a large effect on J_e [59]. For conductor E, the Bi-2212 round wire, only the magnitude of the magnetic field is relevant.

The magnetic field range for which data are presented is limited by the performance of available background magnets and the occurrence of irreversible degradation of superconducting properties. Irreversible degradation sometimes results from the mechanical load on samples at relatively high current and magnetic field, always above 20 T for the conductor investigated here, if it occurred at all. To verify reversibility of $J_e(B_A)$, the measurement at 17.5 T is repeated after measurements in magnetic field above 20 T. Data on irreversibly damaged conductors are excluded from analysis here.

Noise levels in combination with short voltage tap lengths allow accurate determination of J_e for criteria not less than 5 μV/cm. Conversion to the 1 μV/cm criterion is based on a power-law fit through the *E-J* curve[29].

The critical current density of conductor A in the parallel orientation shows a monotonous decrease with applied magnetic field; its slope however decreases and is fairly small above about 20 T. The initial decrease of $J_e(B_A)$ for the sample in the perpendicular orientation is much steeper and larger in value, a slightly sloped plateau characterizes the curve between 5 and about 20 T. The onset of the second step is observed for higher magnetic field values. The data are shown in Figure 3-2.

Hysteresis is often observed in the magnetic field dependence of J_e, as illustrated in Figure 3-2. A detailed discussion of the physics explaining the hysteresis is outside the scope of this thesis. Conductor $J_e(B_A)$ data is used to predict $J_e(B_A)$ of insert coils for increasing magnetic field (see chapter 5), so conductor $J_e(B_A)$ data for increasing magnetic field is desirable. However, conductor $J_e(B_A)$ can not be measured for monotonically increasing magnetic field values as periodic magnetic field reductions are required for reasons explained in section 2.2.4. Therefore specific procedures as listed in section 2.2.4 are required to prevent hysteresis effects from affecting the desired data.

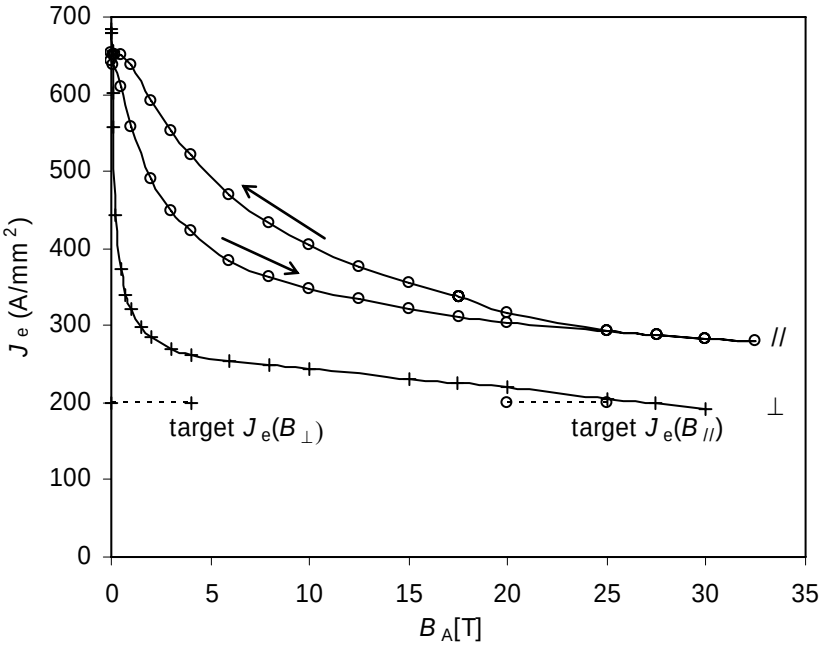

Figure 3-2. Measured engineering critical current density (J_e) of conductor A versus applied magnetic field, for parallel and perpendicular orientations between magnetic field and current. Arrows indicate chronology of applied field. Lines are a guide to the eye.

[29] Further discussion of the measurement technique is given in Chapter 2 and [81].

Curves representing conductors B and C are similar in shape, albeit at slightly lower current density levels. Both the limiting effect of self-field on J_e and the second step are more readily observed in log-linear representation of the properties of conductors B and C as presented in Figure 3-3. Figure 3-3 is also illustrative of the sample-sample variations commonly found between batches (B vs. C) and within a batch (C-1 vs. C-2). Sample-sample variations are further addressed in the next section. Coated-conductor F shows similar behavior; conductor E (Bi-2212 round wire) behaves somewhat like the tapes for perpendicular magnetic fields albeit with a noticeably steeper slope above 10 T. Qualitatively, the measurements confirm to expectations based on the two-step model and anisotropy as described in the previous section. The measured dependence of the critical current density on parallel and perpendicular applied magnetic fields is the basic data on which the subsequent analysis in this chapter is based.

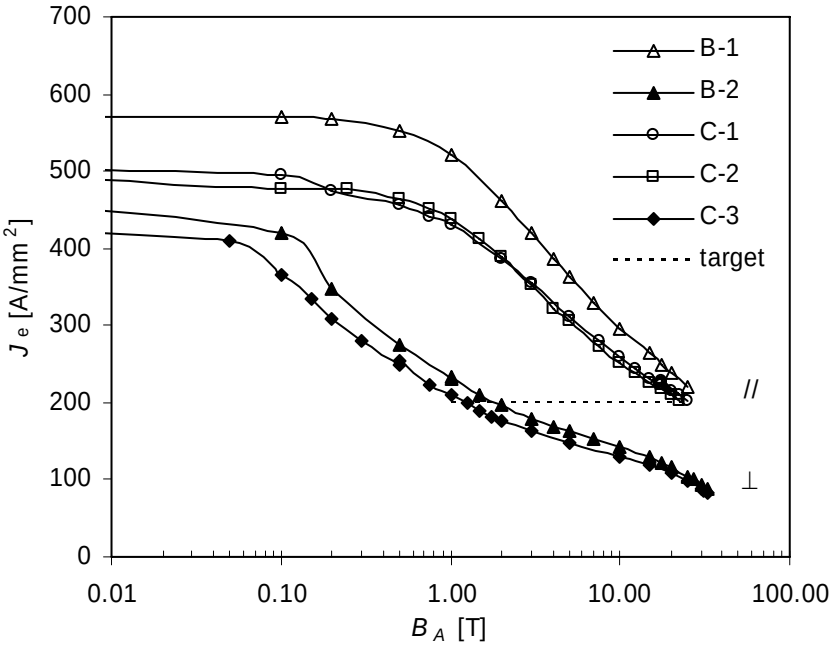

Figure 3-3. Measured critical current density of samples of conductors B and C versus applied magnetic field. Solid lines are a guide to the eye; the dashed line indicates the target value for J_e.

Conductors E and F do not show a double-step behavior in the range from self-field to 45 T applied magnetic field, as shown in Figure 3-4. Equations that do describe the magnetic field dependence are presented in sections 3.3.4 and 3.3.5.

To establish the relevance of the conductors, a comparison between their current density and generic requirements for their use in 25 T magnets is in order. Average current densities in the winding of around 100 A/mm^2 lead to reasonably compact magnets designs[30]. Taking a ratio between average current density and engineering critical current density of 0.5 to 0.7 to be typical leads to a minimum desirable engineering critical current density in the range of 140-200 A/mm^2. The latter value is indicated as the target value in Figure 3-3. The relevant applied magnetic field conditions for the conductor are up to 25 T in parallel orientation and in the order of 2-3 T in perpendicular orientation. The latter number varies with the degree of anisotropy of the conductor and design of the

[30] The relation between current density and compactness is addressed in section 1-3.

magnet[31]. Regardless of the exact value of the applicable perpendicular magnetic field, it is clear that conductors B, C and E perform around the $J_e = 200$ A/mm^2 target while conductors A and F exceed this value. All conductors investigated here are suitable candidate conductors for 25 T magnets on the basis of current density.

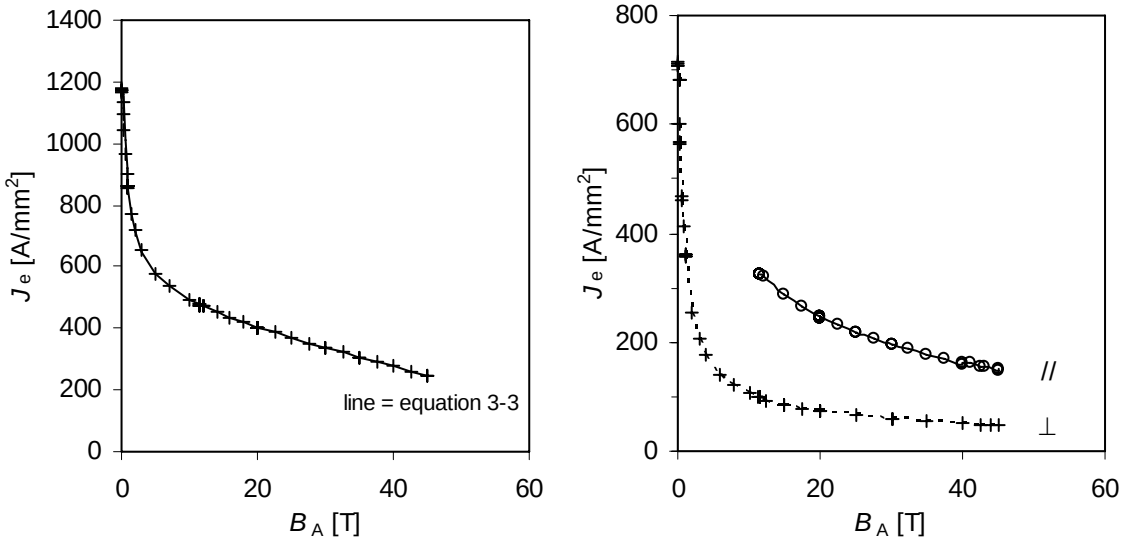

Figure 3-4. Measured magnetic field dependence of J_e for conductors E (left, Bi-2212 round wire) and conductor F (right, YBCO CC). The lines connecting the data points are a guide to the eye for conductor F and represent equation 3-3 for conductor E.

3.3 Modeling the $J_e(B_A)$ behavior for perpendicular magnetic fields

3.3.1 Model for BSCCO tape

The expression for the magnetic field dependence of the critical current density is based on a parallel network model. Here J_e is described as the sum of the critical current densities of a strongly and a weakly linked network of paths as expressed in equation 3-1. Subscripts w and s indicate weak and strong respectively.

$$J_e(B) = J_{ew}(B) + J_{es}(B) \qquad (3\text{-}1)$$

The magnetic field used in this model is $B_{eff,}$ the effective local magnetic field component perpendicular to the tape. This is a calculated field value nearly identical to the applied perpendicular field, B_{eff} being 0.1 to 0.5% smaller for the conductors under consideration[32]. The limiting effect of conductor self-field is not included in the parallel network model itself and is taken into account by setting the calculated J_e to the measured self-field J_e if the sum of the contributions from the strongly linked and weakly linked networks exceeds the measured conductor self-field J_e.

$$J_e(B) = \frac{J_{ew}}{1+\left(\frac{B}{B_0}\right)^{\beta}} + J_{es}\exp\left(\frac{-B}{B_{sc}}\right) \text{ for } J_e(B) \le J_e(self),\ J_e = J_e(self) \text{ otherwise} \qquad (3\text{-}2)$$

The weak links term in equation 3-2 reflects the assumption that weak links behave like Josephson junctions [82], where β reflects the geometry of the weak links and ranges

[31] The anisotropy-design relation is addressed in detail in Chapter 4.
[32] B_{eff} is discussed in detail in section 3.4.

between one and two. The strong links term is a simplified expression based on flux pinning. B_0 and B_{sc} are referred to as the characteristic field values for the magnetic field dependence of the respective networks.

The physics behind this parallel path model, and specifically the weak links aspect, is subject of continued debate and research. Multiple models and variations thereof have been proposed. Different equations and parameters based on different physical phenomena may fit the measurements discussed below equally well. However, finding mathematical relations that accurately describe the measurements is the main focus here. The expressions "strongly-linked" and "weakly-linked" serve as convenient handles to the terms of the fit function in equation 3-2. As such, a fit function that accurately describes measured data remains valid even if new insights would suggest a name or equation associated with different physical phenomena to be more appropriate.

3.3.2 Fits to data on BSCCO tapes

The measured properties of conductors A, B and C are adequately described with equation 3-2 using the parameters from Table 3-1. This is illustrated for sample A-2 of conductor A in Figure 3-5. The junction-geometry parameter β is set to unity for simplicity, with no significant loss of accuracy. The value of J_{es} is fairly well determined by the measurement, somewhat less so for B_{sc} Different combinations of the weak link parameters result in a very similar fit. To quantify this, a maximum error of 2% is set, compared to 1.7% for the best fit, and all parameters are varied independently. The maximum fit error remains below 2% with variations of J_{es} of 1%, B_{cs} can be varied 7%, and J_{ew} and B_0 can be varied about 16%. The 2% maximum value is an arbitrary choice, but the result of this exercise is indicative of the precision of each fit parameter. The strong links parameters are fairly well defined; the weak links properties can be described with a larger range of parameter combinations.

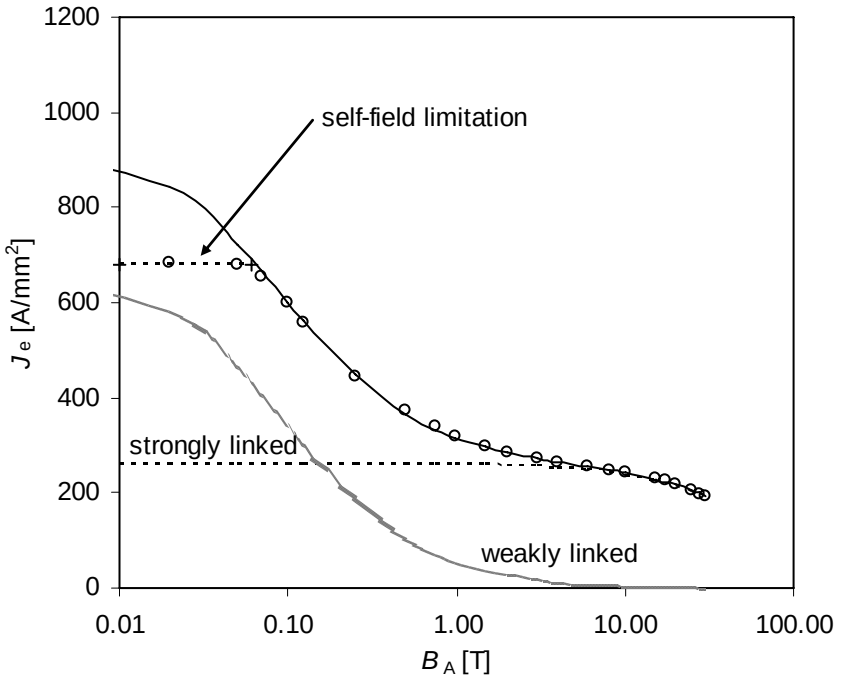

Figure 3-5. Measured critical current density of conductor A versus B_A, for B_A perpendicular to the surface of the tape. The data (◦) are modeled as the sum of a strongly and a weakly-linked current path using equation 3-2 and the parameters of Table 3-1.

Table 3-1. Parameters used in the model of equation 3-2 to model the measured critical current density for applied magnetic fields in the perpendicular orientation. Also listed are the average deviation between the model and the measured data and the ratio between measured self-field J_e and the modeled zero-field J_e.

Conductor	**A**	**B**	**C**	**B, C#**	**D**
J_{es} **[A]**	261	162	150	161, 151	90
B_{sc} **[T]**	99	54	54	54	54
J_{ew} **[T]**	695	373	293	361, 303	209
B_0 **[T]**	0.094	0.223	0.255	0.24	0.24
β	1	1	1	1	0.73
Average deviation (≥0.1 T)	0.8%	0.9%	1.0%	1.0%	1.1%
Maximum deviation (≥0.1 T)	1.7%	2.6%	2.3%	2.6%	2.7%
J_e**(self)/ (**J_{es}**+**J_{ew}**)**	72%	90%	94%		93%

#: Fit parameters for conductors B and C when using the same scaling fields for both sets of data.

3.3.3 Batch to batch variations

Comparing the properties of conductors B and C provides the first insights in batch-to-batch variations that can be expected. The production process of Conductors B and C is nominally identical except for the peak temperature during partial melt phase of the heat treatment [25]. While specific J_e values differ, J_e can be modeled using the same scaling field for the strongly-linked and weakly-linked networks. The loss in precision compared to using separate scaling fields for each conductor is marginal, as shown in Table 3-1. The strong-links parameters are clearly more reproducible between conductor batches than the weak-links parameters. This implies that weak links properties are more sensitive to the details of the production process than the strongly linked network.

To obtain an indication of the precision of the fit parameters for conductor B the maximum error is set to 3%, compared to 2.6% for the best fit, while varying all fit parameters. This condition allows a 3% variation of J_{es}, 5% in B_{sc}, while J_{ew} and B_0 can be varied about 7%.

Some further insight regarding the variation of properties between different conductor batches is obtained by considering conductor D as well. Conductors B, C and D are produced by the same company using the same thermo-mechanical processing. The ceramic starting powder for conductor D, however, is from a different source with a slightly different composition. The best fit using equation 3-2 with $\beta = 1$ is not as close as for conductors B and C. First, the curvature of the weak-links contribution does not quite match the measurements. Second, the calculated J_e value for B_{eff} approaching zero is lower than the measured value. One would expect a higher calculated value for $J_{es}+J_{ew}$ as conductor self-field is not taken into account. However with β as a free parameter, a close fit is once again obtained with the same scaling fields for the strongly and weakly-linked networks as for conductors B and C. The value of β, below unity, does not match with the theoretical range of 1 to 2 when β is interpreted as a geometrical factor in the magnetic field dependence of the properties of Josephson junctions. An alternate model for weak links behavior, based on classical flux creep, with exponential field dependence similar to the links term in equation 3-2 is proposed by Van der Laan [82]. While such a term fits the weak links contributions for conductors B and C as well as the power law term used here, it does not match the curvature in $J_{ew}(B_A)$ for conductor D either. The best exponential fit shows an average deviation from the measurements of 4%, with a

maximum error of over 6%, where a power law fits within 1% on average. If anything, the above points to the difficulty to develop physical models for the field dependence of weak-link superconducting properties that apply universally.

Of more importance are the similarities between the properties of conductors from different batches, if one aims to model the properties of a magnet consisting of multiple batches of conductor without measuring the properties of each batch over the entire magnetic field range. When the models that best fit the properties of conductors B, C and D are each normalized to their self-field J_e, the curves as shown in Figure 3-6 are found to overlap in the range of $0.5 < B_A < 3$ T. This mostly covers the range of interest for BSCCO conductors in 25 T magnets. This suggests that the dependence of J_e on perpendicular magnetic fields for other batches similar to conductors B,C and D can be approximated by multiplying their self-field J_e with the normalized $J_e(B_A)$ data of conductor B-1.

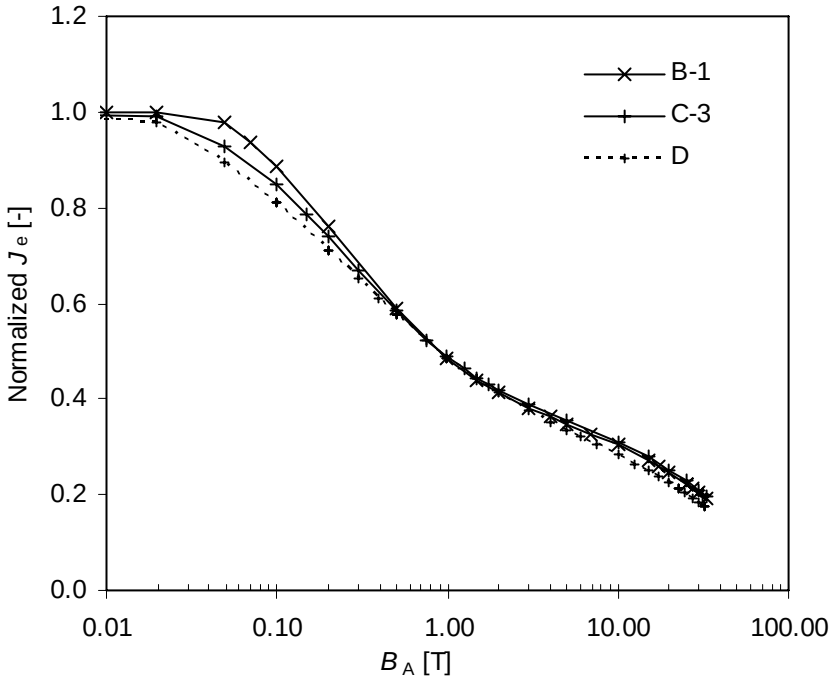

Figure 3-6. $J_e(B_A)$ models for conductors B,C and D normalized to measured self-field values.

3.3.4 Bi-2212 round wire

The measured magnetic field dependence of J_e in conductor E does exhibit a clear "double-step" behavior, indicative of two parallel networks with different current limiting mechanisms. However, it can not accurately be described by equation 3-2. The self-field regime is significantly larger than for the tapes, approaching 1 T versus ~ 0.1 T, and is beyond proportionality with J_e. Differences in geometry are a more likely explanation. Assuming the magnetic flux lines follow the circumference of the conductor, one can estimate the self-field on the surface of the conductor using Ampere's law. For the BSCCO tapes this yields an estimate of about 0.1 T versus 0.8 T for the Bi-2212 wire, as the round wire has a much smaller perimeter for a given cross sectional area. These estimates are consistent with the data.

At high magnetic field the dependence of J_e is nearly linear. The summation of a linear term and a power term, as in equation 3-3, describes the measured characteristics above 1 T with an average error of 0.2% and a maximum error of 1%. The fit error is only marginally larger than the repeatability of the measurements. The linear term dominates at high magnetic fields, but the power term still represents a significant fraction of J_e above 10 T. The linear and exponential terms are not based on specific physical phenomena but represent the simplest mathematical terms found that accurately describe the data. Thus a fit of the magnetic field dependence of J_e in this Bi-2212 round wire is given; one that is significantly different from Bi-2212 tapes:

$$J_e(B_A) = 417 - 4.99 \cdot B_A + 449 \cdot B_A^{-0.55} \text{ for } B_A > 1\text{T}, J_e(\text{self}) = 1172 \text{ A/mm}^2. \quad (3\text{-}3)$$

The measured data and the above equation are presented in Figure 3-7.

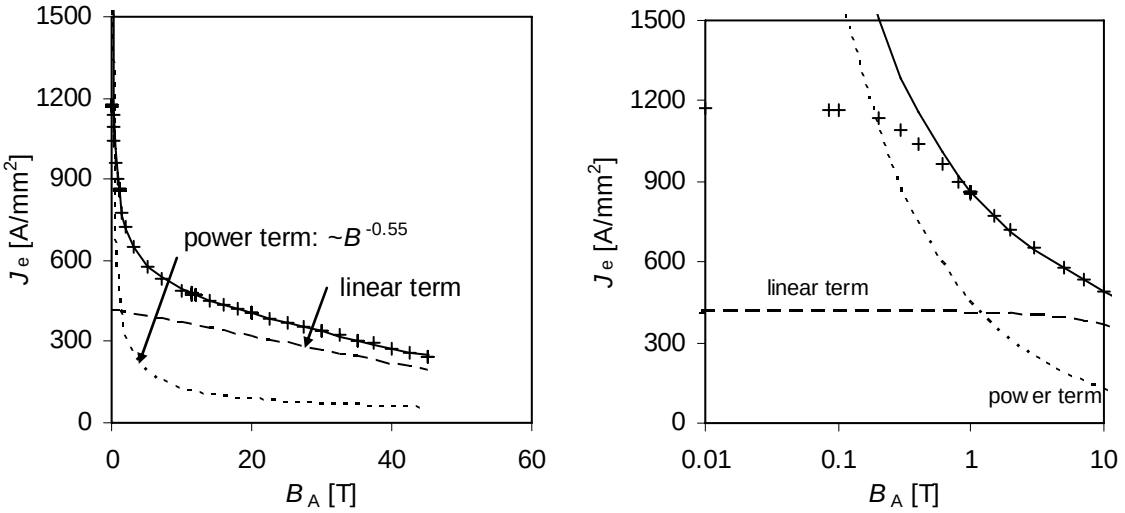

Figure 3-7. Measured J_e for conductor E versus applied magnetic field (+ symbols). The solid line is a fit based on an exponential and a linear term.

3.3.5 YBCO Coated Conductor

The measured field dependence in conductor F does not exhibit the double-step behavior as seen for conductors A-E, and bulk YBCO [79], but a single flux-pinning mechanism appears to determine $J_e(B_A)$. Its properties outside the self-field dominated regime can be accurately described using a power term, as has been observed in other YBCO coated conductors [83, 84]. Equation 3-4 fits the data with an average deviation of 1% and a maximum deviation of 3.3%. While the deviation is clearly larger than the corresponding equations for the Bi-2212 data, which had slightly better reproducibility, it is close to the level of deviations seen for conductors B and C. In comparison, application of the strong-links plus weak-links model of equation 3-2 would have resulted in deviations more than twice as large as the power term does. The Kramer relation [85] with $p = 0.5$ and $q = 2$ provides a slightly better fit than equation 3-2, but still at nearly twice the average and maximum deviations as equation 3-4. Leaving p and q free as fit parameters does not significantly improve the fit. Therefore equation 3-4, with its implication of a single flux-pinning mechanism, provides the best available fit using a minimal number of fit parameters, while the Kramer equation provides for a slightly inferior but still quite reasonable fit. A graph of the model and measured data are presented in Figure 3-14.

$$J_e(B) = 358 \cdot B_A^{-0.53} \text{ for } B_A > 0.4 \text{ T}, J_e(\text{self}) = 711 \text{ A/mm}^2. \quad (3\text{-}4)$$

For reasons that will be addressed in chapter 4, it is desirable to have a direct fit of the $J_e(B_A)$ relation for the parallel field orientation as the basis for further analysis as opposed to $J_e(B_\perp)$. Such fits are also addressed in chapter 4.

3.4 Angular dependence of $J_e(B)$ in BSCCO tapes

The notion proposed by Kes [78], that the current carrying capacity of a grain colony is determined by the component of $\boldsymbol{B}$ perpendicular to its *ab*-plane, provides the basis for the approach used to model the angular dependence of $J_e(\boldsymbol{B})$ in BSCCO tapes. For the strongly linked network, generally associated with small angles between well-connected grains and limited by intra-grain flux pinning, one expects the colony properties to carry over to the level of conductor properties. This implies simple scaling of $J_e(\boldsymbol{B})$ with the magnetic field component perpendicular to the flat side of the tape for all field angles except in conditions where the small angles between grains become significant. The weakly-linked network is generally associated with larger grain angles, and grain boundary properties that limit the super-current, rather than intra-grain properties. It is therefore not clear whether the model by Kes should hold for the weak links network, but we will start with assuming that it does and introduce a single scaling function for $J_e(\boldsymbol{B})$, similar to the scaling function developed in [86]. Thus the intent is to derive a scaling function $f(\phi)$ such that the effective perpendicular magnetic field $B_{eff}^{\perp}$ relates to the magnitude of $\boldsymbol{B}$ and the magnetic field angle ϕ as:

$$B_{eff}^{\perp} = B \cdot f(\phi), \quad (3\text{-}5)$$

and $J_e(B)$ for any magnetic field angle can be calculated by substituting $B_{eff}^{\perp}$ in the measured $J_e(B_\perp)$ relation:

$$J_e(B,\phi) = J_e(B \cdot f(\phi), 90^\circ) = J_e(B_{eff}^{\perp}, 90^\circ). \quad (3\text{-}6)$$

X-ray diffraction measurements [87, 88] indicate that a more or less symmetrical distribution of grain misalignment angles around the plane of the tape can be expected. An example of such a microstructure is presented in Figure 3-8 (left). The definition of magnetic field angle ϕ and the grain misalignment angle α are introduced in Figure 3-8 (right).

A Gaussian distribution of the grain misalignment angle with standard deviation σ is assumed as in equation 3-7, although it will be shown below that the exact shape of the distribution function $G(\alpha)$ is not critical.

$$G(\alpha) = \frac{1}{\sigma\sqrt{2\pi}} e^{-(\alpha^2/2\sigma^2)}, -90 \le \alpha < 90^\circ. \quad (3\text{-}7)$$

In a slight deviation from [86], which uses the standard deviation σ as parameter to characterize the degree of misalignment, the average grain misalignment angle α^* is used instead. This approach is more general, since the average misalignment angle α^* can in principle be calculated for any distribution. For a Gaussian distribution one has $\alpha^* = \sqrt{(2/\pi)} \cdot \sigma$.

For a single grain the magnetic field component perpendicular to its *ab*-plane is $B \cdot |\sin(\phi+\alpha)|$. For all grains combined the average perpendicular component is calculated as in equation 3-8:

$$B_{ave}^{\perp}(\phi) = B \cdot \int_{\alpha=-90^{\circ}}^{90^{\circ}} G(\alpha) \cdot |\sin(\alpha+\phi)| \, d\alpha \,. \tag{3-8}$$

If the $J_e(B_\perp)$ curve can be considered linear for the relevant range around $B_{ave}^{\perp}$ then the average magnetic field component is equal to the effective magnetic field component $B_{eff}^{\perp}$.

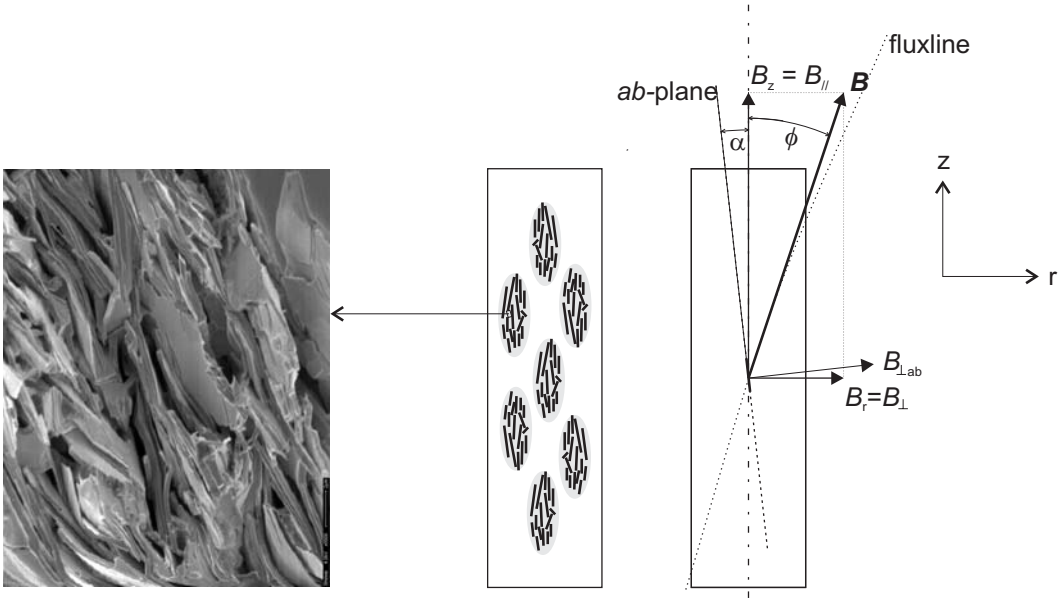

*Figure 3-8. Schematic cross-section of a 7-filament tape conductor with grain colonies in black (middle) and an enlargement of a small area of the characteristic transverse cross section of a filament (left). A grain colony with misalignment angle α is indicated on the right with the total magnetic field **B** and its projections in radial (r) direction, axial direction (z) and on the ab-plane ($B_{\perp ab}$).*

$$B_{eff}^{\perp}(\phi) = B \cdot \int_{\alpha=-90^{\circ}}^{90^{\circ}} G(\alpha) \cdot |\sin(\alpha+\phi)| \, d\alpha \,. \tag{3-9}$$

The assumption of local linearity in $J_e(B_\perp)$ is also (implicitly) made in [86]. Taking the case of a magnetic field perpendicular to the tape ($\phi = 90°$) as reference, a scaling function $f(\phi)$ can be defined as

$$f(\phi) = \frac{B_{eff}^{\perp}(\phi)}{B_{eff}^{\perp}(90^{\circ})}. \tag{3-10}$$

It follows from 3-9 and 3-10 that the scaling function $f(\phi)$ can be calculated as

$$f(\phi) = \frac{\int_{\alpha=-90^{\circ}}^{90^{\circ}} G(\alpha) \cdot |\sin(\alpha+\phi)| \, d\alpha}{\int_{\alpha=-90^{\circ}}^{90^{\circ}} G(\alpha) \cdot |\sin(\alpha+90^{\circ})| \, d\alpha}. \tag{3-11}$$

Note that the scaling function is independent of the magnitude of the magnetic field. As a Gaussian distribution function is fully known once the average deviation is known, the dependence of $f(\phi)$ on grain misalignment is thus determined by a single parameter: the

average grain misalignment α^*. For the hypothetical case of perfect *c*-axis texture (when all grains have $\alpha = 0$), the scaling function is the sine function. For practical conductors with finite misalignment angles, the scaling function deviates from $\sin(\phi)$ for small magnetic field angles and levels off to a constant value for $\phi = 0$. Example curves are shown in Figure 3-9. Note that the scaling functions are always monotonously increasing with magnetic field angle. This derivation follows Van der Meer [86] but replaces I_c with J_e and defines the magnetic field angle relative to the plane of the conductor.

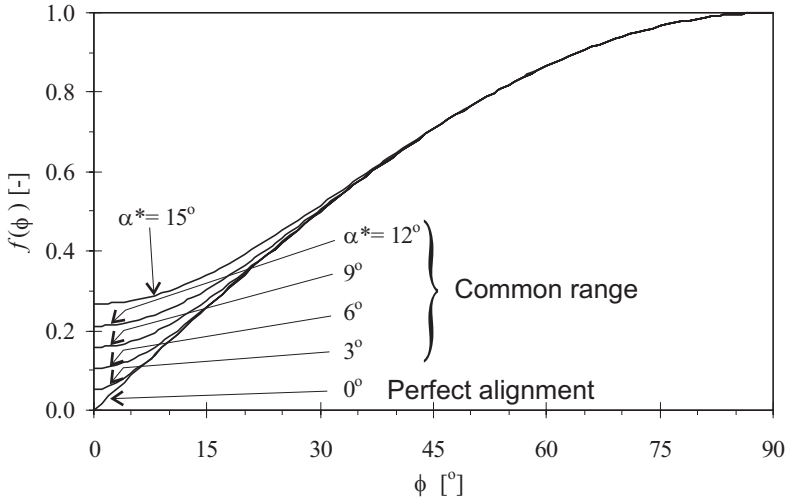

Figure 3-9. Magnetic field scaling function f(ϕ) for several values of the average grain colony misalignment angle α^*.

To assess how critical the assumption of a Gaussian distribution for α is, we compare the scaling function using three different grain alignment distributions with an average misalignment of 8°. The Gaussian, triangular and somewhat extreme case of a rectangular distribution are depicted in Figure 3-10 (left). The resulting differences in *f* are small (≤ 0.01) for the range depicted in Figure 3-10 (right) and negligible for other angles.

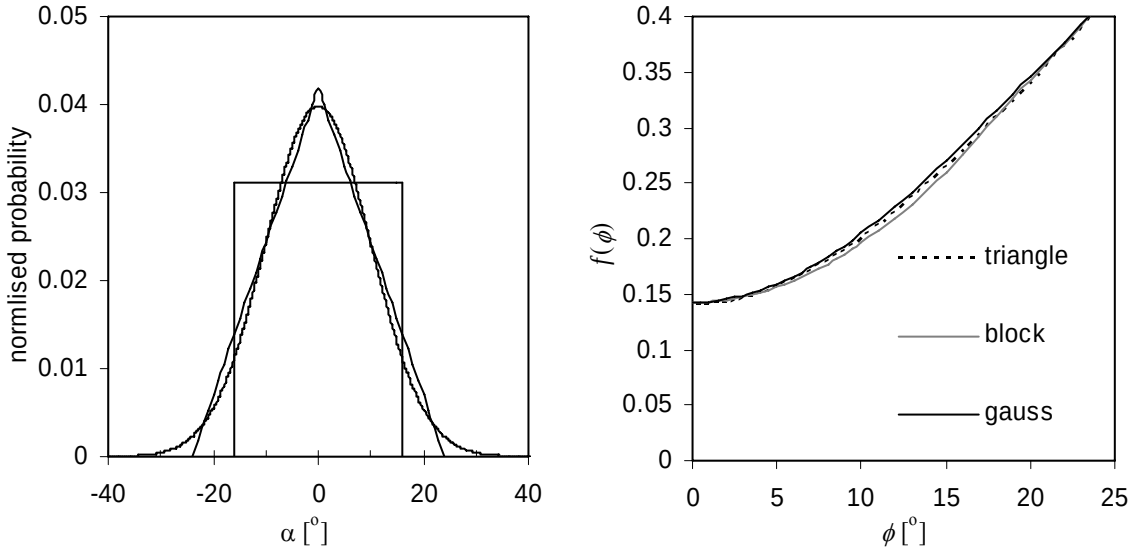

Figure 3-10. Distribution functions with an average deviation of 8° (left). Detail of the scaling function for these distribution functions (right).

So the scaling function f is only weakly related to the assumed distribution function. It is therefore likely that the presented scaling function based on a Gaussian grain misalignment distribution will accurately reflect the angular dependence of J_e, even if the distribution function is not precisely Gaussian.

A remaining question is the determination of α^* itself. Considering Figure 3-8 and equation 3-8, one can see that the average component perpendicular to the *ab*-planes is $B\cdot\sin(\alpha^*)$ for $\phi = 0$ and $B\cdot\cos(\alpha^*)$ for $\phi = 90°$. The average grain misalignment angle α^* can therefore be determined from normalized critical current densities using the ratio of parallel ($\phi = 0$) and perpendicular ($\phi = 90°$) magnetic field values that result in the same short sample J_e, as illustrated in Figure 3-11. As J_e decreases monotonously with B_{eff}, the respective effective magnetic field values must be identical when the J_e values are identical. The average grain misalignment α^* thus follows from:

$$B_{\perp}\cdot\cos(\alpha^*) = B_{//}\cdot\sin(\alpha^*). \qquad (3\text{-}12)$$

Using this method, an α^* value can be calculated for every J_e value on the $J_e(B_{//})$ curve. In the case of perfect scaling, this value is independent of B. For field values well above the self-field range, the $J_e(B_{//})$ curve should then scale with the $J_e(B_{\perp})$ curve as follows:

$$J_e(B_{\perp}) = J_e(B_{//}\cdot f(0)), \qquad (3\text{-}13)$$

i.e. the $J_e(B)$ curves for parallel and perpendicular magnetic field should fall on top of each other when the $B_{//}$ values are multiplied by $f(0)$.

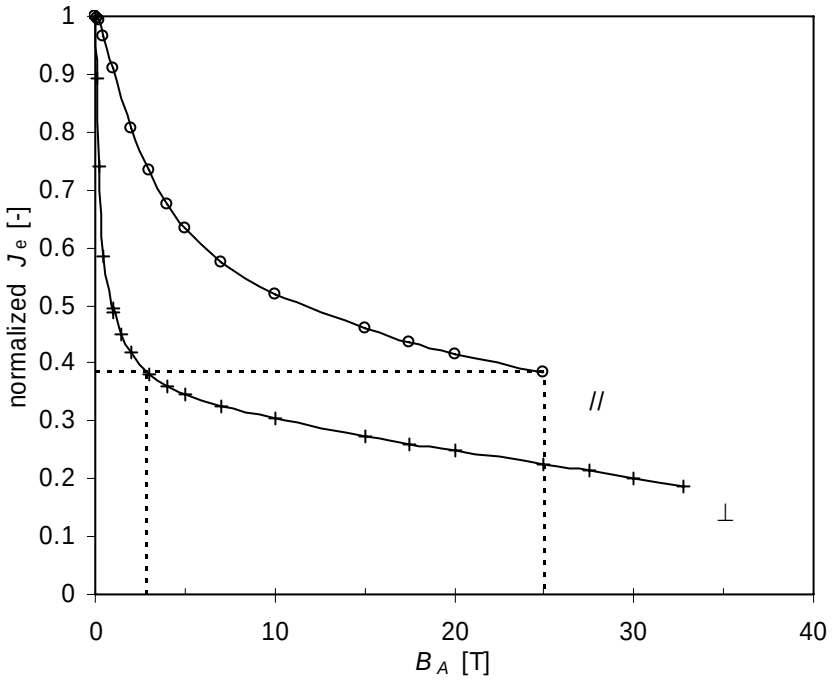

Figure 3-11. Normalized critical current density of conductor B at 4.2 K for applied magnetic field parallel (//) and perpendicular (⊥) to the flat side of the tapes. The J_e in 25 T parallel magnetic field resembles the J_e in 2.91 T perpendicular magnetic field. From the ratio of these two field values α^* is calculated, as explained in the text.

For practical conductors the scaling for arbitrary angles has been verified mostly by measurements on Bi-2223 at various temperatures but usually above 15 K and for

relatively low magnetic field (< 6 T). [86, 89, 90, 91, 92]. Explicit and accurate calculations of α^* at 4.2 K for a range of magnetic field values relevant to BSCCO sections of 25 T magnets were not found in the literature.

The above discussion explains the choice of α^* as the single parameter describing the anisotropy in $J_e(B)$ in BSCCO tapes and presents a method to determine α^*. Determination of α^* for conductors A, B [93] and C is presented in the following section. The applicability of this parameter to calculate $J_e(B)$ of coils is studied in chapter 5. The effect of α^* on the design of BSCCO and ReBCO inserts is the topic of chapter 4, which also features a discussion on the applicability of α^* to ReBCO coated conductor.

3.5 Grain misalignment angle

3.5.1 BSCCO tape conductors

The average grain misalignment angle is assessed on its suitability to describe the anisotropy in $J_e(B_A)$ for conductors A, B and C, particularly the relation between $J_e(B_\perp)$ and $J_e(B_{//})$. The upper limit of the range over which α^* can be calculated is determined by the highest $B_{//}$ value. The lower limit is chosen at 0.1 T, to avoid the magnetic field range where conductor self-field effects have a dominant effect on J_e. This is of little consequence since the axial and radial magnetic field components in insert magnets generally exceed this range[33] by far.

The experimental setup, using different samples for each orientation, does not allow a sharp determination of the error margin. The uncertainty in α^* as a result of sample-to-sample variations is larger than the uncertainty in α^* as a result of the uncertainty in the J_e determination. For the Bi-2212 conductors investigated here, the margin of error in the average grain misalignment is estimated between 0.5 and 1 degree as explained below. For the Bi-2223 conductor an equal or smaller margin of error is expected, as batch-to-batch variability in superconducting properties appears to be lower.

Determination of α^* as shown in Figure 3-11 points out that the average grain misalignment angle in conductor A, the Bi-2223 conductor, is less than for the Bi-2212 conductors B and C. The observed difference qualitatively corresponds to the observed microstructure. The longitudinal cross sections of Figures 2-2 and 2-3 show less sausaging in the Bi-2223 conductor and generally a better alignment of the grains with the longitudinal axis of the conductor, compared to the Bi-2212 conductors. The patterns in calculated α^* for the two types of conductor appear to be consistent within each type. The data for perpendicular and parallel magnetic field data scale for both types of conductor without large errors. Therefore, the general concept of modeling anisotropy in conductor $J_e(B_A)$ through the average grain misalignment angle seems reasonable. The results for Bi-2212 and Bi-2223 are discussed separately and in more detail below.

Conductor A

The calculated values of α^* for conductor A, presented in Figure 3-12, are understood within the model. The calculated average grain misalignment angle ranges from 2.7 to 2.8 degree for perpendicular magnetic fields above 0.5 T, consistent with the model that only the component perpendicular to the *ab*-plane affects J_e. This angle corresponds to a ratio of 20 between the parallel and perpendicular magnetic field values that result in the same J_e. $J_e(B_{//})$ and $J_e(B_\perp)$ scale accurately in this range, as shown in Figure 3-13.

[33] The range of radial, axial and effective perpendicular field components is addressed in Chapter 4.

The scaling is less accurate and the calculated value for α^* is less constant and higher for $B_{eff} < 0.5$ T, i.e. the conductor is less anisotropic. This is consistent with the association of the weakly-linked network with higher grain angles. The magnetic field range below 0.5 T is relevant for sections of double pancake coils at self field and applied parallel fields in the order of several tesla as shown for example in Figure 5-13. Models of coil J_e based on short sample $J_e(B)$ and a magnetic field independent value for α^* can be expected to deviate somewhat from actual (measured) values in that field range.

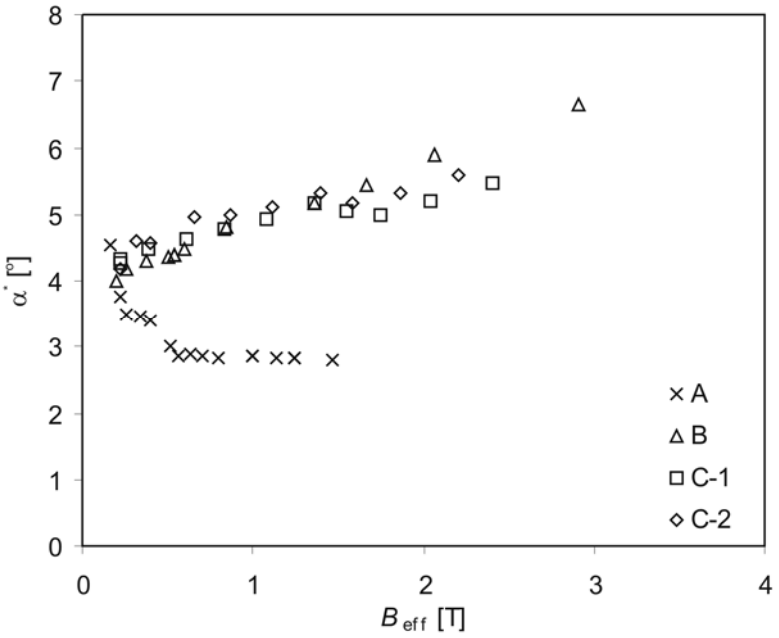

Figure 3-12. Calculated average grain misalignment angles versus B_{eff}. The margin of error is discussed in the text.

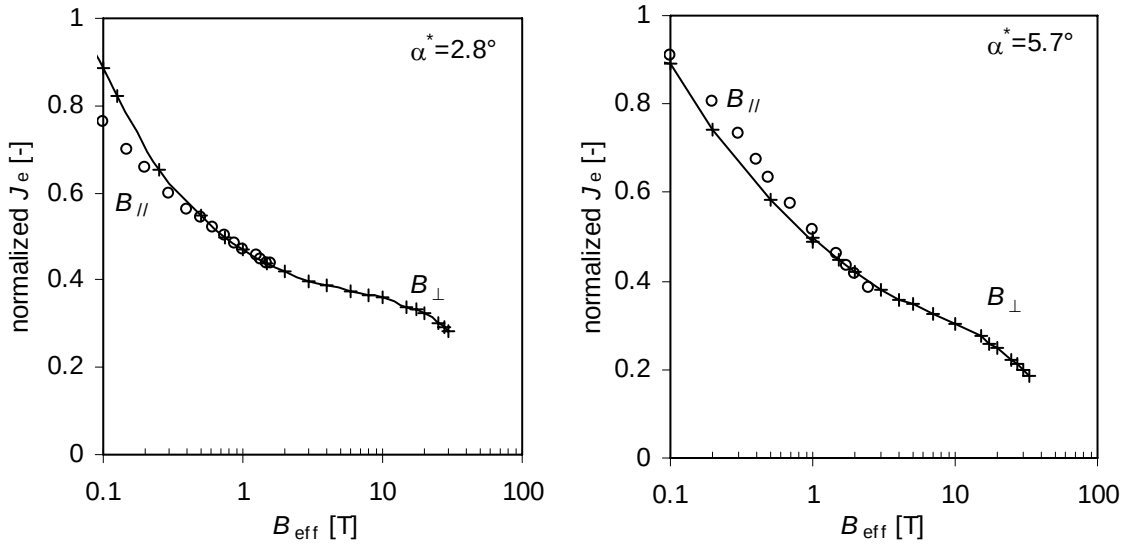

Figure 3-13. Scaling of the critical current with B_{eff} for conductor A (left) and B (right). The line through the $J_e(B_\perp)$ data is a guide to the eye.

To quantify the quality of the scaling, the difference in J_e is calculated at all B_{eff} values, as far as the $B_{//}$ and $B_{\perp}$ curves overlap, taking α^* as 2.8 degrees. Comparison of Tables 3-1 and 3-2 shows that scaling is as accurate as the $J_e(B)$ data itself for $B_{eff} > 0.5$ T. This leads to the expectation that taking α^* as 2.8 degrees will allow accurate modeling of coil $J_e(B_{A)}$ for conditions in which B_{eff} is predominantly > 0.5 T.

Table 3-2. Average grain misalignment angles used to relate the perpendicular and parallel magnetic field values to the effective magnetic field, i.e. scaling, and a quantification of the differences in the resulting $J_e(B_{eff})$ curves.

Conductor	**A**	**B**
α^* [°]	2.8	5.7
Average deviation in J_e for B_{eff} ≥0.1 T	3%	5%
Maximum deviation in J_e for B_{eff} ≥0.1 T	14%	9%
Average deviation in J_e for B_{eff} ≥0.5 T	1%	3%
Maximum deviation in J_e for B_{eff} ≥0.5 T	2%	7%

Conductors B & C

An explanation of the margin of error in α^* is in order before discussing the results. Assuming the average grain misalignment is constant and the value determined at $B_{eff} = 1$T (corresponding to $B_{\perp} = 1$ T and $B_{//} \approx 12$ T) is correct, a $J_e(B_{//})$ curve can be calculated by scaling the $J_e(B_{\perp})$ curve. The difference between this constructed curve and the measured data in parallel magnetic field for sample C is less than 10 A for $B_{//} > 12$ T. This is beyond the estimated error margin in the determination of J_e, but is within the range of observed sample-to-sample variations in shape of the $J_e(B_A)$ curve for Bi-2212 conductors. Comparing C-1 and C-2 in Figure 3-3 provides an example of such variations. Thus, based on margin of error in the J_e determination plus sample-sample variations, the estimated error in the average grain misalignment is about 0.8 degree.

The calculated α^* values for conductors B and C appear to increase with magnetic field, but can at the same time be considered constant within the margin or error. Taking α^* constant as 5.7 degrees for conductor B leads to a scaling factor of 10 between parallel and perpendicular magnetic fields resulting in the same J_e. A parallel magnetic field of 25 T is then equivalent to a perpendicular magnetic field of 2.5 T. This scaling is illustrated in Figure 3-13 (right) for conductor B. In the range of overlapping B_{eff} (0.1-2.5 T), J_e differs by an average of 5% with a maximum of 9%. Choosing different α^* values will shift the $J_e(B_{//})$ curve to the left or right, but the slope remains different from the $J_e(B_{\perp})$ curve and the error does not change significantly. It is concluded that scaling with a field independent α^* is approximately correct but does not describe the measured results accurately. The calculated grain misalignment varies less for $B_{eff} \geq 0.5$ T in conductor C, as is observed in Figure 3-12, corresponding to a more accurate scaling with an α^* of about 5° and a scaling factor of 11. As for conductor B, scaling is far from perfect for any choice of α^*.

The magnetic field dependence of J_e of conductors B and C has also been investigated by Xu [92] over a smaller magnetic field range (0-5 T) but at multiple magnetic field angles. Xu finds accurate scaling with $\sigma = 6°$, equivalent to $\alpha^* = 4.8°$ for $0 < B_{eff} < 0.4$ T. This matches the data of Figure 3-12 over that range of B_{eff} and also confirms that the average grain misalignment model can be used to predict J_e at intermediate angles if $J_e(B_{//})$ and $J_e(B_{\perp})$ are known. However, the range of magnetic field values is too limited to determine

if α^* can be considered constant, and thus whether scaling with a magnetic field independent α^* value would be accurate, over the magnetic field range relevant to insert coils.

Scaling would be accurate with a magnetic-field dependent α^* following the trend discernable in Figure 3-12, but this is not consistent with the concept of α^* as a geometric parameter determined by the microstructure.

The apparent upward trend of α^* with B_{eff} is contrary to expectation, as the field-range over which the critical current is measured extends into the strong-links dominated regime and a constant value for α^* is expected in particular in this range. Furthermore, strongly linked networks are generally associated with small grain misalignment angles, and weakly- linked networks with larger angles, so a decrease of the calculated α^* value with B_{eff} is more plausible than an increase. The physics behind a possible upward trend in α^* versus B_{eff} is not yet understood.

An alternative to more sharply determine the magnetic field (in-)dependence of α^* is through modeling of the measured $J_e(B_A)$ curves of double pancakes. The longer length of conductor in a coil is a bypass to the sample-sample variation problem to some extent. Comparing the quality of the fit between models with a constant α^* and a magnetic-field dependent α^* will indicate weather α^* can be considered constant or not. This test is addressed in chapter 5.

3.5.2 ReBCO conductor

Conductor F does not have the 3-D polycrystalline microstructure that lead to the concept of the average grain misalignment angle to model anisotropy in $J_e(B_A)$. However, the magnetic field dependence of J_e does scale when α^* is assumed to be 6.1° as shown in Figure 3-14.

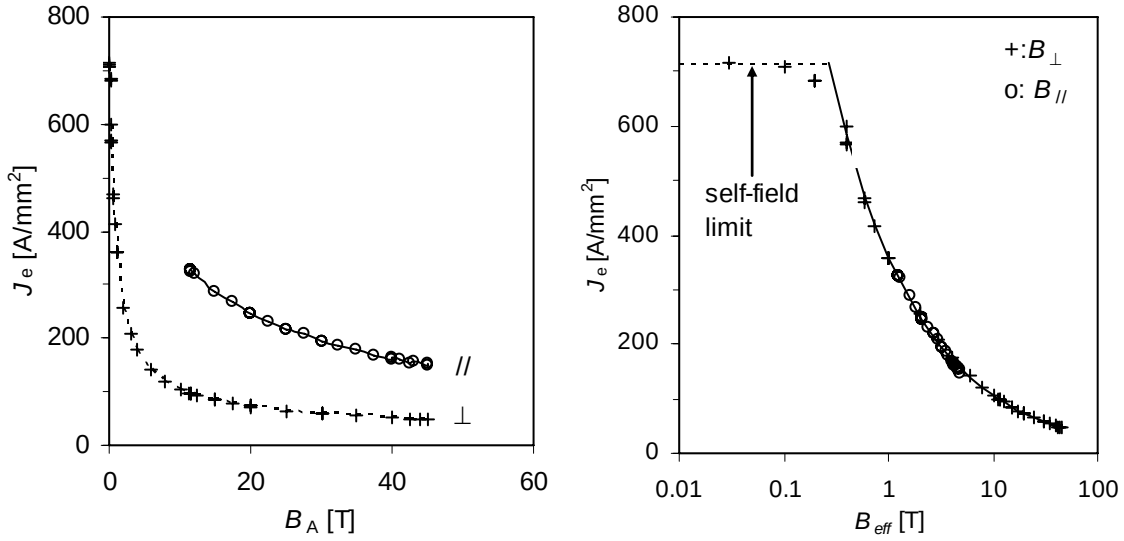

Figure 3-14. (left) Measured engineering critical current density (J_e) versus applied magnetic field for Conductor F. Lines are a guide to the eye. (right) Scaling of J_e with B_{eff} for conductor F. The lines represent the fit to the measured data for perpendicular magnetic field as given in equation 3-4.

3.6 n-values versus *B*

For metallic superconductors it is assumed that the operating current is limited by the lowest value of $J_e(B)$ at a small, localized section of the magnet[34]. This assumption is only accurate for conductors with high *n*-values. For low *n*-values, like for many of the current and previously produced BSCCO conductors, lenient criteria like 1 μV/cm, and with low gradients in B_{eff} around the peak value, this assumption does not hold. Large areas can exist in BSCCO sections of 25 T magnets with $0 < E < E_c$. The shape of the super-conducting-to-normal transition must therefore be taken into account to accurately model the voltage and therefore J_e of a coil, i.e. the relation between *n*-value and *B* should be known. To determine this relation, *n*-value versus magnetic field data are presented and analyzed for the BSCCO tapes (conductors A, B and C) first, and Bi-2212 wire and YBCO coated conductor second.

3.6.1 BSCCO tape conductors

Conductor A

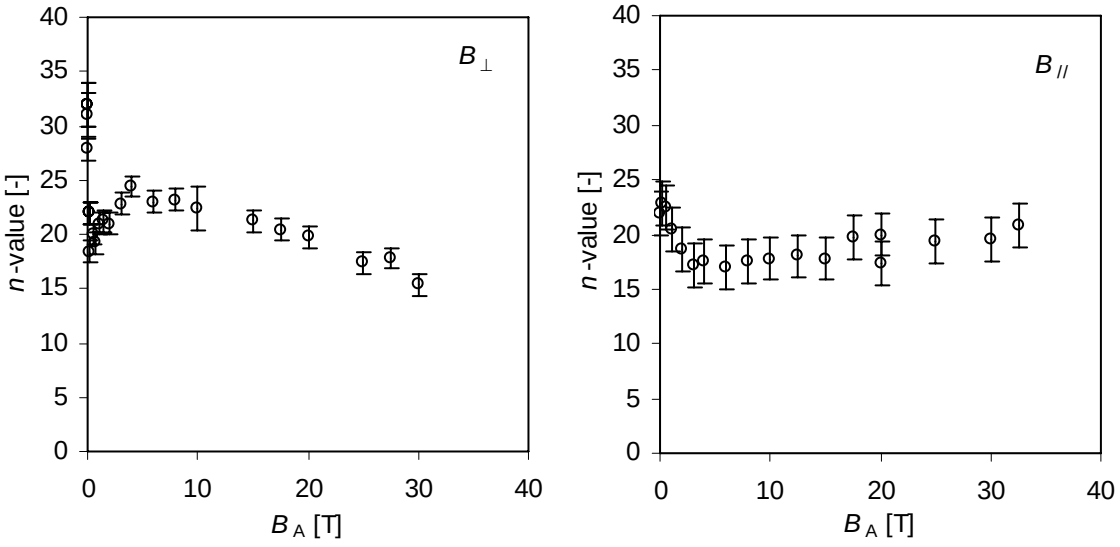

Figure 3-15. n-value versus applied magnetic field for conductor A; sample A2 in perpendicular magnetic field (left,) and sample A1 in parallel magnetic field (right).

The *n*-value for conductor A with $B_\perp$ shows three regimes as shown in Figure 3-15. The cross-over points between those regimes that correspond to the cross-over points between self-field, weak links and strong links regimes in $J_e(B_A)$. The n-B_A relation is at a maximum at self-field and is constant for the field range in which the critical current is determined by self-field. A minimum is observed at 0.25 T, followed by a local maximum at 4 T. This corresponds to the magnetic field range over which weak links behavior is dominant. The range from 4 to 30 T shows a linear decrease of the *n*-value. An extrapolation of this linear behavior equals unity around 80 T and can be interpreted as a rough estimation of the irreversibility field. This estimate of the irreversibility field is lower than the scaling field from the modeling in section 3.3.2. Note that the strong links

[34] Other mechanisms like conductor motion, flux jumps and strain limits may limit the operating current to lower values.

term in equation 3-2 equals J_{es}/e, not zero at $B = B_{sc}$. The physical relevance of the slope is not further considered here.

The *n*-value for magnetic field applied in the parallel direction (see Figure 3-16, right) shows again a constant value for the self-field dominated range, while the minimum of the curve is shifted to around $B_A = 5$ T. When the applied magnetic field is scaled with the scaling factor obtained from the anisotropy in $J_e(B_A)$, the magnetic field dependence of the *n*-value is found to be very similar to the dependence for the case of perpendicular magnetic field as shown in Figure 3-17, left. The main difference in the results for the two orientations is a different *n*-value at self-field. No clear conclusions can be drawn from this fact since the data are obtained on different samples and it is observed that conductor-conductor variations in *n*-values and in J_e appear larger at self-field than in-field. It does appear that the *n*-value is determined by B_{eff} for both directions of the applied magnetic field.

Conductor B

Conductor B exhibits a significantly lower *n*-value than conductor A. Its *n*-value is constant within the error margins, as presented in Figure 3-16. However, within that margin, the *n*-value vs. *B* dependence shows a similar pattern as conductor A and scaling with B_{eff}, as shown in Figure 3-17. The properties of conductor C are nearly identical to conductor B, including the pattern of maxima and minima within the error margin.

It is concluded that the principle of scaling, as originally proposed to describe anisotropy in $J_e(B_A)$, is a valid method for describing the magnetic field dependence of the *n*-value for the BSCCO tapes. The $n(B_A)$ relation exhibits three regimes corresponding to self-field, weak links and strong links dominated magnetic-field ranges respectively. For the purpose of modeling $J_e(B_A)$ respectively E-J_{op} curves of insert coils, and considering the relevant range of B_{eff}, it suffices to ignore the magnetic field dependence and take $n = 20$ for conductor A and $n = 8$ for conductors B and C.

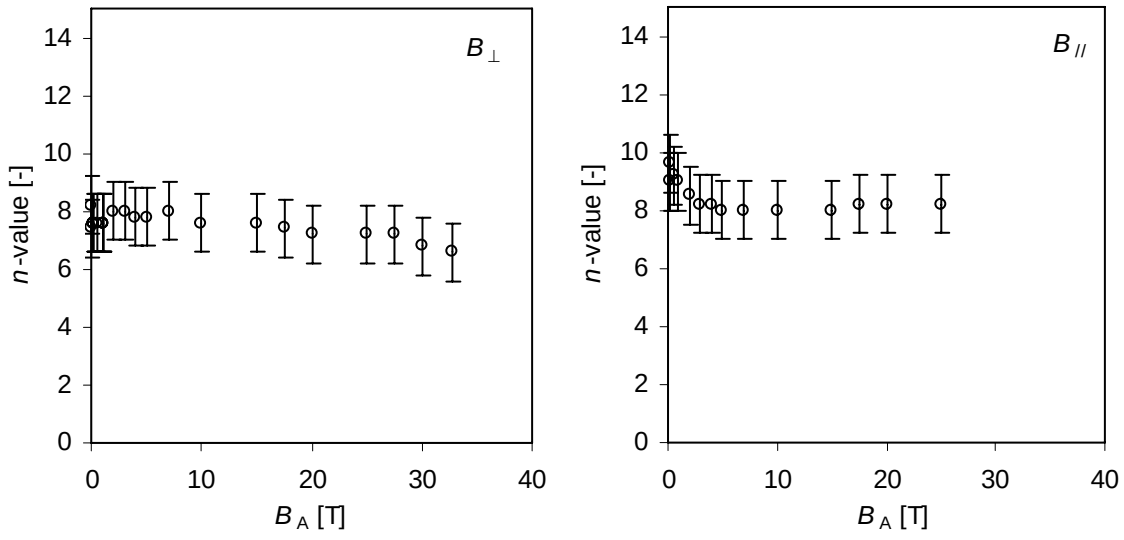

Figure 3-16. n-value versus applied magnetic field for conductor B, samples B-1 (left) and B-2 (right).

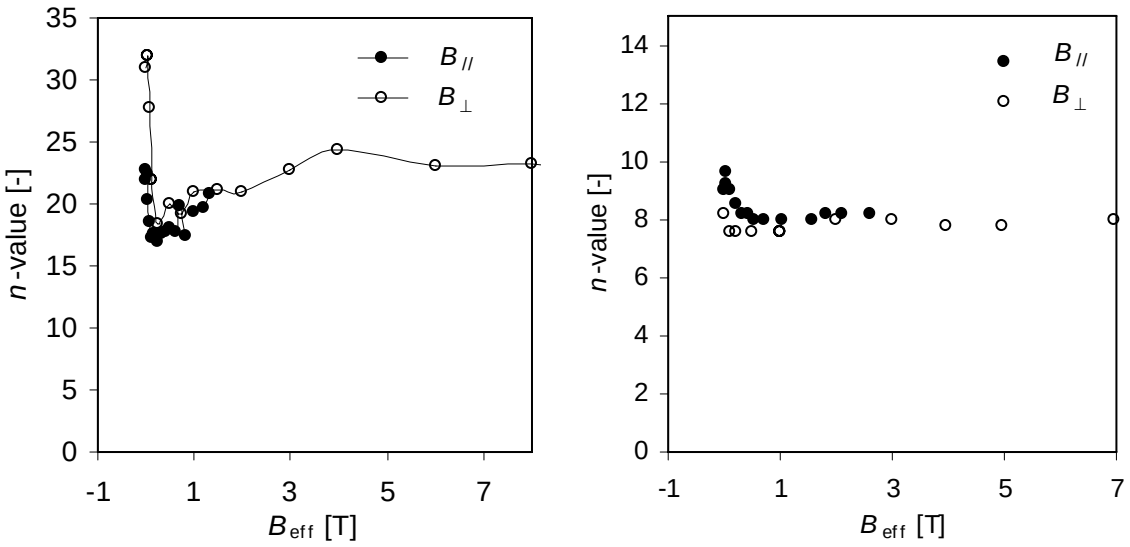

Figure 3-17. Dependence of n-value on B_{eff} for conductors A (left) and B (right). The line is a guide to the eye.

3.6.2 Bi-2212 wire and YBCO coated conductor

The Bi-2212 wire and YBCO CC do not show field dependence of the *n*-value, as shown in Figure 3-18, although the scatter for the latter conductor is large enough to mask possibly significant magnetic field dependence[35]. The principle of scaling is therefore not challenged, nor clearly confirmed for both Bi-2212 wire and YBCO coated conductor. For the purpose of modeling, the *n*-values can be taken as 18 ± 2 and 25 ± 5 for conductors E and F respectively.

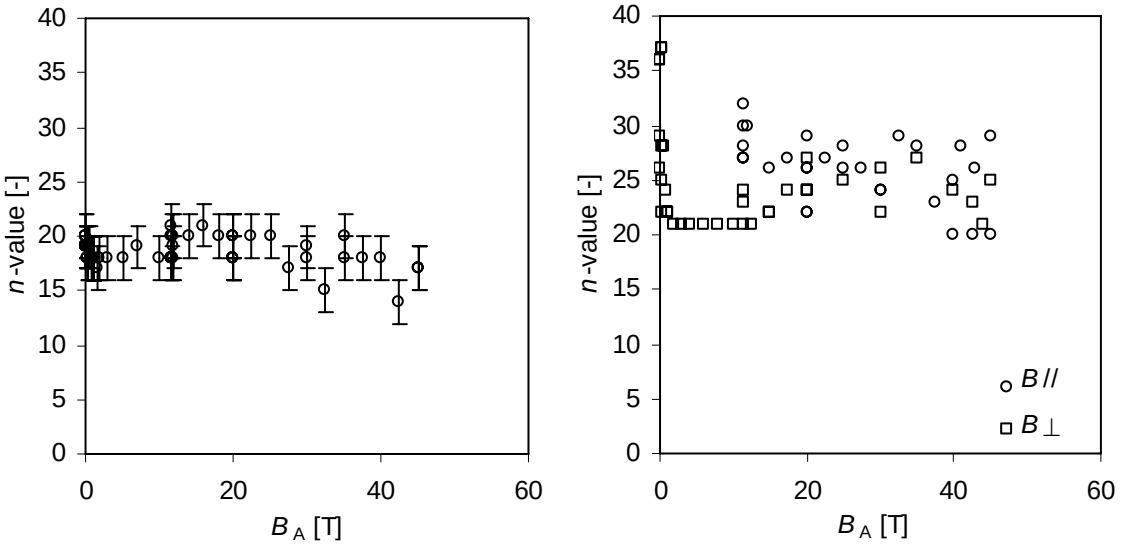

Figure 3-18. n-value versus applied magnetic field for conductors E (right) and F (left) (Bi-2212 wire and YBCO Coated Conductor respectively).

[35] *n*-value variability is discussed on Chapter 2.

3.7 Conclusion

Both the engineering critical current density and *n*-value of Bi-2212 and Bi-2223 tapes, a Bi-2212 round wire and a YBCO coated conductor are characterized over the magnetic field range of interest to HTS sections of 25 T magnets, and to higher magnetic field values as facilities allowed. The magnetic field is either parallel or perpendicular to the tape surface and always perpendicular to the current. The current carrying capabilities suffice for candidate conductors. Fit functions describe the current carrying capacity beyond the self-field regime for magnetic field oriented perpendicular to the tapes with an average deviation of about 1%. The fit function for BSCCO tapes is based on the parallel network model, with contributions from strongly- and weakly-linked current transfer networks that exhibit different magnetic field dependencies.

Significant sample–to-sample variations in the engineering critical current density are observed in the Bi-2212 samples. However, their properties can be described using the same characteristic magnetic field values in the fit functions. Furthermore, magnetic field dependence of the engineering critical current density of each conductor normalized to the measured self-field value is reproducible for perpendicular magnetic fields between about 0.5 and 3 T, the range of most interest for BSCCO conductors in 25 T magnets.

The fit function for the Bi-2212 round wire is quite accurate, but is based on a different, two-term mathematical expression, and suggests a parallel network with different current limiting mechanisms compared to BSCCO tapes. The best fit function for the YBCO coated conductor consists of only a single power term of the applied magnetic field.

The average grain misalignment angle is used as the sole free parameter in modeling the angular dependence of conductor engineering critical current density for tape conductors. It follows from the model that curves of the magnetic field dependence of the engineering critical current density for different magnetic field angles scale if the magnetic field value is multiplied with a scaling function whose value only depends on the magnetic field angle and the average grain misalignment angle.

Verification of scaling using measured engineering critical current density data for parallel and perpendicular applied magnetic field gives mixed results. Scaling works well for the Bi-2223 tapes and the YBCO coated conductor. It does not work very well in any part of the measured range for the Bi-2212 tape samples. The average grain misalignment angle appears to be field dependent, which would contradict the basic assumptions of the model. Unfortunately, the uncertainty in the average grain misalignment angle is too large for the result to be decisive. Analysis of the magnetic field dependence of the engineering critical current density in double pancakes and larger coils, which are also affected by conductor anisotropy, can help to clarify whether the used model of conductor anisotropy is appropriate.

The *n*-values for BSCCO tapes show anisotropy and scaling with the effective perpendicular magnetic field, but can be considered constant, within a margin of ±1 for the range of interest in insert for 25 T magnets. *n*-values can be considered constant within a margin of ±2 and ±5 for Bi-2212 round wire and YBCO coated conductor tape respectively.

4 Conductor anisotropy affecting the design of HTS insert coils in 25 T class solenoids

For three insert coils the relationship between the degree of conductor anisotropy and the priorities in the coil design process is investigated. Two BSCCO tape inserts and one ReBCO tape insert are considered, each generating 5 T in a 20 T background magnetic field. In combination these insert and outsert dimensions bracket the size range of expected 25 T solenoids. The magnetic field distribution within the inserts is very similar. The J_e-limiting magnetic field component, the effective magnetic field, depends on the degree of anisotropy of the conductor. Anisotropy is modeled using the concept of the average grain misalignment angle, which varies between conductors. A generic pattern of 3 distinct regimes exist in the relation between the limiting magnetic field component and the average grain misalignment. For each regime, parameters are identified that are most relevant to the magnet design optimization.

4.1 Introduction

Many magnet technology issues for BSCCO and ReBCO based inserts are similar to those of NbTi and Nb_3Sn magnets. However, the strong anisotropy of the critical current with respect to the orientation of the magnetic field is unique to HTS tape conductors. Magnetic field perpendicular to the surface of a tape, i.e. the radial magnetic field component in a magnet, has a much stronger suppressing effect on the critical current density than the parallel magnetic field. This has often lead to the assumption that the performance of HTS magnets is radial magnetic field limited at the position of peak radial magnetic field. However, the axial magnetic field in a magnet, parallel to the tapes, is generally much higher than the radial magnetic field in the case of high-field solenoids. Therefore, a more comprehensive analysis of the limiting effect of anisotropy is warranted.

The subject of this chapter is to present the influence of anisotropy on the design process of insert coils, considering various degrees of anisotropy in the conductors and a relevant range of magnetic field and magnetic field angle values. Three insert-outsert combinations are considered and serve to determine the relevant magnetic field range. The goal here is to highlight *in general* the effect various degrees of conductor anisotropy have on the design optimization process of 25 T solenoids using BSCCO and ReBCO conductors.

4.2 Three cases of anisotropy

In BSCCO tape conductors the average grain misalignment angle is a suitable parameter to describe anisotropy for all magnetic field angles. The average grain misalignment angle α^* is determined from the ratio of magnetic field values for parallel and perpendicular magnetic field resulting in the same J_e. This ratio equals $\cos(\alpha^*)/\sin(\alpha^*)$ as introduced in section 3.4. The grain misalignment will vary from conductor to conductor depending on the details of the production process and may have apparent magnetic field dependence[36] but can be considered independent of B over the limited range occurring in inserts of 25 T magnets as delineated in section 4.5. Thus α^* can be used as a constant that quantifies the degree of anisotropy in a particular conductor.

[36] See Chapter 3 and [81].

Use of the average grain misalignment angle concept to describe anisotropy in $J_e(B)$ implies scaling[37] of $J_e(B,\phi)$ with the effective perpendicular magnetic field component and predictability of the scaling function $f(\phi)$ if $f(0°)$ and $f(90°)$ are known. Thus knowledge of just $J_e(B_{//})$ and $J_e(B_{\perp})$ is sufficient to determine $J_e(B,\phi)$ for all values of ϕ. It follows from the average grain misalignment model that the scaling function that relates the vector $\boldsymbol{B}$ to the value B_{eff} is always monotonously increasing with the magnetic field angle. Correspondingly, $J_e(\phi)$ for a fixed value of B will monotonously decrease as the magnetic field angle is increased from 0 to 90° for any conductor with anisotropy that can be described with the average grain misalignment angle.

The effective magnetic field scaling function for some conductors, particularly ReBCO-coated conductors, is not necessarily monotonously increasing with angle, but more importantly not fully determined by its values at 0 and 90 degrees [94, 95, 96, 97]. It is no longer the component perpendicular to a grain that solely determines its J_e, as pinning on stacking faults, [96], artificial pinning sites and 124-type intergrowths [98] can have significant influence on the anisotropy in J_e. Scaling functions based on the average grain misalignment angle model, where α^* is determined through the ratio of parallel and perpendicular magnetic field resulting in the same J_e, can therefore not completely describe $f(\phi)$ and $J_e(\phi)$.

While the use of the average grain misalignment concept may not be suitable to describe the complete anisotropic behavior of $J_e(B)$, models based on this concept are only required to be accurate within the range of magnetic field angles present in insert coils, typically 0 to about ~ 7°. So we arrive at the second case, where $J_e(\phi)$ between $\phi = 0$ and $\phi = \phi_{max}$ for a fixed magnetic field value can be described using the measured $J_e(B)$ for a single magnetic field angle and a scaling function based on a single α^* value.

This case requires knowledge of $J_e(B)$ for multiple magnetic field angles in the range of interest. Most measurements of anisotropy in HTS conductors in literature are presented as $J_e(\phi)$ for a fixed magnetic field value, although $J_e(B)$ data for various fixed angles would be more directly applicable to insert design. Devices that allow measurement of J_e at 4.2 K for variable angles in magnetic fields up to ~ 25 T are desirable but such experiments on candidate conductors carrying hundreds of amperes at this magnetic field are extremely challenging. In practice one must often rely on data taken at substantially lower magnetic field and sometimes higher temperature and then extrapolate.

Thus, anisotropic HTS conductors can be separated in three categories, depending on whether the anisotropy in the magnetic field dependence of the engineering critical current density can be described using the average grain misalignment angle α^* for:

1. all magnetic field angles ($0 \le \phi \le 90°$),
2. only the magnetic field angles relevant to insert coils ($0 \le \phi \le \sim 7°$) or,
3. not at all.

The first case typically applies to BSCCO tape conductors and is discussed in detail in section 4.6, where the first HTS insert to generate 25 T in combination with a resistive magnet is used as example. The second case applies to some ReBCO conductors, based on the premise that anisotropy observed at higher temperatures is indicative of behavior at 4.2 K. This is discussed in detail in section 4.7 using the example of the SP-YBCO insert (see Table 1-1) in a resistive magnet. The same example is used in section 4.8 to straightforwardly illustrate the relation between conductor anisotropy and coil design with a single graph. In the third case, when anisotropy can not be described using the average

[37] As defined in equations 3-3 and 3-4.

grain misalignment, the effect of anisotropy can be illustrated via a simple graph comprising two curves: one representing the design requirements and a second representing the conductor properties.

4.3 Typical insert coils

A *typical* insert coil features:

- one or multiple sections,
- radial separation between sections,
- axial and midplane symmetry for each section,
- a rectangular cross section for each section,
- uniform current density per section,
- and a section height such that, at the center, each section generates at least 80% of the magnetic field an infinitely long but otherwise similar coil would generate.

The last feature reflects that insert coils tend to be relatively long[38], longer than for example minimum volume coils, as radial space is usually valued more in coil design than the extra materials cost for a longer section of more limited radial dimensions. Other factors, including magnetic field homogeneity, usually also provide arguments favoring relatively long sections. The magnetic field generated by an infinitely long section is given by equation 1-3. Most inserts built or designed to date generate a magnetic field increment ΔB between 80 and 96% of B_∞ with an average of 85%. One insert that is designed using a fixed conductor length, as opposed to limited radial dimensions, is the SP-YBCO[39] coil [28, 52]. It is a minimum volume coil generating 71% of B_∞. However, the pattern of magnetic field strength and angles in its windings is comparable to typical insert coils, as will be demonstrated in section 4.5.

4.4 Examples of 25 T magnet designs using an HTS insert

Three insert-outsert combinations with a central magnetic field of 25 T and a background magnetic field of 20 T are considered. These examples span the range from a tall NMR-style system optimized for high homogeneity of the magnetic field around its center to a minimum volume insert designed to maximize the magnetic field increment in a resistive outsert of limited homogeneity.

The first design concerns a hypothetical modification of the 900 MHz/21.1T NMR magnet referred to as Modified900. The original magnet design included an option to modify the inner sections to upgrade to a 25 T magnet [31]. Sections 4 through 12 as listed in Figure 4-1 form a high-homogeneity 20 T outsert. Sections 1 through 3 form an insert that generate an additional 5 T. The height of each insert section is different, affecting the peak radial magnetic field in each section as compared to an equal-height configuration. Reduced radial magnetic field means smaller magnetic field angles, in line with the high-homogeneity philosophy of NMR magnets. Winding geometry and current densities are listed in Table 4-1.

The second design closely resembles the 5T insert as tested in combination with a resistive outsert [45][40]. Current densities and insert geometry are slightly different from the as-built version in order to create a more generic insert with sections of equal height and a magnetic field increment of exactly 5 T. Having insert sections of equal height

[38] Single and double-pancake coils are therefore not considered insert coils.
[39] See table 1-2.
[40] See also sections 1.5 and 4.6.

Table 4-1. Dimensions and average current densities of the windings of the Modified900 outsert and an NMR style insert.

		IR	***OR***	***-z***	***+z***	J_{ave}		**Characteristic feature**
Name	Section	m	m	m	m	A/mm^2		
NMR-style insert	1	0.048	0.062	0	0.30	100		Tall sections High magnetic field homogeneity
	2	0.066	0.079	0	0.33	100		
	3	0.084	0.097	0	0.36	100		
Modified900 outsert	4	0.101	0.125	0	0.41	48.5		Tall sections High magnetic field homogeneity
	5	0.131	0.158	0	0.50	68.0		
	6	0.172	0.201	0	0.59	92.5		
	7	0.227	0.252	0	0.67	121		
	8	0.286	0.309	0	0.75	114		
	9	0.339	0.363	0	0.75	131		
	10	0.420	0.439	0	0.113	142		
	11	0.390	0.439	0.299	0.621	142		

Table 4-2. Dimensions and average current densities of the windings of the 5T and SP-YBCO insert and parameters of the Large Bore Resistive Magnet.

		IR	***OR***	***-z***	***+z***	J_{ave}		**Characteristic feature**
Name	Section	m	m	m	m	A/mm^2		
5T insert	1	0.021	0.048	0	0.093	87		Moderate height Moderate magnetic field homogeneity
	2	0.053	0.073	0	0.093	87		
	3	0.078	0.082	0	0.093	80		
SP-YBCO insert	1	0.0095	0.0436	0	0.026	165		Short section Minimum volume design Low magnetic field homogeneity
		IR	***OR***	***-z***	***+z***	***I***	**turns**	
Name	Section	m	m	m	m	kA		
Large Bore Resistive Magnet outsert	4	0.108	0.128	0	0.157	8.80	81	Relatively short Power limited design Limited homogeneity
	5	0.108	0.128	0.160	0.253	8.80	13	
	6	0.128	0.197	0	0.154	30.38	70	
	7	0.128	0.197	0.154	0.255	30.38	10	
	8	0.200	0.340	0	0.166	39.10	81	
	9	0.200	0.340	0.166	0.305	39.10	17	
	10	0.343	0.500	0	0.244	39.10	59	
	11	0.343	0.500	0.244	0.309	39.10	4	

maximizes the contribution of radial magnetic field between neighboring sections and consequently maximizes the magnetic field angle. This hypothetical insert is referred to as the Modified 5T. The outsert [10, 99] is also used with other BSCCO [40, 41, 42] and YBCO inserts [52] and is known as the Large Bore Resistive Magnet (LBRM). It is modeled here with the operating current scaled to obtain a central magnetic field of 20 T. The Large Bore Resistive magnet is relatively short as power was a limiting factor in its design. Table 4-2 provides the main parameters.

The third design features a single-section minimum-volume coil as insert. This insert built from YBCO double pancakes generated 7.8 T in a 19 T background magnetic field provided by the LBRM [52]. Here we consider this SP-YBCO insert in a 20 T background magnetic field at an operating current density that corresponds to a magnetic field increment of 5 T to be compatible with the two systems above.

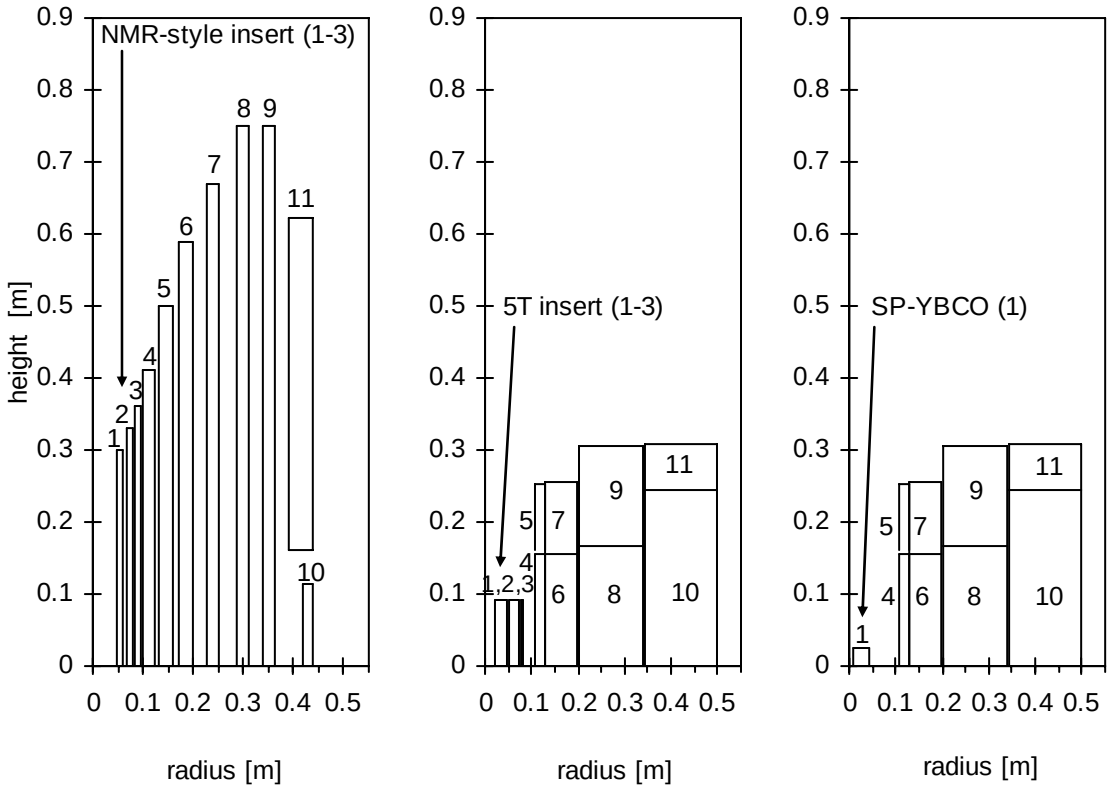

Figure 4-1. Quarter cross-sections of the windings of an NMR-style insert to the Modified900 outsert (left); the 5T insert in the Large Bore Resistive Magnet (middle) and the SP-YBCO insert in the Large Bore Resistive Magnet (right). Dimensions and current densities for each numbered section are listed in Table 4-1.

4.5 Magnetic field distribution

The distribution of the magnetic field ***B*** in typical inserts for 25 T class magnets is quite different from stand-alone magnets of any geometry and of consequence for the relationship between the anisotropy of the conductor and design of the insert coil. This is illustrated with the three example inserts.

In the midplane of an insert coil, the magnitude of ***B*** will decrease from approximately the central magnetic field value B_{CF} at the inner diameter of the insert to $B_{CF} - \Delta B$ of the insert at its outer diameter. The lowest value for ***B***, B_{min} occurs generally at the turns with the highest radial and axial position. This overall minimum value is somewhat below $B_{CF} - \Delta B$, depending on the height of the insert relative to the height of the outsert. For example, consider the three insert-outsert combinations that are described in section 4.4. The inserts and outsert generate the same magnetic field increments, but cover a large range in terms of coil height and magnetic field homogeneity. In all cases, B is never less than 77% of B_{max}, and within 0.7 T of the outsert magnetic field $B_{CF} - \Delta B$. While these numbers vary somewhat for other insert designs, it is expected that the value of B will show a very similar dependence on position.

The magnetic field angle, defined as the angle between ***B*** and the magnet longitudinal axis, determines the radial magnetic field component B_r. Note that both insert and outsert are contributing to B_r. The magnetic field angle and B_r are always zero on the midplane for reasons of symmetry. $B_{r,max}$ is about 2 T in the example inserts. Generally, the range of

B_r is more sensitive to the design than the range of B, but the maximum in B_r remains much smaller than B in all cases. The position of the maximum magnetic field angle and maximum B_r coincide to within 1 mm in these examples as a result of the weak variation in B and B_z respectively. The magnetic field angle is less than 7° everywhere. Consequently, the values of B and the axial magnetic field component B_z are nearly identical. Figure 4-2 and Table 4-3 provide a sketch with the typical position of various magnetic field components in a generic insert and specific values for the three examples. It follows from the above considerations that the distribution of $\boldsymbol{B}$ within the windings of the insert of a 25 T system follows a fairly predictable pattern and does not vary significantly from insert to insert.

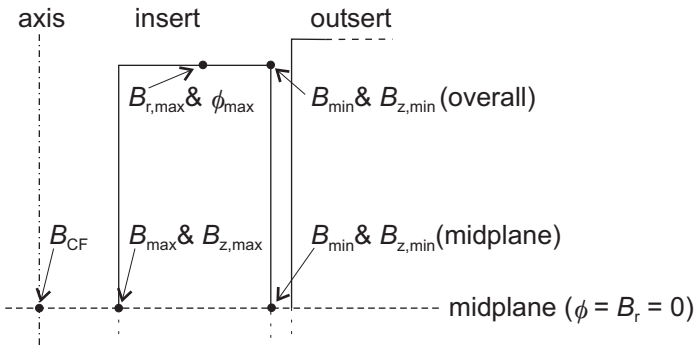

Figure 4-2. Position of various magnetic field components in a generic insert [41].

*Table 4-3. Variation of **B** across three insert designs. See section 4.4 for coil parameters. The scalar value is given in tesla and as percentage of the central magnetic field value.*

Insert-outsert	$\boldsymbol{B_{max}}$ **Overall**	$\boldsymbol{B_{min}}$ **At midplane**	$\boldsymbol{B_{min}}$ **Overall**	$\boldsymbol{B_{r,max}}$	$\boldsymbol{\phi_{max}}$
unit	T	T	T	T	°
Modified900	25.00 (100%)	19.90 (80%)	19.40 (78%)	1.80 (7.2%)	5.1
Modified 5T-LBRM	25.06 (100%)	20.24 (81%)	19.28 (77%)	2.27 (9.1%)	6.7
SP-YBCO at 5 T-LBRM	25.02 (100%)	19.60 (78%)	19.60 (78%)	1.73 (6.9%)	4.7

4.6 Case 1: the average grain misalignment angle describes anisotropy across all possible angles

The analysis presented in this section is based on the premise that anisotropy is solely determined by α^* and is generally applicable to BSCCO tape conductors. As shown in chapter 3, knowledge of α^* and of the perpendicular magnetic field dependence of the critical current $J_e(B_\perp)$ are sufficient to calculate the critical current at any arbitrary magnetic field orientation by converting vector $\boldsymbol{B}$ to the effective perpendicular magnetic field B_{eff}. For the purpose of this section, the $J_e(B_\perp)$ characteristic of conductor B is used to represent a generic BSCCO tape conductor. Characteristics of other conductors can be substituted without affecting the generality of the following considerations.

The position and value of the maximum in B_{eff} determine the value and position of the minimum in J_e. The effective magnetic field B_{eff} is determined by B, ϕ and α^*, *i.e.* by the design and degree of anisotropy in the conductor. Assume a preliminary design has been

[41] A minor variation is found for very short insert coils like the SP-YBCO coil. The values of B and B_z at the outer radius are then nearly independent of axial position, but with the overall minimum at the midplane. This variation has no practical consequences.

calculated, *i.e.* a geometry and current density resulting in the desired ΔB have been selected. It is informative to consider how B_{eff} changes, without changing the design, depending on the conductor dependent parameter α^*. This relation will first be explored at the two most relevant positions, namely the position of the maximum magnetic field value B_{max} and the position of the maximum magnetic field angle coinciding with $B_{r,max}$. The same analysis is then performed over the entire cross section of the insert. The results have implications for the optimization of the design. The 5T insert is used as an example design to illustrate general patterns typical for BSCCO inserts in 25 T class systems.

4.6.1 Comparison of B_{eff} versus α^* at the positions of maximum radial and axial magnetic field

From the analysis in section 3-4 it follows that for a hypothetical conductor with zero grain misalignment $B_{eff} = B_r$. Therefore, the maximum in B_{eff} then coincides in value and position with the maximum in B_r. The position of $B_{r,max}$ is typically at the top and bottom surfaces of an insert (see Table 4-3 and Figure 4-3). The other extreme in grain misalignment is random orientation, *i.e.* isotropic behavior in which case the position of the maxima in B_{eff} and B_{max} coincide. The position of B_{max} is typically at the midplane at the inner diameter of the insert. So, an insert can be J_e-limited at the position of maximum B_r for small α^* or limited in the midplane at maximum B_z for large α^*. To quantify small and large, the example of the 5T insert is considered. The components of the magnetic field at the positions where B_r and B_z are at their maximum are given in Table 4-4 for the 5T insert. The relation between B_{eff} and α^* for the 5T insert is depicted in Figure 4-3.

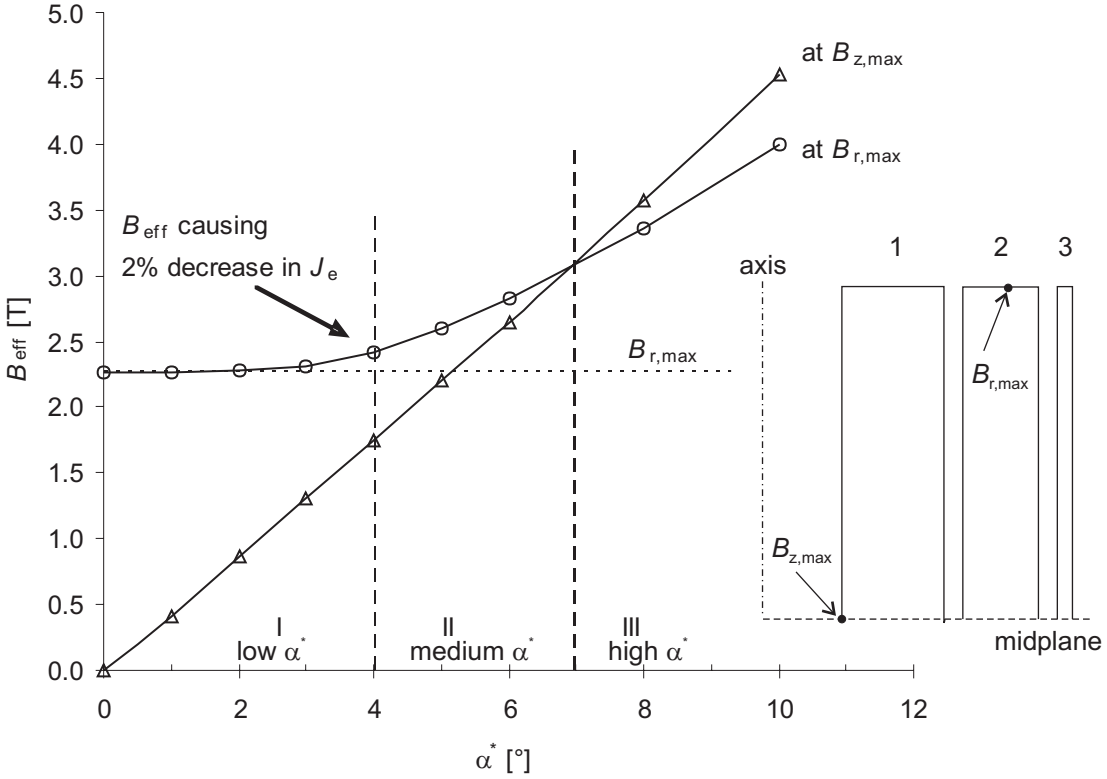

Figure 4-3. B_{eff} versus α^* at the positions of maximum axial and maximum radial magnetic field respectively for the Modified 5T insert, which are shown in the inset (detail from Figure 4-1, middle). Three qualitatively different regimes: I, II and III, can be distinguished.

Table 4-4 Magnetic field at the position of $B_{r,max}$ and $B_{z,max}$ for the modified 5T insert in the 20 T background of the LBRM (see Figure 4-3).

	B_r	B_z	B	ϕ
unit	T	T	T	°
Position of $B_{r,max}$	2.27	19.48	19.62	6.7
Position of $B_{z,max}$	0	25.06	25.06	0.0

The following three regimes are observed and indicated in Figure 4-3:

Regime I: For low values of α^*, the maximum in B_{eff} is nearly equal to $B_{r,max}$. The insert is radial magnetic field limited and J_e is virtually insensitive to small variations of α^*.

Regime II: For higher α^*, the position of the maximum in B_{eff} coincides with $B_{r,max}$ but significantly exceeds the value of $B_{r,max}$. Both $B_{r,max}$ and B_z at that position are important.

Regime III: Above a certain crossover value of α^*, the position of the maximum of B_{eff} coincides with $B_{z,max}$. The insert is axial magnetic field limited.

To provide an intuitive association between α^* and the regime classifications, the regimes are labeled as Low α^*, Medium α^* and High α^* respectively.

The crossover from regime I to regime II is somewhat ambiguous as it is determined by the definition of a *significant* rise in the maximum in B_{eff}. One might take significant to be an increase in B_{eff} corresponding to a decrease in J_e of some percentage relative to the J_e at maximum B_{eff}. With such a criterion, the slope in the $J_e(B)$ curve for the maximum value of B_{eff} determines the value of magnetic field increment that is significant. The cross over between regimes I and II as shown in Figure 4-3, is calculated using the properties of the example conductor and a 2% criterion, resulting in $\alpha^* = 4.05º$ for the magnetic field distribution of the 5T insert. The $J_e(B)$ slope will vary somewhat between conductors and the crossover value will vary accordingly. The crossover from regimes II to III is unambiguously determined by the α^* value for which the calculated values of B_{eff} at the positions of maximum B_r and B_z are equal. This pattern of three regimes is generic to inserts with anisotropic conductor.

In regime III, the maximum in B_{eff} is $\sin(\alpha^*)\cdot B_{z,max}$, as the magnetic field angle is zero in the midplane. A simple approximation of B_{eff} is $\alpha^*\cdot B_{CF}$, since $B_{z,max}$ is nearly identical to B_{CF} in typical inserts and α^* is small. In other words, B_{eff} in regime III is fully determined by the product of α^* and the target magnetic field value.

It should be stressed that these considerations are indeed very relevant for typical insert designs using actual BSCCO conductors: the range of α^* values relevant in this design example overlap with the range of α^* values observed in various BSCCO tape conductors as reported in literature [100, 101, 102[42], 85, 81]. This implies that, between various designs and conductor properties, each of the three regimes can occur.

4.6.2 B_{eff} in the entire cross section of an insert

The relationship between B_{eff} and α^* has so far been explored at two positions: maximum B_r and maximum B_z. To verify that these are also the positions of maximum B_{eff}, and to determine what 2D patterns exist, B_{eff} is considered in the same manner across the entire cross section of the example 5T insert.

[42] The paper suggests $\sigma = 17.5°$ based on a model that does not fit the measured data accurately. However, the same data combined with the method of section 3-4 equation 3-7 result in $\alpha^* = 11 \pm 1.5°$ and $\sigma = 14 \pm 2°$.

The dependence of B_{eff} on α^* is listed in Table 4-5 and shown in Figure 4-4. As discussed in the previous section, the position of maximum B_{eff} does indeed correspond with the maximum in B_r for regimes I and II, and with the maximum in B_z for regime III.

Table 4-5. B_{eff} and J_e variation vs. α^* in the Modified 5T insert.

	$\alpha^*=0^o$	$\alpha^*=1^o$	$\alpha^*=3^o$	$\alpha^*=6^o$	$\alpha^*=9^o$
Maximum B_{eff} [T]	2.27	2.29	2.33	2.84	4.04
Minimum B_{eff} [T]	0.00	0.33	1.05	2.14	3.26
Variation in B_{eff} [T]	2.27	1.96	1.28	0.70	0.78
J_e max [% of self field J_e]	100	65	48	41	38
J_e min [% of self field J_e]	41	41	41	39	37
Variation in J_e [% of self field J_e]	59	25	7	2	1

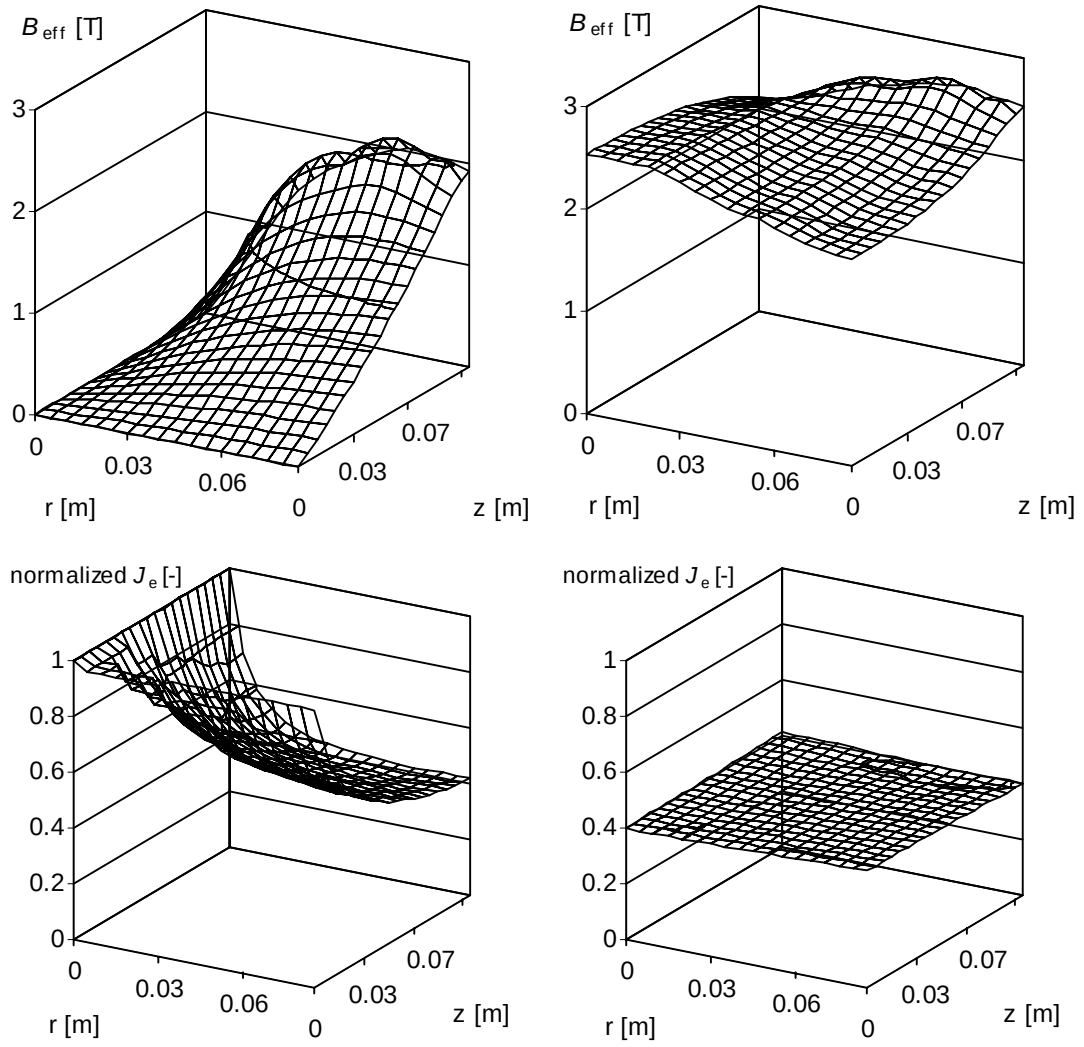

Figure 4-4. B_{eff} and J_e normalized to the conductor self-field J_e for $\alpha^* = 0°$ (left) and $\alpha^* = 6°$ (right), for the Modified 5T insert in the 20 T background of the Large Bore Resistive Magnet.

Regime I is represented in the table for $\alpha^* = 0°$, 1° and 3°, where the case of $\alpha^* = 3°$ is close to the crossover point. Regime I is characterized by a strong gradient in B_{eff} with a maximum at the position of $B_{r,\max}$ at the top of the insert. The gradient is weaker in regime

II represented by $\alpha^* = 6°$ and a ridge develops at the inner radius of the insert with a local maximum on the midplane. The variation of B_{eff} over the entire insert, *i.e.* the maximum minus minimum value, is at its minimum at the cross over between regimes II and III. The overall maximum of B_{eff} shifts to the midplane in regime III, but shows a ridge of nearly equal height along the inner radius and the top of the insert. Both regimes II and III show a gradient in B_{eff} at the midplane towards its minimum at the outer radius of the insert. The gradient in B_{eff} at the midplane is proportional to the average current density in the windings. This is understood by considering that $B_{eff} = \sin(\alpha^*) \cdot B_z$ at the midplane. The gradient of B_z in the midplane of a typical insert is proportional to the local current density, thus the same applies to B_{eff} in this regime.

To translate the patterns in B_{eff} to patterns in J_e we consider the normalized $J_e(B_{eff})$ relation for the example conductor. As B_{eff} for $\phi = 90°$ is practically equal to $B_\perp$, the data of conductor B are used, which are shown normalized within the range of interest in Figure 4-5. The results of converting B_{eff} to J_e are also listed in Table 4-5 and Figure 4-4. In regime I, the pattern in B_{eff} results in a large variation of calculated J_e values across the insert. The minimum J_e in regime I is almost constant, but the maximum J_e depends strongly on α^*. The effect of higher values for α^*, as in regimes II and III, is to reduce the minimum in J_e somewhat but greatly reducing the variation in the J_e distribution.

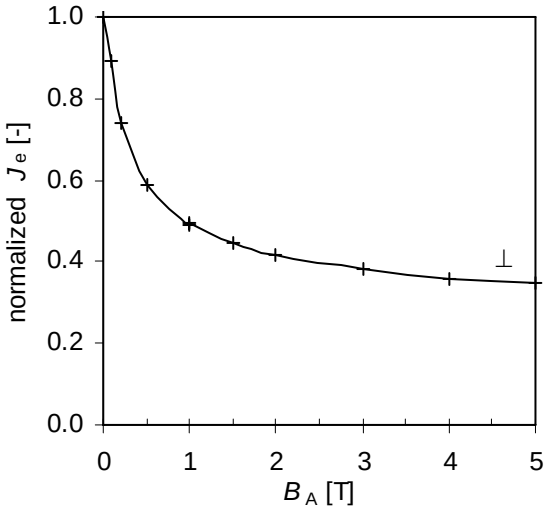

Figure 4-5. $J_e(B_\perp)$ normalized to the measured self-field J_e of conductor B.

For different conductors and different designs, the numbers of Table 4-5 and the cross-over values for α^* will vary accordingly. However, the same trends in B_{eff} and J_e will occur as for the 5T insert. This was verified by applying the same analysis of B_{eff} and J_e versus α^* to a 3 T insert [103]. The shape of the resulting distributions of B_{eff} and J_e are so similar to Figure 4-4 that reproduction of the graphs here is not useful.

It is the limited range for ϕ in inserts that makes the maximum value of B_{eff}, and therefore the minimum of J_e, strongly dependent on both ϕ and the grain misalignment α^*. This relationship is unique to coil sections using conductors which are anisotropic in $J_e(B)$, where the ratio of $B_\perp$ and $B_{//}$ resulting in the same conductor J_e is comparable to the ratio of $B_{r,max}/B_{z,max}$ for the section. This is common to BSCCO sections in 25 T magnets, but need not be unique to this application.

4.6.3 Impact of anisotropy on coil design

The above results are used to develop guidelines for optimizing BSCCO insert designs. The starting point is a defined initial design and a known or assumed value for α^*. These determine the corresponding regime. The crossover values of α^* that separate the regimes depend to some extent on the design, so significant design changes during the optimization process may cause a regime change.

Three regimes exist in the relationship between α^* and B_{eff}. The general trend in the anisotropy-design relation is that, everything else being equal, a higher value of α^* means a lower J_e of the insert. Regime I is the most desirable when efficient use of superconductor is required, followed by regime II. On the other hand, a design in regime III might be the most cost effective, assuming superconductor with less perfect alignment is also less expensive, if the reduction in conductor cost outweighs the increased volume of superconductor needed.

An overview of aspects in the anisotropy-design relation is presented in Table 4-6. A framework for analysis and discussion is provided by assuming a fixed outer radius and a fixed target for the magnetic field increment generated by the insert. These assumptions do not reduce the general validity of the results. Most details in Table 4-6 have already been discussed here and remaining aspects are discussed below.

Table 4-6. Effect of BSCCO anisotropy on the insert design optimization.

	Regime I, low α^*	**Regime II, medium α^***	**Regime III, high α^***
Defining feature	B_{eff} dominated by $B_{r,insert+}$ $B_{r,outsert}$. *Insert is radial magnetic field limited.*	Insert J_e is limited at location of maximum B_r, but maximum axial magnetic field at midplane is nearly equally limiting.	B_{eff} is ~ uniform and the resulting J_e distribution is more so. *Insert is axial magnetic field limited.*
Value of $B_{eff,max}$	$B_{eff,max} \sim B_{r,max}$	$B_{r,max} < B_{eff,max} < \sin(\alpha^*) \cdot B_{z,max}$ with $\sin(\alpha^*) \cdot B_{z,max} \approx \alpha^* \cdot B_{CF}$	$B_{eff,max} = \sin(\alpha^*) \cdot B_{z,max}$ with $\sin(\alpha^*) \cdot B_{z,max} \approx \alpha^* \cdot B_{CF}$
J_e is *most* sensitive to:	B_r $J_e(B_\perp)$ slope	B_r $J_e(B_\perp)$ slope Value of α^* B_{CF}	Value of $\alpha^* \cdot B_{CF}$
J_e is *least* sensitive to:	Value of α^*	-	B_r
Design focus	Minimize $B_{r,max}$. Winding thickness (radial sectioning). Differentiate section heights.	All parameters are relevant.	Optimize design based upon other considerations, *e.g.* cost, strain, magnetic field homogeneity.
Opportunities	Use lower grade conductor in areas subject to low B_{eff}. Requires axial divisions.	Use lower grade conductor in areas subject to low B_{eff}. Requires both axial and radial divisions and a high current density.	Coil height and radial division not constrained by J_e considerations.
In comparison	Most efficient designs, highest possible insert-J_e for a given conductor.	Most complex to optimize.	Reduced efficiency compared to regime I might be offset by lower cost.

$J_e(B_\perp)$ slope

The sensitivity of J_e to small variations in the maximum in B_r respectively B_{eff} depends on the slope of the $J_e(B_\perp)$ curve at that magnetic field. Minimization of B_r is most effective in optimizing J_e when the slope of $J_e(B_\perp)$ is steep, *i.e.* for values of B_{eff} below about 1 T. The slope also varies from conductor to conductor.

Below-grade conductor

For the purpose of this discussion, below-grade conductor is defined as conductor with sufficient J_e for the minimum value of B_{eff} but below the requirement at maximum B_{eff}. Such a conductor can be applied in those regions of the insert where B_{eff} is relatively low, and therefore requires a significant variation in B_{eff}. This is an important issue for inserts constructed via a stack of double pancakes.

Section height

In typical regimes I and II inserts, minimization of the radial self-field is accomplished by radial sectioning and varying the height of each section. The difference in height required for a significant reduction in the radial magnetic field contribution of one section to an adjacent insert section is proportional to the winding thickness. However, increasing the height of a section is only effective if the reduction in B_r contribution from the adjacent insert section is larger than the increase in B_r contribution from the outsert. Alternately, if a section is shortened, the increase in J_e through reduction in B_r should exceed the reduction in the magnetic field constant. The optimization of a design through variation of section height is most effective with a relatively tall outsert, such that outsert B_r is small at the top of the tallest insert section.

α^* approaching zero

One can expect that α^* values will decrease with continued development and thus improvement of BSCCO tape conductors. The usual tape geometry, and more so the thin-film coated conductor geometry, appear to offer the possibility of α^* values below 1°. However, as the angle between the tape surface and the *ab*-planes of the grains approaches zero, the dominant cause of misalignment will change from grain misalignment within the conductor to misalignment between the conductor and the magnetic field lines. Tolerances in the flatness of the conductor, alignment of conductor within the windings, alignment between double pancakes and tolerances in the alignment of insert sections with the outsert all contribute to the misalignment angle. Therefore, it is not likely that the extreme variation in B_{eff} as depicted in Figure 4-4 for $\alpha^* = 0$ will occur in practical systems, even if the conductor itself has nearly perfect grain alignment.

Reinforcement

The choice of the reinforcement technique, *i.e.* co-winding or external overbanding, affects the average current density in the windings and therefore the radial self-field distribution within the insert. The use of external reinforcement if the outer diameter of the reinforced windings is fixed, as assumed here, will result in a reduced winding thickness. To maintain the generated field increment, a higher average winding current density is required resulting in a higher radial self-field per section. This is an argument in favor of co-wound reinforcement, at least for single-section inserts in regimes I and II. The situation is more complex for multi-section inserts as external reinforcement has two opposing effects on B_r: an increase in radial self-field of a section is mitigated somewhat

by the increased radial distance to the next section thereby reducing the contribution to the radial magnetic field by the neighboring section.

4.7 Case 2: the average grain misalignment angle describes anisotropy only for small angles

The reduction in J_e for angles close to zero is typically sharper in ReBCO conductors than found for BSCCO conductors with the same ratio of J_e for magnetic field angles between 0 and 90 degrees. To illustrate this the measured angular dependence of conductor K is compared in Figure 4-6 with the calculated angular dependence for a hypothetical BSCCO conductor with the same ratio between $J_e(0°)$ and $J_e(90°)$ (α^*=8.4°).

No value of α^* results in an accurate description of the measured $J_e(\phi)$ data over the entire range. A value for α^* can be found that matches measured values and calculated values at 0 and 90 degrees, but it does not describe the angular dependence for intermediate angles. To fit the steeper slope in $J_e(\phi)$ for the small angles relevant to insert coils, a lower value of α^* must be assumed. If a value can be found that results in an accurate match between the measured $J_e(\phi)$ values and the calculated $J_e(\phi)$ curve up to the maximum magnetic field angle ϕ_{max}, it is designated α^{**}. For conductor K, α^* = 8.4° results in the correct ratio between $J_e(0°)$ and $J_e(90°)$ and α^{**} = 4.0° results in an accurate $J_e(\phi)$ for $\phi < \phi_{max}$.

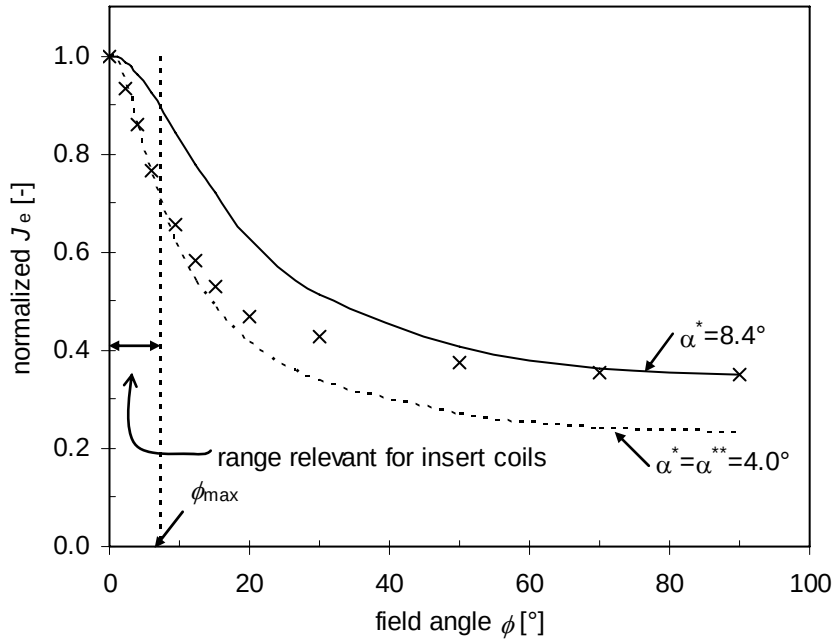

Figure 4-6. Measured angular dependence J_e of conductor K (x-symbols) plus two predicted angular dependence curves using the average grain misalignment angle model. J_e is assumed to be proportional to $B^{-0.55}$.

A smaller value for the anisotropy parameter mathematically corresponds to a larger ratio between $J_e(0°)$ and $J_e(90°)$. Thus a calculated curve for $J_e(B,90°)$ based on this α^{**} value and $J_e(0°)$ will be below the measured values. In effect a virtual $J_e(B_\perp)$ curve is constructed, without physical meaning. However, this constructed $J_e(B_\perp)$ curve can serve to calculate $J_e(B,\phi)$ for small angles with the scaling function $f(\phi)$ based on α^{**}.

It is repeatedly found [88] that $J_e \sim B^{-x}$ with x about 0.5 for a range of conductors and a range of temperatures, as long as T remains well below T_c and B is above self-field

dominated range. This allows mathematically simple modeling of $J_e(B,T)$ data and extrapolation. A more significant consequence of the apparent power-law magnetic field dependence of J_e is that the $J_e(B_{//})$ and $J_e(B_\perp)$ curves can be scaled with a single *current* multiplication factor. Substituting equation 3-4 into 3-13, it follows that:

$$J_e(B_{//}) = f(0)^{-x} \cdot J_e(B_\perp), \text{ and} \tag{4-1}$$

$$J_e(B_\perp) = f(0)^{x} \cdot J_e(B_{//}), \tag{4-2}$$

i.e. $J_e(B_{//})$ and $J_e(B_\perp)$ curves should fall on top of each other when the $J_e(B_{\perp})$ values are multiplied by $f(0)^x$. This is in addition to the *magnetic field* scaling that follows from equation 3-13: the $J_e(B_{//})$ and $J_e(B_\perp)$ curves should fall on top of each other when the $B_{//}$ values are multiplied with $f(0)$.

The observed current scaling of J_e for parallel and perpendicular magnetic field implies that $J_e(B)$ for intermediate angles can be calculated through multiplication of $J_e(B_\perp)$ with an appropriate factor. However, the value of $f(0)^{-x}$ in equation 4-1 is based on α^*, but α^{**} is applicable for small angles so the current scaling factor for all angles can not be based on $f(\phi)$ for a single value of α^*. The current scaling factor is further addressed below.

Use of the effective perpendicular magnetic field as reference magnetic field value would be confusing as the calculated J_e for a given effective perpendicular magnetic field value would not correspond to measured values in actual perpendicular magnetic field. It is therefore more relevant to take the parallel magnetic field component as reference and calculate an effective parallel magnetic field value for the total magnetic field vector using a new magnetic field scaling function $g(\phi)$. The scaling function is described analog to equations 3-5 and 3-6 as follows:

$$B_{eff}^{//} = B \cdot g(\phi) \tag{4-3}$$

such that
$$J_e(B,\phi) = J_e(B \cdot g(\phi),0) = J_e(B_{eff}^{//},0)\,. \tag{4-4}$$

The effective parallel magnetic field is equal to the total magnetic field if the magnetic field angle is zero. With $f(\phi)$ based on α^{**} we have:

$$B_{eff}^{//} = \left(\frac{f(\phi)}{f(0)}\right) \cdot B \text{, for } \phi < \phi_{\max}, \tag{4-5}$$

where B is the length of the $\boldsymbol{B}$ vector, and the magnetic field scaling factor is

$$g(\phi) = \left(\frac{f(\phi)}{f(0)}\right) \text{for } \phi < \phi_{\max}. \tag{4-6}$$

This magnetic field scaling is valid independently from the shape of $J_e(B)$. Substituting equation 3-4 in its general form of $J_e = \text{constant} \cdot B^{-x}$ in equation 4-2 and raising both sides to the power $-x$ gives

$$J_e(B_{eff}^{//},0) = J_e(B,\phi) = \left(\frac{f(0)}{f(\phi)}\right)^x \cdot J_e(B_{//}) \text{ for } \phi < \phi_{\max}, \tag{4-7}$$

thus the current scaling factor is

$$\left(\frac{f(0)}{f(\phi)}\right)^x \text{ for } \phi < \phi_{\max}, \text{ if } J_e \sim B^{-x}. \tag{4-8}$$

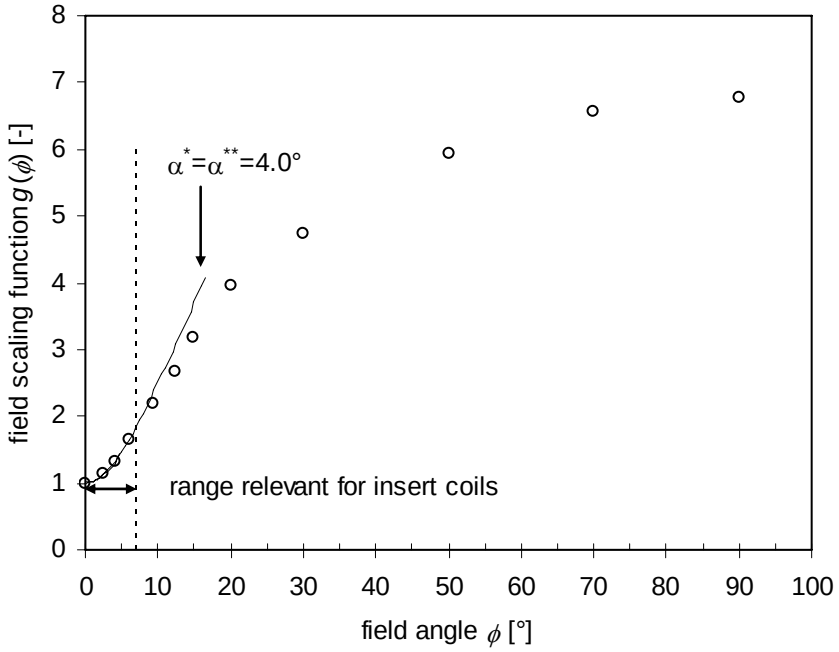

Figure 4-7. Magnetic field scaling function for the effective parallel magnetic field of conductor K. The continuous curve is based on equation 4-8 for $\alpha^{**} = 4.0°$. The data points (o) follow from measured $J_e(\phi)$ at 1 T, 77K [27] and an assumed magnetic field dependence of $B^{-0.55}$. The magnetic field angle range of interest for insert coils is 0 to ~ 7°.

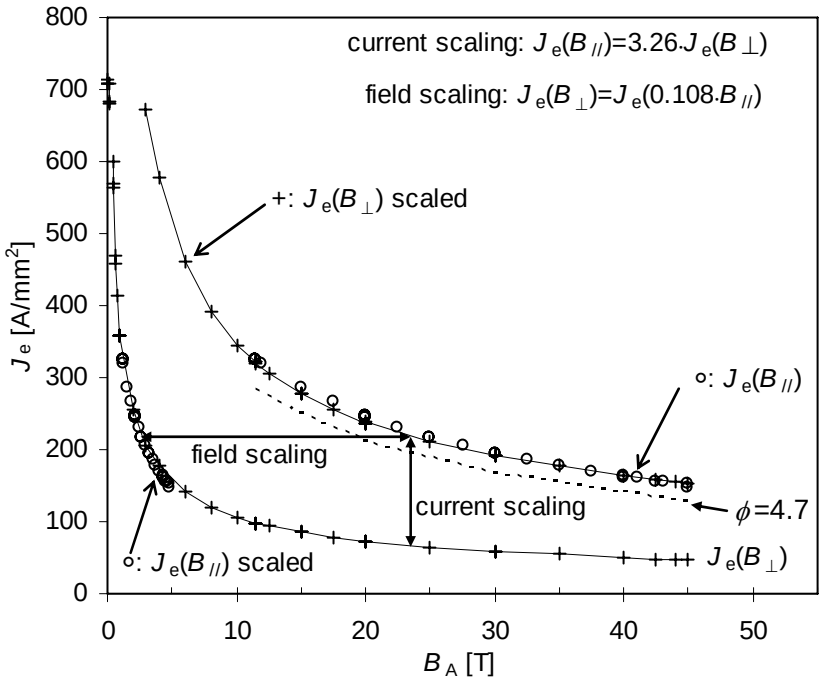

Figure 4-8. Scaling of J_e with magnetic field and current for conductor F. Magnetic field scaling follows from the average grain misalignment model with $\alpha^* = 6.1°$ and f(0) = 0.108; current scaling follows from the power law dependence of J_e on B ($J_e \sim B^{-x}$ with x = -0.53 in this case). The dashed line represents the calculated $J_e(B)$ for a magnetic field angle of 4.7° using current scaling via equation 4-7. Continuous lines are drawn as a guide to the eye through the scaled and un-scaled data for perpendicular magnetic field.

Note that $f(\phi) \geq f(0)$, so $J_e(B,\phi) \leq J_e(B_{//})$. The anisotropy term in equations 4-7 and 4-8 is independent of the absolute value of J_e(self), thus the J_e value for a given magnetic field value and angle is proportional to J_e(self). This is a consequence of the power law dependence of J_e on B^{-x}, not necessarily valid for other expressions for $J_e(B)$. Note also that the Kramer expression gives a magnetic field dependence of J_e that is very close to that of a power law, as briefly discussed in section 3.3 above equation 3-4. Thus current scaling may apply to $J_e(B,\phi)$ of conductors that obey the Kramer relations [104] as well, albeit with reduced accuracy. Again, the validity of these equations is limited to a small range of magnetic field angles using α^{**}, as illustrated in Figure 4-7 for equation 4-8, but sufficient for the purpose of insert coil design. The equations allow the calculation of the $J_e(B)$ at the maximum magnetic field angle in an insert, exemplified with the $J_e(B,4.7°)$ curve based on current scaling of $J_e(B_{//})$ for conductor F with $\alpha^{**} = 4.0°$ as shown in Figure 4-8.

An effective parallel magnetic field can also be calculated for BSCCO conductors and the equations would then apply for all magnetic field angles, as anisotropy in BSCCO can typically be described with a single α^{*} value over the range of interest for HTS inserts.

4.7.1 Comparison of $B^{//}_{eff}$ versus α^{**} at the positions of maximum magnetic field and maximum magnetic field angle

The relation between anisotropy and insert coil design is explored using the SP-YBCO insert in the Large Bore Resistive Magnet using a hypothetical conductor with variable α^{**}. It is assumed that $J_e(B)$ of this conductor is of the form $\sim B^{-0.55}$. The analysis below is not sensitive to the value of the power. First a comparison is made between $B^{//}_{eff}$ at the location of $B_{z,max}$ and at the location of the ϕ_{max} respectively versus α^{**}. J_e is normalized to J_e ($B_{z,max}$). Similar to BSCCO tapes, three regimes can be distinguished as indicated in Figure 4-9.

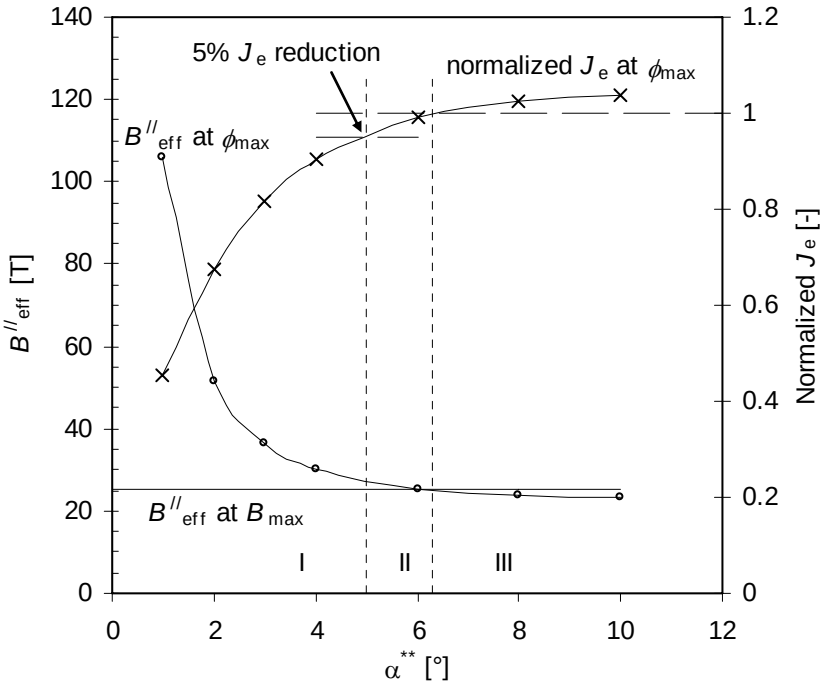

Figure 4-9. $B^{//}_{eff}$ versus α^{**} at the positions of maximum axial magnetic field and maximum magnetic field angle respectively for the SP-YBCO insert. Three qualitatively different regimes: I, II and III, can be distinguished. J_e is normalized to $J_e(B_{max})$.

Regime I: For low α^{**}, the maximum $B^{//}_{eff}$ exceeds by far the value of $B_{z,max}$. The insert is magnetic field angle limited and J_e is sensitive to small variations in α^{**}.

Regime II: For higher α^{**}, the maximum $B^{//}_{eff}$ occurs at the location of ϕ_{max}, but $B^{//}_{eff}$ at the position of B_{max} is nearly equally limiting and the difference in J_e is small.

Regime III: Above a certain crossover value of α^{**}, the maximum $B^{//}_{eff}$ is B_{max} and is at the same location. The insert is axial magnetic field limited at ~ 25 T.

The cross over between regimes I and II is somewhat ambiguous as it is determined by the quantification of a *small* difference in J_e, which is set at 5% here. The cross over between regimes II and III is unambiguously determined by the α^{**} value for which the calculated values of $B^{//}_{eff}$ at the positions of ϕ_{max} and B_{max} are equal.

This pattern of three regimes is generic for ReBCO inserts with anisotropic conductor. Lack of $J_e(\phi)$ data at 4.2 K and $B > 20$ T makes it uncertain what the actual range of α^{**} is in real conductors. If $J_e(\phi)$ data at 77 K and low magnetic field values are indicative, then regimes I and II are most common.

4.7.2 Comparison of $B^{//}_{eff}$ versus α^{**} in the entire cross section of an insert

The relationship between $B^{//}_{eff}$ and α^{**} has been explored at two positions: at maximum ϕ and maximum B_z. To verify that these are also the positions of maximum $B^{//}_{eff}$, and to determine what 2D patterns exist, $B^{//}_{eff}$ is considered in the same manner within the entire cross section of the example 5T insert. The dependence of $B^{//}_{eff}$ and J_e on α^{**} is listed in Table 4-7 and shown for $\alpha^{**} = 4°$ in Figure 4-10. J_e is again taken as proportional to $B^{-0.55}$ and is normalized to the operating current density at the central magnetic field of 25 T. The position of maximum $B^{//}_{eff}$ is close to the maximum in ϕ for regimes I and II, and at the position maximum in B_z for regime III. The position of minimum $B^{//}_{eff}$ is at the midplane for this insert, where $\phi = 0°$, and thus independent of α^{**}. $B = B_z = B^{//}_{eff}$ at the midplane for the same reason for any regime. For $\alpha^{**} < 4°$, the peak in $B^{//}_{eff}$ and the dip in J_e at ϕ_{max} become more pronounced and for larger α^{**} they flatten out until the peak of $B^{//}_{eff}$ at ϕ_{max} is lower than $B_{z,max}$ at the midplane and no longer limiting the design.

Table 4-7. $B^{//}_{eff}$ and J_e variation versus α^{**} in the SP-YBCO insert.

	$\alpha^{**}=1^o$	$\alpha^{**}=2^o$	$\alpha^{**}=3^o$	$\alpha^{**}=4^o$	$\alpha^{**}=6^o$	$\alpha^{**}=8^o$	$\alpha^{**}=10^o$
Maximum $B^{//}_{eff}$ [T]	106	51	36	30	25	25	25
Minimum $B^{//}_{eff}$ [T]	19.6	19.6	19.6	19.6	19.6	19.6	19.6
Variation in $B^{//}_{eff}$ [T]	86	32	17	11	6	5	5
J_e max [% of J_{op}]	115%	115%	115%	115%	115%	115%	115%
J_e min [% of J_{op}]	45%	67%	82%	90%	99%	100%	100%
Variation in J_e [% of J_{op}]	70%	47%	33%	24%	16%	15%	15%
Regime	I	I	I	I	II	III	III

A summary of key aspects in the relation between conductor anisotropy and insert coil design is presented in Table 4-8. As in the previous section, it is assumed that the coil outer radius is fixed as well as the target value for the magnetic field increment generated by the insert. These assumptions do not reduce the general validity of the results. Each regime has been generically associated with a low, medium or high value of α^*, as the cross over values are conductor and design specific. Aspects of Table 4-8 that have not already been discussed are discussed below.

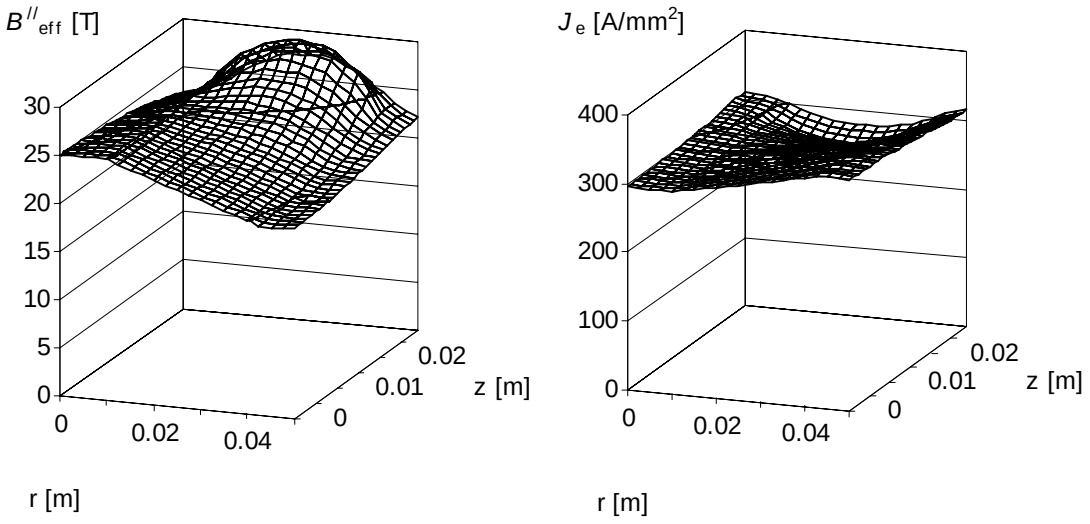

Figure 4-10. $B^{//}_{eff}$ (left) and J_e (right) for the SP-YBCO insert with $\alpha^{**} = 4°$ and $J_e \sim B^{-0.55}$.

Table 4-8. Effect of ReBCO anisotropy on the insert design optimization.

	Regime I, low α^{**}	**Regime II, medium α^{**}**	**Regime III, high α^{**}**
Defining feature	$B^{//}_{eff}$ sharply peaks and J_e sharply dips at ϕ_{max} *Insert is magnetic field angle limited.*	Insert J_e is limited at location of maximum ϕ_{max}, but maximum axial magnetic field at midplane is nearly equally limiting.	$B_{eff} \cong B$ and the resulting J_e distribution is accordingly. *Insert is axial magnetic field limited.*
Value of $B_{eff,max}$	$B^{//}_{eff,max} >> B_{z,max}$	$B^{//}_{eff,max} \cong B_{z,max}$	$B_{eff,max} = B_{CF}$
J_e is *most* sensitive to:	ϕ_{max} α^{**}	ϕ_{max} α^{**} B_{CF}	B_{CF}
J_e is *least* sensitive to:	-	-	ϕ_{max} α^{**}
Design focus	Minimize ϕ_{max} Winding thickness (radial sectioning) Differentiate section heights.	All parameters are relevant.	Optimize design based upon other considerations, *e.g.* cost, strain, magnetic field homogeneity.
Opportunities	Use lower grade conductor in areas subject to low $B^{//}_{eff}$. Requires axial divisions.	Use lower grade conductor in areas subject to low B_{eff}. Requires both axial and radial divisions and a high current density.	Coil height and radial division not constrained by J_e considerations.
In comparison	Confidence is needed in reproducibility of $J_e(\phi)$.	Most complex to optimize.	Reduced anisotropy may have come at the expense of lower J_e for small ϕ.

Correlation between α^{**} and J_e

In the above analysis a hypothetical conductor is used where α^{**} is varied, keeping all other parameters the same. A lower value for α^{**} results in a reduction of insert J_e when the $J_e(B_{z,max})$ is unchanged. It appears that improvement of the superconductor production process can lead to a correlated decrease in α^{**} and increase of the peak value of $J_e(B_{//})$

[104], so an increase in $B^{//}_{eff}$ with small α^{**} may be balanced by an increase in conductor J_e. It is also possible that there is a net gain.

Artificial pinning centers

Artificial Pinning Centers (APC) like nanometer sized non-superconducting inclusions are in use to increase $J_e(B)$ in ReBCO conductors and sometimes touted as a mechanism to reduce anisotropy [106]. It is crucial to realize that anisotropy defined as the ratio of the J_e in parallel and J_e in perpendicular magnetic field has no meaning in the context of insert coils, as magnetic field angles above about 10° are unlikely in inserts[43]. APC improve flux pinning and J_e most around magnetic field angles of 90 degrees, with reduced benefit for smaller angles often approaching no measurable benefit below magnetic field angles of 20° [107] or 10° degrees [94]. While useful in other applications, such APC are useless for insert coils. Only mechanisms that improve pinning for angles below 10 degrees have a place in conductor technology aimed at 25 T class inserts, which implies planar pinning as the preferred mechanism.

4.8 Case 3: the average grain misalignment does not describe anisotropy

If the measured $J_e(\phi)$ from $\phi = 0$ to $\phi = \phi_{max}$ can not be modeled using a single value for α^{**}, an effective magnetic field can not be defined using a magnetic field scaling function as introduced in section 3.4 and applied in sections 4.6 and 4.7. Thus an alternate method is required to make a straightforward representation of the relation between anisotropy and coil design. The following general method always generates such a representation independent of models, like the average grain misalignment concept, to describe anisotropy.

The relationship between conductor anisotropy and coil design can be evaluated by showing the conductor characteristics and the design requirements in one $J_e(\phi)$ plot as follows:

1. Determine $J_e(\phi)$ of the conductor for the maximum magnetic field value at the mid-plane, $B_{max}(\phi = z = 0)$, through direct measurement or scaling of $J_e(B,\phi)$ and plot this over the magnetic field angle range of interest.
2. Calculate B_{total} and magnetic field angle ϕ at the design J_e across the windings of the insert coil.
3. Plot the design current density at the maximum magnetic field at the mid-plane at ϕ=0°. This magnetic field is close to but not identical to the central magnetic field.
4. Determine B_{total} at the unique position of the maximum magnetic field angle ϕ_{max}. This magnetic field is typically less than B_{total} at the mid-plane where $\phi = z = 0$. Assume that J_e is the design value J_{op} at $B_{total}(\phi_{max})$ and extrapolate that J_e value to $B_{max}(\phi = 0)$. This is the required minimum $J_e(B_{//})$ for that position.
5. Take a number of ϕ-values that are a fraction of ϕ_{max}, say at quarter increments: $0.25\cdot\phi_{max}$, $0.5\cdot\phi_{max}$ and $0.75\cdot\phi_{max}$. Determine the maximum value of B_{total} across the positions with equal magnetic field angle. This results in a number of $(B_{total,max},\phi)$ pairs.
6. Assume that the conductor J_e is the design value J_{op} at each of those $B_{total,max}(\phi)$ values and extrapolate that J_e value to $B_{max}(\phi = 0)$. Plot the resulting J_e values at the corresponding ϕ values. The latter points describe the design requirements on the superconductor. The resulting plot contains both the design requirements and the anisotropic conductor properties, projected on the $J_e(\phi)$ plane for the maximum

[43] In the three example inserts used in this Chapter the maximum field angle is always below 7°.

magnetic field on the midplane. Such a plot straightforwardly illustrates the margin between the current carrying capacity of the conductor and the design requirements as well as the magnetic field angle, and thereby position, at which the minimum of that margin occurs.

The above approach is applied for two example conductors, K and L, for which $J_e(\phi)$ data are taken from [98], and J_e is scaled to match the required $J_e(\phi_{max})$. The data for conductor K are also used in Figure 4-7. A design for the SP-YBCO insert thus based on conductor L would be almost equally limited by the central magnetic field and the magnetic field at the position of maximum magnetic field angle. This is equivalent to a regime II design bordering on regime III as J_e is reduced by ~ 1% by $B(\phi_{max})$ compared to $B_{max}(\phi = 0)$. That J_e reduction is 9.5% if conductor L were employed, making such a design comparable to regime I. If data at relevant magnetic field, temperature and angles are available, a plot like Figure 4-11 will show the margins between the conductor requirements and conductor performance by which the relation between conductor anisotropy and coil design can be evaluated.

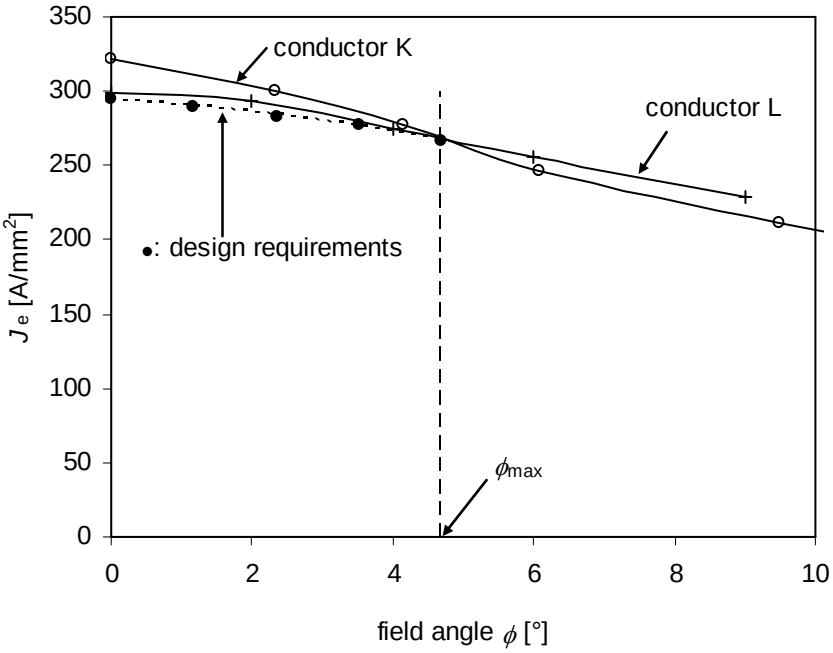

Figure 4-11. Calculated requirement for Je(ϕ) for the SP-YBCO insert at 25 T and the properties of two conductors scaled to the required J_e at ϕ_{max}. To meet the design specification, a conductor with the anisotropy of conductor K needs to carry 322 A/mm^2 at 25 T parallel magnetic field and similarly 299 A/mm^2 is required for a conductor exhibiting the anisotropy of conductor L.

4.9 Conclusion

The critical current of typical BSCCO and REBCO tapes are anisotropic with respect to the magnetic field vector, which adds a new aspect to the design of HTS insert coils compared to those with metallic superconductors. The maximum magnetic field angle in HTS inserts is expected to be small. In three example of 5 T inserts for 25 T magnets, the maximum field angle is 7 degrees or less.

Here, this anisotropy is characterized through a single parameter, the average grain misalignment angle, determined directly from critical current data. A model is proposed

describing the magnetic field dependence of the engineering critical current density of a conductor as a scalar function of the effective perpendicular magnetic field, by which knowledge of the magnetic field vector and the average grain misalignment angle suffice to determine the effective perpendicular magnetic field. This model is applicable to typical BSCCO tape conductors.

The absolute value of the engineering critical current density for a specific magnetic field value determines the current density in a conductor and therefore the magnetic field generating capacity of a BSCCO insert based on that superconductor. The initial optimization process of a design based on such a current density is mostly driven by the average grain misalignment angle.

Analysis of the relationship between the average grain misalignment angle and the position and value of the maximum effective magnetic field, corresponding to the minimum in the engineering critical current density, reveals three insert coil design regimes. A combination of design and superconductor with low average grain misalignment angle corresponds to regime I and a radial magnetic field limited insert. Regime III corresponds to a high value of the average grain misalignment angle and an axial magnetic field limited insert. Axial and radial magnetic field components combine to limit an insert in regime II for intermediate values of the average grain misalignment angle. The crossover between these regimes depends on both conductor properties and the initial design. Depending on the regime, the relative importance of design parameters in optimizing the design varies greatly. To design BSCCO inserts, the average grain misalignment angle should either be known or specified.

The mathematical formulism associated with the average grain misalignment angle is suitable to describe anisotropy in some ReBCO conductors for the small range of angles present in typical insert coils, but not beyond. Expressions for the effective parallel magnetic field are derived. Three regimes are identified in the relation between anisotropy and effective parallel magnetic field, with design implications that partially match those for BSCCO conductors.

Regardless whether the anisotropy can be described using the average grain misalignment or not, a straightforward approach is presented that can be used to illustrate the relation between conductor anisotropy and coil design with a single graph containing just two curves representing the design requirements and the conductor properties respectively.

5 Magnetic field dependence of the engineering critical current density in insert coils

The magnetic field dependence of the engineering critical current density in Bi-2212 and Bi-2223 double pancake coils and the 5T Bi-2212 insert magnet are correlated to the properties of the constituent conductor using calculations and empirical data. Anisotropy in the magnetic field dependence of the engineering critical current density is included using the average grain misalignment and, for the Bi-2212 double pancake coil, also using an explicit model.

5.1 Introduction

HTS coil design involves many of the traditional topics, i.e. packing factors, reinforcement, insulation, magnetic field homogeneity in the bore. Anisotropy in the magnetic field dependence of the critical current, however, differentiates the BSCCO and ReBCO conductors from NbTi and Nb_3Sn conductors when it comes to the process of modeling the magnetic field dependence of J_e. Anisotropy, and to some extend *n*-values if they are low, complicate the prediction of the engineering critical current density of the conductor in a coil as well as the reverse: determining conductor requirements based on design magnetic field and current density. Whether the approach to describe conductor $J_e(B)$ and its anisotropy as developed in chapter 3 is sufficient to model BSCCO magnet $J_e(B)$ is the leading question in this chapter. [44]

5.1.1 Qualification criteria

A qualification criterion is required to determine if prospective batches of conductor are suitable for application in insert coils. An often used approach is to set a minimum for the short sample self-field J_e based on the limiting magnetic field value and field angle in the insert at design conditions. The criterion is derived via measurement of $J_e(B_A)$ of short samples of a reference batch whose properties presumably are representative of all prospective batches.

Disadvantages of short sample self-field testing are self-evident: questions remain whether the samples are representative of the entire batch, and whether the reference magnetic field-dependence is representative. However, few practical alternatives exist. Short samples can be characterized in-field but require routine access to high-field magnets and this still does not address the issue of property variations along the length of a batch. Piecewise measurement of the current density along the entire length, either by a transport current or a magnetization method [108] is currently an option for temperatures around 77 K. However, this technique is not widely practiced nor widely available and relies on an accurate understanding of the J_e ratio between 4.2 K and 77 K. While this technique is feasible for Bi-2223 conductors, it generally is not for Bi-2212 conductors as their T_c values are too close to, or even below, 77 K. End-to-end J_e characterization for Bi-2212 at 4.2 K was developed at OST but is not in routine use. A reliable and widely applicable method to set qualification criteria based on conductor measurements only remains elusive.

[44] At the time of writing no useable data on $J_e(B)$ and its angular dependence at 4.2 K for ReBCO conductor was found nor a reliable and complete data set on the magnetic field dependence of $J_e(B_A)$ in a ReBCO coil.

As discussed in section 3.3.3, the largest batch-batch variations in J_e occur for low magnetic field values. To reduce the uncertainty in the step between short-sample self-field properties and in-field magnet properties, a step from a centimeter to kilometer length scale, it is useful to study sub-size coils: large enough to encompass a significant amount of conductor and small enough to be affordable compared to the cost in time, effort and materials of unsatisfactory performance and possible replacement of the entire insert. This is a natural approach when the insert consists of double pancake coils [46, 42, 43, 47, 109] and can be used for layer wound inserts as well, albeit generally without the option to re-use the sub-units in the final product. The sub-units investigated here are all double pancake coils and are also referred to in brief as coils or units.

The resulting process is schematically indicated in Figure 5-1. Measurements of coils in magnetic fields that equal or approach the values applicable to the insert in-field condition establish a relation between the properties of units at self-field (point B) and at in-field conditions (point C). Based on the design magnetic field values (point D), a qualification criterion for the coil self-field critical current can be set. Comparison of coil self-field properties (point B) and its conductor properties yields a qualification criterion for conductor self-field critical current (point A), which completes the link from coil J_e to conductor requirements.

The conductor qualification process thus becomes a two-step process: batches with conductor properties close to or exceeding their qualification criteria are selected for double pancake coil winding and testing. Double pancake coils meeting or exceeding their separate qualification criteria are selected for inclusion in the insert coil.

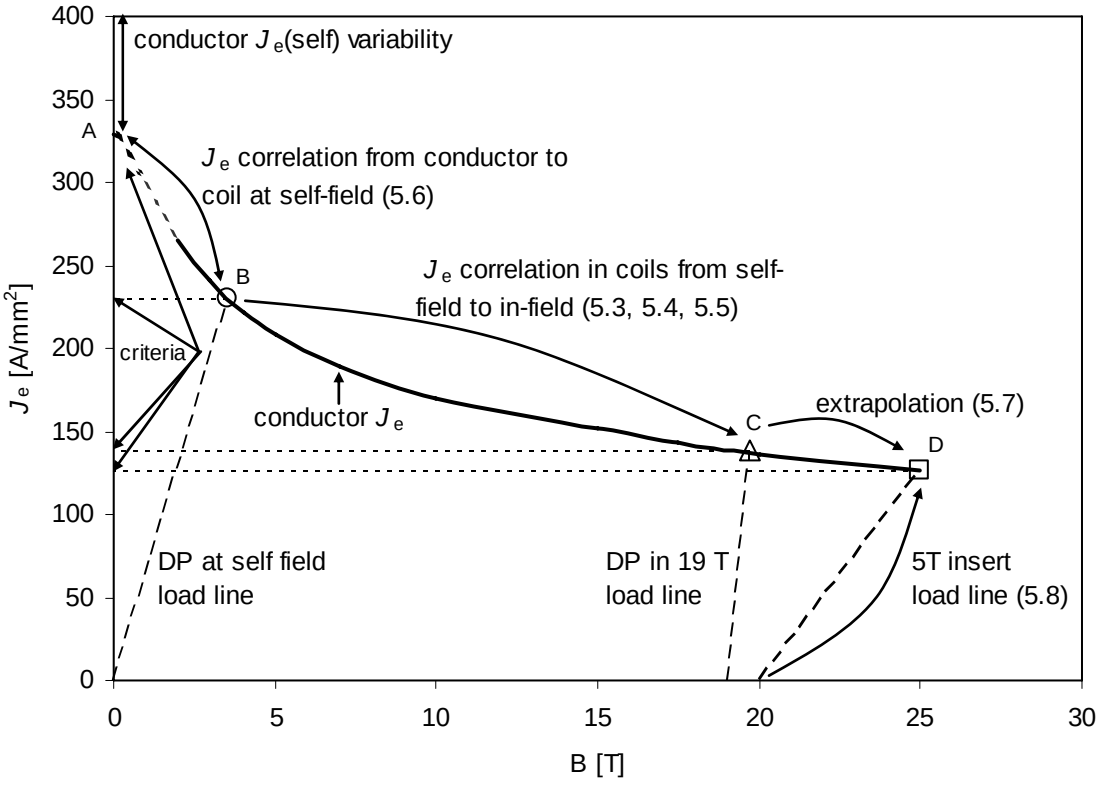

Figure 5-1. Schematic representation of a conductor J_e(B) curve with load lines and qualification criteria. The section where each aspect is discussed in listed between parenthesis.

5.1.2 Modeling

The most complex situation to model exists in double pancake coils in self-field. The angle between flux lines and the coil axis varies from zero to 180° and gradients exist in the magnetic field strength across the width of each turn. Such gradients are also present in the value of B_{eff} and remain large for applied magnetic fields of several teslas. Furthermore, the 0 to 0.7 T range shows the largest sample to sample variation in the magnetic field dependence of J_e. Also, the average grain misalignment model for anisotropy in $J_e(B)$ is least accurate in this range as pointed out by the relatively poor scaling of $j_e(B_\perp)$ and $j_e(B_{//})$ at low magnetic fields (section 3-5).

In contrast, B_{eff} is quite homogeneous in a coil in higher background magnetic fields. The magnetic field angle range is reduced by almost two orders of magnitude as the maximum magnetic field angle is about 1°. Based on this homogeneity and with knowledge of $J_e(B)$ and α^* of the conductor, one expects that the coil critical current density for high applied magnetic fields B_A is predictable. This is reinforced by the observation that for 7 different double pancake coils from OST conductor, from 7 different batches produced over 6 years, normalized $J_e(B_A)$ properties from 10 to 19 T are reproducible. All measurements in the above comparison are normalized to the 19 T values as shown in Figure 5-2. The variation in normalized J_e below 7.5 T applied magnetic field is attributed to variations between conductors in absolute critical current and its magnetic field dependence, and differences in winding geometry between coils, both affecting the coil self-field. Double pancake coils with a relatively large radial build and large current density have a lower normalized J_e in self-field conditions.

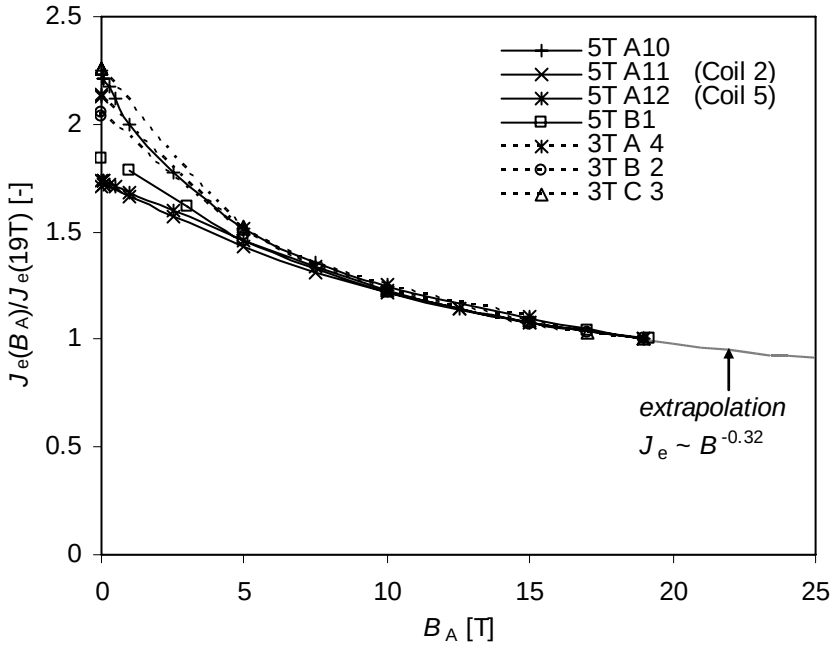

Figure 5-2. Engineering critical current density of double pancake coils normalized to their 19 T value. OST supplied all the conductor batches used. In the absence of a unique B_{eff} value, the applied magnetic field value at the center of the insert is used to plot measured and calculated magnetic field dependence of J_e. The legend identifies the project and project coil identification; between parentheses is the coil identification used in this work according to Table 5-4. An extrapolated fit of the general trend to 25 T is indicated.

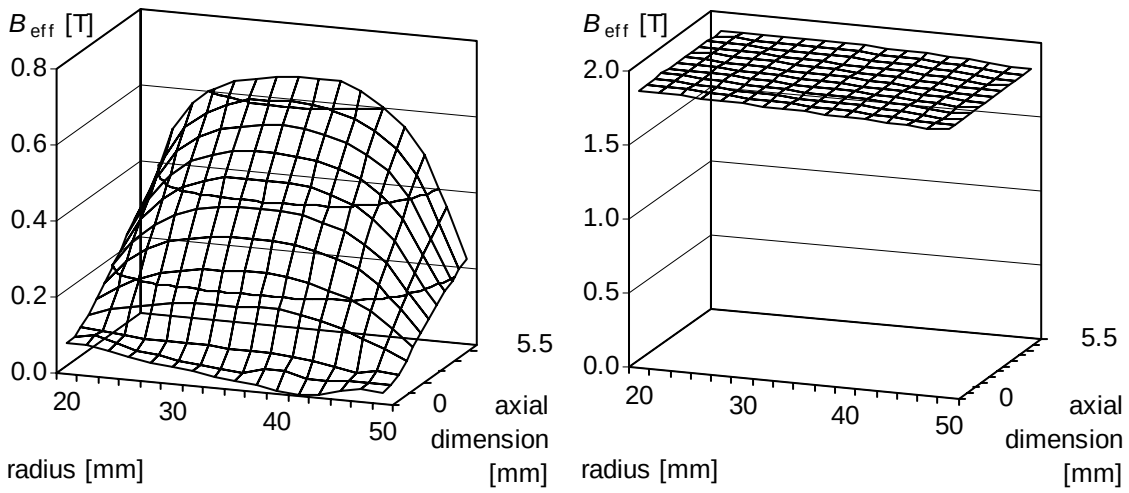

Figure 5-3. The effective magnetic field in the windings of Coil 2 (see Table 5-4) at self-field and in 19 T background magnetic field. The magnetic field patterns are symmetric with respect to the midplane (z = 0) and axis (r = 0).

The considerations of B_{eff} and normalized coil $J_e(B_A)$, which are summarized in Figures 5-2 and 5-3, lead to the expectation that it should be possible, for coils in applied magnetic fields of ~ 7.5 T and higher, to accurately model the $J_e(B_A)$ curve. Optimum accuracy is reached when the average error between model and measurement is in the order of 1%, which is the accuracy of the conductor $J_e(B_\perp)$ modeling. Specifically, this chapter will address:

a) how the measured $J_e(B_A)$ properties of double pancake coils can be modeled using parameters derived from the properties of short samples of a representative conductor batch, and which approaches are less successful;

b) how $J_e(B_A)$ properties of larger inserts can be modeled using short sample parameters and double pancake coil self-field properties.

5.1.3 Coils

Background magnetic field magnet

The background magnetic field for coil testing is generated by the NHMFL Large Bore Resistive Magnet[45], which is normally limited to 19 T. A feature of the background magnetic field is a significant gradient in strength and direction over the volume of the HTS insert coils, specifically the 5T insert introduced below. Hence the measured performance of an HTS insert coil is unavoidably affected by the inhomogeneity of the background magnetic field. The models take this inhomogeneity into account; omission of this feature would lead to significant errors.

Double pancake coils

Two double pancake coils are discussed in the following sections and are shown in Figure 5-4. Both coils are epoxy-impregnated and wound with already reacted conductor. The conductor in Coil 1 is very similar to Conductor A, except for a reduced width. The conductor in Coil 2 is nominally identical to conductor C. Geometric parameters are listed in Table 5-1.

[45] The Large Bore Resistive Magnet is described in Figure 4-1 and Table 4-1.

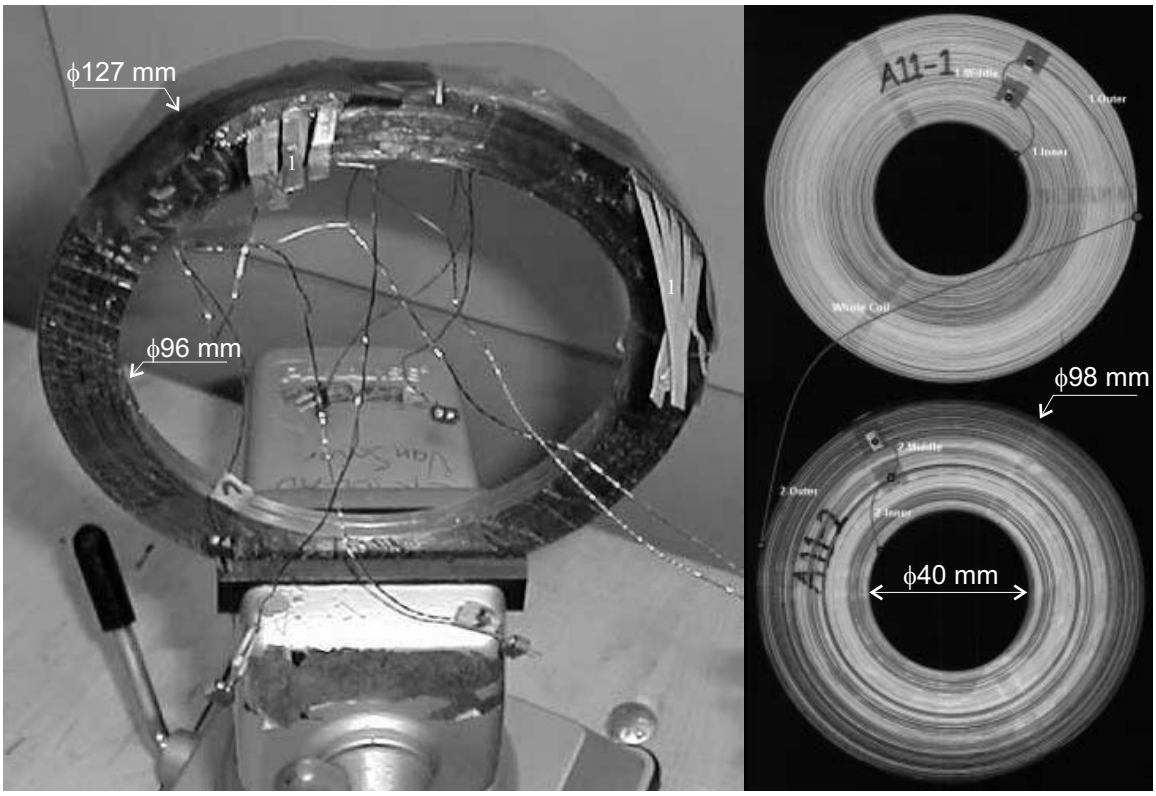

Figure 5-4. Coil 1 in a vise (left) and top and bottom of Coil 2 (right). Coil 1 is shown just before the in-field measurement. Visible are the voltage tap wires and the terminals formed by soldered pieces of Bi-2212 tape. The soldered joint on the coil is reinforced with glass fiber and blue STYCAST 2850 epoxy.

Table 5-1. Geometric properties of Coils 1 and 2.

Property	Unit	Coil 1	Coil 2
Conductor width	mm	3.0	5.0
Conductor thickness	mm	0.24	0.20
Winding inner radius	mm	48	21
Windings outer radius	mm	63.5	49.0
Winding height	mm	7	11
Total # turns	-	98	231
Conductor length	m	35	50

As the goal here is to study the magnetic field dependence of J_e, it is pertinent to verify that strain does not affect J_e as well. Strain induced degradation can become irreversible, therefore only coil $J_e(B_A)$ data are considered that are reversible within 1 A. Most of the coil data shown in Figure 5-2 meet that criterion and could be analyzed in detail as well. However, as the data shows very similar patterns from coil to coil, it is expected that such an additional study would lead to the same conclusions as for Coil 2.

The 5T insert coil

The 5T insert is a Bi-2212 demonstration coil named after the magnetic field increment it is designed to generate [24, 45, 46]. It consists of 3 concentric sections labeled A, B, C from the inside out. All sections are electrically in series. A schematic cross-sectional view is presented in Figure 1-8. Most of the coil volume is taken up by two double pancake coil stacks. The outer section is layer wound. All are shown in Figure 5-5 .

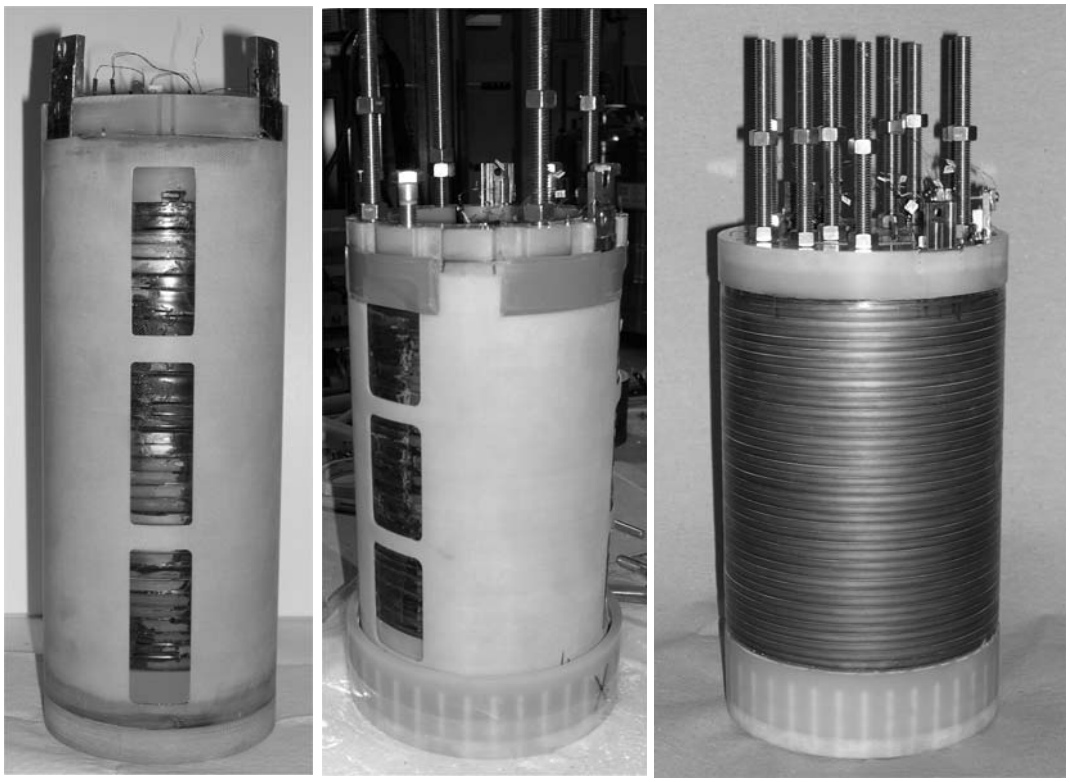

Figure 5-5. Pictures of the A-stack (left), B-stack (middle) and of the assembled 5T insert (right).

All sections use React&Wind technology and the insert was designed such that no conductor grading between sections is required. The conductor used is from batches similar to conductors B, C and D. The ceramic powder used in the latter is from a different source, resulting in a slightly different magnetic field dependence of j_e and generally a significantly higher conductor J_e(self). Units from conductors like B and C limit the performance of the insert. The main parameters of the insert are given in Table 5-2.

Table 5-2. 5T insert coil parameters.

Property	Unit	Section A	Section B	Section C
Conductor width	mm	5.0	5.0	5.0
Conductor thickness	mm	0.2	0.2	0.2
Winding inner radius	mm	21	53	78
Windings outer radius	mm	48	73	82.5
Winding height	mm	185	185	209
Design J_{op}	A/mm^2	126	126	126
Double pancake units	-	17	17	-
Actual # turns	-	3723	2611	532
Total conductor length	m	801	1034	269

5.2 n-value in double pancake coils

Modeling of $J_e(B_A)$ of a BSCCO coil based on the properties of its constituent double pancakes requires knowledge of the magnetic field dependence of their *n*-value. To that effect, two coils, Coils 1 and 2, are investigated in axially oriented background magnetic field. The resulting data are shown in Figure 5-6. Similar to the short samples in applied parallel magnetic field, the coil *n*-values have a maximum at self-field and are constant,

within the error margins, at a lower value from 5 to 19 T applied axial magnetic field. Short sample data[46] suggest that this trend can be extrapolated to 25 T. The *n*-value of the coils is about 2/3 of the short sample *n*-value for applied magnetic field from 5 to 25 T, and a higher fraction for $B_A < 5$ T. This pattern is consistent with the observed scaling in *n*-values, which can be seen in Figure 3-14, but is not further addressed here as the above understanding of *n*-values in double pancake coils is sufficient for modeling larger stacks thereof.

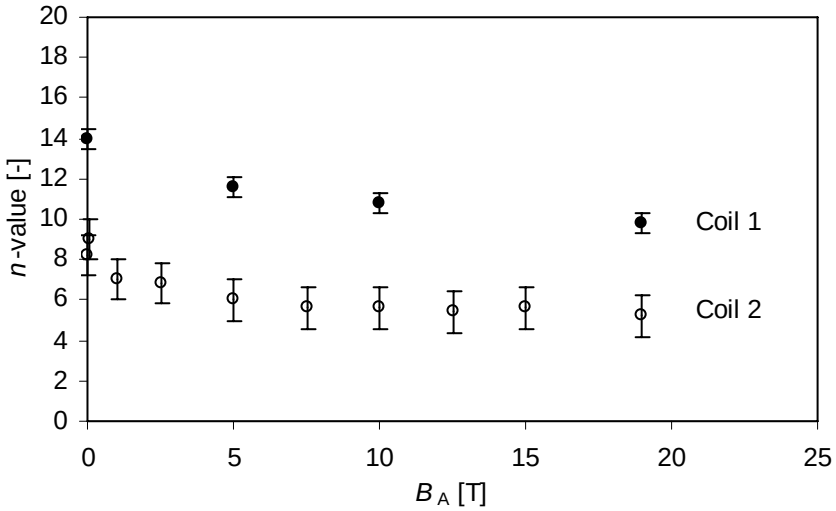

Figure 5-6. n-value versus applied magnetic field with error margins for double pancake coils 1 and 2.

5.3 Modeling of the measured $J_e(B_A)$ curve of double pancake coils

5.3.1 Method to model $J_e(B_A)$ of double pancake coils

The modeling of coil $J_e(B_A)$ is facilitated by subdividing the windings into cells, assigning a single value to all relevant parameters in that cell and calculating the voltage across that cell using the equations and parameters derived in chapter 3 for short samples. A quarter cross section of the coil is divided into cells of 0.5 mm axially by 2 mm radially as indicated in Figure 5-7.

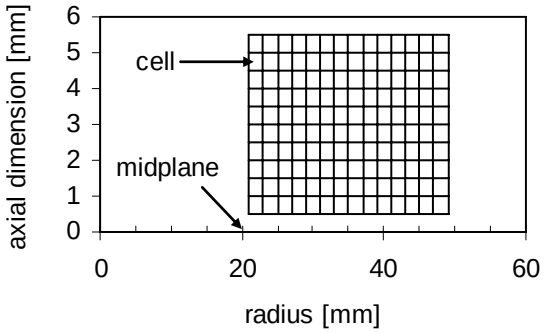

Figure 5-7. Schematic quarter cross-section of the windings of double pancake Coil 1.

[46] Figures 3-15 and 3-16

The values for B_r, B_z, B_{total}, and ϕ are calculated in each cell based on the background magnetic field and the operating current density in the insert coil. Then, $f(\phi,\alpha^*)$ is calculated using a lookup table with a resolution of 0.1 degrees in ϕ. B_{eff} follows from the $B_{eff}^{\perp} = B_{total} \cdot f(\phi,\alpha^*)$ and determines the normalized $J_e(B_{eff})$ value. This dimensionless value is written as j_e, and ranges from one to zero. The electric field E along the conductor is calculated using:

$$E = E_c \cdot \left(\frac{J_{op}}{j_e \cdot J_e^{calc}(self)} \right)^n , \qquad (5.1)$$

where E_c is the 1 μV/cm criterion, J_{op} the operating current density, $J_e^{calc}(self)$ the assumed short-sample conductor self-field J_e and n the index of transition. The voltage per cell is found by multiplying E with the conductor length in each cell, based on the average radius and number of turns per radial mm. The set operating current density corresponds to the calculated critical current when the cumulative voltage over all cells equals the critical voltage (criterion in V/m times total conductor length).

There is a small part in the windings where $B_{eff} \approx 0$ and might be lower than the short sample self-field. So J_e is potentially higher than the measured self-field J_e.[47] The model for normalized J_e is truncated to unity for magnetic field values that would otherwise give a value above 1. However, this affects only a small part of the coil and the effect on the total coil voltage is negligible. In all cases the normalized conductor $J_e(B)$, is taken from chapter 3 and anisotropy is mostly[48] incorporated following the average grain misalignment model introduced in chapter 3. The remaining free parameters are α^*, n-value and $J_e^{calc}(self)$. The latter is chosen such that, in combination with the remaining parameters, the calculated coil J_e in the 19 T background matches the measurement. The calculated relation of coil J_e versus the background magnetic field is then completely determined with the choice of α^* and n-value, and a comparison with the measured $J_e(B_A)$ relation and measured short sample J_e's can be made. The above describes the basic model.

5.3.2 Non-uniform current density

Large variations in B_{eff} within a double pancake coil are observed and especially for low applied magnetic field which is not consistent with the assumption of uniform current density. This is discussed and illustrated in detail, for a Bi-2223 pancake stack, in [110].

As a refinement of the basic model a non-uniform conductor current density is introduced here in which the current density varies with axial position within a turn, but is independent of radial position. The effect of axial redistribution of transport current on the magnetic field generation by the insert coil is taken into account in the calculations of the magnetic field components. The axial current density distribution is varied, using an iterative process, such that the cumulative voltage for all cells with the same axial position equals the critical current density criterion of 1 μV/cm. Thus optimized, the axial current density distribution $J_e(z)$ is typically as shown in Figure 5-8.

As expected, the current density is relatively high near the midplane where B_{eff} is relatively low. The result of allowing axial variation of the current density on the calculated $J_e(B_A)$ curve is an increase in the coil self-field J_e and the initial slope of the $J_e(B_A)$. There is, however, little change in the calculated $J_e(B_A)$ curve above 5 T applied magnetic field. An example is given in Figure 5-9, and will be further explained below.

[47] See Figure 3-5.
[48] An explicit model for anisotropy is introduced in section 5.4.3.

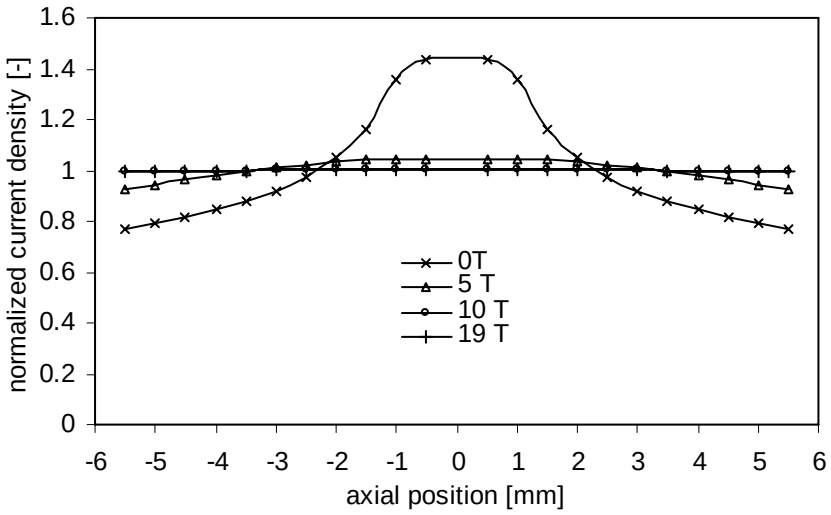

Figure 5-8. Typical axial variation of the calculated current density within a turn of a double pancake for different applied magnetic field values.

Despite the fact that in the example the calculated coil self-field J_e closely matches the measured value, this fit must be considered inadequate as the slope in $J_e(B)$ still varies significantly from the measured values, especially since the slope > 5 T is the most reproducible feature between double pancake coils from this type of conductor.

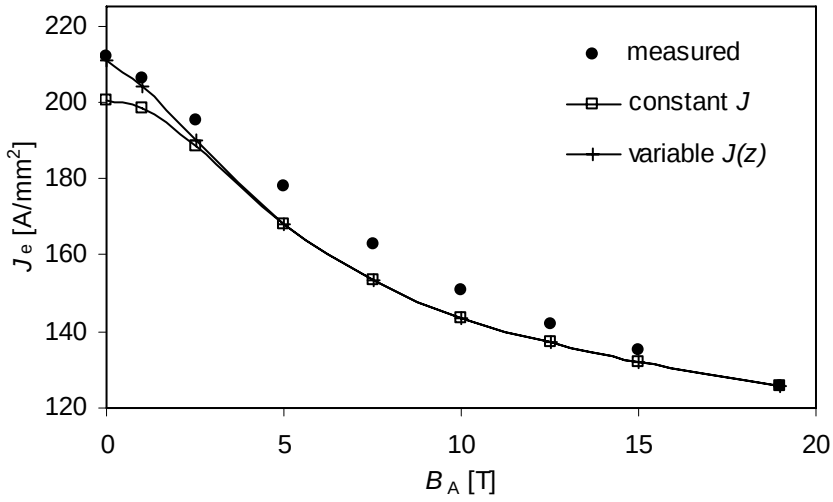

Figure 5-9. Measured and calculated $J_e(B_A)$ for Coil 2 using the basic model (squares) and the refinement of an axially variable current density (+ markers).

5.3.3 Magnetic field dependent α^*

$J_e(B_A)$ is also calculated assuming a magnetic field dependent α^* to address the question that remained unanswered in chapter 3: is α^* for this type of Bi-2212 conductor magnetic field independent, as assumed in the model, or does α^* increase with B as suggested by Figure 3-12. The α^* vs. B_{eff} data of Figure 3-12 can not be used directly for the purposes of this chapter to describe the magnetic field dependence of α^*, as B_{eff} is strongly dependent on α^* except for magnetic field angles very close to zero. This leaves $B_\perp$ and $B_{//}$, *i.e.* B_r and B_z, as the sole remaining independent parameters.

The axial magnetic field component is dominant at higher background magnetic fields while radial magnetic field components strongly affect coil properties at low applied magnetic fields, so neither choice is appropriate within the entire range of applied magnetic field. As a compromise, the relation of α^* versus $B_{//}$ from short sample measurements is used in which B_{total} is substituted for $B_{//}$. For higher applied magnetic fields B_{total} and the axial magnetic field component are nearly identical. At lower magnetic field, radial magnetic field components, whose effect on J_e would be ignored if only B_z was considered, do contribute to B_{total}. The $\alpha^*(B_{//})$ values from section 3-5 and a linear fit are plotted in Figure 5-10. From the linear fit parameters follows:

$$\alpha^* = 4.06 + 0.071 \cdot B_{total}, \qquad (5\text{–}2)$$

which is used to calculate α^* in every cell. The average value of α^* for each applied magnetic field is used to calculate B_{eff}. Thus a magnetic field dependent α^* is introduced.

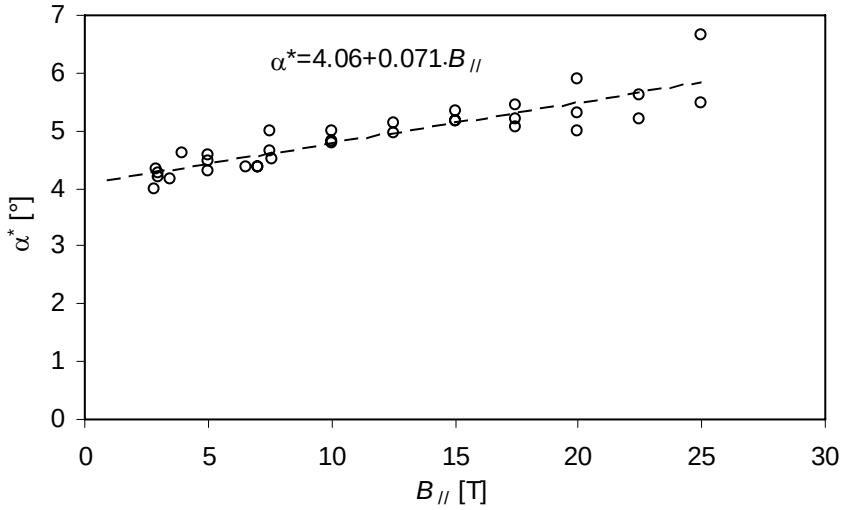

Figure 5-10. The α^* values for conductor B from Fig. 3-10 versus $B_{//}$ plus a linear fit.

5.4 Results of modeling $J_e(B_A)$ properties of a Bi-2212 double pancake coil

5.4.1 Magnetic field independent anisotropy parameter

In this paragraph the average grain misalignment α^* and the *n*-value are assumed magnetic field independent, conform the basic formulation developed in chapter 3. Allowing axial redistribution of the current density results in a more accurate fit than a uniform current density does, as illustrated for α^* and *n* equal to 6 in Figure 5-9. However, in both cases the calculated $J_e(B_A)$ curve for Coil 2 is below the measured values for all magnetic fields < 19 T and the slope in the range of 10-19 T is about half of the measured values.

Increasing α^* to 8 to increase the sensitivity to the axial magnetic field component requires an increase in the conductor J_e(self) value in order to fit the calculations to the measurements at 19 T. The calculated coil $J_e(self)$ and the initial slope of the $J_e(B_A)$ curve do increase, but the effect of increasing α^* on coil $J_e(B_A)$ above 3 T is small.

Decreasing α^* decreases the sensitivity to axial magnetic fields and the calculated $J_e(B_A)$ curve flattens. This is shown in Figure 5-11 and the quantitative accuracy of the fit is listed in Table 5-3. Changing the *n*-value of the conductor from 6 to 8 to 10 has little effect; the largest change in the calculated coil J_e is 0.5 A. Therefore, choosing a different

magnetic field-independent value for α^* or the *n*-value within the range of observed short samples is not likely to result in a better match between measured and calculated values for coil $J_e(B_A)$. Also, the calculated value for conductor J_e(self) varies significantly from measured values. So, modeling solely based on short sample properties and geometry of the magnets, with either uniform J_e or $J_e(z)$ and a magnetic field independent α^* is not sufficiently accurate.

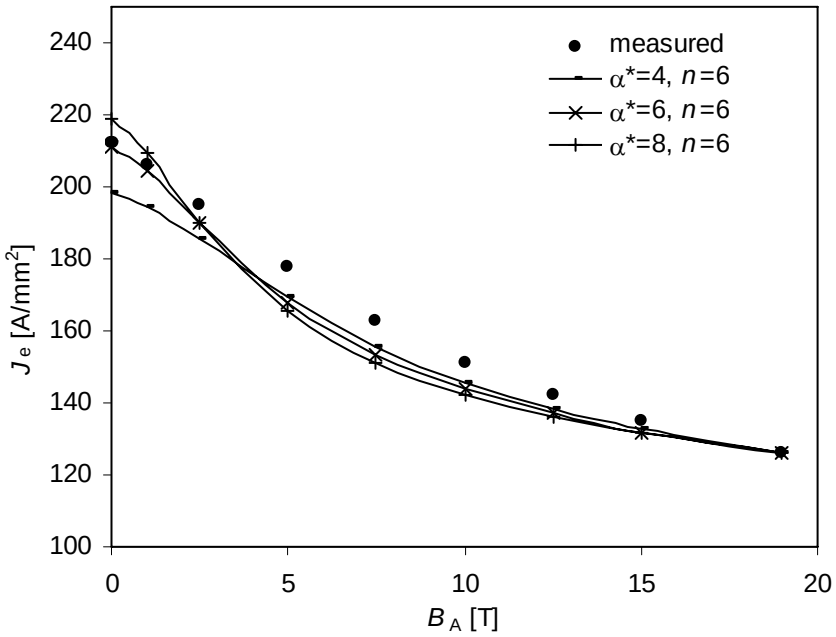

Figure 5-11. Measured and calculated $J_e(B_A)$ for Coil 2 using a magnetic field independent α^*, an n-value of 6 and axially variable current density.

5.4.2 Magnetic field dependent anisotropy parameter

Using a magnetic field dependent anisotropy parameter α^* as in equation 5-2 leads to a reasonable fit of the calculated $J_e(B_A)$ curve to the measurements as shown in Figure 5-12.

Variation of the *n*-value within the range of 6 to 10 has no significant effect. While not perfect, the obtained accuracy as listed in Table 5-3 (page 119) is sufficient. The error in the calculated coil $J_e(B_A)$ is actually slightly smaller than the accuracy of the conductor $J_e(B_\perp)$ relation the calculation is based on (see Table 3-1). Considering the accuracy obtained so far, it appears that there is little room for improvement with further refinement of the model in a mathematical sense. However, the calculated values for conductor J_e(self) are significantly below the measured values for short samples cut from the same conductor batch as the coil.[49]

5.4.3 Explicit model

An explicit empirical model for anisotropy based on measured short sample $j_e(B)$ for parallel ($j_{e,//}$) and perpendicular magnetic fields ($j_{e,\perp}$) is proposed in [111] and is found to adequately describe anisotropy of a Bi-2223 conductor at 77 K. Use of this model allows for a direct comparison with the grain misalignment model since it does not require the use of additional relations or parameters.

[49] Short sample J_e values are listed in section 5.4.4.

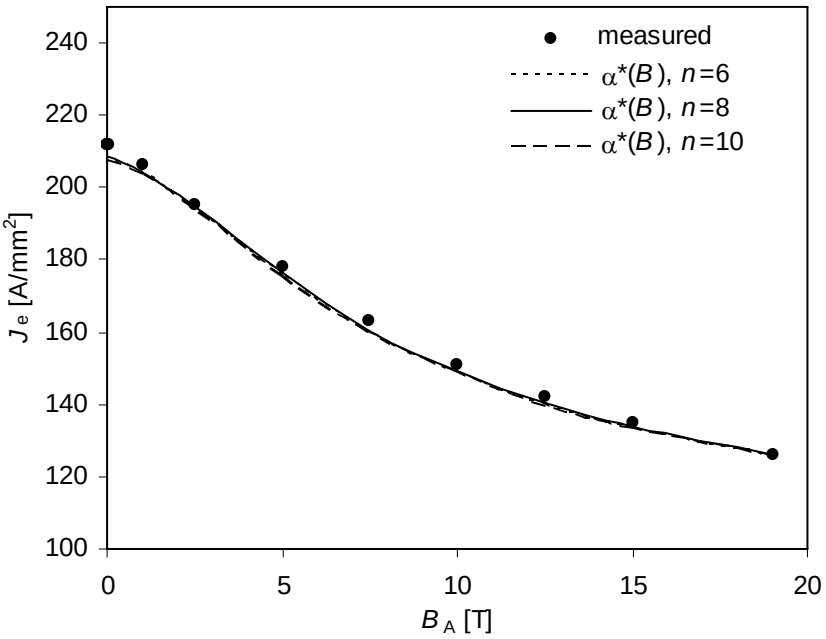

Figure 5-12. Measured and modeled engineering critical current density for Coil 2 using models with a magnetic field dependent anisotropy parameter α^*. The model results for n-values between 6 and 10 are nearly identical.

The normalized $J_e(B,\phi)$ relation is expressed as the product of the normalized current density relations for both orientations, with B_r substituted for $B_\perp$ and B_z substituted for $B_{//}$.

$$j_e(B,\phi) = j_{e,\perp}(B_r) \cdot J_{e,//}(B_z) . \qquad (5\text{-}3)$$

Thus $j_e(B)$ corresponds by definition to the measured short sample properties for $\phi = 0°$ and 90° and features a smooth transition for angles in between. The model as introduced in 5.3.1 and 5.3.2 is modified by replacing the calculation of $j_e(B)$ based on B_{total} and an angle dependent scaling function f via $B_{eff}^{\perp} = B_{total} \cdot f(\phi,\alpha^*)$ with the equation above. This results in an excellent fit to the measured data from 5 to 19 T applied magnetic field with axial grading of the current density and a fairly good fit, albeit slightly low, without axial grading of the current density, see Figure 5-13.

The conductor J_e(self) assumption required to match the model result at B_A = 19 T to the measurement is in line with measured batch short sample values. However, the calculated self-field J_e with axial grading exceeds the measurement by 17% and for the case without axial grading with 13%. Since the scenario with axially variable J shows a larger error at self-field than the uniform current density case, it is likely that refining the current distribution within the conductor by allowing different axial distributions at different radii would only increase the deviation at self-field. Therefore it appears that the explicit model of equation 5-3 is not suitable to accurately predict Coil 2 J_e, mostly because at self-field and low applied magnetic field, when the largest variations in magnetic field strength and angle occur, calculated values exceed the measurement by well over 10%.

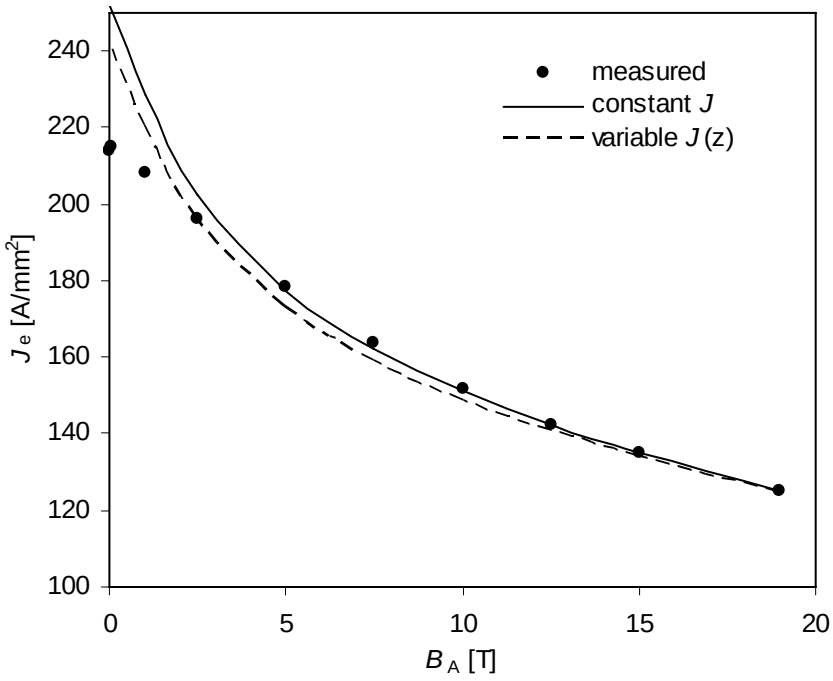

Figure 5-13. Measured and modeled engineering critical current density in double pancake coil 2 using an explicit equation (5-3) to model anisotropy.

5.4.4 Bi-2212 double pancake $J_e(B_A)$ modeling summary

Comparing the accuracy of the models to the measured properties of Coil 2, expressed as the maximum and average error in Table 5-3, it is clear that the best fits are obtained when the current is allowed to have axial variation and the grain misalignment parameter is taken to be magnetic field dependent as derived from short sample measurements.

Table 5-3. Models and parameters used to fit the measured $J_e(B_A)$ relation of Coil 2.

Anisotropy model	**Current density**	**Conductor J_e(self)**	**α^***	***n*-value**	**Maximum error**	**Average error**
		A/mm^2	°	-	-	-
Average grain misalignment	uniform	300	6	6	6%	4%
Average grain misalignment	$J_e(z)$	296	4	6	6%	4%
Average grain misalignment	$J_e(z)$	302	6	6	6%	3%
Average grain misalignment	$J_e(z)$	319	8	6	7%	4%
Average grain misalignment	$J_e(z)$	296	$4.06 + 0.071 \cdot B_{total}$	6	2%	1%
Average grain misalignment	$J_e(z)$	296	$4.06 + 0.071 \cdot B_{total}$	8	2%	1%
Average grain misalignment	$J_e(z)$	296	$4.06 + 0.071 \cdot B_{total}$	10	2%	1%
explicit $j_e(B,\phi)$	uniform	403		8	15%	4%
explicit $j_e(B,\phi)$	$J_e(z)$	368		8	19%	4%

In this case, α^* can be referred to as the anisotropy parameter but loses its meaning a simple geometric parameter. However, the correlation is poor between the measured

conductor J_e(self) [50] and the value used in the models that fit the coil data accurately. This correlation is further addressed in section 5.6.

5.5 Results of modeling $J_e(B_A)$ properties of a Bi-2223 double pancake coil

The measurements on a Bi-2223 coil, Coil 1, are modeled using α^* as the anisotropy parameter as outlined in chapter 3 and section 5.3. The $j_e(B_{eff})$ data are taken from sample A-1, assuming an average grain misalignment angle of 2.7°. Axial grading of the current density is applied to minimize the calculated coil voltage for a given transport current. Application of a magnetic field independent α^* value as suggested by the short sample measurements on conductor A and axial optimization of J_e immediately leads to a reasonable fit, see Table 5-4 and Figure 5-13.

Table 5-4. Models and parameters used to fit the measured $J_e(B_A)$ relation of Coil 1.

Anisotropy model	Current density	Conductor J_e(self)	α^*	*n*-value	Maximum error	Average error
		A/mm^2	°	-	-	-
Average grain misalignment	J_e(z)	433	2.7	20	4%	2%

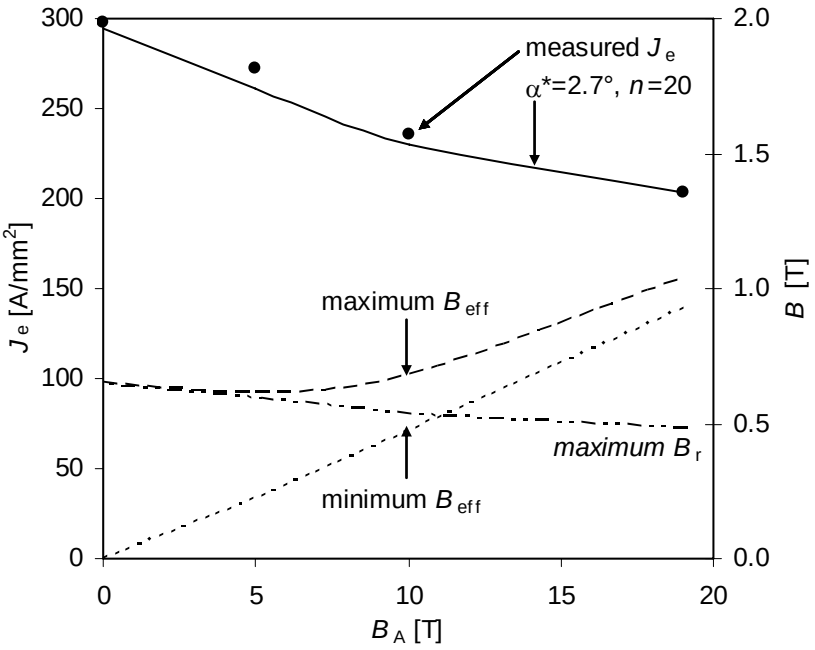

Figure 5-14. Measurement and calculation of J_e for Coil 1. The calculated maxima and minima for B_{eff} are quantified using the right vertical axis, as well as the maximum radial magnetic field component in the windings.

As for Coil 2, the calculation is slightly below the measured values in the range of 5 to 15 T. Unlike the case of the Bi-2212 coil investigated in section 5.4, however, the concept of anisotropy modeled on a magnetic field-independent average grain misalignment angle is tenable. An interesting observation can be made observing the range of B_{eff} in the coil at J_e, as shown in Figure 5-14. With the applied magnetic field increasing from zero to 10 T

[50] Six short samples taken from the same batch as the conductor for coil 2 have an average J_e of 405 A/mm^2 with a standard deviation of 7 A/mm^2.

the reduction in J_e is not caused by an increase in the *maximum* value of B_{eff} but is primarily associated with an increase in the *minimum* value of B_{eff}. This confirms that it is not J_e at the location of peak magnetic field that determines performance but voltages across the entire coil have to be considered.

The radial self-field component mostly determines the maximum effective magnetic field in the self-field condition. With increasing background field the maximum radial magnetic field component decreases as J_e decreases. The increase in maximum effective magnetic field and decrease in J_e is therefore attributed to axial magnetic field components. So the magnetic field dependence of J_e in insert coils can not be understood solely on the basis of radial magnetic field components.[51]

The value for conductor J_e(self) is significantly below measured short sample values of around 575 A. The origin for this discrepancy, comparable in magnitude to the case of Coil 2, is addressed in section 5.6.

5.6 Correlation between calculated and measured conductor self-field J_e

For both Coils 1 and 2, the calculated conductor J_e(self) values are well below the average short sample J_e from ends of the batch. The standard deviation is not very large, indicative of relatively homogeneous properties. This is reinforced for the Bi-2223 conductor by the company-supplied measured J_e values at 77 K covering the entire batch. Specific values are listed in Table 5-5.

Table 5-5. Measured and calculated conductor self-field J_e values for Coils 1 and 2.

Property	Unit	Coil 1	Coil 2
Calculated Conductor J_e(self)	A/mm^2	433	296
Measured Conductor J_e(self)			
Average over 6 short samples	A/mm^2	575	403
Standard deviation	A/mm^2	16	7
Measured Conductor J_e(self, 77K)			
Average over 6 sections of 10 m	A/mm^2	88.8	
Standard deviation	A/mm^2	0.8	

The lack of correspondence between measured and calculated properties is not satisfactory for predicting double pancake J_e from conductor data. Alternatively, available empirical data and scaling of the normalized conductor $J_e(B)$ are employed in this section to establishing that relation.

5.6.1 Calculated correlation between conductor and double pancake self-field J_e

A prediction of the correlation between conductor and double pancake self-field J_e can be made based on:

1. the assumption that normalized conductor $J_e(B)$ is independent of J_e(self), as suggested by the data in section 3.3, and
2. the maximum B_{eff} of 0.69 T in Coil 2 at J_e(self) = 219 A/mm^2. From the normalized $J_e(B_{eff})$ for a conductor follows j_e(0.69T) = 0.50, which determines the load line for Coil 2 and other coils of identical size.

The correlation follows from intersections between the load line and normalized $J_e(B_{eff})$ scaled to values other than unity, as shown in Figure 5-15. The scaling factor represents a relative change in conductor J_e(self) when comparing different batches to the one used for

[51] The interplay of anisotropy, axial and radial field components is extensively studied in Chapter 4.

Coil 2, the intersections correspond to coil j_e(self). The plot of the relative change in conductor J_e(self) versus the relative change in coil J_e(self), as in Figure 5-16, leads to the desired correlation. Coil J_e(self) increases less than linearly proportional with increasing conductor J_e(self). The correlation is weakly dependent on changes in the load line of up to 50% change in slope, so the correlation should apply to a significant range of coil sizes.

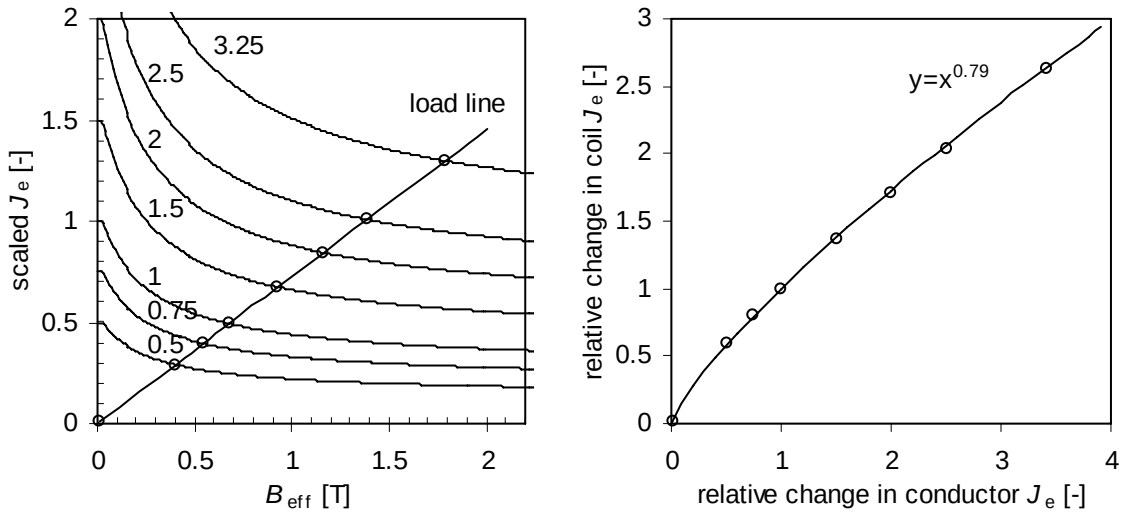

Figure 5-15. (left) Scaled conductor $J_e(B_{eff})$ and the load line for Coil 2. The scaling factors are listed in the graph.
Figure 5-16. (right) Calculated relation between conductor and double pancake J_e, for both A and B type double pancakes. Markers follow from Figure 5-15, the line is a fit curve.

Over the range of interest, spanning from conductor batches with properties close to the qualification criteria to the batch with the highest conductor J_e(self) encountered at 3.3 times the criterion, $y = x^{0.79}$ provides an excellent description of the relative change in coil J_e(self) with conductor J_e(self). A further quantification of the correlation follows from the measured values for conductor and coil J_e(self), 405 A/mm^2 and 219 A/ mm^2 respectively, yielding:

$$\text{coil } J_e(self) = 1.97 \cdot \text{conductor } J_e(self)^{0.79}. \qquad (5\text{-}4)$$

Considering the observed batch-to-batch variations[52] in $j_e(B)$ and inhomogeneity within a batch, some scatter around this trend line is expected when data from multiple coils are compared.

5.6.2 Measured correlation between conductor and double pancake self-field J_e

The correlation between conductor and double pancake coil J_e(self) is somewhat weak for the conductors used in the 5T insert. Generally, coil J_e falls within a certain band around the correlation predicted in the previous section. Some coil J_e's are isolated data points below the general trend. It is suspected that the conductor of those coils is damaged. This describes the observed correlation in general terms.

[52] See section 3.3

Data from candidate 33 double pancake coils for the A-section and 32 candidates for the B-section is used to illustrate the correlation. Each conductor batch is characterized by one or more of the following:

- End-to-end characterization at OST.
- Short sample characterization at OST. Typically ten samples are measured with an experimental system limit of 1000 A, equivalent to 1000 A/mm^2 for the conductor investigated here.
- Short sample characterization at the NHMFL. Typically six samples are measured with an experimental system limit of 650 A.

The results are shown in Figure 5-17 and Figure 5-18 for A and B-section candidate units respectively.

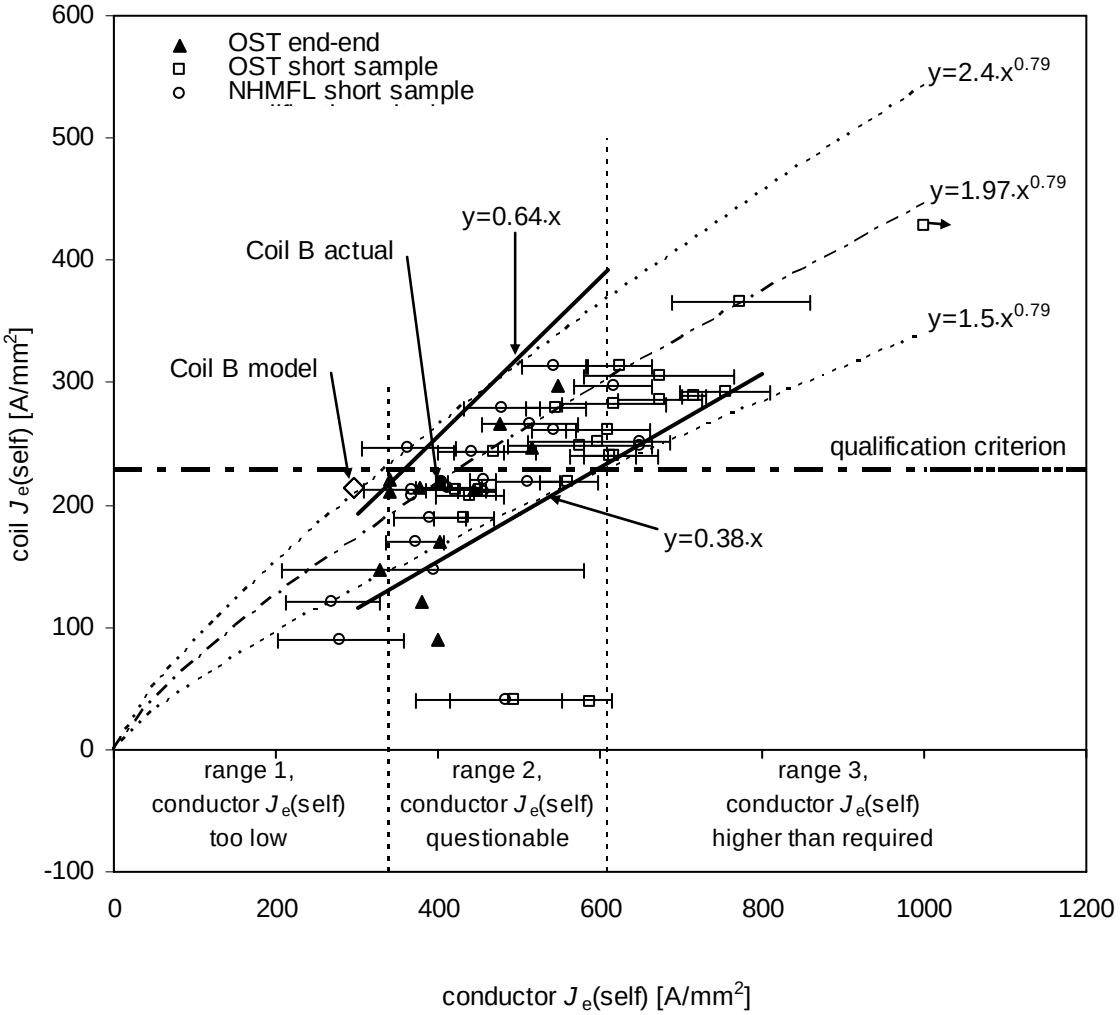

Figure 5-17. Relation between self-field J_e of short samples and A-section double pancake coils. The error bars indicate ± 1 standard deviation in J_e over 6 to 10 samples. The marker with an arrow pointing right indicates a conductor with an average short sample J_e above the experimental range of 1000 A. The triangles represent measured end-end J_e on the length of conductor used for one coil. The prediction of conductor J_e(self) from the modeling of Coil 2 is indicated with a dot-dash line. The correlation between coil J_e(self) and the lowest likely conductor J_e(self), as used to model $J_e(B_A)$ in the 5T insert, is indicated with a solid line.

For both groups coil J_e(self) is generally between 1.5 and 2.4·conductor $J_e^{0.785}$, bracketing the above derived prediction of 1.97·conductor $J_e^{0.785}$. The conductor J_e(self) is taken as the average of all available measurements for that batch. Combining this result with the qualification criteria of 229 and 235 A/mm^2 respectively[53], one finds the following three ranges for conductor J_e(self):

Range 1: batches with conductor J_e(self) below ~ 360 A/mm^2 lead to double pancake coils that do not meet the qualification criterion;

Range 2: batches with 360 A/mm^2 < conductor J_e(self) < 610 A/mm^2 may or may not lead to acceptable coils. This range encompasses the majority of the available conductor batches;

Range 3: batches with conductor J_e(self) ≥ 610 A lead to double pancake coils that exceed the qualification criterion.

The qualification criterion for B-stack coils is slightly higher than for A-stack coils, which reflects the somewhat different self-field distribution in the windings on account of geometric differences. However, the maximum B_{eff} in each section under operating conditions of the complete insert is comparable and it is therefore not surprising to find the same short sample current density values delimiting the ranges that may or may not lead to acceptable coils.

The practical consequence of the correlation as described above combined with the calculated qualification criteria and properties of the available batches is a need to test each double pancake coil at self-field to assess its suitability for use in the 5T insert. Nearly half the coils were rejected while over 90% of the batches have conductor properties that could have lead to acceptable coils. The conductor-coil J_e(self) correlation for this type of conductor is not strong enough to make conductor characterization, end-end or via short samples, a suitable tool to predict coil performance. In reverse, the somewhat weak correlation explains the discrepancy between the measured and calculated values of conductor J_e(self) resulting from the modeling of measured double pancake $J_e(B_A)$ as observed in section 5.4. Nonetheless, the model prediction of conductor J_e(self) based on coil J_e(self) is on the edge of the correlation and may be used as a prediction of the lowest conductor J_e(self) value that can lead to a double pancake coil with the J_e(self) value being modeled.

In the early stages of coil production for the 5T insert only a few of the data points shown in Figure 5-17 and Figure 5-18 were known. Based on those data points a simple linear relation between conductor J_e(self) and coil J_e(self) was derived. The intent was to find a criterion by which to reject conductor batches that had no chance of resulting in coils that meet the coil J_e(self) criterion, but accept any batch that might lead to an acceptable coil. The resulting conductor J_e(self) to coil J_e(self) relation is therefore opportunistic. A batch rejection criterion of conductor J_e (self) = 360 A/mm^2 followed from:

$$\text{coil } J_e(self) = 0.64 \cdot \text{ conductor } J_e(self) \tag{5-5}$$

for the A-section double pancakes and:

$$\text{coil } J_e(self) = 0.68 \cdot \text{ conductor } J_e(self) \tag{5-6}$$

for the B-section double pancakes. As more data points became available it became clear that a conservative estimate of coil J_e(self) is 38% of conductor J_e(self). In words: the coil self-field is expected to reduce J_e to 64% and 68% respectively at best, and to 38% of

[53] See section 5.7.

conductor J_e(self) at worst. These relations are indicated in Figure 5-17 and Figure 5-18 respectively. While these linear relations are adequate to bracket the data points for batches and coils that are close to their qualification criteria, it is expected that the less-than-proportional dependency following from the power value of 0.79 is the more fundamental one and applicable over a larger range.

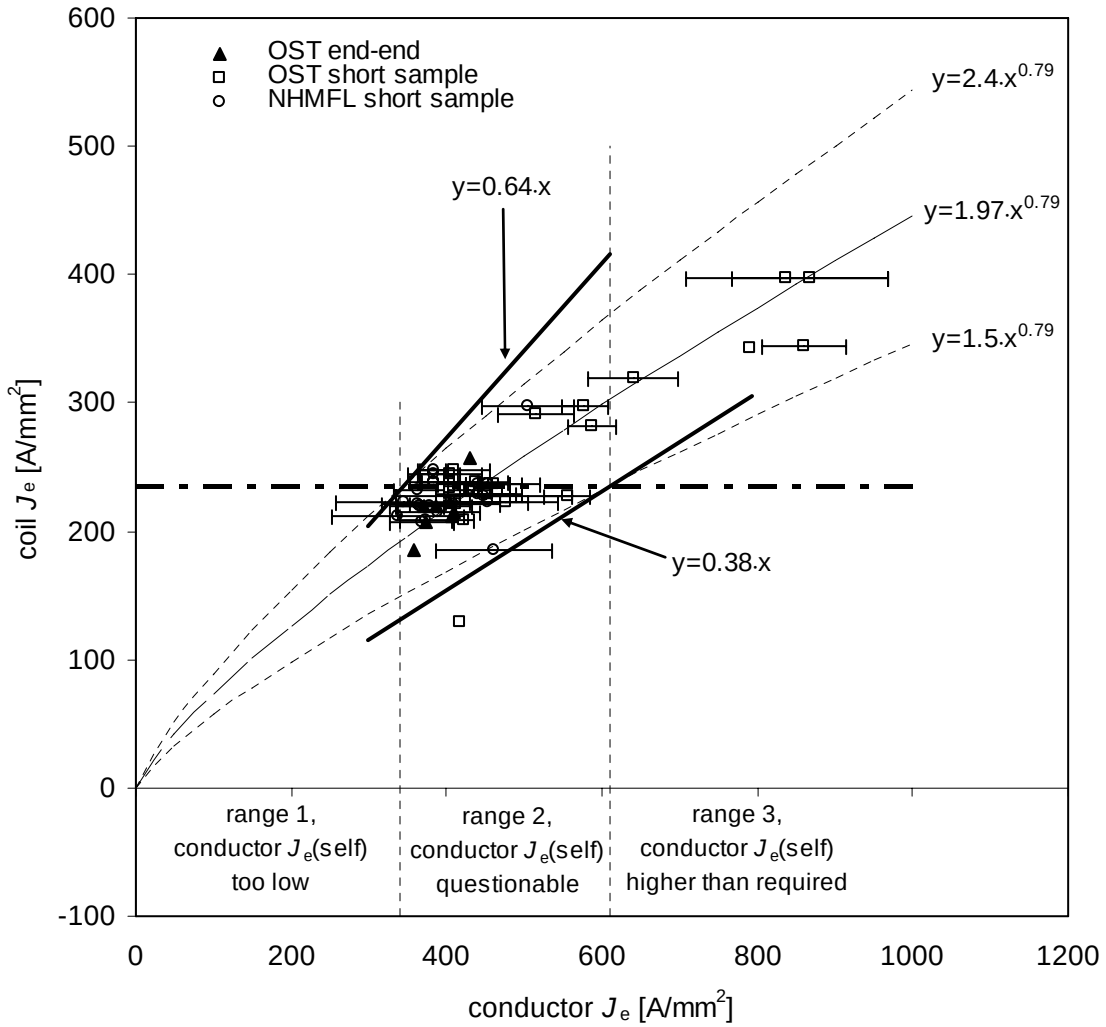

Figure 5-18. Relation between self-field J_e of short samples and B-stack double pancake units. Markers and lines have the same meaning as in Figure 5-17.

5.7 The 5T insert

5.7.1 Introduction

This section describes the process of developing qualification criteria for the double pancake coils in the 5T insert, how the calculated effective perpendicular magnetic field values guide the stacking sequence of the coils, followed by the prediction of insert $J_e(B_A)$ and comparison with experimental results.

5.7.2 Double pancake coil qualification criteria

The modeling of the applied magnetic field dependence of the engineering critical current density $J_e(B_A)$ of double pancake coils points out that the calculated value of J_e(self) is not a suitable criterion to determine the suitability of a given conductor for use in the insert.

As presented in the previous section, the conductor self-field J_e parameter values in the model do not correspond to measured J_e values on actual conductors. As an alternative, a criterion for coil J_e(self) is developed using measuring $J_e(B_A)$ properties of a number of coils. Extrapolating the results to the magnetic field conditions present in the insert at full magnetic field allows a determination of the minimum acceptable coil J_e(self). Two methods of extrapolation are described below, resulting in nearly identical criteria.

Criteria derived via $J_e(B_A)$ extrapolation

The first method is based on measured $J_e(B_A)$ properties of double pancake units and is independent of the anisotropy model. Normalized $J_e(B_A)$ curves for the Bi-2212 coils, as shown in Figure 5-2, fall on top of each other for 10 T < B_A < 19 T. It is reasonable to assume that this can be extrapolated to the magnetic field values present in the A-section (22.2 to 25 T in the midplane) and B-section (22.2 to 20.4 T in the midplane). A power law fit with an exponent of -0.3 typically fits well to conductor $J_e(B_{//})$ in this magnetic field range as well as to the coil data between 10 and 19 T, so this expression is used to extrapolate coil data. With j_e normalized at B_A = 19 T, one finds j_e(22.2T) = 0.954 and j_e(25T) = 0.921. Given a design current density of 126 A/mm^2, qualifying coils in the A- and B stack should carry ≥ 137 A/mm^2 and ≥ 132 A/mm^2 respectively at B_A = 19 T.

The next step is to correlate these in-field values with self-field values. Six coils intended for use in the 5T insert have been measured at both self-field and B_A = 19 T, with the results shown in Figure 5-19. The ratio between J_e(19 T) and J_e(self) is not constant, so interpolation or the indicated power law fit is more appropriate than scaling, *i.e.* a linear fit through the origin. The result of this interpolation exercise is summarized in Table 5-6.

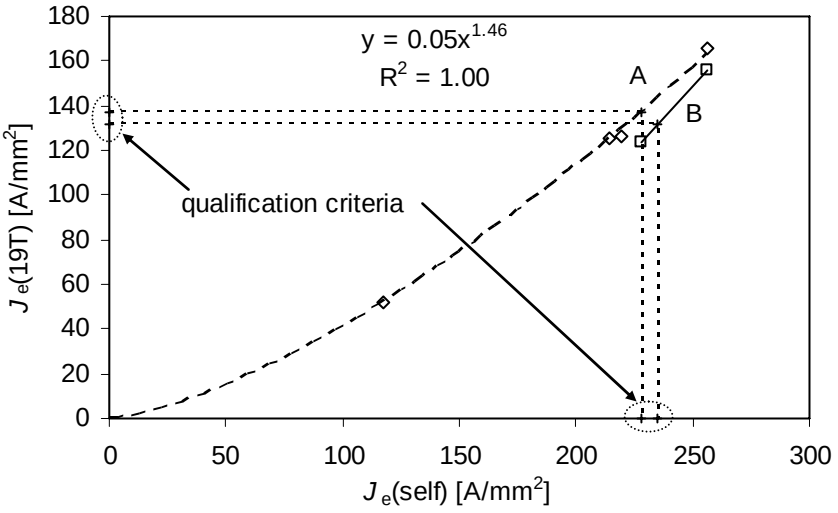

Figure 5-19. Relations between engineering critical current density in a background magnetic field of 19 T and at self-field for double pancake coils. The relation for A-type coils can be described with a power law as indicated.

Table 5-6. Qualification criteria for double pancake coils via extrapolation of $J_e(B_A)$.

Property	**unit**	**A-stack coils**	**B-stack coils**
Design B_{max}	T	25.0	22.3
$J_e(B_{max})$/ J_e(19T)	A/mm^2	0.921	0.954
J_e(19T) for design J_e in full insert	A/mm^2	137	132
J_e(self) for design J_e in full insert	A/mm^2	228	235

Criteria through load lines and $J_e(B_{eff})$ extrapolation

The second method to develop J_e(self) criteria for double pancake coils does take anisotropy explicitly into account by extrapolating measured J_e values versus B_{eff}, as opposed to B_A, within a coil. Plotting the measured J_e values of Coil 1 for $10\ T < B_A < 19\ T$ versus the calculated $B_{eff,\,max}$ values is the starting point. An extrapolation to the load line of the A-stack within the full insert yields a projected J_e value of 116 A/mm^2, 9% below the design value. Scaling[54] the fit through the measured $J_e(B_{eff,\,max})$ by multiplying with 1.09, so it runs through the design point for the full insert, gives the minimum acceptable J_e values for A-type coils. The intersection with the load line for $B_A = 19$ T identifies the qualification criterion for a coil in the background of 19 T, as shown in Figure 5-20. The self-field value is again derived through Figure 5-19. The criteria developed through $J_e(B_{eff})$ and $J_e(B_A)$ extrapolation are close for the A-stack coils (see Tables 5-6 and 5-7). Similar correspondence is expected for the B-stack.

Table 5-7. Qualification criteria for A-stack coils based on extrapolation of coil $J_e(B_{eff})$.

Property	**unit**	**A-section coils**
Design $B_{eff,max}$	T	2.52
$J_e(B_{eff,max})$/ $J_e(B_A$=19T)	A/mm^2	0.913
J_e(19T) for 126 A/mm^2 in full insert	A/mm^2	139
J_e(self) for 126 A/mm^2 in full insert (via Figure 5-19)	A/mm^2	229

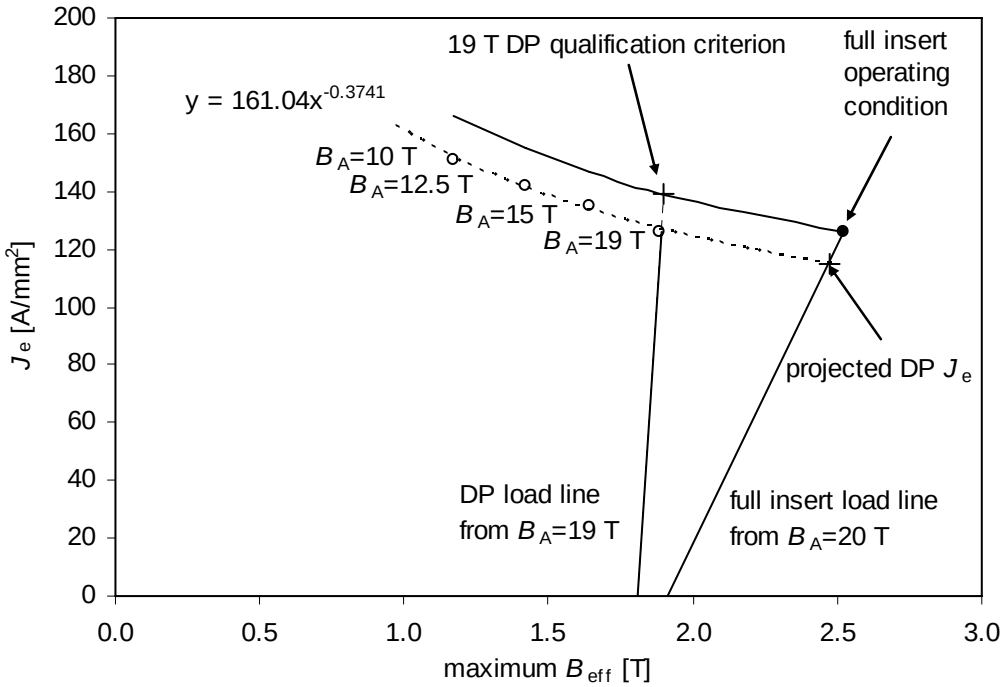

Figure 5-20. Extrapolation of measured $J_e(B_{eff})$ of Coil 1, load lines for this double pancake coil (DP) in a 19 T background and for the entire insert in a 20 T background. A fit through the measured values is indicated with a dashed line. This fit is scaled to run through the full insert design point.

[54] Figure 5-2 suggests that scaling of J_e is applicable for $10\ T < B_A < 19$ T, but not to self-field ($B_A = 0$ T). The latter is confirmed by the non-linearity of the curve for A-coils in Figure 5-19.

5.8 Predicting $J_e(B_A)$ of the 5T insert

5.8.1 Modeling $J_e(B_A)$ of the 5T insert

The model used to predict $J_e(B_A)$ of the 5T insert is an adaptation of the model that gave the most accurate description for $J_e(B_A)$ for Coil 2 to the geometry of the 5T insert. The cell size is increased to 3 mm radially and 11 mm axially. The latter corresponds to the total thickness of a double pancake coil in the stacks. Gradients in B_{eff} within a stacked coil are much smaller than in the stand-alone configuration so axial grading of J is omitted and the current density considered uniform. Conductor J_e(self) is a variable for each coil and calculated via the measured coil J_e(self) using equations 5-5 and 5-6, as the measured conductor J_e(self) is not an accurate indicator for coil properties. The anisotropy parameter α^* is calculated in every cell, and the average value of α^* over all cells is used to calculate B_{eff} in every cell. The model parameters are summarized in Table 5-8; Figure 5-21 presents a sketch of the insert cross section in which the middle of each cell indicated.

Table 5-8. Model parameters for the 5T insert.

Section	Current density	Conductor J_e(self)	Coil J_e(self)/ conductor J_e(self)	α^*	*n*-value
		[A/mm^2]	[-]	[°]	[-]
A	constant	374-667	0.642	$4.06 + 0.071 \cdot B_{total}$	8
B	constant	340-584	0.682	$4.06 + 0.071 \cdot B_{total}$	8
C	constant	387	0.682	$4.06 + 0.071 \cdot B_{total}$	8

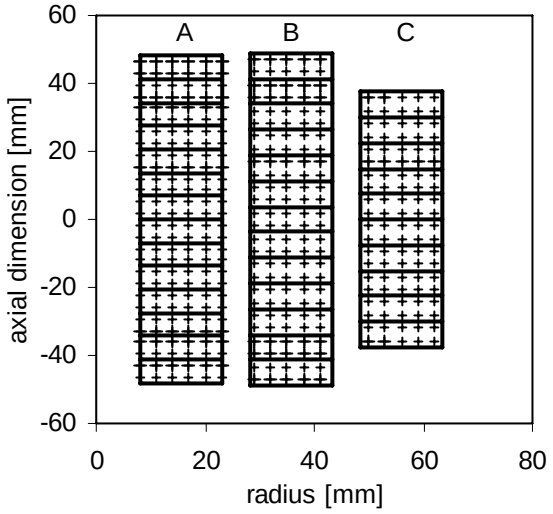

Figure 5-21. Schematic cross section of the 5T insert, with rectangles indicating double pancake coils in the A and B sections. The C section is layer wound. Grid points, for the calculation of electric field, at the center of each cell are indicated with + symbols.

A prediction of the applied magnetic field dependence of the engineering critical current density and effective magnetic field in the 5T insert resulting from the above model and the stacking order as introduced below are listed in Table 5-9 and Figure 5-22. As seen before in for example the Bi-2223 coil (section 5.5) and the 3T insert coil [42, 103], the decrease of J_e with the first 5 to 10 T applied magnetic field is primarily associated with an increase in the minimum B_{eff}. Interestingly, the maximum B_{eff} in the A-stack is slightly

reduced with increasing B_A as the decreased self-field contribution to B_{eff} more than compensates the increased contribution to B_{eff} of the background magnetic field. The maximum values always occur near the top and bottom surfaces of the stacks; the minima are mostly at the midplane with one exception. Only for the A-stack in high background magnetic fields is there a double minimum at the axial locations where the background magnetic field is significantly below its midplane value and sufficiently separated from the increased radial magnetic field components near the top and bottom of the stack. The B_{eff} for the central coils is mostly determined by the axial magnetic field components, while the radial magnetic field contributions to B_{eff} become dominant for the outermost coils, as illustrated in Figure 5-23[55].

Measured data for the 5T insert do not allow a verification of these predictions. In the 3T insert, however, the very same patterns are found [46] and use of the average grain misalignment model for anisotropy with measured conductor $J_e(B)$ leads to accurate modeling of the measured properties for each of the three sections. A full discussion is too lengthy for inclusion here. However, the 3T analysis does support the 5T insert predictions.

Table 5-9. Predicted properties of the 5T insert

B_A	J_e	*n*-value	α^*
[T]	[A/mm^2]	[-]	[°]
0	207		4.3
1	204		4.3
5	186		4.6
10	165		4.9
19	142	6	5.5

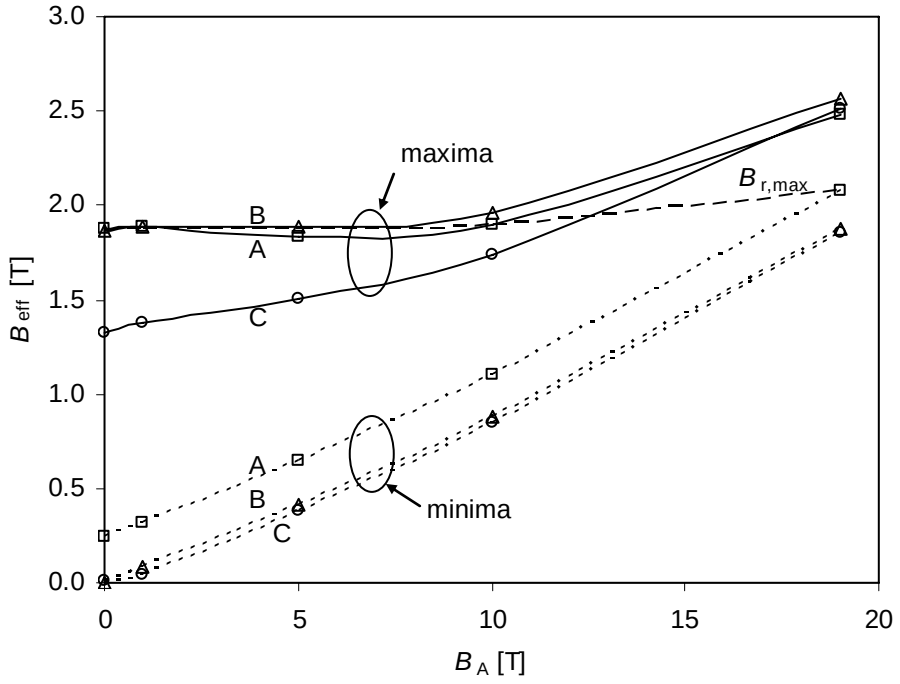

Figure 5-22. Prediction of the maximum (markers connected by solid lines) and minimum values of the effective perpendicular magnetic field in the 5T insert at the critical current density.

[55] Relations between anisotropy and patterns in B_{eff} are explored in more detail in Chapter 4.

5.8.2 Stacking

Stacking is the selection and co-axial assembly of double pancake coils into a stack. An optimal configuration is reached when the magnetic field increment generated at the center of the insert in the full background magnetic field is maximized given the properties of the available coils. The starting selection involves all coils that meet or exceed the qualification criterion. Coils with the highest J_e(self) are placed at locations with the highest B_{eff} and the remaining coils in descending order matched with locations of descending B_{eff}. A calculation of J_e in the full background magnetic field for that configuration is calculated and serves as a point of reference. The outcome of further optimization depends on the properties of coils around the qualification criterion. To fully optimize the stacking order, insert J_e is also calculated when one or more of the least performing coils are removed or alternatively one or more of the next-best coils are added to each stack. Adding the next-best coil lowers J_e for the stack involved but increases its magnetic field constant and also changes B_{eff} in the entire insert, so the overall effect is typically not intuitively predictable. However, the optimum is relatively broad for the 5T insert, given the number of coils available with J_e(self) around the criterion and the gradual increase in radial magnetic field component from the background magnet with increasing distance from the midplane. Omitting a detailed description of the near-optimum stacking orders, the chosen order is given in Figure 5-23.

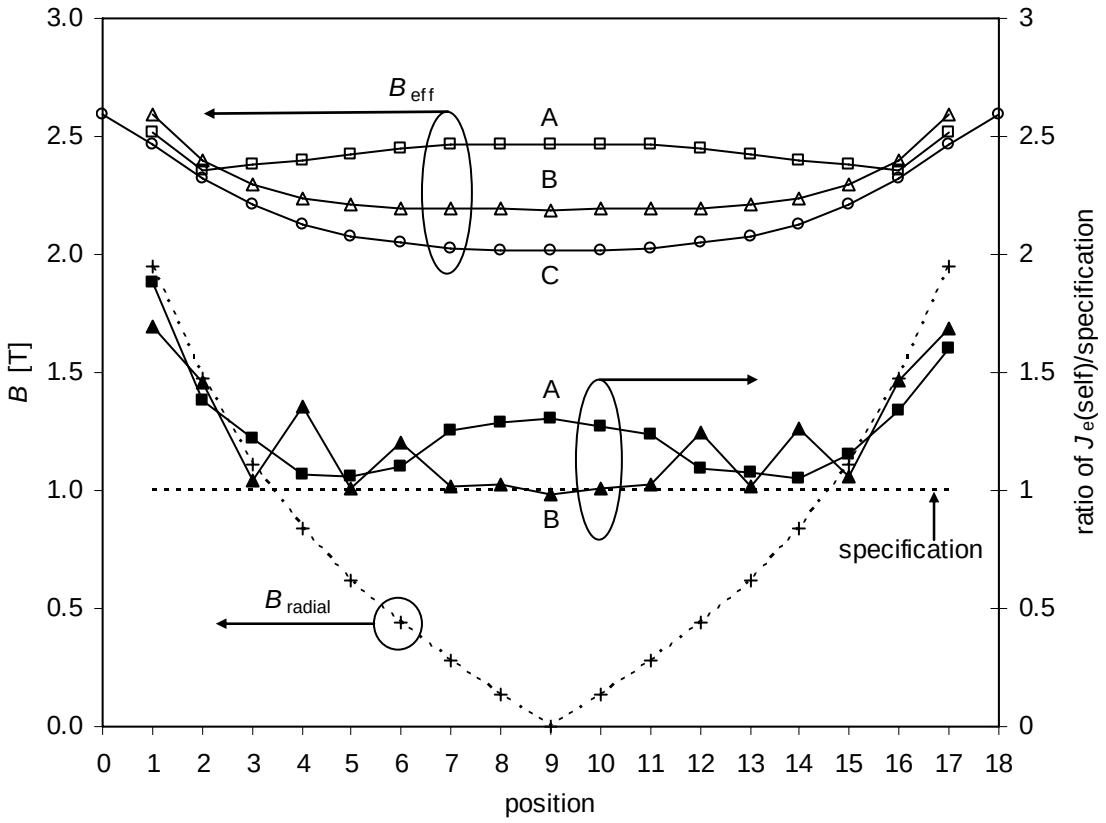

Figure 5-23. The solid markers represent the stand alone self-field J_e of the double pancake coils in sequence as stacked in the 5T insert, normalized to the qualification criteria of 228 and 235 A/mm^2 for the A- and B-section units respectively. The top set of curves represent the maximum effective perpendicular magnetic field with the insert generating 5 T in the background of 20 T from the Large Bore Resistive Magnet, the dashed curve represents the maximum radial magnetic field for each coil in the A-stack.

5.8.3 The 5T insert in self-field

During testing the insert quenched before the steady-state voltage across the terminals reached the 1 μV/cm criterion. Quenches occur below the predicted J_e and develop slowly, taking 10 to 100 seconds. As the time between data points ranges from 19 to 34 seconds when the current is changed stepwise, some data points are taken during the thermal runaway. An example can be seen in the E-J_{op} data at 176 A/mm^2 for the first run at self-field as shown in Figure 5-24. A quench occurs at 85% of the predicted J_e(self) and originates in the A-stack. A power law with an n-value of 7 describes the data[56] and extrapolates to 208 A/mm^2 at the 1 μV/cm criterion. The margin of error in the extrapolation (in the order of 5%) exceeds the difference between measurement and model prediction (1 A/mm^2 or 0.5%), so the prediction was accurate to within 5% and possibly better. Three subsequent measurements, with smaller current steps when approaching the quench current, show reductions in the quench current density to 166, 162, 157 A/mm^2 respectively. This irreversible reduction is believed to be caused mostly by a short damaged section of the conductor in one of the units of the A-section that degrades further as a result of the quenches. This degradation is subject of continued investigations and will not be addressed further in this work. Thermal runaway and irreversible reduction of J_e limits the comparison between the predictions and experimental results. However, the self-field J_e prediction based on both conductor and double pancake coil data, appears accurate for the 5T insert.

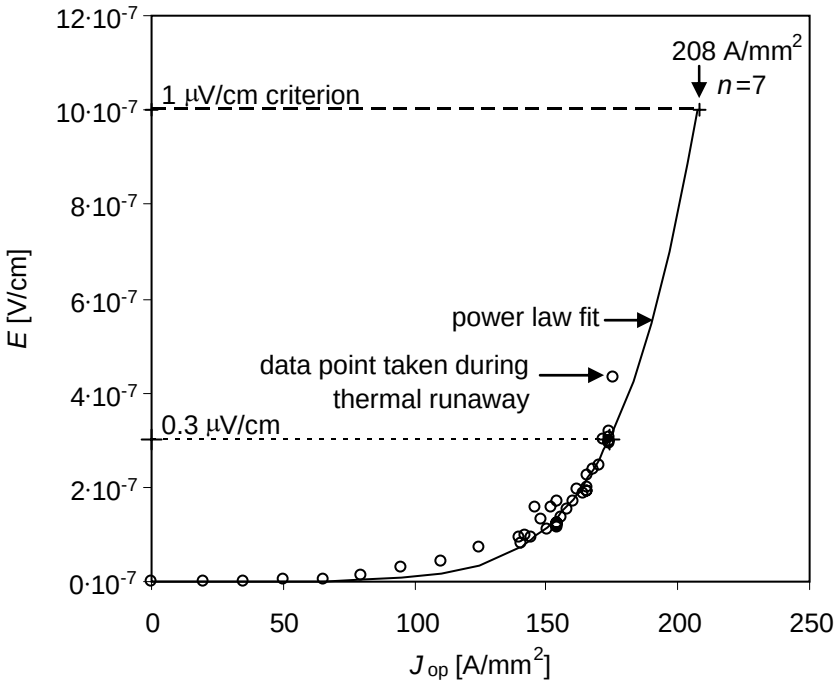

Figure 5-24. Electric field-current density data of the 5T insert measured during the first test at self-field. The operating current is increased stepwise. The curved line is a power law fit to the measurements with an n-value of 7 which extrapolates to 208 A/mm^2 at the 1 μV/cm criterion. The last data point at 176 A/mm^2 was measured in the early phase of thermal runaway.

[56] Inductive voltages resulting from large current steps compared to the dwell time are present in some data points, mostly between 60 and 140 A/mm^2, causing the measured voltage to exceed is DC-value as well as the power law fit.

5.8.4 The 5T insert in background magnetic field

In-field data obtained on the 5T insert fall into two categories. First, the insert current is increased stepwise and voltages measured 10 to 25 seconds later to allow induced voltages to settle. As for the self-field measurement, the insert quenches before reaching 0.1 V *i.e.* an average electric field of less than 0.5 μV/cm which is less than half of the critical electrical field. The quench current density is reduced to ~77% of the predicted $J_e(B_A)$ after the three initial quenches at self-field. The insert current is returned to zero and the applied magnetic field in increased after each in-field quench. The maximum background magnetic field is 19.95 T, 0.95 T above the maximum value assumed in the initial design.

Second, the insert current is ramped with 3.7 A/s. Starting with the maximum background magnetic field of 19.95 T, the background magnetic field is reduced after each E-J_{op} measurement. Higher quench currents result at around 82% of the predicted critical current density. An overview of the results is given in Table 5-10 and Figure 5-25. The measured magnetic field increment of 5.11 T in the background of 19.95 T represents the first time 25 T was generated using a superconducting insert and represents a milestone in the development of 25 T superconducting magnet technology.

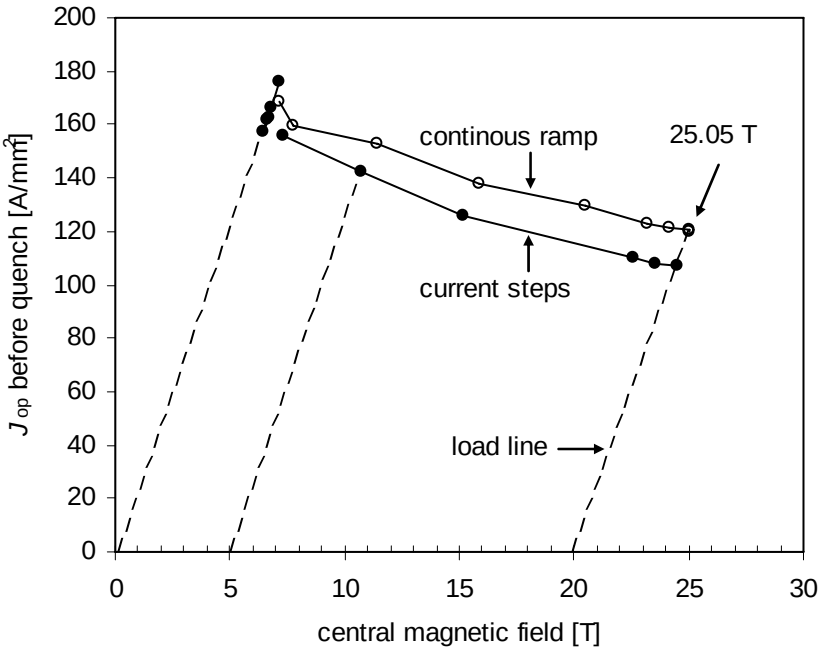

Figure 5-25. Properties of the 5T insert at self-field and in background magnetic field up to 20 T.

A direct comparison between the predicted critical current density, derived using the 1 μV/cm criterion, and the measured data is not possible due to thermal runaway as described above. The error margins on the extrapolated in-field E-J_{op} data are at least as large as for the self-field case making the extrapolations marginally useful at best. However, assuming that the section of the insert that is limiting its performance has the same normalized magnetic field dependence as the insert as a whole does lead to a meaningful comparison. As the quench data obtained by changing the insert current in a step-like manner has the higher resolution in J_{op}, as shown in Figure 5-25, it is selected.

Table 5-10. Predicted and measured properties of the 5T insert.

B_A [T]	Predicted J_e [A/mm^2]	Quench* J_e [A/mm^2] Current steps	Quench J_e [A/mm^2] At 3.7 A/s	Magnetic field increment at highest quench current [T]	Central Magnetic field [T]
0	207	>176-157	169	7.15	7.15
1	204	>156	159	6.76	7.76
5	186	>142	152	6.47	11.47
10	165	>126	138	5.85	15.85
15				5.50	20.50
18		>110	123	5.22	23.22
19	142	>108	121	5.13	24.13
19.95		107.4	120	5.11	25.05

*: The listed value is the highest measured J_e before the quench, the quench current is 0.5-1 A/mm^2 higher.

The calculated normalized magnetic field dependence is identical to the measured quench values within the margin of error; both sets of data are depicted in Figure 5-26. The average deviation is 0.3% with a maximum deviation of 0.8% between normalized quench current and normalized predicted J_e. So the quench current in stepped-current mode scales accurately with the predicted J_e, suggesting that the prediction method used is adequate.

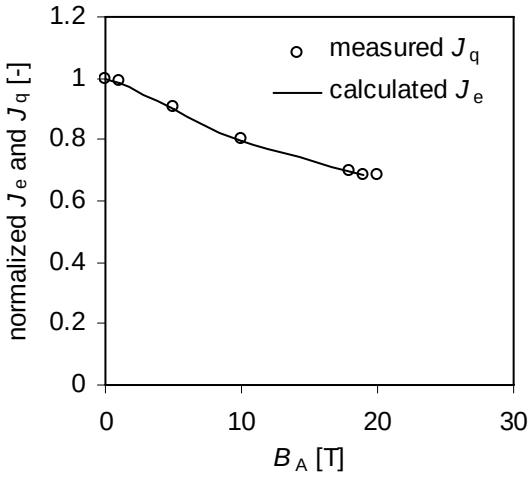

Figure 5-26. Calculated J_e and measured J_q for the 5T insert magnet, each normalized to its self-field value.

5.9 Conclusion

The accurate prediction of the magnetic field dependence of the engineering critical current density in HTS inserts based on conductor properties involves several intermediate steps, including the correlation between the engineering critical current density in the conductor and sub-size coils, the magnetic field dependence of the engineering critical current density in sub-size coils, and the modeling of the magnetic field dependence of the engineering critical current density of the complete insert based on measured properties of the conductor and the sub-size units. A Bi-2212 and Bi-2223 double pancake coil serve in the role of sub-sized coil here, and the magnetic field dependence of the transport critical current density in the 5T insert, consisting mostly of Bi-2212 double pancake units, is predicted and verified experimentally. A comparable line of research for ReBCO conductors is desirable.

For a Bi-2212 double pancake coil at self-field, the correlation between conductor and coil J_e is calculated as coil $J_e(self) = 1.97 \cdot \text{conductor } J_e(self)^{0.79}$, based on scaling of the normalized conductor $J_e(B)$ and a load line. This does describe the average correlation for 64 double pancake coils produced for the 5T insert but there is significant scatter around this average. Conductor J_e(self) did usually not give a useful prediction of coil J_e within the context of the 5T insert project as the qualification criterion was within the scatter range of likely coil J_e(self) for most batches, so nearly every double pancake had to undergo qualification testing, resulting in a near 50% rejection rate.

Double pancake coil $J_e(B_A)$ can be modeled based on conductor properties once a single point of the curve is known. Allowing an axial variation of the current density improved the modeling at self-field and low applied magnetic fields. Modeling of $J_e(B_A)$ for a Bi-2212 double pancake points out that an explicit model for anisotropy in conductor $J_e(B)$ and the average grain misalignment model with a magnetic field independent anisotropy parameter α^* are less accurate than the average grain misalignment model with a magnetic field dependent α^*, which resulted in an average error < 1%. A magnetic field dependent α^* is consistent with Bi-2212 conductor data but not the concept of α^* as a purely geometric parameter. Modeling of measured $J_e(B_A)$ for a Bi-2223 double pancake coil using a magnetic field independent average grain misalignment angle to incorporate anisotropy, as suggested by conductor characterization, does lead to a satisfactory calculation of $J_e(B_A)$. However, the calculated conductor J_e(self) is well below the measured value in both cases.

Double pancake coil J_e(self) qualification criteria for use in insert coils can be determined from extrapolation of measured $J_e(B_A)$ data or extrapolation of $J_e(B_{eff})$. The resulting criteria for A-type coils for the 5T insert are practically the same.

Prediction of $J_e(B_A)$ of a Bi-2212 insert coil consisting mostly of double pancake coil stacks is based on normalized conductor $J_e(B)$ data supplemented with measured J_e(self) of each coil. The conductor J_e(self) values are calculated based on the observed conductor to coil J_e(self) correlation using the lowest conductor J_e(self) value likely to result in the measured coil J_e(self). The anisotropy parameter is again taken as magnetic field dependent.

A Bi-2212 insert consisting mostly of 34 double pancakes in two concentric stacks is constructed and tested in a resistive background magnet. Thermal runaway occurs at self-field and in a background magnetic field well below the predicted engineering critical current density. The extrapolated *V-J* data does extrapolate to the predicted value. The normalized quench current density and predicted engineering critical current density coincide, suggesting that the prediction method used is adequate. This insert generated 5 T in a magnetic background field of 20 T, and thus for the first time (August 2003) a magnetic field of 25 T is reached in a superconducting magnet.

6 Stress and strain dependence of the engineering critical current density in insert coils for 25 T central magnetic field and beyond

The strain tolerance of HTS conductors is severely limited and the engineering critical current density is irreversibly reduced when the critical strain is exceeded. The design process of HTS inserts thus requires profound understanding of the strain dependence of the engineering current density in the conductor and the ability to predict the strain state of the conductor in a coil. This chapter covers three aspects of the stress-strain properties of HTS superconductors and the relation with the engineering critical current density.

1) Behavior of conductors under linear stress and strain at room and cryogenic temperatures. Measurement of the critical current density after the conductor is subjected to a specific load reveals the relation between critical current density and stress-strain properties under uni-axial loads.

2) Bending of the conductor. This room-temperature process is neither purely elastic nor purely plastic. It is studied using a wind-and-release method leading to an equation that describes the maximum bending strain in the filaments of BSCCO conductors and the thin superconducting layer of ReBCO conductors. The critical bending diameter is determined for conductors used in coils operated in applied magnetic field and thus subjected to large stress and strain values.

3) Properties of React-and–Wind coils in applied magnetic field up to 20 T. Both bending strain induced during coil winding and additional Lorentz-force induced strain during operation are significant. By cycling the operating current between zero and increasingly higher peak values, the relation between the critical current density and the peak current density is established. Bending strain and Lorentz-force induced strain are calculated at these peak current density values to assess the predictability of coil performance based on conductor properties and the models used to calculate strain.

Testing of trial coils is used to determine if the 5T insert as designed can tolerate the design conditions. The 5T inert as built is operated in applied magnetic field of up to 20 T, leading to high stress levels and a record central magnetic field value of 25 T. A comparison is made with the stress levels and central magnetic field values in the first ReBCO inserts. Finally, an outlook is given for 30 T magnets with HTS inserts.

6.1 Introduction

Any conductor in high-field coils is subject to strain of a magnitude that can cause large and irreversible J_e degradation through cracking of the ceramic filaments once a certain critical strain level is exceeded. This strain originates primarily in the Lorentz-force during operation at cryogenic temperatures and conductor bending during construction at room temperature. Differences in thermal expansion coefficients between the turns and adjacent material can cause strain in the conductor during and after cool down, but this is generally not applicable to the coils considered here.

The Lorentz-force results in a locally generated hoop stress in the conductor equal to the product of operating current density, the axial magnetic field B_z and the radius r, as expressed in equation 6-1, and is perpendicular to both current and magnetic field.

$$\sigma_L = J_{op}.B_z.r \quad (6\text{-}1)$$

Axial and radial forces also exist in any coil and the mechanical coupling between turns changes the stress state of each conductor, effectively resulting in a redistribution of the locally applied hoop stress to a radius-dependent stress state that significantly deviates from equation 6-1. The strain state of the conductor is primarily determined by the stress-strain properties of the composite conductor, insulation and reinforcement materials.

The second main source of strain in windings results from bending the conductor during the winding process. The bending strain is in first order approximation proportional to the inverse of the bending radius: $1/r_{bend}$. When the conductor is reacted before winding (React&Wind technology), the bending strain is maintained during cool down of the magnet and operation. When the conductor is wound before reaction (Wind&React) all strain is released during the heat treatment, and cracks in the ceramic are healed during the partial melt phase. Therefore, bending strain is typically insignificant in Wind&React coils in normal operation. Wind&React processing is feasible for Bi-2212 conductor. However, React&Wind is used for Bi-2212 conductor in some applications [45, 46] and in all cases for Bi-2223 and ReBCO conductor. Understanding of the dependence of the engineering critical current density on bending strain is therefore essential for the application in coils of both BSCCO and ReBCO conductors.

Bending and Lorentz-force induced strain occur simultaneously in React&Wind coils, which makes tests of the conductor under these conditions relevant for magnet technology development. Understanding their combined effect is essential to predict the onset and progression of strain induced degradation in coils. Here we assume that those strains are cumulative [112].

The intent of the investigations described in this chapter is to determine the effect of uni-axial load and bending, separately and combined, on the strain state of the ceramic filaments and the engineering critical current density of HTS conductors. Using the conductors A through I as listed in Table 2-1 in experimental insert coils, the stress and strain effects on coil J_e will be discussed and compared with calculations. When applicable, the results are also compared to the 5T insert design requirements to reach 25 T central magnetic field. Lastly, the relationship between design strain limit and required conductor current density is investigated for a hypothetical coil of a magnet targeted at 30 T central magnetic field.

6.2 Uni-axially strained conductors

The starting assumption is that the uni-axial properties of single bare samples are representative of the behavior of the conductor in the windings under Lorentz-force. The properties of interest considering uni-axial loads are the tensile stress-strain curve and the current density-strain relation, for loads applied while the conductor is at 4.2 K. Data taken at 77 K is substituted when measurements at 4.2 K are not practical.

6.2.1 Tensile stress-strain curves

The mechanical properties of the conductors vary significantly, as shown in Figure 6-1. These should be considered relative to the estimated range of maximum Lorentz-force induced stress in the HTS windings of 25 T class magnets of 77-215 MPa[57]. Conductor I with a pure Ag matrix has the lowest strength. This conductor is susceptible to necking: a bundle of 3 conductors impregnated together is significantly stronger with a higher yield

[57] For J_{ave} = 100 A/mm^2 and typical radii. See section 1.3 for a broader discussion.

strain than a single bare conductor [113]. Regardless, it is clear that conductor I can not be applied unless it is heavily reinforced. Conductors with a dispersion hardened matrix are significantly stronger than conductors with a pure Ag matrix. The stress-strain properties of the round wire conductor are comparable to the tapes of this type. They are also likely to require reinforcement, considering that additional loads from bending or other sources may be present and a safety margin between the design load and failure of the conductor is desirable. The externally reinforced conductor A shows a strength well exceeding the expected requirements for Lorentz-force induced loads. Without this reinforcement, the strength of conductor A would be comparable to conductor I. Conductor A can be applied without additional reinforcement unless unusually large bending or hoop strain is present. Conductor G, a ReBCO conductor, has a strength that exceeds by far the estimated maximum stress in the windings of 25 T class magnets operating at ~100 A/mm^2, making its stress-strain characteristics suitable for applications at higher current density and magnetic field.

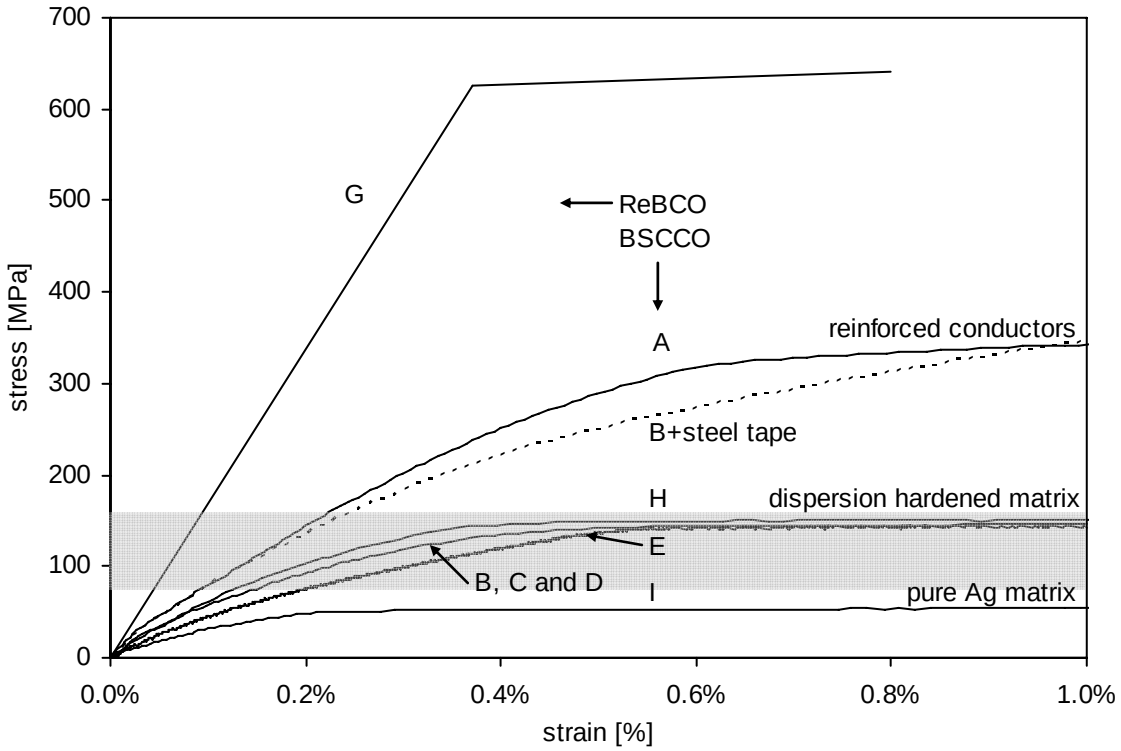

Figure 6-1. Measured tensile stress-strain curves at 77 K. Curves for the BSCCO conductors (A through E, H and I) are measured using the device introduced in section 2.3.2. Data on the ReBCO conductor G originates at NIST and is provided by the manufacturer. The estimated range of maximum hoop stress in 25 T inserts for research magnets is indicated in grey (see section 1.3.2).The range extends to 215 MPa in case of HTS inserts for NMR magnets.

6.2.2 Details of the tensile stress-strain curve

BSCCO conductors

The traditional (ASTM) description of measured σ–ε curves is centered on the initial slope, the 0.2% offset strain (offset from the initial slope), Young's modulus, and the ultimate tensile strength (*UTS*). This formalism does not work well for materials in which the initial slope is poorly defined as in composites like Nb_3Sn and BSCCO where the heat

treatment to form the superconductor leaves the matrix relatively soft and plastic [114]. For example, to develop an international standard for the description of the σ–ε curve of Nb_3Sn superconductors, a power law relation is now proposed, while a standard specific to BSCCO conductors is under development [114]. Graphs of the first derivative of the σ–ε curve of conductors A through E suggest a linear decrease of the slope with increasing strain until close to the onset of nearly complete plasticity at ε_p[58]. In the plastic regime the slope E_p is small compared to the initial slope E_i and the σ–ε curve linear. Therefore a two-regime description of the σ–ε curve is proposed as in equations 6-2 and 6-3 and is illustrated in Figure 6-2:

$$\sigma = \sigma_p = UTS_{intercept} + \varepsilon \cdot E_p \text{ for } \varepsilon > \varepsilon_p. \quad (6\text{-}2)$$

The intercept is not equal to the usual meaning of *UTS* (σ_p at ε_p) but can serve as an unambiguous reference, as ε_p can not always be precisely determined. For the elastic regime:

$$\sigma = p \cdot \varepsilon^2 + E_i \cdot \varepsilon + \sigma_{offset} \text{ for } \sigma < 0.95 \cdot \sigma_{p,} \quad (6\text{-}3)$$

in which the parameter *p* is a measure for the degree of plasticity.

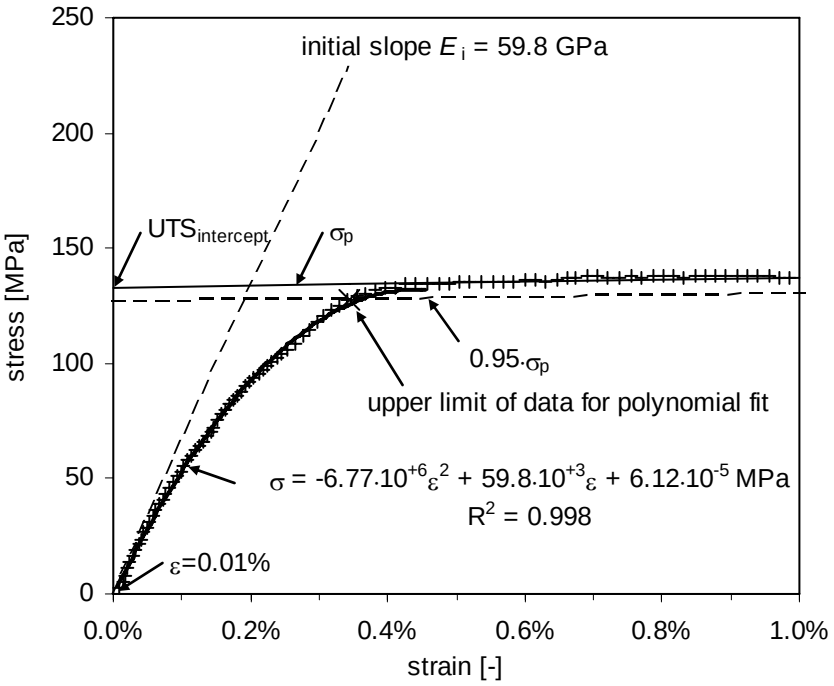

Figure 6-2. Measured stress-strain data (+) for conductor H sample 2 and a description (solid lines) based on a linear fit to the plastic regime and a second order polynomial fit to the data up to 95% of the plastic regime fit.

A description of the stress-strain curves shown in Figure 6-1 using the formalism introduced in equations 6-2 and 6-3 is given in Table 6-1. The polynomial fit is found to describe the σ-ε curve to 95% of the plastic regime extrapolation for conductor B, and for all other conductors to at least 98%. This covers the range of interest for magnet design, as the transition to the plastic regime coincides with widespread cracking of the ceramic filaments and a major reduction of the engineering critical current density. Coils are

[58] ε_p is introduced in Figure 2-20.

normally designed with a safety margin and are operated at a maximum design strain that is in the order of 70% of the critical strain or lower.

Table 6-1. Mechanical properties of conductors A-G at 77 K.

	unit	A samples 1 and 2	B	C	E samples 1 and 2	I	H samples 1 and 2
ε at 10% degradation	%	0.45*	0.40-0.45	0.40-0.45	-	-	0.38
Matrix		Ag	AgMg	AgMg	AgMg	Ag	AgMg
Reinforcement		stainless steel	-	-	-	-	-
E_i	GPa	77, 65	56	58	48, 55**	33	66, 60
p	10^3·GPa	-4.0, -2.5	-5.3	-6.3	-5.3,-9.7**	-5.3	-7.8, -6.8
$\sigma(\sigma=0.95\cdot\sigma_p)$	MPa	305±1	147	133	133±2	46	138, 128
$\varepsilon(\sigma=0.95\cdot\sigma_p)$	%	0.57, 0.63	0.45	0.42	0.49±0.01	0.20	0.35
Average error for $\varepsilon\geq0.00\%$, $\sigma<0.95\cdot\sigma_p$	%	0.7, 0.5	0.8	1.7	1.0,0.7**	0.7	2.0, 2.4
Average error for $\varepsilon\geq0.01\%$, $\sigma<0.95\cdot\sigma_p$	%	0.4, 0.4	0.7	1.6	0.8, 0.5**	0.7	0.6, 0.9
$UTS_{intercept}$	MPa	303	146	133	138±2	46	144, 133
E_p	GPa	3.0	0.5	0.5	0.4	0.4	0.4

* company specification, ** second order polynomial fit to 0.15% only.

As commonly observed, sample-to-sample variations in the stress-strain curves occur in which the individual curves deviate more than the noise level in the data and the error margin in the curve fit. However, the general trend in the stress-strain curve for each sample within a batch is similar and some fit parameters vary little or none from sample to sample. The variation in stress values for any given strain value is well below 10% of the *UTS* stress value. Fit parameters for two samples from conductors A, E and H are listed in Table 6-1. Therefore two numbers are listed sequentially for each parameter, unless the difference is small or negligible. In those cases, a narrow range or a single number is listed.

The average difference between measured and calculated stress values as a percentage of the *UTS* intercept value ranges from 0.5 to 2% for all conductors. The highest deviations are found for conductor H and predominantly near the origin (0-0.01% strain), which points to possible experimental problems. This is illustrated in Figure 6-2. This curve fit is adequate for magnet design purposes, as the fit error is smaller than the typical sample-sample variation. The curve for the Bi-2212 wire (E) can be fit with a second order polynomial with an average error of 2%. However, to arrive at an accurate fit to the initial slope and a lower average error, only the data up to 0.15% strain are considered for that polynomial. The lowest deviations are found for sample A, which shows the least amount of plasticity resulting from the stainless steel reinforcement. However, all sets of stress-strain curves can be accurately described with the two-regime formalism explained before.

This method to describe the mechanical properties leads to an un-ambiguous characterization of the initial slope, as long as the fit follows the data closely, i.e. the average error is low enough. No method, however, can prevent the variation in measured

properties, even between nominally identical samples, whether these variations are due to sample-sample variations or experimental errors.

Despite the differences in conductor architecture, there are a number of commonalities in the stress-strain properties at 77 K. The slope of the stress-strain curve in the plastic regime is 0.4 to 0.5 GPa for all Ag and Ag-alloy matrix conductors investigated here, which is in the order of 1% of the initial slope. Significant J_e-degradation typically occurs at 90 to 95% of *UTS*. Moreover, it is striking that the stress-strain properties of various conductors considered here can all be described over much of the non-plastic regime with a simple second order polynomial.

ReBCO conductor

As the conductor cross-section of ReBCO conductors consists mostly of the substrate and Cu stabilizer, the mechanical properties of the substrate and stabilizer dominate the stress-strain characteristic of the conductor. The production process of ReBCO conductors allows the use of high-strength substrate materials like Ni-W, stainless steel and Hastelloy, resulting in more traditional stress-strain curves. Conductor G for example can be described accurately with a modulus of 170 GPa up to 0.37% strain and 4 GPa for higher strains. Note that Conductor G features about twice the strength and twice the modulus of conductor A.

6.2.3 Engineering critical current density versus tensile strain

Knowledge of the relation between tensile strain and J_e of a conductor is essential in the design process of HTS insert coils, in combination with the stress-strain properties of the conductor. It also allows an analysis of strain induced degradation in coils subjected to large Lorentz-force, like the coils investigated in section 6.4. Here, the tensile strain-J_e relation is determined for conductors A, H and conductor from a batch representative of conductors B,C,D, that are used in those coils. Data on ReBCO conductors obtained by others are presented for comparison.

Generic strain dependence of J_e in BSCCO

Generally, the dependence of J_e on applied strain at cryogenic temperatures for BSCCO conductors features three regimes [74]. For compressive strain J_e decreases reversibly with a slope of ~ 30 to at least -0.5% strain. In tension there is a range, up to the critical strain, where J_e is weakly dependent on strain. Different values for this slope are reported in the literature, generally between 2 and 10. The slope is not an intrinsic property of the ceramic, but may depend on geometric parameters like the number, size and porosity of the filaments. A slope of 7 and a critical strain of 0.38% are used in Figure 6-3 to represent conductor H. The onset of degradation also varies from conductor to conductor and depends on the integrated difference in thermal expansion between the matrix and the ceramic [116]. The onset of degradation coincides with significant crack formation in the ceramic and increased plasticity in the conductor stress-strain curve. The rate of J_e degradation beyond the critical strain tends to be higher for free-standing samples in tensile testers (like sample H) compared to samples mounted on bending springs [117], presumably because the sample support provided by the bending springs prevent necking in the conductor and thereby limit crack propagation.

Generic strain dependence of J_e in ReBCO

Here the strain dependence of J_e for three different YBCO conductors obtained using a bending spring [118] at 76 K is used to illustrate the generic strain dependence of J_e on

ReBCO conductors. One of these three conductors, represented by the thin un-interrupted black curve in Figure 6-3, is similar to conductor L. From a compressive strain of -0.9% to the critical tensile strain of ~ 0.5%, the strain dependence of J_e is reversible and can be described using equation 6-4.

$$\frac{J_e(\varepsilon)}{J_e(0)} = 1 - a \cdot \varepsilon^{2.2} . \qquad (6\text{-}4)$$

The strain sensitivity parameter a ranges from $6.9 \cdot 10^{-3}$ (representative for conductor L) to $9.5 \cdot 10^{-3}$ for these conductors.

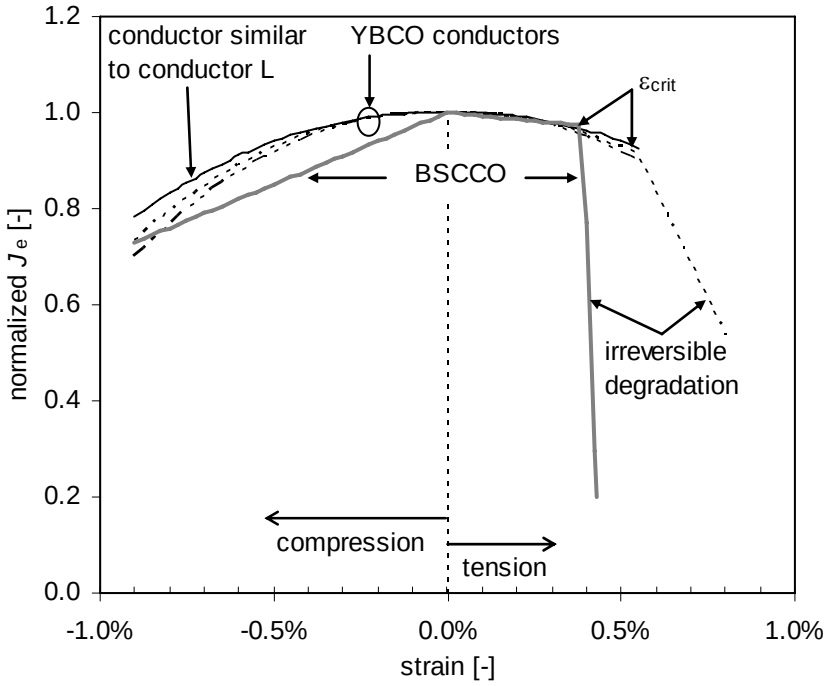

Figure 6-3. Generic strain dependence of J_e in BSCCO and ReBCO conductors. J_e degradation is irreversible for strain above the critical strain (ε_{crit}).

Comparing the strain dependence of J_e in ReBCO and BSCCO conductors in tension, it is apparent that their properties are similar for practical purposes: J_e degrades slightly (< 10%) up to the critical strain, beyond which J_e irreversibly collapses. In compression, BSCCO conductors are initially more strain sensitive than ReBCO conductors, but this reduction is reversible for both types of conductors. Properties under compressive strain are relevant in two cases, but neither apply for the purpose of this section:

1. When differences in thermal expansion coefficients between conductor and other materials in the windings or surrounding structures place the conductor in compression. This is negligible for the coils considered here.
2. When bending conductors, typically during coil winding, and part of the superconductor is on the concave side (inside) of the neutral line. Conductor bending is discussed next in section 6.3.

Conductor A

The manufacturer of conductor A specifies a critical tensile strain value of more than 0.4 % at 77 K and below. A graph of measured J_e-strain data indicates $\varepsilon_{crit} = 0.45\%$.

Conductors B,C,D

Since the T_c of the Bi-2212 samples is close to or above 77 K[59], the approach of measuring J_e versus strain at 77 K for multiple strain values on a single sample is not suitable. Instead, multiple samples (36) are subjected to a single peak strain level at 77 K followed by a J_e(4.2K) measurement[60]. Up to 0.39% strain the samples exhibit an average J_e of 524 A/mm^2 with a standard deviation of 9% (47 A/mm^2). In the range of 0.39% to 0.49% strain, the majority of samples show degradation of both J_e and *n*-value, but a significant minority does not, as shown in Figure 6-4. Statistical analysis using Weibull distribution functions can be applied to such data [119]. The range over which some samples degrade but others do not is larger than 0.1%. For a more complete understanding, data should be taken to larger strain values until all samples show degradation at the maximum strain value. As for conductor H, *n*-value degradation precedes J_e degradation with increasing strain, although this is less obvious on account of data scatter. The scatter in J_e and *n*-value is well beyond experimental errors and is attributed to inhomogeneities in the micro-structure of the conductor.

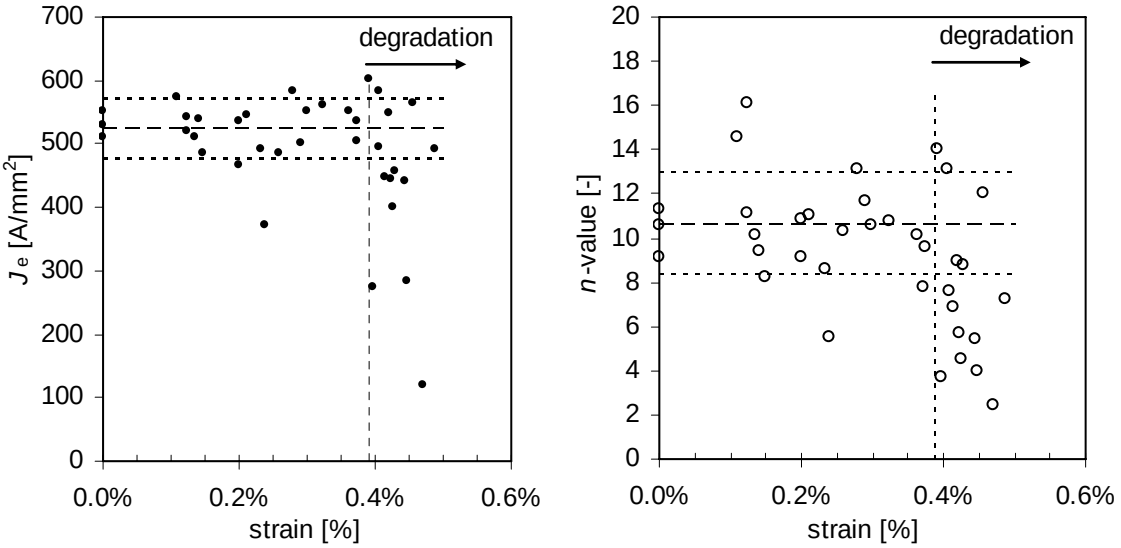

Figure 6-4. (left) Measured strain dependence of J_e for a conductor representative of conductors B,C and D. The onset of strain induced degradation is indicated with a vertical line. The long-dash line indicates the average J_e before the onset of degradation. The short-dash lines delineate ± one standard deviation. (right) Corresponding n-values.

It is not possible to determine the slope of the J_e-strain curve below ε_{crit} from the data in Figure 6-4. Measurements on samples of older batches of Bi-2212 tapes from the same manufacturer using a bending spring [117] and a Lorentz-force device [76] show a slope of 2 to 7 in normalized-J_e versus strain up to 0.4% and significant degradation above 0.4%. Considering the similarities in the conductor and data, it seems reasonable to assume a that a comparable slope exists in J_e versus strain below ε_{crit} for conductors B, C and D.

[59] The heat treatment conditions of the Bi-2212 conductors considered here are optimized to maximize J_e at 4.2 K, at the expense of T_c.
[60] As introduced in section 2.4.

For the purpose of insert coil design, ε_{crit} is set at the lower end of the range for which degradation is observed: 0.39%. This value may be somewhat conservative. J_e-degradation is associated with cracking of the ceramic and local yield in the matrix. Crack formation and propagation may be suppressed in impregnated coil windings compared to bare samples in a tensile tester, as neighboring turns and reinforcement limit local yielding. A similar effect occurs when samples are strained on a bending spring: the slope of $J_e(\varepsilon)$ is much lower than in Figure 6-5 and Figure 6-4, although the strain at the onset of significant degradation is comparable [117].

Thus the critical tensile strain is determined of the conductors used in the experimental coils that are exposed to both bending strain and Lorentz-force induced strain, as reported in section 6.4. The critical tensile strain values are summarized in Table 6-2.

Conductor H

Data on J_e and *n*-value for conductor H are obtained using the tensile tester. The behavior as shown in Figure 6-5 is very characteristic. The relation between normalized J_e and strain for low strain values can be described with a relatively small slope, in this case 7±2. The error margins in the *n*-value in this setup (±2) are too large to determine whether a similar slope exists in the *n*-value versus strain relation.

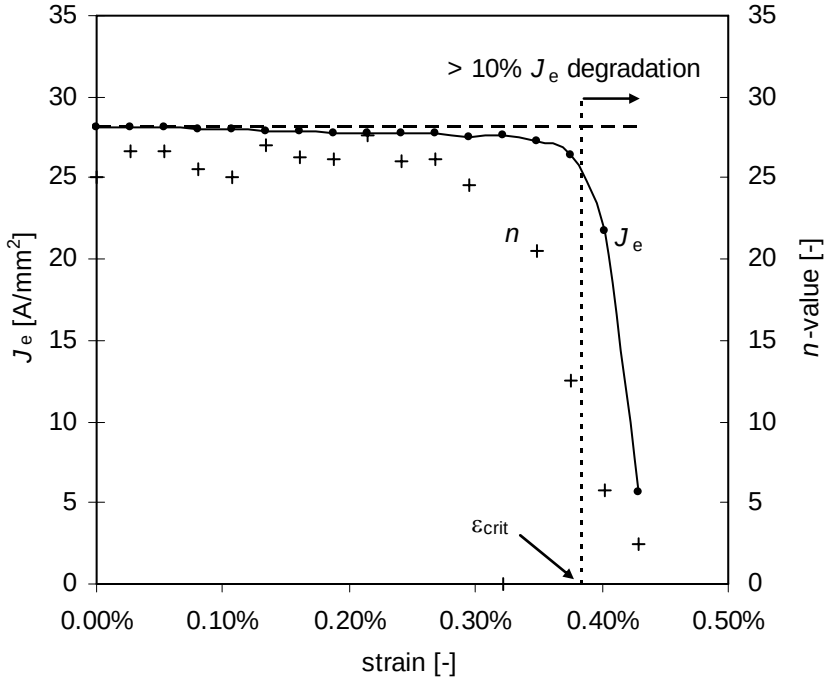

Figure 6-5. Engineering critical current density and n-value versus tensile strain for conductor H at 77 K. The line connecting J_e data points is a guide to the eye.

The departure from the linear J_e -ε behavior is the onset of significant J_e degradation and is preceded by a reduction in *n*-value. Increasing strain levels at the onset of degradation first affect the E-J_{op} characteristic of the superconductor at voltage levels below the J_e -criterion, reducing the *n*-value without a significant effect on J_e. Further increase of strain causes a much higher rate of degradation of J_e and *n*.

For the purpose of comparing strain induced degradation between short samples and coils, a critical strain level, ε_{crit}, is defined as the strain level corresponding to 10% degradation of J_e. The critical strain level of conductor H is thus estimated at 0.38%.

Conductor G

Typical stress-strain data is presented in Figure 6-1 for a batch similar to conductor G. J_e degradation coincides with the onset of significant and plastic yield of the conductor at close to 600 MPa and 0.38% strain [52].

Conductor I

The relation between strain and J_e is not explicitly measured for conductor I. However, it is reasonable to assume that the critical strain is equal or less than the onset of significant plasticity at 0.2% strain.

Summary

The relation between tensile strain and J_e is determined for conductors A, B, C, D, G, H and I. The critical strain values, corresponding to 10% irreversible J_e degradation, are summarized in Table 6-2. Although the critical strain values are practically the same for all but conductor I, the corresponding stress levels vary significantly as can be deduced from Figure 6-1. These critical strain values are essential input parameters when designing an HTS insert coil, like the 5T coil based on conductors B,C,D. Additionally, these values are indispensable in the analysis of observed J_e degradation, or lack thereof, in inserts subject to large Lorentz-force induced strain like those studied in sections 6.4 and 6.5.2 which use the conductors listed in Table 6-2.

Table 6-2. Critical tensile strain values of conductors A,B,C,D and G, H and I.

Conductor	unit	A	B, C, D	G	H	I
ε_{crit}	[%]	>0.40	0.39	0.38	0.38	≤0.2

6.3 Bending conductors

Conductor bending is one of the two dominant factors contributing to strain in the superconductors of insert coils, which in turn affects the engineering critical current density J_e. Of primary interest is the tensile strain in the filaments as it will, in combination with Lorentz-force induced strain which is also mostly tensile, cause degradation of J_e in insert coils when a certain critical tensile strain is exceeded. Specific issues addressed in this section are:

1. The relation between bending radius and the resulting tensile strain on the filaments in the conductor,
2. The critical bending radius at which J_e degradation occurs.

As stated above, the maximum tensile strain within the filaments is of primary interest. There are minor and reversible variations of J_e with compressive strain and for tensile strain below the critical strain as shown in section 6.2.3 and by others [74], but these variations generally do not exceed 10% degradation and will be ignored for the purpose of this section. Tensile strain, once a critical strain level is exceeded, is by far the dominant factor determining J_e.

6.3.1 Bend-and-release

Bend-and release experiments[61] allow the determination of the maximum tensile strain in the ceramic filaments for conductors that are not straight when unrestrained (the curvature is mostly determined by the conductor diameter during heat treatment), and that show partially plastic deformation during bending. For conductors A, D, H, and I a limited set of data points is obtained, but sufficient to estimate bending strain in the coils wound from these conductors that are discussed later in this chapter. For conductor D, representing the conductor used in the 5T insert coil, the data set is more complete. To support the design of the 5T insert, the critical bend diameter is determined and two different methods of bending are used and compared.

Often a rough estimation of bending strain is made by dividing the conductor thickness by the bending diameter, i.e. using equation 2-5. Figure 6-6 and Figure 6-7 illustrate that this leads to a large overestimation of the surface strain. The bend diameter during heat treatment of the conductors is not large, it is smaller for example than the outer diameter of the 5T insert B- and C-sections, and this factor can significantly reduce the surface strain. Plasticity in conductor bending during coil winding also has a reducing effect on the surface strain. The filament strain is significantly lower again than the surface strain, by about 30% for the conductors investigated. Using equation 2-5 would lead to an over-estimation of the maximum bending strain on the filaments by a factor of 2 to 4 at the smallest bending diameter for each of the conductors investigated here, where bending strain is most likely to be a critical factor, and a larger error at larger radii. Therefore, equation 2-9 should be used to estimate bending strain for BSCCO tapes and 2-10 is proposed for ReBCO tapes.

Bend-and-release experiments on conductors A, D and H and I show that the degree of plasticity is approximately constant for each conductor over the range of radii as used in coils in this chapter. Conductors H and I retain about half of the bending strain in the filaments; conductor D retains 70 to 80% as shown in Figure 6-6 and Figure 6-7. Conductor A is nearly perfectly elastic, which is attributed to the stainless steel reinforcement strips. A high degree of elasticity similar to conductor A is expected for ReBCO conductors that use substrates or reinforcement with mechanical properties comparable to stainless steel.

Not only the bend diameter, but also the method of bending has an effect on J_e. This is illustrated for conductor D in Figure 6-7. Bend-and-release data points obtained using the machine-winding method can be described if one assumes the conductor retains 80% of the elastic bending strain. The finger press method results in a larger degree of plasticity that can be described as 70% of the elastic strain. These correlations are applicable in the absence of J_e-degradation only (bend diameter ≥ 30 mm). The calculated retained strain at the outer filaments is again lower by the ratio of the filament zone thickness to the conductor thickness. Thus the bending of conductors in bending experiments should preferably be done in a manner that mimics the coil winding process as closely as possible.

[61] Introduced in section 2.5.2.

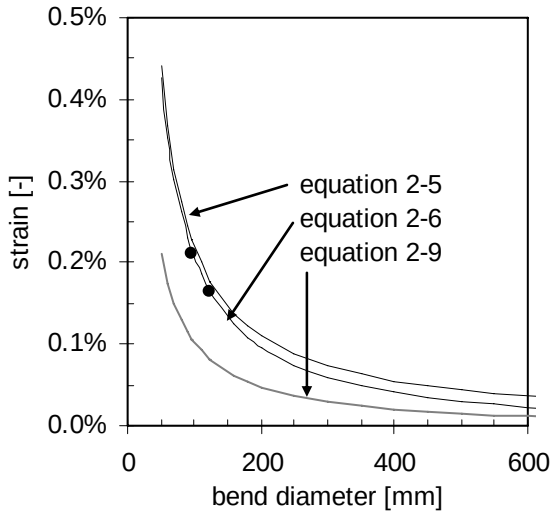

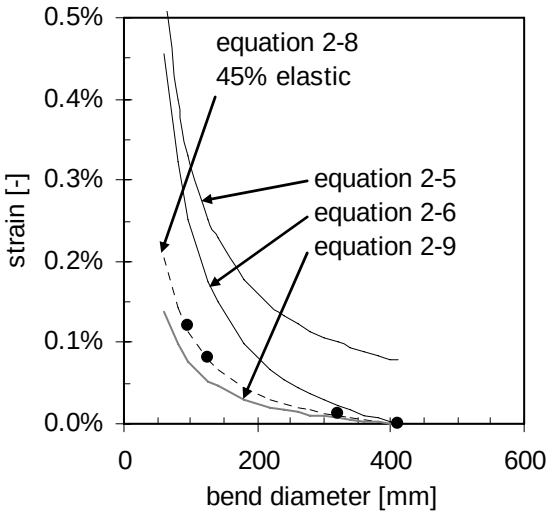

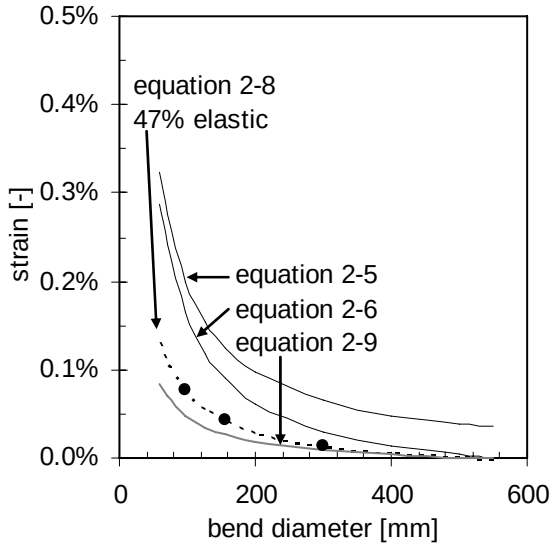

Equation 2-5: Calculated maximum surface strain in the case of elastic bending of initially straight conductor.
Equation 2-6: Calculated maximum surface strain in the case of elastic bending of conductor that is initially curved.
Equation 2-8: Calculated maximum surface strain considering the initial curvature and partially-plastic bending.
Equation 2-9: Calculated maximum strain on the filaments.

Figure 6-6 (top left, conductor A) (top right, conductor I) (bottom left, conductor H). Calculated surface strain and maximum filament strain versus observed properties in bend-and-release experiments. The line through the data points represents a fit based on scaling of the surface strain of elastic bending. The estimated maximum strain in the filaments is represented by the lowest curve.

Equations 2-5 through 2-9 are based on the assumption that the neutral line lies in the middle between the inner and outer surface. This assumption no longer holds when significant J_e-degradation occurs as a result of breaking filaments. The onset of J_e-degradation coincides with increased plasticity, as Figure 6-7 illustrates. Equation 2-9 can therefore only be used to predict filament strain in the absence of J_e-degradation.

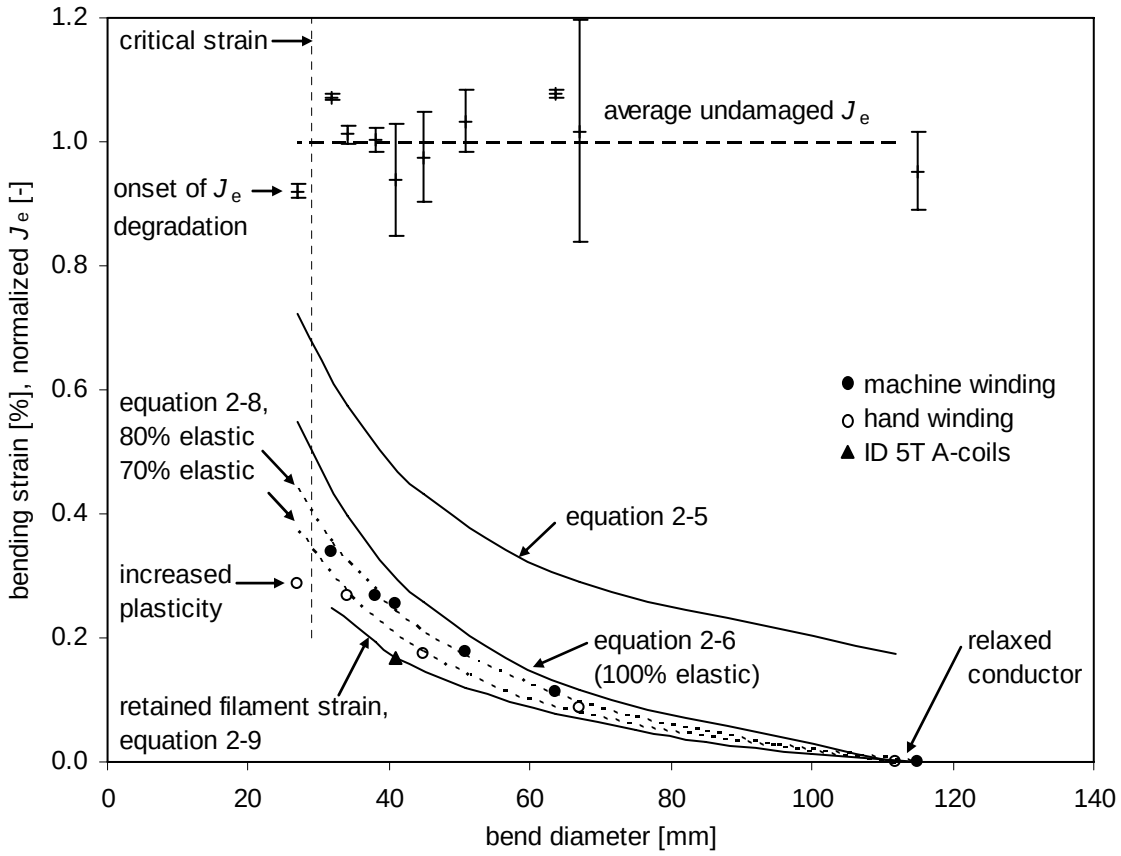

Figure 6-7. Bend-and-release results and strain calculations for conductor D. The top data points represent the average J_e (normalized) with error bars indicating standard deviation.

6.3.2 Bending diameter dependence of J_e

The parameters used to describe the relation between bending diameter and J_e for conductors A, D, H and I are summarized in Table 6-3. Conductor D is taken to represent conductors B and C as well. In combination with equation 2-9, these parameters can be used to calculate the maximum bending strain in the filaments as long as the bending diameter is larger than the critical bending diameter. The conductors listed are used in the coils investigated in section 6.4, when both bending strain and hoop strain are applied.

Table 6-3. Properties of samples of conductors A-I as used in bending experiments.

	unit	A	B, C, D	H	I	L
Heat treatment diameter	mm		102-105		550	straight
Diameter spooled	mm	≥254	205-250	300	320	>254
Diameter in relaxed state	mm	>1000	118±8	405	410±10	
Critical bending diameter (10% degradation)	mm	no degradation at 50 mm*	29±2	no degradation at 97 mm	~100	11
Elasticity (*e*)	%	>99	80	47	45	
f_{fil}		0.50	0.61	0.62	0.68	-
f_{cc}		-	-	-	-	0.52

* Manufacturer's specification of the critical bend diameter is < 35 mm.

6.4 Strained conductors in coils

6.4.1 Combined bending and Lorentz-force induced strain

Both bending strain and Lorentz-force induced strain are substantial in insert coils. Additionally, the mechanical properties of reinforcement and insulation affect the strain state of the conductor. Insulation material typically has a low modulus of elasticity and varies in thickness depending on the required voltage stand-off among other factors. For strain in the circumferential direction the insulation is mechanically in parallel with the conductor providing usually a minor to insignificant amount of reinforcement. For strain in the radial direction the insulation is in series with the conductor and its mechanical properties together with its thickness determine the degree of mechanical coupling between turns. Thus the choice of insulation should therefore ideally not only be driven by electrical requirements, but by its influence on the radial distribution of stress and strain as well. The strongest and thinnest insulation available may not be the optimum.

In the previous sections the effects of bending and uni-axial tension are discussed. Here we consider coils in which bending strain and hoop stress (as the equivalent of uni-axial tension) are dominant sources of mechanical load. Winding tension is set to a negligible low value. There are no structural materials incorporated in the coils in order to avoid thermal pre-stress originating in differences in thermal expansion. It is assumed that the strain in the conductor can be calculated as the sum of bending strain (equation 2-9 for BSCCO and 2-10 for ReBCO) and hoop stress induced strain. The latter will be referred to as hoop strain or ε_{hoop}. Thus equation 6-5 described the maximum strain in the filaments of BSCCO conductors:

$$\varepsilon_{filament} = \varepsilon^{bend}_{max,\,filament} + \varepsilon_{hoop}, \text{ with } \varepsilon_{hoop} \text{ and } \varepsilon^{bend}_{max,\,filament} > 0. \qquad (6\text{-}5)$$

For ReBCO conductor, bent with the superconducting layer to the inside of the neutral line equation 6-6 applies:

$$\varepsilon_{filament} = \varepsilon^{bend}_{filament} + \varepsilon_{hoop}, \text{ with } \varepsilon_{hoop} > 0 \text{ and } \varepsilon^{bend}_{filament} < 0. \qquad (6\text{-}6)$$

J_e degradation is expected when $\varepsilon_{filament}$ exceeds the critical strain ε_{crit} as determined in section 6.4.3 through the uni-axial J_e-strain experiments.

6.4.2 Trial coils

The relation between J_e and strain is investigated in six BSCCO double-pancake coils and a BSCCO layer wound coil over as large a strain range as large as practically possible. The measured J_e and calculated stress values of two ReBCO coils are presented for comparison, but are not part of the J_e-strain investigation presented here. The properties of the BSCCO and ReBCO coils are listed in Table 6-4.

Conductors from five different manufacturers are used with a range of J_e values and different methods and amounts of reinforcement. Four of these coils are candidate coils for the 5T insert, with radial dimensions, reinforcement and all other aspects that match the design. Their properties are not only of generic academic interest regarding HTS insert coils, they are the primary test to determine whether the initial design for the 5T insert[62] is effective in keeping the strain in the conductor below the critical strain. The key question is thus not whether each separate candidate coil can operate at its J_e in a 19 T background magnetic field without degradation, but if it can operate at an equivalent strain state as in the completed 5T insert without degradation. The second question is how much margin

[62] See section 1-6 and table 1-2 for details on the initial design.

there is between the J_e at the onset of degradation and the J_e for which the strain is equivalent to the 5T design. Implicitly, it is assumed that the onset of J_e degradation is driven by strain only and not the absolute value of J_e. [63]

Table 6-4. Properties of trial Coils 1 through 9.

Coil name in thesis	**unit**	**Coil 1**	**Coil 2**	**Coil 3**	**Coil 4**	**Coil 5**	**Coil 6**	**Coil 7**	**Coil 8**	**Coil 9**
Conductor		A	B	I	H	C	C	C	G	G
Coil name in original project		ASC01	A-11	KIMM-01	NST-03	A-12	B-2	TC-5	SP-YBCO	NHMFL-YBCO
Conductor thickness	mm	0.24*	0.20**	0.32	0.19	0.19**	0.19**	0.19**	0.10	0.10
Conductor width	mm	2.93	4.95	4.09	2.97	4.95	4.95	4.95	4.0	4.0
Winding style		DP	DP	DP	DP	DP	DP	LW	DP	DP
Impregnation method		vacuum	vacuum	vacuum	vacuum	vacuum	vacuum	wet-wound	-	-
Inner Diameter (*ID*)	mm	97	41	97	97	41	106	156	19	24
Outer Diameter (*OD*)	mm	127	98	128	126	96	147	161	87	36
Winding thickness	mm	14.7	28.5	15.4	14.4	27.5	20.5	2.6	34	6.0
Height (*h*)	mm	7.0	10.5	8.8	6.6	10.6	10.2	194	52	46
Number of turns (*N*)	mm	98	231	80	113	230	166	286	2580	380
Reinforcement thickness	μm	2×30	1×27	none	none	1×27	1×27	1×27	none	none
Insulation material	-	Kapton	ceramic	Kapton	Kapton	ceramic	ceramic	ceramic	Kapton	varnish
Insulation thickness	μm	35	15	35	35	15	15	15	13	~15
Initial# J_e(19 T)	A/mm^2	204	126	27	101	134	162	123	485	580***

* Including reinforcement; ** excluding reinforcement, *** at 31 T, # in absence of stress induced degradation
DP = Double Pancake, LW = Layer Wound

5T design equivalent strain

As the candidate coils have the same radial dimensions as the section they will be mounted in if selected, they are considered to be at the equivalent stress and strain state if the product of operating current density and average magnetic field in the windings is the same as the 5T design values. As the magnetic field in the windings of the 5T insert is higher than in the coils under test, on account of lower background magnetic field and lower coil self-field in the candidate coils, the J_e value for design-equivalent strain for the candidate coils are 35%, 16% and 6% above the design J_e value of 126 A/mm^2 for the A, B and C section candidates respectively.

[63] The question what the minimum coil J_e in a 19 T background magnetic field is for a candidate coil to be included in one of the section of the 5T insert is addressed in Chapter 5.

Safety margin

The safety margin in the 5T design is defined as the ratio of the highest degradation-free J_e value observed in a candidate coil over the J_e value for design-equivalent strain. This safety margin should be larger than one for the 5T design to be considered sound regarding strain considerations. A safety margin far above one is undesirable however; as it implies that less reinforcement could have been used with a corresponding gain in average winding current density.

Coil description

Coils 1, 3 and 4 [113, 120] are nearly identical in size and use conductor as supplied by the different manufacturers. These coils are constructed in a similar manner, so differences in the coil behavior under strain can be directly correlated to the conductor properties. The coil diameters are in the middle of the range of diameters expected in inserts. Correspondingly, both bending and Lorentz-forces are significant but neither are at their maxima. The conductors in Coils 1 and 3 have a pure Ag matrix, but the former conductor features two stainless steel reinforcement strips. The conductor in Coil 4 derives its strength from an Ag-alloy matrix. Self-adhesive Kapton tape provides turn-to-turn insulation in these three coils.

Coils 2, 5 and 6 are candidate units for the A and B sections respectively of the 5 T insert [46], featuring a single co-wound stainless steel strip as reinforcement. The reinforcement strip is MgO-ZrO_2 coated [121] and provides the turn-to-turn insulation. All six double-pancake coils feature a Kapton sheet for pancake-pancake insulation and are vacuum epoxy-impregnated with STYCAST™ 1266.

Coil 7 is a half-thickness prototype of the 5T C-coil [46]. It is a tall, thin layer wound coil that is wet-wound using the same type of conductor, reinforcement, epoxy and insulation as Coils 2, 5 and 6. The radial gradients in bending and Lorentz-force induced strain are negligible because of its limited winding thickness, allowing for the most direct comparison of its properties with those of the bare conductor.

6.4.3 Measured properties of coils at high stress and strain levels

Initial J_e value

Of primary interest is determination of the operating current density at which strain induced J_e degradation occurs. A problem inherent to measuring coil J_e in a background magnetic field is that the stress at the initial J_e value is considerable and may already have caused degradation for $J_{op} < J_e$. However, it was verified that each of the coils discussed could be operated in a 19 T background magnetic field to J_e and the corresponding stress levels without J_e-degradation. It is assumed that once J_e degradation is observed, any increase in stress will further decrease J_e, as routinely observed in short sample experiments. If the first increase of stress by raising J_{op} above J_e does not cause J_e degradation, it is likely that no degradation has occurred by raising J_{op} to the initial J_e. Also, the absence of degradation at the initial J_e is verified by the reversibility of the E-J_{op} and $J_e(B_A)$ characteristics. Thus it is ensured that the initial J_e level represents an undamaged state and is a suitable reference value.

Hoop stress at outer radius

As an un-ambiguous measure of mechanical load, the calculated Lorentz-force at the outer diameter σ_{OD} is used with OR, IR and h as in Table 6-4 and B equal to the central magnetic field generated by the outsert. The current density is averaged over the windings

and thus takes the volume taken up by the insulation and any reinforcement into account. It is a first order approximation of the maximum hoop stress in the conductor. In more precise calculations, as in section 6.5, the stress in the conductor is determined as a function of the radius and its maximum is likely to be somewhat higher than σ_{OD}. However, a key feature of σ_{OD} is that it can be calculated based on parameters that are usually listed in publications without requiring knowledge of the stress-strain properties or precise amounts of all the materials in the windings:

$$\sigma_{OD} = J_{ave} \cdot B \cdot OR, \tag{6-7}$$

$$\text{with } J_{ave} = \frac{I \cdot N}{h \cdot (OR - IR)}. \tag{6-8}$$

Peak stress estimates based on σ_{OD} allow a reasonably fair comparison of maximum stress levels between different coils, as presented in Table 1-1 for example, and is consistent with the estimates of the stress range in insert coils as presented in section 1.3.2.

Stress dependence of J_e in coils

Once the initial J_e is determined, the operating current is increased to a specific peak value to increase the peak stress value in the coil, quantified via σ_{OD}. Then J_e is measured again by lowering the current sufficiently and measuring J_e on the ramp up to the next peak value of J_{op}. Thus the second σ_{OD}-J_e data point is obtained. This sequence is repeated until

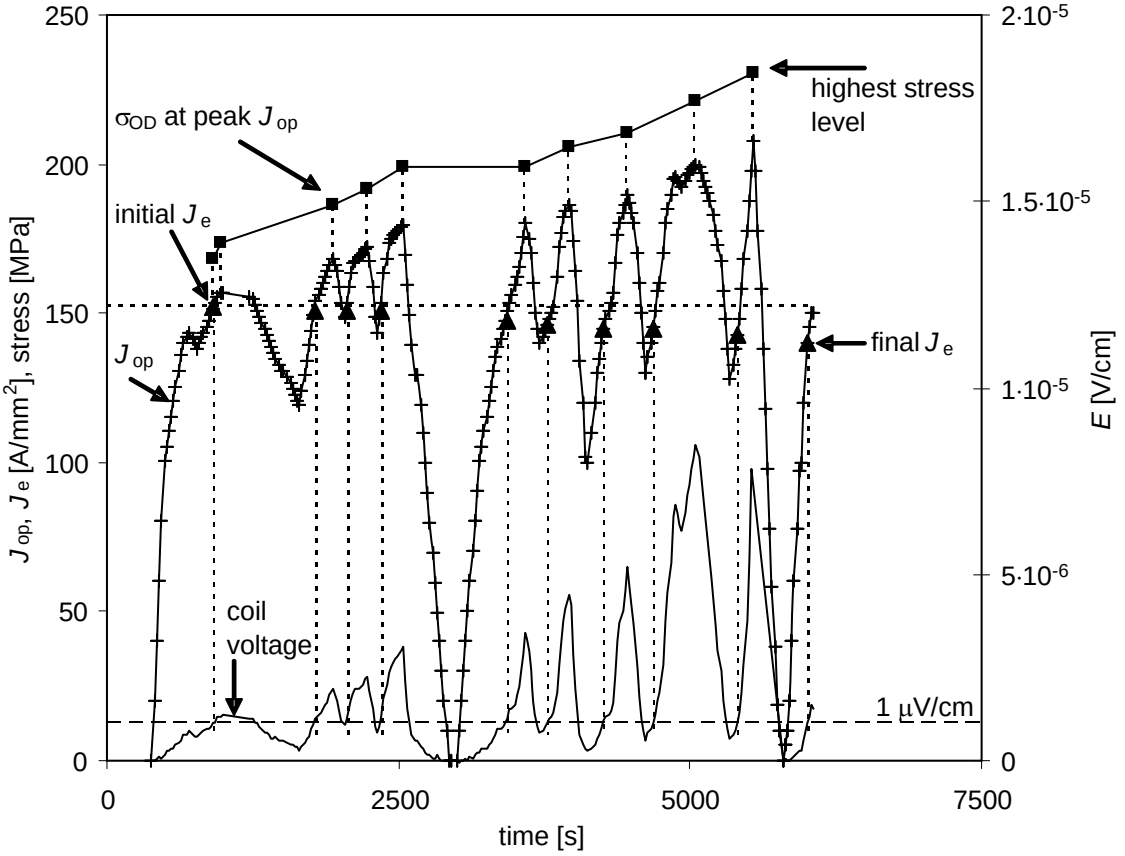

Figure 6-8. Measured coil voltage and operating current density versus time for Coil 6 in a 19 T background magnetic field. For each peak J_{op} value the corresponding σ_{OD} is indicated. The resulting J_e value (solid triangle) is determined by lowering J_{op} and raising it again until the coil voltage equals the 1 μV/cm criterion.

the quench current is reached and J_{op} can no longer be increased. The difference between J_e and the quench current density thus determines the range over which the relation between stress, strain and coil J_e can be studied. An example of voltage and current density data of a coil at high stress levels, and the resulting σ_{OD} and J_e data points, is given in Figure 6-8. A summary of the degradation of coil J_e with increasing stress levels for all the coils in Table 6-4 is presented in Figure 6-9.

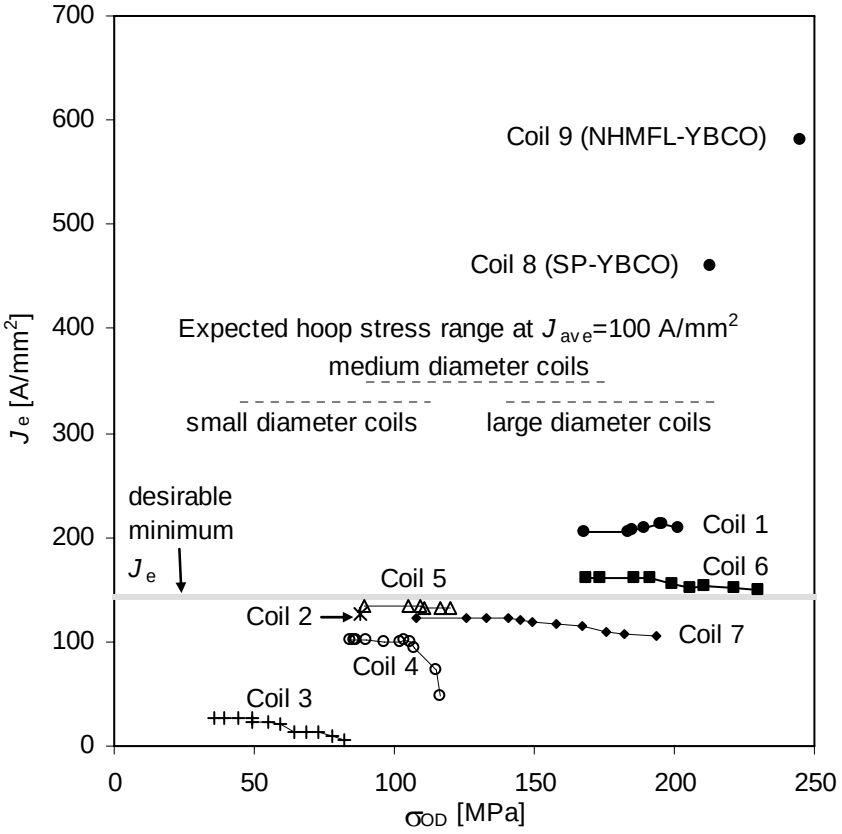

Figure 6-9. Dependence of J_e on hoop stress for Coils 1 through 9 in a 19 T background magnetic field. Equations 6-7 and 6-8 are used to calculate σ_{OD}. Any J_e degradation with increasing stress is irreversible. Lines between data points are a guide to the eye. The generic desirable minimum J_e is indicated as $J_e = 143\ A/mm^2$, corresponding to the benchmark current density of $J_{ave} = 100\ A/mm^2$ if the packing factor is 70%. A range of expected hoop stress is indicated, for three ranges of coil dimensions for $J_{ave} = 100\ A/mm^2$.[64] For a coil to be considered a viable candidate for an insert of a certain diameter range, it should carry a J_e comparable to or higher than the desirable minimum J_e and not show J_e degradation for at least part of the stress range corresponding to its diameters. Coils 2 and 5 can be considered "small", and most others 'medium", based on their diameters. Coil 7 features diameters that are at the lower end of the "large diameter" range and is also the only "thin" coil.

Coil 3

Both current density and strength of the conductor in Coil 3 fall well short of the values expected of candidate conductors in insert coils of any size, as shown in Figure 6-9.

[64] The relevance of small, medium and large is introduced in section 1-4.

However, the conductor is unusually stable because of its low J_e and relatively large fraction of Ag in the conductor cross section. Consequently, the quench current density of this coil in a 19 T background is more than twice J_e. That makes it possible, as shown in Figure 6-10, to observe the growth of the zone where the critical strain is exceeded until the J_e is degraded in almost the entire coil. Clearly, the first degradation of J_e occurs at the inner diameter and progresses radially outward with increasing stress. This is as expected, as will be shown in section 6.5, Figure 6-16. The near-identical data for the top and bottom pancake confirm that this behavior is systematic and reproducible.

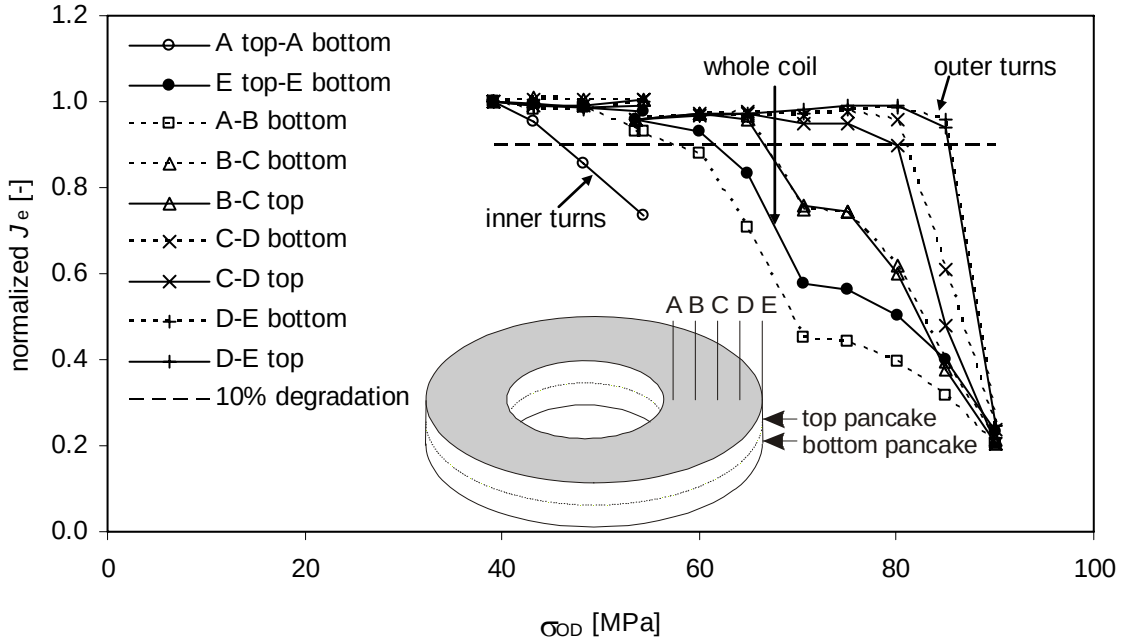

Figure 6-10. Dependence of J_e on hoop stress at the outer diameter σ_{OD} for sections of Coil 3 and as a whole (E top- E bottom). The voltage taps are spaced ~3.5 mm apart radially on both the top and bottom pancake.

Coil 4

Coil 4, using conductor with a higher J_e compared to Coil 3 and with an Ag-alloy matrix, has an initial J_e of 101 A/mm^2 at σ_{OD} = 84 MPa. It can be operated to a quench current 40% above its initial J_e, with degradation starting below σ_{OD} = 100 MPa as shown in Figure 6-11. Significant J_e degradation first occurred at the inner diameter, in the transition turn between the pancakes, as for Coil 3. As the conductor length in this section is short, the degraded transition turn does not have a significant influence on the J_e of the entire coil. Degradation spreads into the next radial section with increasing stress. A maximum of σ_{OD} = 117 MPa is calculated at the highest quench current. The J_e of Coil 4 is reduced by half at this point, which is completely determined by the voltage generated in the inner 3.4 mm of the windings.

Both the absolute value of J_e and the onset of J_e-degradation make this conductor a marginal candidate for HTS insert coils. Adding reinforcement would reduce the winding current density to impractical levels, limiting applicability of this conductor to small diameter coils.

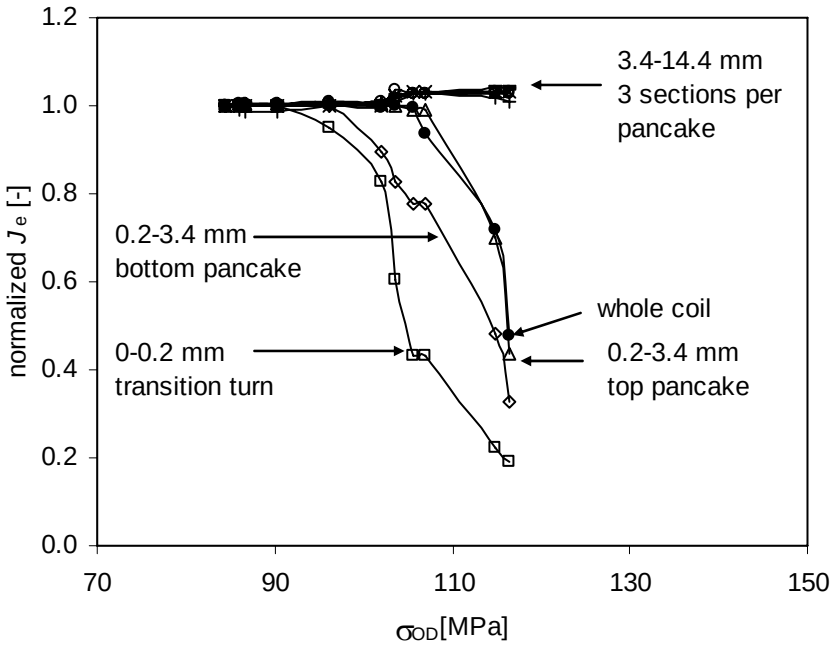

Figure 6-11. Dependence of J_e on the hoop stress at the outer diameter σ_{OD} for Coil 4. The radial position of each voltage tap section is indicated in the graph.

Coil 1

Coil 1, featuring the highest J_e and the largest fraction of reinforcement of the seven BSCCO coils considered here, can be operated to the quench current (120% of J_e) and σ_{OD} = 201 MPa without J_e degradation. A slight increase in J_e is observed, resulting from improved flux pinning after operating the coil at voltages well above the critical voltage without fully entering the normal state. This increase is reversible via an excursion of the superconductor to the normal state. Without reinforcement, this conductor has mechanical properties comparable to the conductor in Coil 3. Clearly, the reinforcement strips are effective. Current density and stress tolerance make this conductor a suitable candidate for HTS inserts to 25 T class magnets of any diameter.

Coils 2 and 5

Coils 2 and 5 are nearly identical candidate double-pancake modules for the A-section of the 5 T insert coil. Both coils have an inner diameter of 41 mm, which is close to the critical bend diameter of 29 ± 2 mm. Coil 2 is only operated to J_e while Coil 5 is operated 35% beyond its J_e of 134 A/mm^2 until a quench occurs. No significant J_e degradation (< 1%) is observed with increasing Lorentz-force induced stress up to σ_{OD} = 120 MPa at the quench current density of 181 A/mm^2, so this conductor meets the generic minimum requirements for application at smaller radii in inserts to 25 T class magnets. A more detailed analysis, calculating stress and strain in the conductor and insulation separately as opposed to the averaged value based on J_{ave}, is presented in section 6.5.

Coil 6

Coil 6, a candidate double-pancake module for the B-section of the 5 T insert coil, shows minor degradation of its initial J_e of 162 A/mm^2 with increasing stress. Degradation first appears in the inner 1.5 mm of the windings. As can be deduced from Figure 6-9, this

conductor[65] also meets the minimum requirements for medium to large insert coils to 25 T class magnets. A more detailed analysis is presented in section 6.5.2.

Coil 7

Coil 7, a prototype for the C-section of the 5 T insert, has a quench current 79% above its initial J_e of 123 A/mm^2. It shows an onset of degradation at an operating current density between 151 and 160 A/mm^2, corresponding to σ_{OD} = ~ 136 MPa, with a gradual degradation of J_e for higher stress. At σ_{OD} = 193 MPa Coil 7 still maintains 85% of its initial J_e and does not show the sharp reduction of J_e characteristic of bare conductors under tensile stress/strain as illustrated in Figure 6-5 and Figure 6-4. This comparison is further addressed in section 6.4.4. The stress tolerance of the J_e of this conductor batch is sufficient for medium to large coils; its current density is marginal. Similar conductor but with a higher initial J_e is used for the actual C-section of the 5T insert.

Coil 8 (SP-YBCO)

Coil 8, named SP-YBCO in section 1.4, could not be operated above J_e as the J_e and the quench current coincide. The E-J_{op} curves below J_e are reversible, indicating an absence of irreversible degradation to current densities that exceed the minimum practical J_e by at least a factor of three at magnetic field well above 25 T. The maximum σ_{OD} of 215 MPa in the coil demonstrably without J_e degradation is high enough to consider this conductor a suitable candidate for HTS inserts to 25 T class magnets of any diameter. The degradation-free range stress range is likely to be larger considering the stress tolerance demonstrated in short samples of this conductor (> 600 MPa).

Coil 9 (NHMFL-YBCO)

Coil NHMFL-YBCO is operated to J_{op} = 549 A/mm^2 at 31 T applied magnetic field without a measureable voltage rise and its J_e value is likely to be significantly higher. Considering that σ_{OD} = 245 MPa is reached without observable degradation, and none was expected, it is clear that this conductor is an excellent candidate for HTS inserts to 25 T class magnets of any diameter.

6.4.4 Comparison between conductor and coil behavior at high strain

The data on Coil 7 are suitable for a comparison between the behavior of bare conductor and conductors in a coil. The bending strain at the coil diameters is small, so this is mostly a comparison between tensile strain in bare conductor with hoop strain in a coil. The tensile strain-J_e data of Figure 6-4 show that strain between 0.39 and 0.49% resulted in no detectable J_e degradation for six out of fourteen samples but between 13 and 80% J_e degradation for the other eight samples. Correspondingly, the conductor critical strain is 0.39%. The properties of Coil 7 are summarized in Table 6-5.

Table 6-5. Strain and J_e in Coil 6.

Property	J_{op}	J_e	ε_{hoop}	$\varepsilon^{bend}_{filament}$	$\varepsilon_{filament}$	J_e degradation
Onset of degradation	155 A/mm^2	123 A/mm^2	0.39%	0.02%	0.41%	1%
Maximum strain condition	220 A/mm^2	105 A/mm^2	0.67%	0.02%	0.69%	10%

An onset of J_e degradation at 0.39% in bare conductor matches with a calculated maximum strain state of 0.41% in Coil 7 at its onset of degradation. However, the

[65] Same conductor as used in coils 2 and 5.

observed degradation of more than 10% of J_e in the majority of short samples at 0.5% strain is hard to reconcile at first sight with only 10% degradation in Coil 7 at 0.69% strain. This is further discussed in 6.5.2.

6.5 Calculation of the stress-strain state

The intent of calculating the stress-strain state is to predict the onset of strain induced degradation in coils. Lorentz-force induced strain and bending strain are the primary sources of mechanical loads on the conductor and are considered to be cumulative [112], following equation 5-3. The relevant measure of bending strain is the maximum bending strain on the outside filaments of each turn, calculated via equation 2-9. Regarding Lorentz-forces, it is the hoop strain that will first lead to strain-induced degradation.

Simulation Model

An in-house developed software package [122] is used to calculate all components of the Lorentz-force induced strain at the midplane of insert coils. Each coil is modeled as a number of cells, containing one turn of conductor plus insulation. This model considers all components of the Lorentz-force in each turn of the windings as well as the mechanical coupling between the turns. Although the self field of the insert coil is calculated correctly, the background field is modeled as homogeneous. This leads to a slight underestimation of the axial forces and very minor changes in the hoop stress at the midplane for relatively tall coils like the 5T insert. A second simplification, one that allowed this code in its original form to be analytical, is that the axial strain at the midplane is considered independent of the radius, i.e. planar. This approximation is valid for relatively tall coils [123], which HTS insert coils typically are (see section 4.3). Moreover, these effects are negligible for double pancake coils as verified using an ANSYS finite element model [124].

The original code been modified by inclusion of non-linear stress-strain properties for the conductor and insulation separately. The model of the conductor stress-strain properties is based on the measured properties of the bare conductor as shown in Figure 6-1. For the conductors used in the 5T insert, this is combined with the co-wound reinforcement with a measured modulus of 208 GPa at 4.2 K, using the Rule Of Mixtures. The code requires stress-strain curves to be converted into four straight segments. This is illustrated in Figure 6-12 for conductors A and H as manufactured and conductor C with co-wound reinforcement. The segmented curve for conductor I is modeled after the stress-strain properties of a thin coil of conductor I [113] for reasons that will be explained below. In all cases both the conductor and insulation are assumed to be isotropic, with a modulus of 6 GPa for the epoxy and 12 GPa for the Kapton HN insulation [125]. Uncertainty in the mechanical properties of the insulation is probably the most significant source of inaccuracy in the stress-strain calculations.

CYCLN was made available after customization for use with HTS insert coils [126]. However, the code lacks the geometric resolution for the dimensions relevant to HTS insert coils to model each turn with its insulation layer and reinforcement separately. The dimensions of 4 turns plus insulation are therefore combined into one cell, representing two turns radially and two turns axially.

Usually the code is set to provide calculations results for four positions within the cell: three representing the conductor and the fourth representing the insulation. The radial spacing of these positions is equidistant within a cell but not across a cell boundary, explaining the slightly irregular appearance of graphs of stress and strain versus radius.

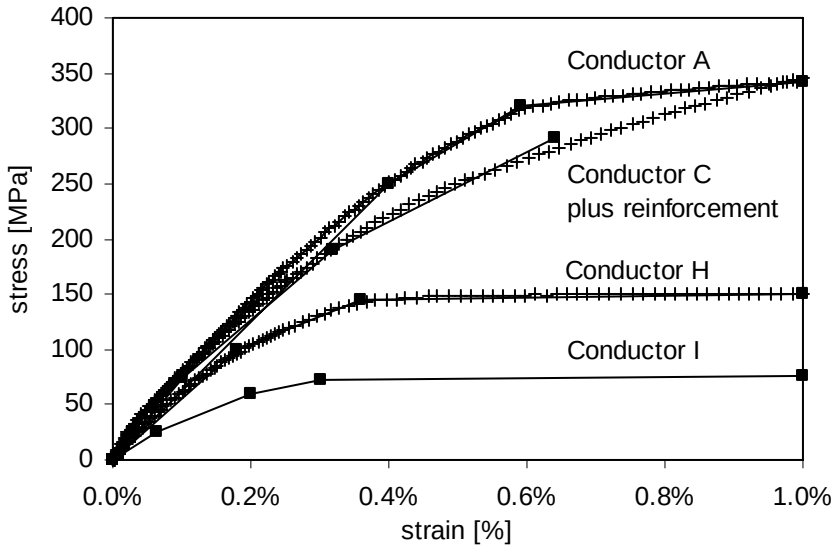

Figure 6-12. Measured tensile stress-strain curves at 77 K for conductors A, H and I, plus the calculated stress-strain curve for conductor C with co-wound reinforcement using measured data and the Rule Of Mixtures. The lines between square markers represent the segmented curves used in the code "CYCLN" to calculate the various stress and strain components in coils.

As an example stress and strain components for Coil 5 at peak Lorentz-force induced loads are calculated. The results for $J_e = 170$ A/mm^2 in a background magnetic field of 19 T are presented in Figure 6-13. Hoop stress is the dominant stress component in the conductor at any radius and its peak value exceeds 170 MPa. This is well above the ultimate strength of the bare conductor. While the locally induced stress, 157 MPa using equation 6-1, is highest at the outer radius, mechanical coupling between the turns results in a transfer of loads such that the hoop stress peaks at the inner radius. Consequently, the calculated radial stress is positive for all radii with a peak value just above 15 MPa.

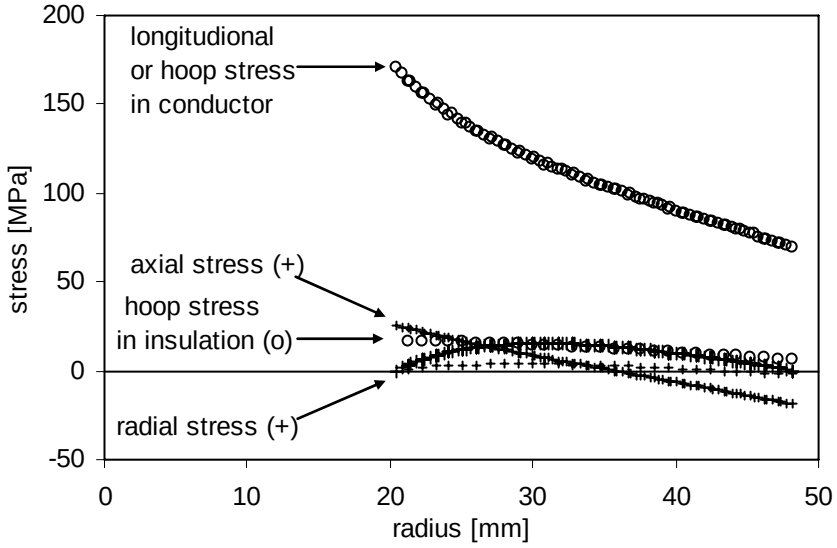

Figure 6-13. Calculated stress values in Coil 5 at the highest strain state Coil 5 experienced (J_e = 170 A/mm^2 in a 19.1 T background magnetic field).

Corresponding strain components for Coil 5 at peak Lorentz-force induced loads are presented in Figure 6-14. Axial strain, resulting from interaction between the current and radial magnetic field components, is taken as independent of radius, as discussed above. The radial displacement is nearly constant with the radius, corresponding to a hoop strain that is nearly inversely proportional to the radius. Adding the bending strain, using equation 2-9, leads to a calculated peak strain of 0.42% in the outer filaments of the inner turn.

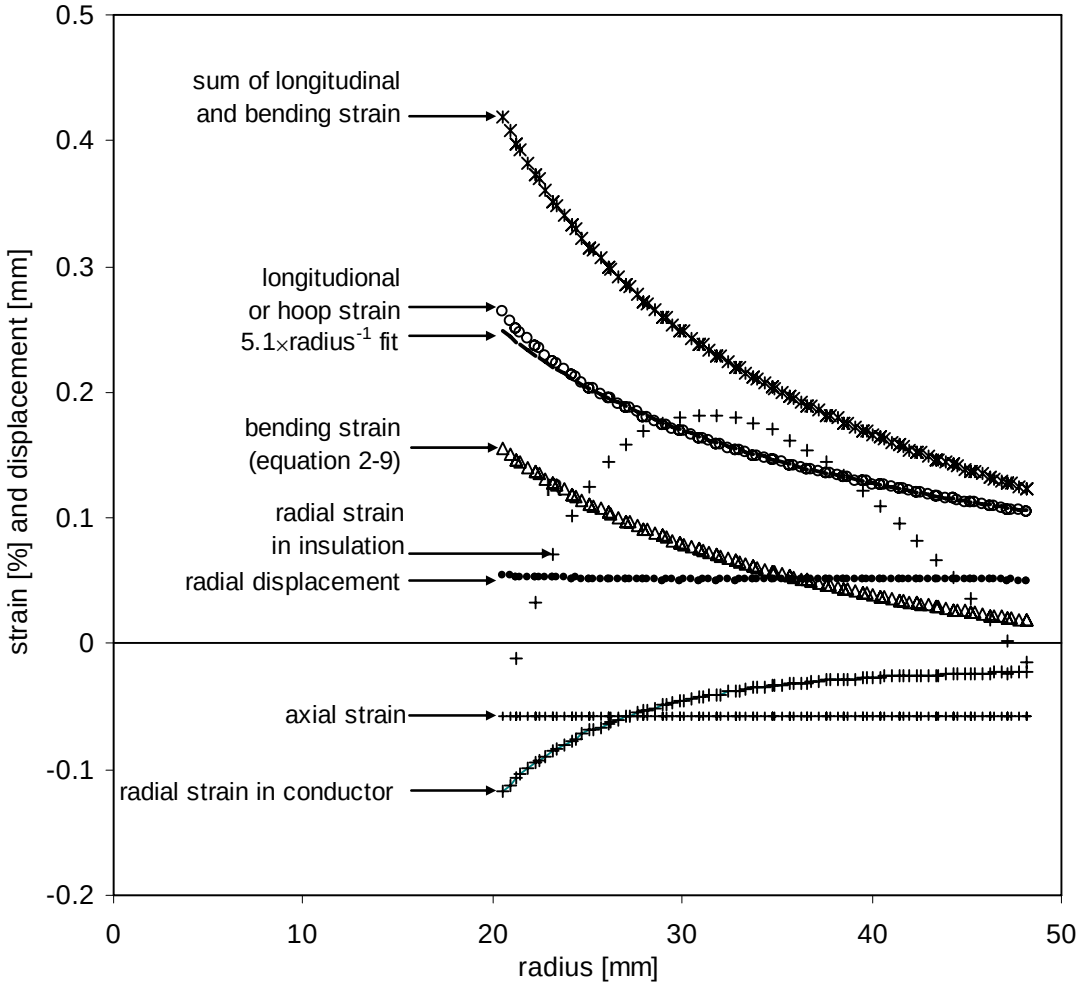

Figure 6-14. Calculated strain in Coil 5 at the highest strain state. Coil 5 experienced (J_e = 170 A/mm^2 in a 19.1 T background magnetic field). J_e is not significantly affected by these conditions.

Thermal strain on the conductor upon cool down from the stainless steel reinforcement is ignored as the thermal expansion properties of conductors are not precisely known. Those properties are known to depend on the matrix/superconductor ratio in the cross section, the porosity of the ceramic and the number of filaments [116, 127]. Literature values for the integral thermal expansion between room temperature and 4.2 K of BSCCO vary: -0.21% and 0.24% upon first cool down and -0.33 to 0.35% for successive thermal cycles are reported [128], while the latter data is interpreted as -0.31% [129] and -0.27% [71]; others find -0.35% [130] and a range of possible values depending on conductor architecture [131]. It seems reasonable to assume that the integral thermal expansion of the conductor will not differ greatly from the -0.31% for 316-grade stainless steel.

6.5.1 Comparing measured coil data to the 5T requirements

Coils 5, 6 and 7 are intentionally operated well above J_e, up to the quench current, such that the conductor in the coils will reach or exceed the peak strain level as calculated for the A, B and C-sections respectively of the 5T insert operating in a 20 T background magnetic field. The calculated strain levels for the initial design are presented in [42], while the calculated strain for the coil as-built is presented in Figure 6-19. The latter is used as the standard for the required strain tolerance.

Coil 5

The calculated peak strain in the A-section with the 5T insert operating at the nominal operating current density of 126 A/mm^2 in a 20 T background magnetic field is 0.41% at the inner turns at the midplane[66]. Coil 5 slightly exceeded that peak strain level (0.42%) with J_e degradation ≤ 1% when it was operated at the 5T strain-equivalent current density of J_{op} = 170 A/mm^2 in a 19 T background magnetic field. This suggests that the A-section can be operated as designed without significant J_e degradation. However, the margin of safety is unknown and the sum of calculated bending strain and Lorentz-force induced strain is in the range that causes J_e degradation in some conductor samples, but not in others, during tensile tests at 77 K. Therefore it appears that one or both of the following may apply:

- The critical strain criterion of 0.39% is conservative when the conductor is supported like in impregnated windings. However, results for Coil 6 imply that the critical strain is between 0.39% and 0.42%, so the criterion is most likely close to its mark.
- The insulation may be weaker mechanically than modeled, leading to a reduced gradient in longitudinal strain versus radius and therefore a reduced peak longitudinal strain value.

Although Coil 5 tolerates the Lorentz-force induced loads equivalent to the operating conditions in the 5 T design without J_e degradation, albeit with possibly a very small margin, the value of J_e itself is just below the acceptance criteria of Table 5-6, so Coil 5 is not used in the 5T insert.

Coil 6

The calculated peak strain in the B-section with the 5 T insert operating at the nominal operating current density of 126 A/mm^2 in a 20 T background magnetic field is 0.34% at the inner turns at the midplane. An equivalent strain state is present in Coil 6 at J_{op} = 146 A/mm^2 in a 19 T background magnetic field, as indicated in Figure 6-15. Strain induced degradation first appeared in Coil 6 for 157 A/mm^2 < J_{op} < 168 A/mm^2, suggesting that also the B-section can be operated at the design conditions without degradation with a safety factor of 1.1 to 1.2. Despite the J_e degradation, the coil still exceeds the qualification criterion for inclusion in the 5T insert.

Coil 7

Coil 7 is at an equivalent strain state as the C-section in the 5 T insert when operated at J_{op} = 132 A/mm^2. While its J_e of 123 A/mm^2 is just short of the current density required for the C-section, it could be operated without degradation to above 151 A/mm^2, suggesting that the actual C-section can be operated at the design conditions with a safety factor of ~ 1.2.

[66] At a background magnetic field of 19 T, the calculated peak strain is 0.40%.

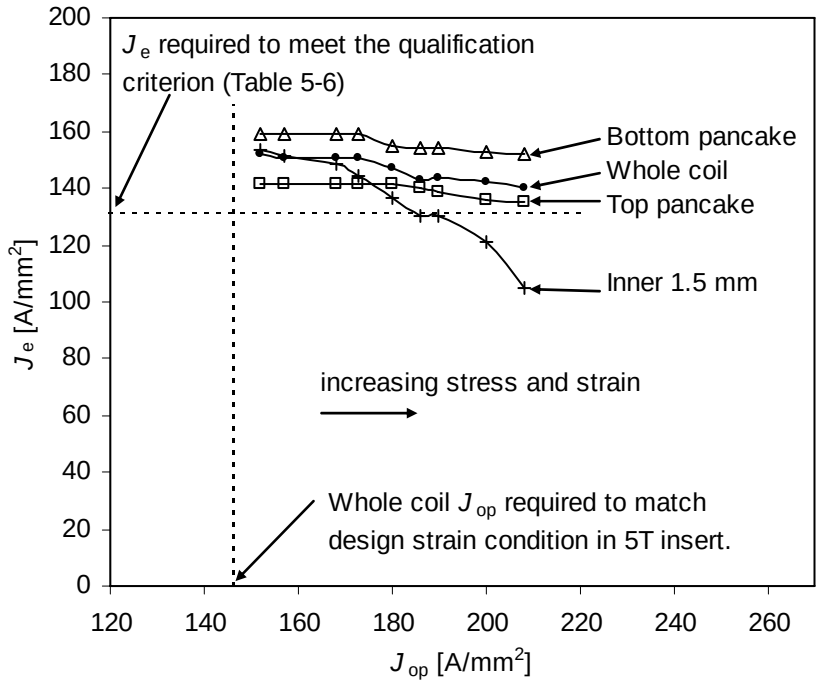

Figure 6-15. Dependence of the engineering critical current density on the operating current density for Coil 6 operated in the 19 T background magnetic field of the Large Bore Resistive Magnet. The observed degradation is irreversible, but only occurs at strain states higher than those calculated for the 5T insert in a 20 T background magnetic field. The "Inner 1.5 mm" voltage tap covers the inner 5 turns of each pancake, the Top and Bottom pancake voltage tap the remaining turns in each pancake, while the Whole coil voltage tap covers all turns.

6.5.2 Comparing measured coil data to model predictions

Coils 3 and 6 provide the best data sets to compare the measured coil data to predictions based on calculated strain values and bare conductor properties. First Coil 3 is considered. The calculated hoop strain in Coil 3 versus operating current density is presented in Figure 6-16. The intersections between the horizontal line of a certain critical strain and the calculated strain curves represents the radius to which J_e degradation is projected to have progressed at that operating current density.

Comparing the measured progression of strain induced degradation with increasing operating current to the projections, one finds that for all sections except the inner turns the measured degradation can be predicted with a critical strain of 0.24-0.25%, as shown in Figure 6-17. Both these critical strain values and the corresponding stress of 65 MPa are well above the measured stress-strain curve of bare conductor as represented in Figure 6-1 and Table 6-1 with the onset of significant plasticity starting at 0.20% strain and 48 MPa. So the stress-strain curve obtained from a bare short sample of this conductor can not be used to accurately predict the strain state of this conductor in a coil. However, the curve obtained from a thin coil, as shown in Figure 6-12, in combination with the code CYCLN, can be used to calculate the progression of strain induced degradation from the inner to the outer radius with increasing operating current.

Next, the measured data on Coil 6 are considered. The steps of degradation observed in Figure 6-15 are summarized in Table 6-6. As the top pancake shows the most straightforward pattern of J_e degradation it will serve as the starting point of a comparison between measurements and model.

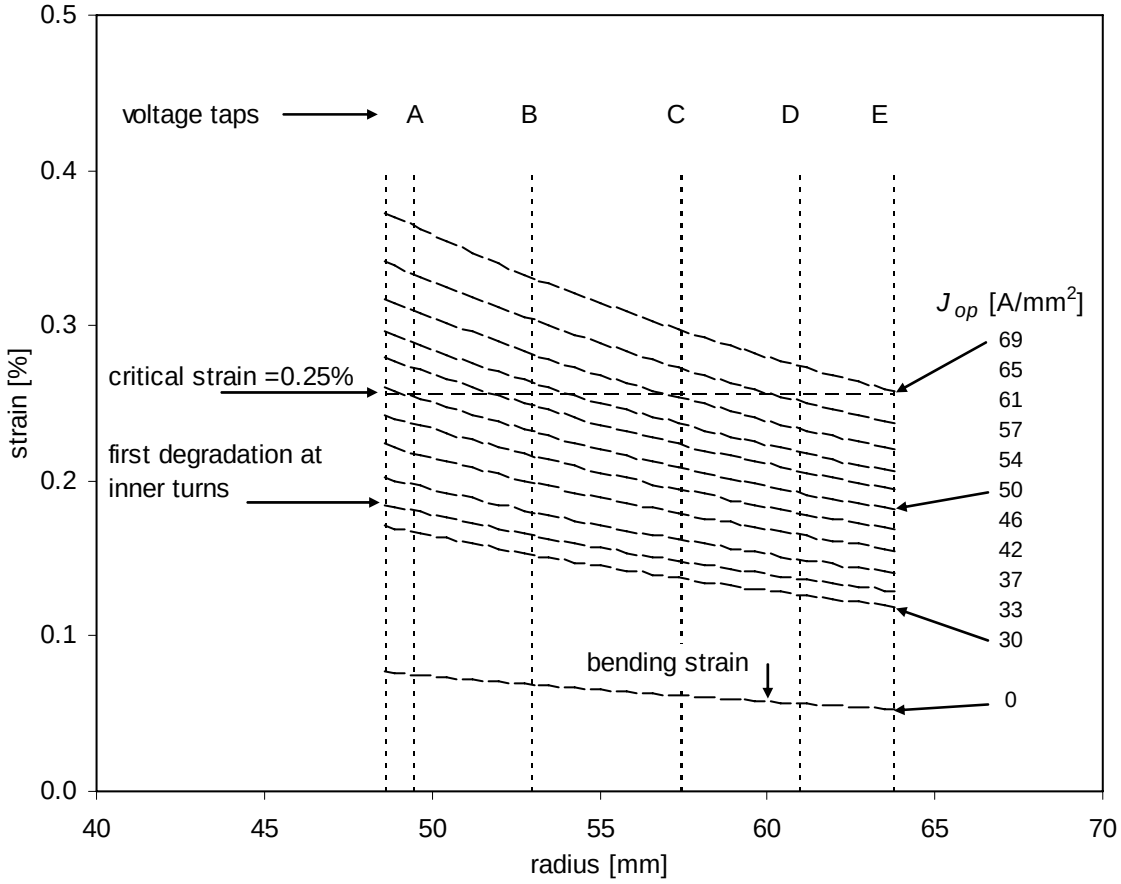

Figure 6-16. Calculated strain in Coil 3 in a background magnetic field of 19 T for various operating current densities. Strain is calculated as the sum of the Lorentz-force induced strain plus the maximum bending strain.

Table 6-6. Steps in the degradation observed in Coil 6 operated in a 19 T background magnetic field.

Peak J_{op} [A/mm^2]	**Observation**
157	No degradation
168	First J_e degradation (1%) observed at inner radius
173	Highest J_e without measurable degradation for whole coil
180	First degradation (3%) observed for whole coil, partly driven by bottom pancake (2.5% degradation)
186	First degradation (1%) observed for top pancake
190	Minor further degradation in all but the inner turns
200	Increased degradation rate observed for bottom pancake
208	Maximum Lorentz-force induced load, < 10% whole coil degradation, 32% at inner turns

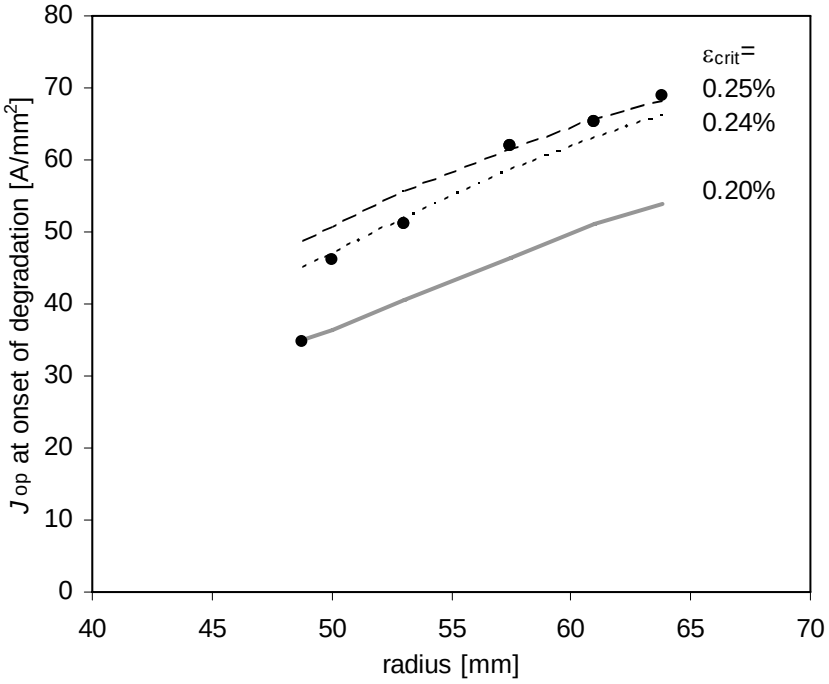

Figure 6-17. Measured operating current at the onset of degradation (dots) and expected dependence (lines) based on Figure 6-16 and different assumptions for the critical strain.

Observation of the onset of strain induced degradation at 186 A/mm^2 in the top pancake implies that the critical strain value is reached at the inner radius of that section. The calculated strain value at that radius is 0.46%, as indicated in Figure 6-18. Assuming the calculated strain curve is correct, the onset of degradation in the inner turns should have occurred at 180 A/mm^2. Instead, first degradation occurred earlier, between 157 A/mm^2 and 168 A/mm^2. Also, at the maximum J_{op} of 208 A/mm^2, degradation should then have progressed to ~ 62 mm radius while the inner turns would be 0.11% over the implied critical strain at that current density. This would cause much more degradation than 10% overall. So it appears that either:

1. there is only limited localized damage involving a small fraction of the conductor length within those voltage taps, or
2. the radial gradient of strain has a lower slope than calculated.

This gradient must have been very close to zero[67] to serve as an explanation for the lack of widespread J_e degradation at 208 A/mm^2, as the average strain is then practically equal to the implied critical strain. It is more likely that localized degradation occurs at weak spots in the conductor, probably at the scale of a single filament, and that the stainless steel reinforcement prevents crack propagation. Other factors that point to a wide distribution function of the critical strain are the known presence of pin-hole leaks and other localized micro-structural defects in this conductor that occur on a length-scale of meters[68] [132], the spread in the J_e(strain) data as shown in Figure 6-4, and the difference in behavior of the top and bottom pancake as shown in Figure 6-15. Coil 3 by comparison, with conductor from a different manufacturer, shows much more consistent behavior between top and bottom pancake, indicative of a narrow distribution of critical strain in the conductor.

[67] Experiments on several coils to directly determine the radial strain gradient using strain gages on the inner and outer diameter were not conclusive.

[68] Conductor used in the 5 T insert has 1-2 bubbles per meter on average and a higher density of pin-holes.

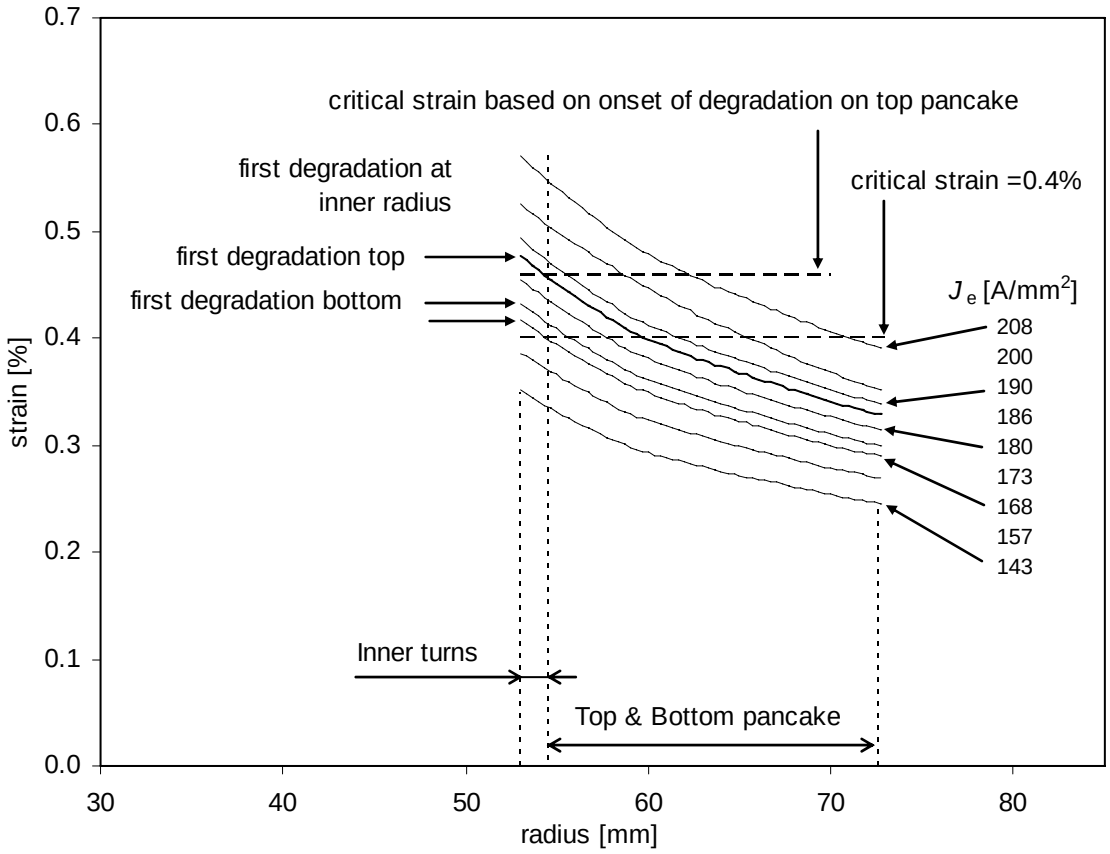

Figure 6-18. Calculated strain in Coil 6 in a background magnetic field of 19 T for various operating current densities. Strain is calculated as the sum of the Lorentz-force induced strain plus the maximum bending strain in the filaments.

The properties of Coil 4 are consistent with the calculated slope of strain versus radius, showing 80% degradation at its inner turns and 50% for the whole coil while all degradation is limited to the inner 3.4 mm at most. The data for Coil 6 lacks that consistency, most likely because the J_e(strain) properties of the conductor vary widely along its length, and the reinforced coil structure limits crack propagation leading to a relatively small slope of coil J_e versus stress/strain. This also implies that determining the J_e-tensile strain relation as in section 6.2.3 is best done on samples reinforced as they would be in a coil, i.e. glued with epoxy to the stainless steel reinforcing tapes rather than on bare samples.

An onset of J_e-degradation at the inner turns between 157 and 168 A/mm^2 corresponds to calculated strain levels between 0.39 and 0.42% at the inner diameter of the coil. This is consistent with the critical strain level determined from conductor J_e(strain) properties. However, the strain in the conductor in nearly the entire coil would exceed the critical strain at J_{op} = 208 A/mm^2 if ε_{crit} = ~ 0.4%, and J_e would have collapsed; which is not the case. So the model used in combination with a critical strain level of ~ 0.40% as derived from conductor data is effective in predicting the onset of strain induced J_e-degradation in Coil 6 but not in modeling the propagation of degradation.

6.6 The 5T insert for 25 T total magnetic field

Design considerations

Chapter 1 provides an introduction to the design goals and geometry of the 5T insert. The radial and axial dimensions were chosen based on early design iterations [45] which featured J_e = 126 A/mm^2 and a peak strain of 0.36% for the conductor in each section. The actual dimensions as listed in Table 1-1 and Table 5-2, vary slightly from the initial design affecting the stress and strain distribution. Another correction originates in refinement of the modeling of bending and tensile stress-strain properties as more data was collected. Finally, the background magnet was operated to 20 T, while the initial design anticipated 19 T. These factors leads to the calculated strain distribution as shown in Figure 6-19. Most notably, the peak filament strain in at the inner diameter of the A-stack has increased to 0.41%, which is slightly larger than ε_{crit} for short samples of the conductor. However, the calculated strain distribution is not expected to cause J_e-degradation based on the properties of Coils 5, 6 and 7, but the margin for the A-stack is possibly very small.

In retrospect, a nearly equal value of calculated peak strain in the three sections of 0.37±0.01% could have been achieved by reducing the winding thickness of the A-section and increasing the winding thickness of the B-section respectively by 2 mm.

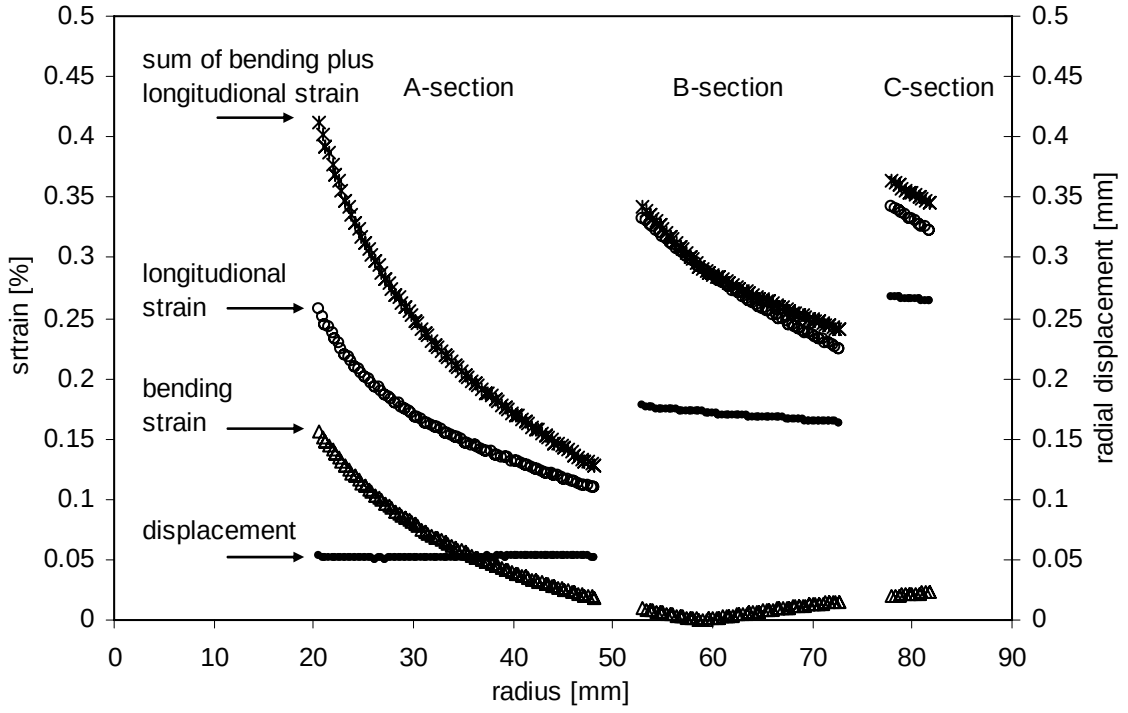

Figure 6-19. Calculated strain and radial displacement at the design current density of 126 A/mm^2 and in a background magnetic field of 20 T for the 5T insert as built.

Operation

During testing of the 5T insert it is observed that the E-J_{op} data can be described using the power law (equation 2-4) as expected. However, the voltage is only stable up to the equivalent of ~ 0.3 μV/cm. Beyond this level section A starts to quench. Thus it is not possible to characterize the 5T insert using J_e at the 1 μV/cm criterion, as is used for all other coils and conductors in this work. Instead the insert is characterized by:

1. its quench current at a given ramp rate and
2. voltage-current data up to ~ 0.3 μV/cm.

An operating current density of 120 A/mm^2 was repeatedly reached in a background magnetic field of 20 T, sufficient to reach a central field of 25.0 T. This milestone was reached without degradation of the insert properties, setting a world record for the central magnetic field inside an HTS insert[69]. The calculated peak stress in the reinforced conductor of the B and C sections is 200 MPa, as illustrated in Figure 6-20. Such stress levels could not have been reached into this conductor without reinforcement, as the stress-strain curve for conductor C in Figure 6-1 clearly illustrates. The chosen conductor reinforcement using a 27 μm thick stainless steel tape is adequate, considering the absence of degradation, and efficient considering that the calculated safety margins range between 1.0 to 1.2 for each of the three sections.

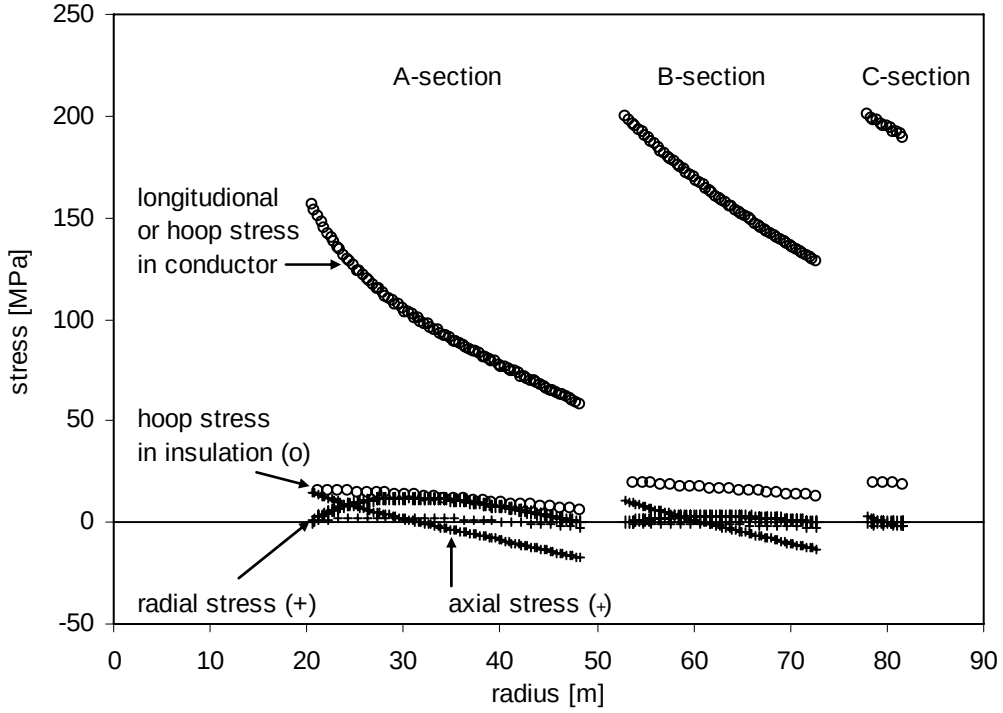

Figure 6-20. Calculated stress at the design current density of 126 A/mm^2 and in a background magnetic field of 20 T for the 5T insert as built.

The hoop stress at the outer diameter σ_{OD} following equation 6-5 is a suitable metric to compare the stress level in the 5T with other insert coils. Also in this respect is the 5T insert found to exceed the performance of other BSCCO insert coils. The value of σ_{OD} in sections B and C (125 and 114 MPa respectively) is well above that of the next highest insert coils (94 MPa for Homer II in 2004 and 97 MPa for the Hitachi coil A of the year 2000 as listed in Table 1-1). The value of σ_{OD} in the 5T A-section (85 MPa) is exceeds that of all other BSCCO coils in Table 1-1.

Using the classification of Table 2-1, the radii of sections A, B and C qualify as small, medium and large respectively. J_e, and correspondingly the stress tolerance, of the A and B sections are suitable for inserts to generic 25 T research magnets and the inner sections of NMR type 25 T magnets, with coil C marginally suitable for large radii NMR sections.

[69] Recent ReBCO insert coils and a small Bi-2212 wire wound coil have eclipsed this record [55].

6.7 Outlook beyond 25 T

To design fully superconducting magnets with central magnetic field above 25 T that remain reasonably compact, it is imperative that the average current density in the windings of the HTS is increased from its benchmark value of 100 A/mm^2 for 25 T magnets. In section 1.3.3 it was observed that a 5 T HTS insert operating at an average winding current density (J_{ave}) of 100 A/mm^2 in a 20 T background magnetic field would hypothetically generate 30 T in the case J_{ave} of the HTS insert was doubled to 200 A/mm^2. Here we will investigate what increase in J_{op} is required for a strain limited conductor for such an increase in J_{ave} using the simple example of a coil with limited winding thickness. This exercise will lead to an outlook on stress-strain management and required engineering critical current densities for magnets beyond 25 T.

An example coil

The 5T C-coil is a suitable starting point as it features the highest hoop stress and strain of any BSCCO insert coil built to date. So a radius r of 80 mm and a local magnetic field of 20 T are assumed. Radial gradients in the hoop stress are ignored initially. Preliminary designs of a 32 T magnet with a 40 mm winding inner diameter also show the highest hoop stress at around 80 mm radius and about 20 T magnetic field, so these values seem to be a reasonable choice. First we compare 3 conductors taking the design strain limit ε_{design} as 0.3%. Conductor B is chosen to represent a generic BSCCO conductor with dispersion hardened matrix, conductor G represents a generic ReBCO coated conductor and third is a generic Nb_3Sn conductor. The Nb_3Sn conductor is included in this analysis as the results have implications for the optimum magnetic field value to cross-over from application of Nb_3Sn to HTS. Nb_3Sn conductors are not suitable for application above ~ 25 T considering the magnetic field dependence of J_e of currently produced Nb_3Sn conductors, as shown in Figure 1-4.

The 0.3% strain limit is reasonable for BSCCO conductors as it is well below the characteristic irreversible strain limit of 0.38 to above 0.40% as listed in Table 6-2 for conductors A,B,C,D and H. The assumption of a design strain of 0.30% for Nb_3Sn conductor is based on bronze-route Nb_3Sn [133] and the stress-strain curve for high current-density Nb_3Sn in [134]. For ReBCO designs strain values of both 0.30% and a more conservative value of 0.25% are considered [135, 136]. For comparison, results for a BSCCO conductor with a pure-Ag matrix based on conductor I are presented using a design strain of 0.15%. The stress values σ_{sc} corresponding to the design strain are listed in Table 6-7. In all cases, reinforcement using a material with a modulus E_{SS} of 208 MPa is assumed, as measured for the stainless steel tape in the 5T insert and a packing factor λ of 70%. The packing factor is taken as the sum of the conductor and reinforcement cross-sectional area divided by the winding cross-sectional area. As we are considering a thin coil, this reinforcement can either be a co-wound tape or overbanding.

Table 6-7. Design strain limits of HTS conductors.

		BSCCO	**Nb_3Sn**	**ReBCO**		**BSCCO**
Description		Hardened matrix		Conductor G		Pure Ag matrix
Design strain limit	%	0.30	0.30	0.30	0.25	0.15%
Stress at ε_{design} (σ_{sc})	MPa	120	150	510	420	35

In the case the hoop stress is below σ_{sc}, the coil is not strain limited and the average winding current density is

$$J_{ave} = \lambda \cdot J_{op} \text{ for } J_{op} \cdot B \cdot r \leq \sigma_{sc}. \quad (6\text{-}9)$$

Straightforward geometric considerations show that the average winding current density in the case the coil is strain limited follows from

$$J_{ave} = \lambda \cdot J_{op} \cdot \frac{1}{1+\left(\frac{J_{op} \cdot B \cdot r - \sigma_{sc}}{\varepsilon_{design} \cdot E_{SS}}\right)} \quad \text{for } J_{op} \cdot B \cdot r > \sigma_{sc}. \tag{6-10}$$

Obviously J_e must be larger than J_{op}. In the extreme case of J_{op} and J_e approaching infinity one has

$$J_{ave} = \lambda \cdot \frac{\varepsilon_{design} \cdot E_{SS}}{B \cdot r} \quad \text{for } J_{op} \to \infty. \tag{6-11}$$

In this example the average winding current density could never reach or exceed 273 A/mm^2 for $\varepsilon_{design} = 0.3\%$. Thus the average winding current density increases proportionally with J_{op} until the design strain limit is reached beyond which the slope progressively decreases and ultimately approaches a constant only determined by the design strain, modulus of the reinforcement and coil geometry. The resulting relation between J_{ave} and J_{op} in this example is shown in Figure 6-21. Four observations are made:

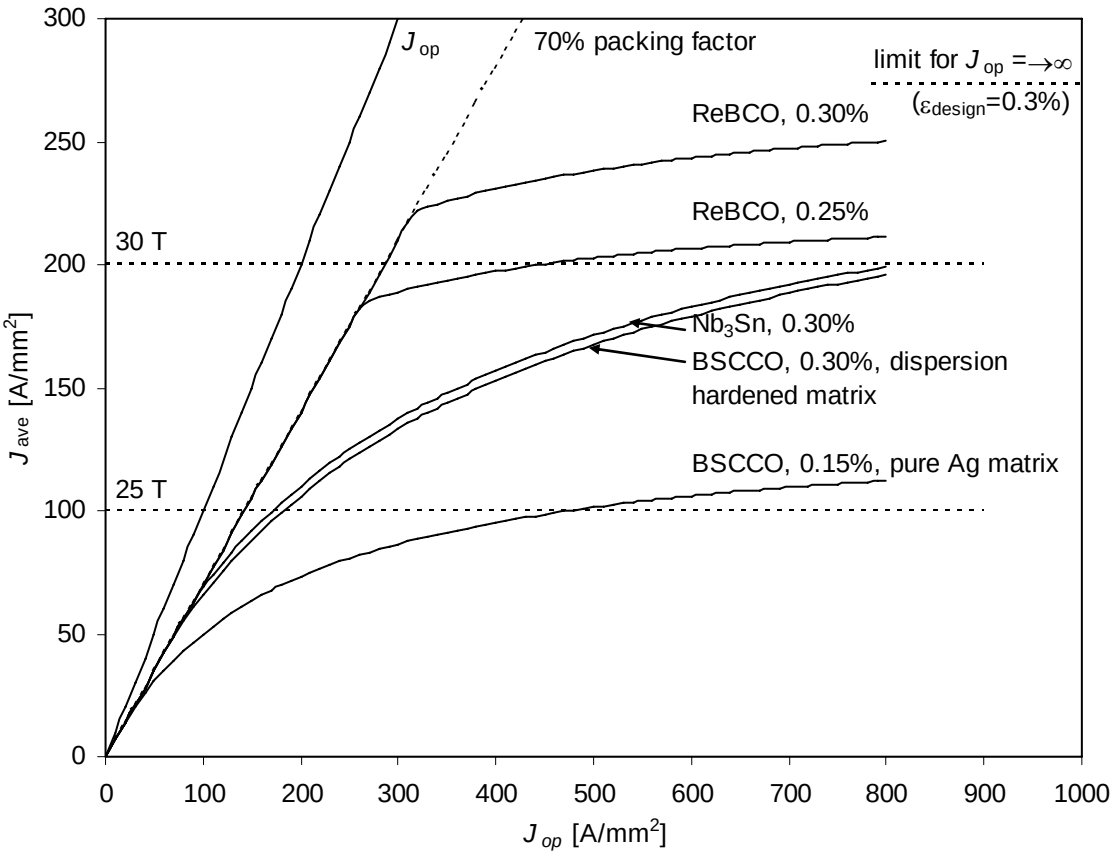

Figure 6-21. Calculated relation between operating current density and average winding current density for strain-limited conductors reinforced with stainless steel. The patterns are generic, the specific numbers used are explained in the text. Benchmark current densities for HTS sections of compact 25 T and 30 T magnets are indicated. The design strain limit is included in the label for each curve representing a conductor. A conductor is strain-limited when its J_{ave} line deviates from $\lambda \cdot J_{op}$. The magnetic field dependence of J_e places additional limits on J_{op}, precluding the use of Nb_3Sn conductors above 25 T

1) First, only the ReBCO example conductor using a design strain of 0.30% can be operated at $J_{ave} = 200$ A/mm^2 without being strain limited. However, at the reduced design strain of 0.25%, the conductor is strain limited. Adding reinforcement is relatively inefficient as the difference in modulus between the conductor and insulation is small, requiring an increase of J_e from 280 A/mm^2 at $\varepsilon_{design} = 0.30\%$ to 450 A/mm^2 at $\varepsilon_{design} = 0.25\%$. Conductor F can not carry such current densities but more recent ReBCO coated conductors can [137].

2) Both Nb_3Sn and BSCCO conductors with a dispersion hardened matrix can reach $J_{ave} = 100$ A/mm^2 with relatively little reinforcement with J_{op} below 200 A/mm^2. However, reaching $J_{ave} = 200$ A/mm^2 requires significant reinforcement and more than a quadrupling of J_{op} to around 800 A/mm^2. This is not feasible with the BSCCO conductors considered here or any currently available commercial BSCCO or Nb_3Sn conductor. Pre-compression as discussed below can improve the outlook for the applicability of Nb_3Sn and BSCCO though.

3) BSCCO conductors with a pure Ag matrix can achieve 100 A/mm^2 at $\varepsilon_{design} = 0.15\%$ if they are significantly reinforced (reinforcement is 2.35 times the cross sectional area of the conductor) and feature $J_e > J_{op} \sim 500$ A/mm^2. However, if the reinforcement is bonded to the superconductor while it is under significant tension, the superconductor is placed in compression. This pre-compression of the HTS conductor allows the conductor-reinforcement composite to be operated at higher strain levels and ε_{design} can be raised using a modest amount of reinforcement. The manufacturer applied this technique to Conductor A, resulting in $\varepsilon_{crit} > 0.4\%$. This conductor is employed in Coil 1 and reached $J_{ave} = 130$ A/mm^2 at 19 T with $J_e = 204$ A/mm^2 while the amount of reinforcement is only 0.24 times the cross sectional area of the conductor. Thus, conductor A performs equal or somewhat better in high-stress coils than BSCCO conductors with dispersion hardened matrices. As stated above, operation at 200 A/mm^2 at $r = 0.08$ m and $B = 20$ T is not feasible. However, this does illustrate the applicability of conductor pre-compression as a tool for strain management in coil design.

4) Determination of the cross-over magnetic field value above which to use HTS conductors instead of Nb_3Sn should not only be based on a comparison of $J_e(B)$ of the two types of conductor. This is appropriate when the design strain and stress value at the design strain are comparable, as is generally the case with BSCCO and Nb_3Sn conductors, as shown in Figure 6-21. However, ReBCO conductors are that much stronger at a given design strain that the cross-over magnetic field value should be based on a comparison of achievable J_{ave} for the applicable magnetic field and stress levels. The resulting cross-over magnetic field value will thus be below the below the cross-over value based on $J_e(B)$.

Outlook

The above analysis is for a relevant but simplified case. Nonetheless, it is clear that among the currently available conductors only the ReBCO coated conductors can be applied with little or no reinforcement at the current densities required for compact superconducting magnets with a central magnetic field around 30 T. Pre-compression of the super-conductor by laminating with a reinforcement tape under tension can be a useful mechanism in coil design with using strain-limited conductors like BSCCO and Nb_3Sn and especially for ReBCO conductors.

ReBCO conductors have the advantage that, due to their asymmetrical layered cross section, the superconducting layer can be put in compression due to bending. Thus a higher hoop strain is tolerable, as opposed to the case of BSCCO conductors where

increased bending strain reduces the acceptable hoop strain. For example, tensile bending strain is up to a third of the total tensile strain in the conductor of the 5T A-section. So if bending hypothetically could have been ignored, the A-section could have been designed to a ~ 50% higher hoop strain. Thus the advantage that bending ReBCO conductors leads to compression rather than tension in the superconductor can be substantial.

The cross-over magnetic field value separating the use of Nb_3Sn and ReBCO in coils is well below 20 T, if that cross-over is determined by the average current density in the windings. To make a first-order estimate one can compare the highest J_{op} observed in ReBCO inserts of ~ 600 A/mm^2 (see Table 1-1) and compare it with the high current-density RRP Nb_3Sn data of Figure 1-4. That would place the cross-over at 17 T. However, the observed maximum J_{op} in the ReBCO coils is likely well below J_e., suggesting a lower cross-over. The ReBCO conductor requires less reinforcement and the resulting advantage in J_{ave} would also favor a lower cross-over. Conversely, the maximum magnetic field angle in such coils will tend to be larger than in coils operating above 20 T [70], with a reducing effect on J_e. But, as can be seen in Figure 1-4, even in the worst case of a 90° magnetic field angle, the cross over for the best Nb_3Sn conductor and ReBCO coated conductor still occurs between 17 and 18 T.

In Nb_3Sn J_e rises more rapidly with reduced magnetic field than in HTS conductors. Considering again the worst case for ReBCO of perpendicular magnetic field, J_e is about 25% higher in Nb_3Sn at 1 T below the magnetic field value of equal J_e. To develop an understanding of the balance between the increase of J_e in Nb_3Sn with reduced magnetic field and the reduction in J_{ave} due to the required reinforcement, the Modified900 outsert is used as an example. Section 5, as listed in Table 4-1, does not require reinforcement while reinforcement takes up 25% of the windings of Section 6. The cross-over between those sections is at a radius of 0.17 m and a magnetic field of 16.3 T. A ReBCO coil at those diameters and current densities would not need reinforcement as equation 6-9 applies. Based on equation 6-10 and the parameters of Table 6-7, the windings of a thin fictitious Nb_3Sn coil would consist of 60% reinforcement. This percentage appears to be somewhat high. If however a design strain of 0.4% is assumed[71], the amount of reinforcement is reduced to 25% of the windings which is consistent with Section 6 of the Modified900. So, at the threshold of Nb_3Sn requiring reinforcement, which happens to be close but below to the magnetic field value where J_e in Nb_3Sn and ReBCO are comparable, ReBCO coils can have 25% lower J_e but still have the same winding J_{ave} as a comparable Nb_3Sn coil. Thus the cross-over between Nb_3Sn and ReBCO, the magnetic field value of equal J_{ave}, can be estimated as in the order of 1 T below the magnetic field value of equal J_e. The considerations on the cross-over magnetic field value are obviously dependent on the specific features of the available Nb_3Sn and ReBCO conductors and specific aspects of the magnet design. However, the optimum cross-over based on winding current density may be predicted in general as at least a few tesla below 20 T.

6.8 Conclusion

The relations between uni-axially applied tensile stress, strain and critical current at cryogenic temperatures are experimentally investigated for a range of BSCCO tape conductors. It is found that the conductor stress-strain curves can all be accurately

[70] In a preliminary design of a 32 T magnet with a cross over between Nb_3Sn and HTS at 16 T the maximum field angle in the HTS section is 20 degrees.

[71] Or for example a design strain of 0.3% and a compressive strain of 0.1% in the Nb_3Sn conductor resulting from the reinforcement.

described with second-order polynomials over the range of interest for magnet design. For conductors with an alloyed matrix, the strain at the onset of critical current density degradation is about 0.40%. The strength of bare conductors at this strain level is insufficient for application in 25 T class insert magnets. Therefore, reinforcement is required, either integrated with the conductor or applied during coil winding.

To estimate the maximum retained bending strain in the filaments one has to consider that the bending process is partially plastic, the diameter at which the conductor is heat treated and the distance from the outer filaments to the surface of the conductor. Bend-and-release experiments on several BSCCO tape conductors provide insight to the degree of plasticity upon bending. Bare conductors are found to retain a fixed percentage of the applied bending strain that varies per conductor (45-80%) whereas bending in a steel reinforced conductor is almost purely elastic. The results are sensitive to the method of applying bending strain.

ReBCO is different in that the superconducting layer is thin compared to the conductor thickness (~ 1% versus 50-70% for BSCCO) and not necessarily symmetric around the neutral line, so there is no significant bending strain gradient. Bending strain is determined by the position of the ReBCO layer relative to the neutral line. By placing the ceramic on the inside of the neutral line, the bending strain is negative and negates some or all of the hoop strain, which is not possible with BSCCO conductors.

For practical purposes regarding inserts BSCCO is insensitive to tensile strain up to the critical strain, whereas the engineering critical current density in ReBCO is intrinsically strain dependent. Although the strain dependence is not large (~ 10% reduction in the engineering critical current density at critical strain), it may be significant for inserts operating at large strain and a large fraction of the engineering critical current density.

A number of trial coils, mostly featuring diameters and current densities relevant to insert coils, were subjected to increasingly larger Lorentz-force induced stress to study the effect thereof on the engineering critical current density. A wide range of behavior is observed, ranging from severe degradation at moderate stress levels in un-reinforced conductor to little or no degradation at high stress levels when reinforcement is present. Two candidate double pancake coils and a prototype layer wound coil for the 5T insert can be operated to 5T design stress without degradation, featuring estimated safety margins between 1.0 and 1.2.

A Generalized Plane Strain model is applied to calculate the Lorentz-force induced strain versus radius for several coils in which strain induced degradation is observed. The conductor strain is calculated as the sum of bending strain and Lorentz-force induced strain. The predicted onset and propagation on an unreinforced coil is accurate, if stress-strain data obtained from a thin coil is used in the model. Stress-strain data obtained from a single bare sample of this pure-Ag matrix conductor is not representative for the coil on account of lower strength and an earlier onset of major plasticity. For the 5T candidate and prototype coils the model is used to correctly predict the onset of degradation of the engineering critical current density degradation using a critical strain of $0.41 \pm 0.01\%$. However, propagation of degradation with increasing stress is not accurately predicted using this model, likely because of inhomogeneity in the engineering critical current density versus strain characteristics in the conductor. It remains necessary to experimentally determine if a coil can tolerate the design strain. Determination of the engineering critical current density versus strain relation on multiple parallel conductors reinforced as

in a coil may yield a more accurate input to the model and thereby a more accurate prediction of the propagation of strain induced degradation in coils.

It appears that calculating the conductor strain as the sum of bending strain and Lorentz-force induced strain is adequate to predict the onset of degradation.

The approach outlined above lead to the insert coil designed with small safety margins that reached its goal of generating 5 T in a 20 T background without strain induced engineering critical current density degradation. It is the first BSCCO insert coil to reach 25 T while the stress levels are comparable (A-section) or significantly higher (B and C section) than in the next two high-stress BSCCO insert coils.

Two ReBCO insert coils operate at comparable or even higher stress levels, and at least twice the current density levels as BSCCO inserts. A systematic study involving model predictions and measurements on the relation between stress, strain and engineering critical current density degradation in coils, comparable to the work on BSCCO coils presented here, is required to develop ReBCO insert coil technology in full.

Looking ahead at possible 30 T fully superconducting magnets it appears that ReBCO conductors are the prime candidates for application in the HTS sections based on demonstrated engineering critical current density and the strength of the conductor. The cross-over magnetic field for the application of ReBCO versus Nb_3Sn is likely to be at least several tesla below 20 T. Reinforcement of the conductor, if required, by lamination with tapes under tension such as to put the conductor in compression is expected to be more efficient than simple overbanding.

7 Conclusion

Several Bi-2212 round wires and tapes as well as Bi-2223 and ReBCO tape conductors from different sources are investigated. The magnetic field dependence of the engineering critical current density, mechanical properties and degradation effects limiting conductor performance within coils are investigated. The development of an HTS insert coil with a target field increment of 5 T for a central field of 25 T is guided by the following crucial question: can the properties of such an insert coil be predicted based on the conductor properties?

A comprehensive list of conclusions drawn from this work is as follows:

1. Benchmark values for HTS coils in 25 T magnets include an average coil winding current density of 100 A/mm^2, a conductor engineering critical current density of 140-200 A/mm^2 and hoop stress levels of 80-160 MPa.
2. Most of the investigated conductors are suitable for use in HTS inserts of 25 T magnets, although most require additional reinforcement.
3. Variability in the self-field engineering critical current density of the Bi-2212 tapes is high and no reasonable conductor qualification criterion for the 5T insert could be set.
4. The magnetic field dependence of the engineering critical current density in double pancake coils can be modeled accurately. This allows the determination of self-field qualification criteria for the coils and determination of the optimum stacking configuration.
5. Routine characterization of the engineering critical current density of conductors at no less than 5 T is likely to be useful, as opposed to characterization at self-field.
6. The highest field angle in 5T HTS inserts of 25 T magnets is likely to be below 10°. Therefore, the ratio of the engineering critical current density for 0°and 90° magnetic field angle is not a useful measure for conductor anisotropy here.
7. Anisotropy in the magnetic field dependence of the engineering critical current density in the BSCCO tape conductors and coils can be modeled using the average grain misalignment parameter, which is determined from measured conductor properties.
8. The modeling of anisotropy in BSCCO tapes leads to the definition of the effective perpendicular magnetic field component that determines the engineering critical current density for all magnetic field angles.
9. A similar model for ReBCO conductors may only be effective for small magnetic field angles, making the effective parallel magnetic field component the relevant parameter.
10. The coil design priorities are strongly affected by the value of the average grain misalignment parameter of the conductor. The design regime can be axial magnetic-field limited, radial magnetic-field limited or an intermediate regime.
11. Beside conductor thickness and bending diameter, the heat treatment diameter, filament zone thickness and conductor plasticity must be taken into account to

determine the bending strain in the superconducting filaments of BSCCO conductors.

12. For conductor characterization, the method of bending matters and should closely mimic coil winding.
13. Unlike for BSCCO conductors, the bending strain in the superconducting layer of ReBCO coated conductors has a narrow range and can be compressive only, which is advantageous from a viewpoint of strain management in coil design.
14. Calculating the conductor strain as the sum of peak bending strain and hoop strain is adequate to predict the onset of strain induced degradation in BSCCO coils.
15. The tensile stress-strain properties of the BSCCO tape conductors at 77 K can, in the elastic regime, be described by a second order polynomial.
16. Modeling of the stress-strain properties of HTS coils using a Generalized Plane Strain code is useful to support the design process. It can predict the onset and propagation of strain induced engineering critical current density degradation.
17. There is significant variability in the critical tensile-strain value of the Bi-2212 tape conductor. Taking the lower bound as representative results in an accurate prediction of the onset of strain induced degradation in coils, but not of its propagation with increasing hoop stress.
18. Tensile stress-strain-engineering critical current density relations should preferably be measured on multiple parallel conductors reinforced as in a coil. Free-standing samples are subject to necking and the observed properties are not necessarily representative for the properties of the conductor in a coil.
19. For the latter two arguments, it was necessary to experimentally verify if the 5T trial coils can tolerate the design conditions.
20. Trial coils for the 5T insert tolerate a design-equivalent stress state without degradation but with little margin, indicating that design is mechanically sound and efficient.
21. The knowledge gained as outlined above proved to be a valuable contribution to HTS magnet technology as the 5T Bi-2212 tape insert was the first superconducting coil to achieve the landmark 25 T central magnetic field value.
22. The 5T insert design is appropriate as strain induced degradation is absent and coil engineering critical current density could be predicted to better than 5%.
23. The average winding current density of ~ 90 A/mm^2 is comparable to other successful BSCCO insert coils and the benchmark value; the peak conductor stress of ~ 200 MPa is higher than in any other BSCCO insert coil and slightly above the benchmark, establishing the relevance of the 5T insert.
24. The first ReBCO insert coils tolerate twice the hoop stress, carry at least twice the current density compared to BSCCO insert coils and have reached central field values of nearly 34 T, which represents an unusually large performance gain.
25. To reduce hoop strain in ReBCO coils it is likely to be more efficient to place the conductor under compressive pre-strain than using plain co-winding or overbanding.
26. ReBCO coils require magnet technology development using a similar approach as used for BSCCO.

27. To design reasonably compact 30 T superconducting magnets it is necessary to target an average HTS winding current density of around 200 A/mm^2.
28. If considerations are limited to the mechanical strength and magnetic field dependence of the engineering critical current density in the conductor for application in 30 T superconducting magnets, then
    a. ReBCO coated conductors are the prime HTS candidate conductor,
    b. the optimum cross over between Nb_3Sn and ReBCO based on technical arguments is in the 16-18 T range.

Based on the experience laid down in this thesis, and provided that a few technical challenges like cabling issues can be solved as well as conductor cost in mass production considerably reduced, we may expect further penetration of HTS material in large quantities in high field magnet systems for 30 T and beyond.

References

1 http://public.web.cern.ch/public/en/LHC/LHC-en.html

2 Seitz-Richardson Panel, 1988, *Final report of NSF panel on large magnetic fields*, National Academy of Science report.

3 M. Decroux, P. Selvam, J. Cors, B. Seeber, O. Fisher, R. Chevrel, P. Rabiller, M. Sergent, *Overview of the recent progress on Chevrel phases and the impact on the development of $PbMo_6S_8$ wire*, IEEE Transactions on applied superconductivity, volume 3, pages 1502-1509, 1993.

4 S. Foner, E.G. McNiff, Jr., E.J. Alexander, *600 kG superconductors*, Physics Letters A, volume 49A, pages 269-270, 1974.

5 Website: http://www.bruker-biospin.com/nmr_magnets_950us2.html, accessed November 26, 2008, original press release: April 25, 2006.

6 M.N. Wilson, *Superconducting magnets*, 1990 ed. (Oxford University Press, Oxford, 1983).

7 Y. Iwasa, *Case studies in superconducting magnets* (Plenum Press, New York, 1994).

8 D.B. Montgomery, *Solenoid magnet design* (Wiley-Interscience, New York, 1969).

9 A. Rimikis, F. Hornung, Th. Schneider, *High field magnet facilities and projects at the Forschungszentrum Karlsruhe*, IEEE Transactions on applied superconductivity, volume 10, pages 1542-1545, 2000.

10 M.D. Bird, G. Aubert, S. Bole, F. Debray, Y.M. Eyssa, B.-J. Gao, W. Joss, M. Ohl, P. Rub, and H.-J. Schneider-Muntau, in *The NHMFL/GHMFL Resistive magnet collaboration*, pages 642-644 (Science Press, Beijing, 1997).

11 T. Kiyoshi, A. Otsuka, S. Choi, S. Matsumoto, K, Zaitsu, T. Hase, M. Hamada, M. Hosono, M. Takahashi, T. Yamazaki, H. Maeda, *NMR upgrading project towards 1.05 GHz*, IEEE Transactions on applied superconductivity, volume 18 pages 860-863, 2008.

12 http://www.manep.ch/pdf/events/21T_features.pdf, accessed February 7, 2009.

13 K. Inoue, T. Takeuchi, T. Kiyoshi, T. Asano, Y.Sakai, K. Itoh, G. Kido and H. Maeda, *High-field installations at the Tsukuba magnet laboratories of NRIM*, Physica B: Condensed Matter, volume 211, issues 1-4, pages 17-22, 1995.

14 T. Kiyoshi, H. Kitaguchi, M. Kosuge, M. Yuyama, H. Nagai, H. Wada, M. Okada, K. Tanaka, T. Wakuda, K. Ohata, J. Sato, *Generation of 23.4 T using two Bi-2212 insert coils,* IEEE Transactions on applied superconductivity, volume 10, issue 2, pages 472-477, 2000.

15 T. Kiyoshi, personal communication, October 2008.

16 A. Otsuka, T. Kiyoshi, S. Matsumoto, K. Kominato, M. Takeda, *Field stability of a 600 MHz NMR magnet in the driven-mode operation*, IEEE Transactions on applied superconductivity, volume 18, pages 852-855, 2008.

17 J.A. Parrell, Y. Zhang, M.B. Field, P. Cisek, S. Hong, *High field Nb_3Sn conductor development at Oxford Superconducting Technology*, IEEE transactions on applied superconductivity, volume 13, pages 3470-3473, 2003.

18 T. Kiyoshi, A. Otsuka, S. Choi, S. Matsumoto, K. Zaitsu, T. Hase, M. Hamada, M. Hosono, M. Takahashi, T. Yamazaki, H. Maeda, *NMR upgrading project towards 1.05 HGz,* IEEE Transactions on applied superconductivity, volume 18, pages 860-863, 2008.

19 W.D. Markiewicz, J.R. Miller, J. Schwartz, U.P. Trociewitz, H.W. Weijers, *Perspective on a superconducting 30 T/1.3 GHz NMR spectrometer magnet*, IEEE Transactions on applied superconductivity, volume 16, issue 2, pages 1523-1526, 2006.
20 T.A. Painter, *Conceptual design of a superconducting 30 T solenoid using wire-in-conduit conductors*, IEEE Transactions on applied superconductivity, volume 15, issue 2, pages 1427-1430, 2005.
21 National Research Council, *Opportunities in high magnetic field science*, National Academies Press, Washington D.C., pages 46-61, 2005.
22 A. Godeke, et al., *Development of wind-and-React Bi-2212 accelerator magnet technology*, IEEE Transactions on applied superconductivity, volume 18, issue 2, pages 516-519, 2008.
23 D.E. Wesolowski, M.O. Rikel, J. Jiang, S. Arsac, E.E. Hellstrom, *Reactions between oxides and Ag-sheathed $Bi_2Sr_2CaCu_2O_x$ conductors*, Superconductor science and technology, volume 18, pages 934-943, 2005.
24 H. Miao, K.R. Marken, J. Sowa, J. Parrell, S. Hong, *Long length AgMg clad Bi-2212 multifilamentary tapes*, Advances in cryogenic engineering, volume 48, pages 709-716, 2002.
25 H. Miao, K.R. Marken, M. Meinesz, B. Czabaj, S. Hong, *Development of Bi-2212 conductors for magnet applications*, Advances in Cryogenic Engineering, volume 50, pages 603-611, 2004.
26 U. Schoop et al., *Second generation HTS wire based on RABiTs substrates and MOD YBCO*, IEEE Transactions on applied superconductivity, volume 15, issue 2, pages 2611-2616, 2005.
27 H.A.A. Fukushima, H. Takahashi, R. Kuriki, S. Miyata, Y. Yamada, Y. Shiohara, *GdBCO and YBCO long coated conductors and coils*, Physica C, volumes 463-465, pages 501-504, 2007.
28 D.W. Hazelton, personal communication July-August 2007, also presented at MT-20 conference, Philadelphia, 2007 and MRS spring meeting 2008 as part of X.X.Y. Chen et al., *Recent progress in second-generation HTS wire technology at Superpower*. See also reference 52.
29 D. B. Montgomery, *Solenoid magnet design*, Wiley-Interscience, New York, 1969.
30 W.D. Markiewicz, L.A. Bonney, I.R. Dixon, Y.M Eyssa, C.A. Swenson, H.-J. Schneider-Muntau, *Technology of 1 GHz NMR superconducting magnets*, Physica B, volume 216, pages 200-202, 1996; also W. D. Markiewicz, I.R. Dixon, J. Schwartz, C.A. Swenson, S.W. Van Sciver, H.-J. Schneider-Muntau, *25 T High resolution NMR magnet program and technology*, IEEE Transactions on Magnetics, volume 32, pages 2586-2589, 1996.
31 T. Kiyoshi, A. Sato, H. Wada, S. Hatashi, M. Shimada, Y. Kawate, *Development of 1 GHz superconducting NMR magnet at TML/NRIM*, IEEE Transactions on applied superconductivity, volume 9, issue 2, pages 559-562, 1999.
32 J.G. Bednorz and K.A. Müller, *Possible high T_c superconductivity in the Ba-La-Cu-O system*, Zeitschrift für physik B, volume 64, pages 189–193, 1986.
33 National Science Foundation, 1990, cooperative agreement no. DMR-9016241.
34 K. Ohkura, K. Sato, M. Ueyama, J. Fujikami, Y. Iwasa, *Generation of 24.0 T at 4.2 K and 23.4 T at 27 K with a high-temperature superconductor coil in a 22.54 T background field*, Applied physics letters, volume 67, pages 1923-1925, 1995.
35 D.W. Hazelton, J.A. Rice, Y.S. Hascicek, H.W. Weijers, S.W. Van Sciver, *Development and test of a BSCCO-2223 HTS high field insert magnet for NMR*, IEEE Transactions on applied superconductivity, volume 5, pages 234-237, 1995.

36 T. Kiyoshi, K. Inoue, M. Kosuge, H. Kitaguchi, H. Kumakura, H. Wada, H. Maeda, *NRIM R&D program on HTS coils for 1 GHz NMR spectrometer*, Advances in cryogenic engineering, volume 43, pages 1099-1102, 1997.

37 M. Okada, K. Tanaka, K Fukushima, J. Sato, H. Kitaguchi, H. Kumakura, T. Kiyoshi, K. Inoue, K. Togano, *Bi-2212/Ag superconducting insert magnet for high magnetic field generation over 22 T*, Japanese journal of applied physics, volume 35, pages L623-L626, 1996.

38 H.W. Weijers, K. Marken, D. Hazelton, Y.S. Hascicek, J. Schwartz, *Recent developments on Bi-2212 insert coils*, 8th US-Japan workshop on high T_c superconductors, Tallahassee, Florida, (National High Magnetic Field Laboratory), pages 247-254, 1997.

39 H.W. Weijers, D. Hazelton, L. Cowey, Y.S. Hascicek, I.H. Mutlu, U.P. Trociewitz, S.W. Van Sciver, *Bi-2212 coils for 1 T class insert coils*, Advances in cryogenic engineering, volume 43, pages 173-179, 1998.

40 D.W. Hazelton, X. Yuan, H.W. Weijers, S. Van Sciver, *HTS insert coils for high field NMR spectroscopy*, IEEE Transactions on applied superconductivity, volume 9, issue 2, pages 956-959, 1999.

41 H.W. Weijers, *Repeated testing of HTS magnets*, Presented at the Cryogenic engineering conference in Montreal, unpublished, MST internal document NHMFL-MST-09-PRES-577-001, 1999.

42 H.W. Weijers, Q.Y. Hu, Y. Viouchkov, E. Celik, Y.S. Hascicek, K. Marken, J. Parrell, J. Schwartz, *Development and testing of a 3 T Bi-2212 insert magnet*, Advances in cryogenic engineering, volume 45, pages 769-778, 2000.

43 M. Okada, *HTS high field magnets*, IEEE Transactions on applied superconductivity, volume 10, pages 462-467, 2000 and M. Okada, K. Tanaka, T. Wakuda, K. Ohata, J. Sato, T. Kiyoshi, H. Kitaguchi, H. Wada, *Bi-2212/Ag high-field magnets*, Physica C, volume 335, pages 61-64, 2000.

44 T. Kiyoshi, A. Atsuka, M. Kosuge, M. Yuyama, H. Nagai, F. Matsumoto, *Generation of high magnetic fields using superconducting magnets*, Fusion and engineering design, volume 81, pages 2411-2415, 2006.

45 H.W. Weijers, Y.S. Hascicek, K. Marken, A. Mbaruku, M. Meinesz, H. Miao, S.H. Thompson, F. Trillaud, U.P. Trociewitz, J. Schwartz, *Development of a 5 T HTS insert magnet as part of 25 T class magnets*, Transactions on applied superconductivity, volume 13, issue 2, pages 1396-1399, 2003.

46 H.W. Weijers, U.P. Trociewitz, K. Marken, M. Meinesz, H. Miao, J. Schwartz, *The generation of 25.05 T using a 5.11 T $Bi_2Sr_2CaCu_2O_x$ superconducting insert magnet*, Superconductor science & technology, volume 17, pages 636-644, 2004.

47 J. Bascuñán, H. Lee, E.S. Bobrov, Y. Iwasa, *A low- and high-temperature superconducting NMR magnet: design and performance results*, IEEE Transactions on applied superconductivity, volume 13, pages 1550-1553, 2003.

48 M. Beckenbach, F. Hornung, M. Klaser, P. Leys, B. Lott, Th. Schneider, *Manufacture and test of a 5T Bi-2223 insert coil*, IEEE Transactions on applied superconductivity, volume 15, issue 2, page1484-1487, 2005.

49 J. Bascuñán, W. Kim, E.S. Bobrov, H. Lee, Y. Iwasa, *An LTS/HTS NMR magnet operated in the range 675-700 MHz*, IEEE Transactions on applied superconductivity, volume 17, issue 2, pages 1446-1449, 2007.

50 S.-Y. Hahn, J. Bascuñán, W-S. Kim, E.S. Bobrov, H. Lee, Y. Iwasa, *Field mapping, NMR lineshape, and screening currents induced field analyses for homogeneity improvement in LTS/HTS NMR magnets*, Transactions on applied superconductivity, volume 18, issue 2, pages 856-859, 2008.

51 N. Amemiya, K. Akachi, *Magnetic field generated by shielding current in high T_c superconducting coils for NMR magnets*, Superconductor science and technology, volume 21, pages 7, 2008.

52 D.W. Hazelton, V. Selvamanickam. J.M. Duval, D.C. Larbalestier, W.D. Markiewicz, H.W. Weijers, R.L. Holtz, *Recent developments in 2G HTS coil technology*, submitted to IEEE Transactions on applied superconductivity, 2008.

53 Y. Yamada, presented at the International symposium on superconductivity, Tsukuba, Japan, October 2007.

54 Y. Yamada, personal communication, Oct 2008.

55 H.W. Weijers, W.D. Markiewicz, K.W. Pickard, P.D. Noyes, U.P. Trociewitz, J. Jiang, D.C. Larbalestier, *Tests of HTS insert coils above 30 T*, presented at the International symposium on superconductivity, Tsukuba, Japan, October 2008. Unpublished to date, MST internal document NHMFL-MST-09-PRES-578-001.

56 http://www.oxinst.com, announced August 21st, 2008, accessed September 6th, 2008.

57 H. Lee, E.S. Bobrov, J. Bascuñán, S-Y Hahn, Y. Iwasa, *An HTS insert for phase 2 of a 3-phase 1-GHz LTS/HTS NMR magnet*, Transactions on applied superconductivity, volume 15, issue 2, pages 1299-1302, 2005.

58 P. Vase, R. Flukiger, M. Leghissa, B. Glowacki, *Current status of high-T_c wire*, Superconductor science and technology, volume 13, pages R71-R84, 2000.

59 H.S. Edelman, D.C. Larbalestier, *Role of c-axis field components in making E(J) characteristics of $(Bi,Pb)_2Sr_2Ca_2Cu_3O_x$ tapes insensitive to the direction of field within the tape plane*, Journal of applied physics, volume 83, pages 4830-4834, 1998.

60 H. Miao, K.R. Marken, J. Sowa, J. Parrell, S. Hong, *Long length AgMg clad Bi-2212 multifilamentary tapes*, Advanced in cryogenics engineering, volume 48, pages 709-716, 2002.

61 H. Miao, K.R. Marken, M. Meinesz, B. Czabaj, S. Hong, *Development of round multifilament Bi-2212/Ag wires for high field magnet applications*, IEEE Transactions on applied superconductivity, volume 15, issue 2, pages 2554-2557, 2005.

62 H. Miao, H. Kitaguchi, H. Kumakura, K. Togano, T. Hasegawa, T. Koizumi, *$Bi_2Sr_2CaCu_2O_x$/Ag multifilamentary tapes with J_c>500000 A/cm^2 at 4.2 K and 10 T by using pre-annealing and intermediate rolling process*, Physica C, volume 303, pages 81-90, 1998.

63 H. Kitaguchi, H. Miao, H. Kumakura, H. Togano, T. Hasegawa, T. Koizumi, *Large J_c enhancement of Bi-2212/Ag tape by PAIR process*, Advances in superconductivity, volume XI, pages 811-816, 1999.

64 T. Kato, S. Kobayashi, K. Yamazaki, K. Okhura, M. Ueyama, N. Ayai, J. Fujikami, E. Ueno, M. Kikuchi, K. Hayashi, K. Sato, *Development of high performance Ag sheathed Bi-2223 wire*, Physica C, volume 412-414, pages 1066, 2004.

65 Y. Yoo, J. Ko, X.D. Su, H. Kim, H. Chung, *Effects of lead content and particle size of precursor powders on formation rate, grain growth and critical current density of BSCCO 2223 tapes*, IEEE Transactions on applied superconductivity, volume 11, pages 3549-3553, 2000.

66 V. Selvamanicam, et al., *Recent progress in second generation HTS conductor scale-up at SuperPower*, IEEE Transactions on applied superconductivity, volume 17, issue 2, pages 3231-3234, 2007.

67 M.W. Rupich, et al., *The development of second generation HTS wire at American Superconductor*, IEEE Transactions on applied superconductivity, volume 17, issue 2, pages 3379-3382, 2007.

68 W.M.W.R. Zhang et al., *Progress in AmSC scale-up of second generation HTS wire*, Physica C, volume 463-465, pages 505-509, 2007.

69 J. Schwartz, H.W. Weijers, *Electrical measurements by transport* in *Characterization of materials*, edited by E. N. Kaufmann, pages 472-489 (J. Wiley & Sons, 2003).

70 H.W. Weijers, S.W. Van Sciver, *Characterizing the S/N transition of VAMAS HTS samples*, IEEE Transactions on applied superconductivity, volume 5, pages 556-559, 1995.

71 International standard IEC 61788-3, Superconductivity-Part3: *Critical current measurement-DC critical current of Ag and/or Ag alloy sheathed Bi-2212 and Bi-2223 oxide superconductors*, http://www.iec.ch/.

72 E.J. McNiff, B. Brandt, S. Foner, L.G. Rubin, R.J. Weggel, *Temperature anomalies observed in liquid ^{4}He columns in magnetic fields with field-field-gradient products > 21 T^2/cm*, Review of scientific instruments, volume 59, pages 2474-2476, 1988.

73 Y. Viouchkov, H.W. Weijers, Q.Y. Hu, Y. Hascicek, J. Schwartz, *Mechanical properties of Ag and AgMg-sheathed $Bi_2Sr_2CaCu_2O_x$ tapes for high field insert magnets*, Advances in cryogenic engineering, volume 46, pages 647-653, 2000.

74 B. ten Haken, *Strain effects on the critical properties of high-field superconductors*, Ph.D. thesis, University Twente, 1994.

75 R.C. Walters, I.M. Davidson, G.E. Tuck, *Long sample high sensitivity critical current measurements under strain*, Cryogenics, volume 26, page 406, 1986.

76 Y. Viouchkov, H.W. Weijers, M. Meinesz, Q. Hu, Y. Hascicek, J. Schwartz, *Stress-strain-I_c characterization of Bi2212 Tapes*, Advances in superconductivity XI, volume 2, pages 1485-1488, 1999.

77 L. Masur, *Long length manufacturing of Bi-2223 wire for motor and cable applications*, Advances in cryogenic engineering, volume 46, pages 871-877, 2000.

78 P.H. Kes, J. Aarts, V.M. Vinokur, C.J. van der Beek, *Dissipation in highly anisotropic superconductors*, Physical review letters, volume 64, pages 1063-1066, 1990.

79 J.W. Ekin, T.M. Larson, A.M. Hermann, Z.Z. Sheng, K. Togano, H. Kumakura, *Double-step behavior of critical current vs. magnetic field in Y-, Bi- and Tl-based bulk high-T_c superconductors*, Physica C, volume 160, pages 489-496, 1989.

80 M.W. Rupich, et al., IEEE transactions on applied superconductivity, volume 11, issue 2, pages 2927, 2001.

81 H.W. Weijers, B. ten Haken, H.H.J. ten Kate, J. Schwartz, *Critical currents in Bi-Sr-Ca-Cu-O superconductors up to 33 T at 4.2 K*, IEEE Transactions on applied superconductivity, volume 11, pages 3956-3959, 2001.

82 D.C. v. d. Laan, *Flux pinning and connectivity in polycrystalline high-temperature superconductors*, Ph.D. Thesis, University of Twente, 2004.

83 L. Stan, et al., *Study of $Sm_xZr_{1-x}O_y$ buffer layer and its effects on YBCO properties*, IEEE Transactions on applied superconductivity, volume 17, pages 3409-3411, 2007.

84 D. Hazelton, personal communications based on presentations to the ONR Generator meeting April 12, 2007 and the Superconductivity for electric power systems annual peer review, August 2-5, 2005 Washington, 2007.

85 E.J. Kramer, *Scaling laws for flux pinning in hard superconductors*, Journal of applied physics, volume 44, pages 1360-1370, 1972.

86 O. van der Meer, B. ten Haken, H.H.J. ten Kate, *A model to describe the angular dependence of the critical current in a Bi-2223/Ag superconducting tape*, Physica C, volume 357-360, pages 1174-1177, 2001.

87 A. Hensel, G. Grasso, R. Flükiger, *Limits to the critical transport current in superconducting (Bi,Pb)$Sr_2Ca_2Cu_3O_{10}$ silver-sheathed tapes: The railway-switch model*, Physical review B, volume 51, pages 15456, 1995.

88 Y.B. Huang, J. Jutson, D.M. Spiller, S. Mills, R. Prowse, W. Blendl, *Micro-XRD phase and texture analysis of the individual filaments of Bi2223 tapes*, Proceedings of 1999 EUCAS conference, Barcelona, Institute of physics Conference series number 167 volume 1, pages 603-606, 2000.

89 Q.Y. Hu, H.W. Weber, H.K. Liu, S.X. Dou, H.W. Neumüller, *Angular dependence of critical currents and grain misalignment in Ag clad (Bi,Pb)$_2Sr_2Ca_2Cu_3O_{10}$ tapes*, Physica C, volume 252, pages 211-220, 1995.

90 D. Bourgault et al, *Misalignment angles and the 2D-3D temperature crossover in Bi2212 multifilaments studied using transport critical current densities*, Superconductor science and technology, volume 17, pages 463-468, 2004.

91 S. Kobayashi, T. Kaneko, T. Kato, J. Fujikami, K. Sato, *A novel scaling of magnetic field dependencies of critical currents for Ag-sheathed Bi-2223 superconducting tape,* Physica C, volume 258, pages 336-340, 1996.

92 B. Xu, J.H. Su, J. Schwartz, *Dependence of transport critical current of magnetic field processed $Bi_2Sr_2CaCu_2O_8$/AgMg tapes on the background magnetic field and magnetic field direction*, Superconductor science and technology, volume 18, pages 503-507, 2005.

93 H.W. Weijers, B. ten Haken, H.H.J. ten Kate and J. Schwartz, *Field dependence of the critical current and its relation to the anisotropy of BSCCO conductors and coils*, IEEE Transactions on applied superconductivity, volume 15, issue 2, pages 2558-2561, 2005.

94 S.M.N. Awaji, K. Wanatabe, M. Miura, Y. Ichino, Y. Yoshida, Y. Takai, K. Matsumoto, *J_c and B_i properties of $Sm_{1+x}Ba_{2-x}Cu_3O_y$ films with nano-particles*, Physica C, volume 463-5465, pages 699-673, 2007.

95 A. Kinoshita, K. Takahashi, H. Kobayashi, Y. Yamada, A. Abi, H. Fukashima, M. Konishi, S. Miyata, Y. Shiohara, T. Kato, T. Hirayama, *Development of a thick GdBCO and ZrO_2-doped GdBCO film with a high critical current on an PLD-CeO_2/IBAD-GZO substrate*, Physica C, volume 463-465, pages 630-632, 2007.

96 K. Nakaoka, J. Matsuda, Y. Itoh, T. Goto, Y. Yamada, T. Izumi, Y. Shiohara, *Influence of the starting composition on superconducting properties of YBCO coated conductors by advanced TFA-MOD process*, Physica C, volume 463-465, pages 519-522, 2007.

97 V. Selvamanickam et al., *Scale up of applications-ready practical Y-Ba-Cu-O coated conductors*, IEEE Transactions on applied superconductivity, volume 15, pages 2597-2599, 2005.

98 W.M.W.R. Zhang et al., Progress in AmSC scale-up of second generation HTS wire, Physica C, volume 463-465, pages 505-509, 2007.

99 J. Gao, M.D. Bird, S. Bole, Y.M. Eyssa, H.-J. Schneider-Muntau, *Design of a 20 T, 200 mm bore resistive magnet,* Transactions on magnetics, volume 32, pages 2562-2565, 1996.

100 Q.Y. Hu, H.W. Weber, H.K. Liu, S.X. Dou, H.W. Neumüller, *Angular dependence of critical currents and grain misalignment in Ag clad (Bi,Pb)$_2Sr_2Ca_2Cu_3O_{10}$ tapes*, Physica C, volume 252, pages 211-220, 1995.

101 S. Kobayashi, T. Kaneko, T. Kato, J. Fujikami, K. Sato, *A novel scaling of magnetic field dependencies of critical currents for Ag-sheathed Bi-2223 superconducting tape*, Physica C, volume 258, pages 336-340, 1996.

102 M. Okada, K. Tanaka, T. Wakuda, K. Ohata, J. Sato, H. Kumakura, T. Kiyoshi, H. Kitaguchi, K. Togano, H. Wada, *A new symmetrical arrangement of tape-shaped multifilaments for Bi-2212/Ag round shaped wire*, IEEE Transactions on applied superconductivity, volume 9, pages 1904-1907, 1999.

103 H.W. Weijers, *Modeling the field dependence of the critical current density in the 3T insert*, MS&T internal note: NHMFL-MST-05-INT-096-002, NHMFL (2005).

104 M. Inoue, T. Kiss, K. Motoyama, S. Awaji, K. Wanatabe, M. Yoshizumi, Y. Yamada, T. Izumi, Y. Shiohara, *Critical current property in YBCO coated conductor fabricated by improved TFA-MOD process*, presented at the 2008 ISS conference, Tsukuba, Japan, to be published in Physica C, 2009.

105 S.B. Kim, S. Murase, Y.Tamada, T. Araki, I. Hirabayashi, *Magnetic-field properties of high critical current density YBCO films deposited by TFA-MOD*, IEEE Transactions on applied superconductivity, volume 15, pages 2645-2648, 2005.

106 M.W. Rupich et al., *The development of second generation HTS wire at American Superconductor*, IEEE Transactions on applied superconductivity, volume 17, pages 3379-3382, 2007.

107 M. Inoue et al., *Enhancement of critical current in YBCO coated conductors in association with c-axis correlated artificial pinning centers*, Physica C, volume 463-465, pages 674-677, 2007.

108 M.D. Bentzon, P. Vase, *Critical current measurements on long BSCCO tapes using a contact-free method*, IEEE Transactions on applied superconductivity, volume 9, pages 1594-1597, 1999.

109 F. Hornung, A. Rimikis, R. Kimmich, T. Schneider, *Investigation of Bi-HTS wires for high field insert coils*, IEEE Transactions on applied superconductivity, volume 11, pages 2304-2307, 2001; F. Hornung, M. Kläser, H. Leibrock, H. Müller, T. Schneider, *Suitability of Bi-HTS wires for high field magnets*, Physica C, volume 401, issue 1, pages 218-221, 2003.

110 K. Higashikawa, T. Nakamura, T. Hoshino, *Anisotropic distributions of critical current density and electric field in Bi-2223/Ag coil with consideration of multifilamentary structure*, Physica C, volume 419, pages 129-140, 2005.

111 Y. Wang, X. Zhao, X. Xu, L. Xiao, L. Lin, G. Lu, D. Hui, S. Dai, *Angular and magnetic field dependence of the critical current density of multifilamentary Bi2223 tapes*, Superconductor science and technology, volume 17, pages 705-709, 2004.

112 H.J.N. van Eck, L. Vargas, B. ten Haken and H.H.J. ten Kate, *Bending and axial strain dependence of the critical current in superconducting BSCCO tapes*, Superconductor science and technology, volume 15, pages 1213-1215, 2002.

113 H.W. Weijers, J. Yoo, B. ten Haken, J. Schwartz, *Bi-Sr-Ca-Cu-O conductors and magnets at high stress-strain levels*, Physica C, volume 357, pages 1160-1164, 2001.

114 International Standard IEC 61788-6 (draft), *Mechanical properties measurement - Room temperature tensile test of Ag/Bi2223 and Ag/Bi2212 composite superconductors*, International Electrotechnical Commision, Technical Committee 90: Superconductivity, 2008.

115 K. Osamura, M. Sugano, A. Nyilas, H.S. Shin, H. Weijers, D.P. Hampshire, N. Morley, K. Morley, S. Keys, M. Leghissa, W. Herkert, K. Katagiri, T. Ogatta, *Report on the first round-robin-test, VAMAS / TWA16-subgroup on mechanical properties of composite superconductors* in Proceedings of the international workshop on mechano-electromagnetic property of composite superconductors, Kobe, Japan, (National Institute for Materials Science, Tsukuba, Japan, 2001).

116 R. Passerini, M. Dhallé, G. Witz, B. Seeber, R. Flukiger, *Engineering the pre-compression of Bi,Pb(2223): the influence of the geometry of the metallic matrix on*

the mechanical properties of tapes, IEEE Transactions on applied superconductivity, volume 11, pages 3018-3021, 2001.
117 B. ten Haken, personal communication, (1998).
118 D.C. v. d. Laan, J.W. Ekin, *Large intrinsic effect of axial strain on the critical current of high-temperature superconductors for electric power applications*, Applied physics letters, volume 90, pages 2007.
119 M. Rabara, et al., *Tensile properties and probability of filament fracture in Bi-2223 superconducting tapes*, Superconductor science and technology, volume 12, pages 1129-1133, 1999.
120 H.W. Weijers, J. Schwartz, B. ten Haken, Bi-based *HTS insert coils at high stress levels*, Physica C, volume 372, pages 1264-1367, 2002.
121 I.H. Mutlu, E. Celik, Y.S. Hascicek, *High temperature insulation coating and their electrical properties for HTS/LTS conductors*, Physica C, volume 370 issue 2, pages 113-124, 2002.
122 W.D. Markiewicz, M.R. Vaghar, I.R. Dixon, *Generalized plane strain analysis of superconducting solenoids*, Journal of applied physics, volume 86, pages 7039-7051, 1999.
123 W.D. Markiewicz, M.R. Vaghar, I.R. Dixon, H. Garmestani, *Generalized plane strain analysis of solenoid magnets*, IEEE Transactions on Magnetics, volume 30, pages 2233-2236, 1994.
124 H.W. Weijers, April 2000, unpublished.
125 A. Spindel, R.P. Reed, M. Tupper, J. Darr, D. Pollock, *Low -temperature electron radiation of insulating films and adhesives*, Advances in cryogenic engineering, volume 40, pages 1169-1176, 1994.
126 Y. Eyssa, personal communication, January 2000.
127 K. Osamura, et al., Advances in cryogenic engineering, volume 38, pages 875, 1992.
128 N. Yamada, K. Nara, M. Okajia, T. Hikata, T. Kaneko, N. Sadakata, *Effect of thermal cycles on thermal expansion of silver-sheathed Bi2223 tape at 10-310 K*, Cryogenics, volume 38, pages 397-399, 1998.
129 J. W. Ekin, *Experimental techniques for low temperature measurements* (Oxford University Press, 2006).
130 H. Kitaguchi, K. Itoh, H. Kumakura, T. Takeuchi, K. Togano, H. Wada, *Strain effect in Bi-based oxide/Ag superconducting tapes*, IEEE Transactions on applied superconductivity, volume 11, pages 3058-3061, 2001.
131 R. Passerini, M. Dhallé, E. Giannini, G. Witz, B. Seeber, R. Flukiger, *The influence of thermal precompression on the mechanical behavior of Ag-sheathed (Bi,Pb)2223 tapes with different matrices*, Physica C, volume 371, issue 3, pages 173-184, 2001.
132 L. Mbaruku, K.R. Marken, M. Meinesz, H. Miao, P.V.P.S.S. Sastry, J. Schwartz, *Effect of processing defects on stress-strain-I_c for AgMg sheathed Bi-2212 tapes*, IEEE Transactions on applied superconductivity, volume 12, pages 3522-3525, 2003.
133 M.R. Vaghar, H. Garmestani, W.D. Markiewicz, *Elastoplastic stress analysis of Nb_3Sn superconducting magnet*, Journal of applied physics, volume 80, pages 2490-2500, 1996.
134 A. Nijhuis, Y. Ilyin, W. Abbas, *Axial and transverse stress-strain characterization of the EU dipole high current density Nb_3Sn strand*, Superconductor science and technology, volume 21, pages 10, 2008.
135 K. Osamura, M. Sugano, K. Nakao, Y. Shiohara, A.Ibi, Y. Yamada, N. Nakashima, S. Nagaya, T. Saitoh, Y. Iijima, Y. Aoki, T. Hasegawa, T. Kato, *Reversible strain limit of critical current and universality of intrinsic strain effect for REBCO-coated*

conductors, Superconductor science and technology, volume 22, pages 021505, 2009.

136 D.C. v. d. Laan, J.W. Ekin, *Large intrinsic effect of axial strain on the critical current of high-temperature superconductors for electric power applications*, Applied physics letters, volume 90, pages 052506, 2007.

137 J. Jaroszynski, personal communication, (October-December 2008).

Summary and outlook

Summary

Properties of various HTS conductors in the form of short samples, small coils and larger prototype coils are studied, predominantly through experiments. The intent is to further develop high-field magnet technology using HTS conductors at 4 K. In the course of this research, conductor batches of Bi-2212 and Bi-2223 tapes, Bi-2212 round wire and YBCO coated conductors are investigated for their applicability in HTS insert coils to high-field magnets. The specific target of demonstrating a proof of principle of 25 T class HTS insert coils is achieved by developing an BSCCO insert coil that generates 5 T in a 20 T background magnet for a central magnetic field of 25 T.

The research is guided in general by questioning how, and to what extent, the properties of short samples can be used to predict properties of smaller and larger coils operated at high magnetic field. The focus in this work is on a number of specific areas in magnet technology, particularly the dependence of critical current density on magnetic field and strain. Models that describe the dependence of the critical current density on magnetic field and strain based on measured short sample properties are used to calculate predicted properties of coils. Those predictions are then compared to observed properties of coils to assess the applicability of the models.

The degree of anisotropy in the magnetic field dependence of the critical current density plays a profound role, as it affects the value of the critical current density and also impacts the design optimization process itself.

Magnetic field dependence of the engineering critical current density

The engineering critical current density of Bi-2212 and Bi-2223 tapes, a Bi-2212 round wire and a YBCO coated conductor are measured and fit equations derived within the magnetic field range of interest, i.e. self-field to at least 25 T and when possible to 45 T. The current densities are sufficient to qualify each conductor as potential candidate for application in HTS coils in 25 T magnets.

The measured magnetic field dependence of the engineering critical current density of a small Bi-2223 coil is accurately described with a model. In this model, the engineering critical current density for perpendicular magnetic field is expressed as the sum of contributions from a parallel network of strongly- and weakly-linked current paths. Values for the parameters in this model are derived from short sample measurements. Anisotropy is modeled using a single parameter, the average grain-misalignment angle. This leads to the concept of an effective perpendicular magnetic field that determines the critical current density. The same approach is applied to a Bi-2212 coil. However, the model is only accurate in predicting coil properties if the average grain misalignment angle is assumed to be magnetic field dependent. This assumption is contrary to the geometric nature of the average grain-misalignment angle but mathematically effective.

In both the Bi-2212 and Bi-2223 case, the correlation between measured self-field critical current density in short samples and coils is poor. An average correlation is established for the 64 double pancake coils characterized for the 5T insert coil project. However, the scatter is too large to allow a useful prediction thus requiring qualification testing of every double pancake. Two sets of qualification criteria are developed. One based on coil

properties versus applied magnetic field and the second based on coil properties versus the calculated effective perpendicular magnetic field, resulting in practically identical criteria.

The 5T insert consists mostly of stacked double pancakes. A model to predict the magnetic field dependence of the engineering critical current density is thus based on 1) the normalized magnetic field dependence of the engineering critical current density as observed in short samples, 2) the observed self-field engineering critical current density of each double pancake coil, 3) the assumption that the anisotropy parameter is magnetic-field dependent. This model is used to determine the most effective stacking order of the available double pancakes and leads to a prediction of the 5T insert coil engineering critical current density versus background magnetic field. The accuracy of the comparison between the predictions and observed properties is limited as thermal runaway in the insert occurs before the average electric field reaches the critical current density criterion. However, the prediction of self-field engineering critical current density matches extrapolations of the data within 5%. The normalized magnetic field dependence of the quench current is accurate to within 1%. So the magnetic field dependence of the coil engineering critical current density is predictable, but not just on the basis of short sample data: small coil data is needed as well. The 5T insert is the first superconducting coil, HTS or LTS, to reach 25 T, while LTS superconducting magnets have not exceeded 22.3 T.

Engineering critical current density affected by strain

Bending strain and hoop-stress induced tensile stain are the main components of strain in the HTS insert coils considered here. Irreversible degradation of the engineering critical current density occurs when the total tensile strain exceeds a critical value, which has to be avoided in any user magnet. However, efficient coil design requires maximizing the winding current density and minimizing the volume of reinforcing materials. To achieve a magnetic field increment of 5T with the available conductor in the available volume requires operating the 5T insert close to the critical strain. The ability to accurately predict the onset of strain induced engineering critical current density degradation is therefore essential.

The effects of bending and tensile strain on short conductor samples are investigated separately. Bending strain varies from filament to filament in the cross section of BSCCO conductors. Several aspects enter in the equations for the relevant parameter including: the maximum tensile strain in the filaments, the heat treatment diameter, the filament zone thickness and conductor plasticity. The latter varies between conductors and can be quantified using bend-and-release experiments. Due to the asymmetric cross section and thin layer of superconductor in ReBCO coated conductors, the bending strain distribution has a narrow range and can be chosen as either tensile or compressive. This provides an extra variable to manage strain in the magnet design process not available in the case of BSCCO conductors.

Tensile stress-strain properties at cryogenic temperatures of selected BSCCO and ReBCO conductors are measured. The critical tensile strain value above which the engineering critical current density degrades is determined. Reinforcement of the BSCCO silver-alloy/ceramic composite to limit strain is required for application of these conductors in 25 T class insert magnets. Bare ReBCO conductors are at least twice as strong as the strongest reinforced BSCCO conductor and can be applied with little or no reinforcement.

Two different ReBCO insert coils are tested at the NHMFL in a background magnetic field of 19 and 31 T respectively. Remarkably high central magnetic field values of nearly 27 and 34 T are reached. The ReBCO inserts operate at comparable or higher stress levels

and at least twice the current density compared to BSCCO coils. Systematic technology development comparable to the work on BSCCO has not taken place yet but is required for future coils. So far, all ReBCO coils that have been tested in a high background magnetic field were limited by magnet technology, not by the conductor itself.

Six different BSCCO coils are deliberately exposed to large Lorentz-forces with the intention to determine the onset and propagation of strain induced engineering critical current density degradation. Of these coils, three are prototype coils for the three sections of the 5T insert. They are found to tolerate the design stress with safety margins of 20% or less. The coil results are correlated to the measured short sample properties, assuming that the maximum strain on the superconducting filaments can be calculated as the sum of hoop strain and bending strain. The hoop strain is calculated using a simulation code. The onset of degradation is generally predicted correctly, but the accuracy of the prediction of propagation varies from adequate to inadequate. It appears that stress-strain and engineering critical current density versus strain data obtained from bare samples may not be representative of conductor behavior in coils because of inhomogeneous yielding in bare samples. Thus these conductor properties should preferably be measured on stacks of conductors fabricated to mimic coil windings. The mechanical aspects of the design of the 5T insert are appropriate as it leads to an insert coil that repeatedly generated 5 T in a 20 T background magnet for a central magnetic field of 25 T. As intended, this was achieved with small safety margins and without degradation of the superconducting properties. The stress levels in this insert coil are equal or higher than other BSCCO inserts in the literature.

Anisotropy affecting the design process of HTS coils in 25 T class solenoids

The role of various degrees of anisotropy in the magnetic field dependence of the engineering critical current density on the insert design optimization process is investigated. Anisotropy is again quantified using the average grain-misalignment angle. Three cases are considered, depending on the magnetic field angle range over which the anisotropic properties can be described with this single parameter.

First is the case when anisotropy for all magnetic field angles (0-90°) can be accurately described with a single value for the average grain misalignment angle, which usually applies to BSCCO tape conductors. Three regimes are found corresponding to high, low and intermediate average grain misalignment angle values. These regimes are characterized as the axial magnetic-field limited regime, the radial magnetic field limited regime and an intermediate regime respectively. Each regime features a different set of factors and parameters that are relevant and irrelevant in the optimization of an insert design.

Second is a case when anisotropy can be accurately described over a limited range of magnetic field angles but sufficient to cover the range expected in insert coils (< 10°) with a single value for the average grain misalignment angle. This applies to data of some ReBCO coated conductors obtained from measurements at 77 K and may fit data of ReBCO conductors at 4 K. Calculating an effective parallel magnetic field is more relevant in this case than the effective perpendicular magnetic field calculated for BSCCO conductors. A similar pattern of three regimes is found and a similar but not identical set of important parameters and factors emerges.

The third case applies when the average grain misalignment angle parameter is found to be unsuitable to describe the conductor anisotropy. Then the presented method is

preferred that allows the relation between conductor anisotropy and coil design to be evaluated using a simple 2-dimensional plot.

Contribution to magnet technology

The research described here has lead to an increased understanding of HTS conductors for high-field insert coils. Specific contributions to magnet technology are

- Presentation of a methodology leading to the predictability of coil engineering critical current density versus background magnetic field over the range of 0 to 20 T.
- Presentation of an efficient design of an insert coil operating close to known strain limits, making operation of the insert coil test a discriminating test of the ability to predict the strain state in the conductor.
- Clarification of the role of anisotropy in the design optimization in general.

Its applicability is illustrated by the development of the first successful HTS insert operated with a central magnetic field of 25 T. Reaching the 25 T central magnetic field value is recognized as a milestone by for example the National Academy of Sciences Committee on Opportunities in High Magnetic Field Science and is in part responsible for its recommendation to develop 30 T superconducting magnets.

Outlook beyond 25 T

Four of the BSCCO conductors investigated here are suitable for application in 25 T magnets, assuming that a 20 T background magnet is available. The conductor current density is high enough that, after adding the required reinforcement, insulation and structural materials, the resulting average current density in the windings is around 100 A/mm^2. This suffices to design practical 25 T magnets. The feasibility of developing 30 T superconducting magnets is discussed below, including remarks on what the ideal HTS superconductor could look like and at which magnetic field level the cross-over between Nb_3Sn and HTS can be expected.

30 T fully superconducting magnet

For HTS sections of a 30 T magnet that is reasonably compact a winding current density of around 200 A/mm^2 is minimal. The use of a 20 T outsert with a comparable cold bore as used here is assumed, and an HTS cold bore of ~ 4 cm, the smallest bore considered useful in a research magnet. The NHMFL 900 MHz NMR magnet design would provide 20 T in a 20 cm bore, slightly larger than the NHMFL Large Bore Resistive Magnet, if the inner Nb_3Sn section were removed. Improvements in Nb_3Sn conductor since the 900 MHz magnet was designed allow such a magnet to be more compact, so the outsert technology exists.

Two hundred A/mm^2 requires HTS conductors with twice the current density and 2 to 2.4 times the strength[72] than those suitable for 25 T magnets. Today only ReBCO coated conductors meet or approach those values. If reinforcement is required, it is likely more efficient to put the conductor in compression by lamination with tapes under tension compared to simple overbanding. The methods to achieve predictability of the strain state in the conductor and engineering critical current density versus background magnetic field for ReBCO coils can be those used for BSCCO coils here.

A topic likely to require a significant development effort is quench protection, as quench propagation by all indications is expected to be slow thus potentially leading to high hot-

[72] See section 1.3.2

spot temperatures. This topic is closely linked to the maximum tolerable current density in the copper stabilizer in the case of a local normal zone. No agreement exists for the maximum tolerable value for the copper current density, but this value may well have a larger impact on coil design and the average current density in the windings than the amount of reinforcement.

Lack of a realistic value for the maximum copper current density makes it hard to generate a specification for the *ideal* HTS conductor for applications at 30 T and beyond. However, the production process of ReBCO conductors provide a degree of flexibility that allows changes in the conductor specifications without changing the most sensitive aspects of the production process. A major drawback of BSCCO and Nb_3Sn is that a change in conductor specification requires reworking the production process, specifically the drawing and, for BSCCO, the rolling process. In contrast, coated conductors allow:

- easy customization of absolute value of I_c by changing the width of the conductor in the slitting process,
- increasing strength by increasing substrate thickness or lamination with additional reinforcement,
- increasing stability (presumably) by increasing the Cu thickness via plating or again lamination,

all without affecting the sensitive process of depositing the buffer layers, superconductor and cap layer. Moreover, most of the conductor cross section is made up of material contributing to either strength or stability, while the superconducting layer plus the buffer layers take up a nearly negligible amount of space. The above aspects are quite favorable for future application of coated conductors in high-field magnets. A number of other aspects, like

- filamentation,
- cabling,
- higher J_c,
- lower cost and
- joints,

require significant development. The level of funding for coated conductor development for applications in the power utility grid should enable considerable progress on at least the first three aspects. It can be concluded that ReBCO coated conductors are the prime candidate and a promising candidate for 30^{+}T magnets.

Nb_3Sn-ReBCO cross-over

ReBCO conductors are stronger than Nb_3Sn and therefore require less reinforcement at the same operating current density, resulting in a higher average winding current density. Thus an argument is provided to place the cross-over magnetic field for the application of ReBCO versus Nb_3Sn below the magnetic field value of equal current density in ReBCO and Nb_3Sn. Such cross-over value is likely to be at least several tesla below 20 T. Higher current density in the insert and expanding HTS coils into the magnetic field range below 20 T will result in higher maximum magnetic field angles so conductor anisotropy will have a larger impact on coil design in 30 T magnets than in 25 T. It is more likely that the HTS coils will be magnetic field-angle limited or radial magnetic field limited. And, as a last remark, it will become appropriate to discontinue the use of the word *insert* with reference to HTS coils, as HTS conductors will generate about half of the total magnetic field in 30 T superconducting magnets.

Samenvatting en vooruitblik (summary and outlook in Dutch)

Samenvatting

Voor dit onderzoek zijn experimenten uitgevoerd om de eigenschappen te bestuderen van verschillende hoge-T_c geleiders, in de vorm van korte tapes, kleine spoelen en grotere prototype spoelen. Het algemene doel is om de technologie te ontwikkelen voor krachtige magneten op basis van hoge-T_c supergeleiders die functioneren bij 4 K. Gedurende dit onderzoek zijn Bi-2212 en Bi-2223 tapes, Bi-2212 ronde draad en YBCO dunne-film geleiders onderzocht op hun toepasbaarheid in spoelen die gebruikt kunen worden in het centrum van sterke magneten. Het specifieke doel van dit onderzoek was aan te tonen dat 25 T supergeleidende magneten mogelijk zijn. Dit doel is bereikt door een Bi-2212 spoelenset te ontwikkelen die 5 T opwekt, concentrisch met een 20 T magneet voor een totaal van 25 T in het centrum.

De leidraad in dit onderzoek is de vraag hoe de eigenschappen van korte staaltjes supergeleider gebruikt kunnen worden om de eigenschappen te voorspellen van kleinere en grotere spoelen die aan een sterk magneetveld bloot staan. Hierbij concentreert het werk zich op een aantal specifieke onderwerpen uit de magneet-technologie, in het bijzonder de afhankelijkheid van de kritieke stroomdichtheid van magneetveld en rek. Modellen zijn ontwikkeld die de magneetveld- en rekafhankelijkheid beschrijven van de kritieke stroomdichtheid. Deze modellen zijn gebaseerd op gemeten eigenschappen van korte proefstukken geleider en worden gebruikt om de eigenschappen van spoelen te voorspellen. Die voorspellingen zijn vervolgens vergeleken met de gemeten eigenschappen van de spoelen om de toepasbaarheid van de modellen te toetsen.

De hoekafhankelijkheid in de relatie tussen magneetveld en de kritieke stroomdichtheid speelt een belangrijke rol omdat het de waarde van de stroomdichtheid sterk beïnvloed en daarnaast het ontwerp optimalisatie proces zelf beïnvloed

Magneetveld afhankelijkheid van de kritieke stroomdichtheid

De kritieke stroomdichtheid van Bi-2212 en Bi-2223 tapes, een Bi-2212 ronde draad en een YBCO dunne-film geleider is gemeten en op basis hiervan zijn beschrijvende vergelijkingen afgeleid. Het relevante bereik van het magneetveld is vanaf het eigenveld tot 25 T, en waar mogelijk is de geleider onderzocht tot 45 T. Voor alle geleiders is de gemeten stroomdichtheid voldoende om de geleiders als potentiele kandidaten voor toepassing in HTS spoelen van 25 T magneten te beschouwen.

De magneetveldafhankelijkheid van de kritieke stroomdichtheid in een kleine Bi-2223 spoel kan nauwkeurig berekend worden met een model waarin de kritieke stroomdichtheid in een loodrecht magneetveld beschreven wordt als de som van de bijdragen van een parallel netwerk van sterk- en zwak gekoppelde stroompaden. De waarden van de parameters in dit model zijn afgeleid van metingen aan korte draadstukken. De hoekafhankelijkheid is gemodelleerd met een enkele parameter: de gemiddelde hoek tussen de korrelvlakken en het vlak van de geleider. In het kort: de gemiddelde fouthoek. Dit leidt tot het concept van het effectieve loodrechte magneetveld dat de kritieke stroomdichtheid bepaalt. Toepassing van dit concept op een Bi-2212 spoel blijkt alleen nauwkeurige voorspellingen op te leveren onder de aanname dat de gemiddelde fouthoek magneetveld afhankelijk is. Die aanname is in tegenspraak met het geometrische karakter van de gmiddelde fouthoek maar wiskundig gezien effectief.

Voor zowel de Bi-2212 en Bi-2223 geleiders is de korrelatie tussen de kritieke stroomdichtheid van proefstukken draad respectievelijk tape en spoelen in het magnetisch eigenveld zwak. Een gemiddelde verhouding is bepaald voor de 64 double pancake spoelen die onderzocht zijn voor het 5T project. De spreiding is echter zo groot dat een zinvolle voorspelling van de spoel-eigenschappen op basis van de proefstukken niet mogelijk is. Daarom moet elke spoel een kwalificatie-test ondergaan, waarvoor twee kwalificatie-kriteria ontwikkeld zijn. Het eerste kriterium is gebaseerd op gemeten eigenschappen van een enkele spoel vergeleken met het achtergrond magneetveld; het tweede kriterium gebruikt het berekende effectieve loodrechte magneetveld voor dezelfde data, hetgeen leidt tot vrijwel identieke kriteria.

De 5T spoelenset bestaat voornamelijk uit gestapelde double pancake spoelen. Het model om de magneetveldafhankelijkheid van de kritieke stroomdichtheid te voorspellen is daarom gebaseerd op het volgende: 1) de genormaliseerde magneetveldafhankelijkeid van de kritieke stroomdichtheid, zoals deze gemeten is in de geleiderproefstukken, 2) de gemeten eigenveld stroomdichtheid van iedere spoel en 3) de aanname dat de gemiddelde fouthoek magneetveld afhankelijk is. Dit model is gebruikt om de meest effectieve stapeling van de beschikbare double pancake spoelen te bepalen en de kritieke stroomdichtheid van de 5T spoelenset in vergelijking met het achtergrond magneetveld te voorspellen. Een vergelijking tussen de gemeten en voorspelde eigenschappen is maar beperkt mogelijk omdat de temperatuur in de spoelenset onkontroleerbaar oploopt voordat het gemiddelde electrisch veld het kritieke stroomdichtheidskriterium bereikt. Desondanks komt de voorspelling van de eigenveld kritieke stroomdichtheid binnen 5% overeen met extrapolaties van de data. De voorspelling van de magneetveld-afhankelijkheid van de kritieke stroomdichtheid komt genormalizeerd binnen 1% overeen met de gemeten maximale stroomdichtheid. De magneetveldafhankelijkheid van de kritieke stroomdichtheid is dus voorspelbaar, maar niet alleen op basis van de eigenschappen van geleiderproefstukken: meetgegevens van de kleine spoelen zijn ook nodig. Met de 5T spoelenset is voor het eerst 25 T bereikt binnen een hoge-T_c supergeleidende spoel, terwijl lage-T_c supergeleidende magneten maximaal 22.3 T genereren.

Rek-afhankelijkheid van de kritieke stroomdichtheid

Aan de belangrijkste rek-componenten in de hoge-T_c spoelen die hier bestudeerd zijn liggen geleiderbuiging en electro-magnetische krachten ten grondslag. Onomkeerbare afname van de kritieke stroomdichtheid treedt op als de rek in de geleider een bepaalde kritieke waarde overschrijdt, iets dat vermeden moet worden in magneten die onderdeel uitmaken van een gebruikersfaciliteit. Tegelijk vereist een efficiënt ontwerp een maximale stroomdichtheid en een minimale hoeveel versterkende materialen. Om de beoogde 5 T op te wekken met de beschikbare supergeleider binnen het beschikbare volume is het noodzakelijk dat de 5T spoelenset dicht-bij en net onder de kritieke rekgrens functioneert. Het is daarom van essentiëel belang om het punt waarop de kritieke stroomdichtheid onomkeerbaar afneemt nauwkeurig te kunnen voorspellen.

De effecten van buiging en electromagnetische rek op draadstukken zijn apart onderzocht. Het effect van buiging varieert van filament tot filament binnen de doorsnede van BSCCO geleiders. De maximale rek in de filamenten is hierbij de meest relevante parameter. De vergelijkingen voor de waarde van de maximale rek in de filamenten bevatten verschillende parameters waaronder: de diameter waarop de geleider de warmtebehandeling heeft gekregen, de dikte van de filamentenbundel en de mate van plasticiteit in de geleider. De mate van plasticiteit varieert van geleider tot geleider en kan bepaald worden met buig-en-strek experimenten. Dankzij de asymmetrische doorsnede en de dunne laag supergeleider

in ReBCO film geleiders heeft de rekwaarde als gevolg van buiging een smalle verdeling die naar keuze zowel positief (rek) als negatief (druk) kan zijn. Dit biedt een extra mogelijkheid om de rekwaarde in de geleider te beïnvloeden gedurende het magneet ontwerpproces. Deze mogelijkheid is echter niet beschikbaar voor BSCCO geleiders.

Trek-rek eigenschappen bij cryogene temperaturen zijn gemeten voor geselecteerde BSCCO en ReBCO geleiders. Daarnaast is ook de kritieke rekwaarde bepaald waarboven de kritieke stroomdichtheid onomkeerbaar afneemt. Versterking van de samengestelde zilverlegering-keramiek BSCCO geleiders is noodzakelijk voordat deze toegepast kunnen worden in spoelen van 25 T magneten. Onversterkte ReBCO dunne-film geleiders daarentegen zijn tenminste twee maal zo sterk als de sterkste versterkte BSCCO geleiders die beschikbaar zijn en kunnen met weinig of geen versterking worden toegepast.

Twee verschillende ReBCO spoelen zijn op het NHMFL getest in een achtergrond-magneetveld van respectievelijk 19 en 31 T. Daarbij bereikte het magneetveld in het centrum waarden van respectievelijk bijna 27 en 34 T. De ReBCO geleiders zijn daarbij, in vergelijking met alle voorgaande BSCCO spoelen, blootgesteld aan vergelijkbare of hogere trek waarden en functioneren op niet minder dan het dubbele van de stroom-dichtheid. Een systematische ontwikkeling van magneet-technologie, zoals die ook voor BSCCO is uitgevoerd, heeft nog niet plaatsgevonden maar is wel nodig voor toekomstige ReBCO spoelen. Tot nu toe zijn de eigenschappen van alle ReBCO spoelen die in een achtergrond magneetveld getest zijn beperkt door magneettechnologie en niet door de geleider zelf.

Zes verschillende BSCCO spoelen zijn bewust aan hoge electro-magnetische krachten blootgesteld met als doel het begin en de verspreiding van door rek veroorzaakte afname van de kritieke stroomdichtheid te bepalen. Drie van deze spoelen zijn prototypes voor de drie verschillende secties van de 5T spoelenset. Ze bereiken de ontwerp-trekwaarde zonder afname van de kritieke stroomdichtheid, terwijl de veiligheidsmarges 20% zijn of kleiner. Door aan te nemen dat de maximale rek in de supergeleidende filamenten berekend kan worden als de som van de electromagnetische axiale rek en de maximale buig-rek, kunnen de eigenschappen van geleiders en spoelen vergeleken worden. Een simulatie programma wordt daarbij gebruikt om de electro-magnetische rek te berekenen. De voorspelling van het begin van de afname in de kritieke stroomdichtheid is in het algemeen korrekt, maar de voorspelling van de spreiding van de afname varieert van nauwkeurig tot onnauwkeurig. Het lijkt erop dat de trek-rek eigenschappen en rek-kritieke stroomdichtheid relaties van de testgeleiders niet altijd representatief zijn voor het gedrag van de geleider in spoelen als gevolg van inhomogene rek in de testgeleiders. Daarom moet voor metingen van de geleidereigenschappen bij voorkeur gebruikt gemaakt worden van pakketjes geleiders die zo veel mogelijk op de wikkelingen in een spoel te lijken. De mechanische aspecten van het ontwerp van de 5T spoelenset blijken afdoende uitgewerkt te zijn omdat de spoelenset herhaaldelijk 5 T heeft bereikt, in een achtergrond magneetveld van 20 T. Dit is bereikt zoals beoogd, zonder afname van de kritieke stroomdichtheid terwijl de veiligheidsmarges klein zijn. De electro-magnetische trekkrachten in deze spoelenset is vergelijkbaar met of hoger dan in alle andere BSCCO spoelen die in de literatuur beschreven zijn.

De invloed van hoekafhankelijkheid op het ontwerp proces van hoge-T_c spoelen in 25 T magneten

In dit onderzoek is onderzocht in hoeverre verschillende mates van hoekafhankelijkheid in het verband tussen het magneetveld en de kritieke stroomdichtheid een rol spelen in het ontwerp-optimalizatieproces. Als parameter die de hoekafhankelijkheid uitdrukt is opnieuw de gemiddelde fout-hoek gebruikt. Er zijn drie mogelijkheden, afhankelijk van het veldhoek-bereik waarover de parameter de hoekafhankelijkheid beschrijft.

In het eerste geval beschrijft de gemiddelde fouthoek de hoekafhankelijkheid voor alle hoeken (0-90°), wat meestal toepasselijk is voor BSCCO tape geleiders. Er blijken drie karakteristieke patronen van eigenschappen te zijn die overeenkomen met grote, kleine en middelmatige gemiddelde fouthoeken. Deze patronen zijn respectievelijk gekenmerkt door a) de kritieke stroomdichtheid is beperkt door het axiale magneetveld, b) de kritieke stroomdichtheid is beperkt door het radieële magneetveld en c) een tussenliggend patroon. In elk patroon zijn de factoren en parameters die belangrijk dan wel onbelangrijk zijn voor de optimalisatie van het ontwerp verschillend.

In het tweede geval is de gemiddelde fouthoek slechts geschikt om de hoekafhankelijkheid te beschrijven voor een beperkt bereik van magneetveldhoeken, maar wel voldoende voor het bereik van veldhoeken die te verwachten zijn (< 10°) in hoge-T_c spoelen in 25 T magneten. Dit is van toepassing op sommige ReBCO dunne-film geleiders op 77 K en is mogelijk ook van toepassing op 4 K. In dit tweede geval is het zinvol om het effectieve parallele magneetveld te berekenen in plaats van het effectieve loodrechte magneetveld dat in het algemeen voor BSCCO geleiders van toepassing is. Opnieuw blijken er drie patronen te zijn met een vergelijkbare maar niet identieke verzameling van parameters en faktoren die belangrijk zijn.

In het derde geval is de gemiddelde fouthoek geen geschikte parameter om de hoekafhankelijkheid in het verband tussen het magneetveld en de kritieke stroomdichtheid uit te drukken. Dan is de methode van toepassing waarmee het verband tussen de hoekafhankelijkheid en de optimalizatie van het ontwerp weergegeven kan worden in een eenvoudige twee-dimensionale grafiek.

Bijdragen aan de magneet technologie

Dit proefschrift draagt bij aan een beter begrip van hoge-T_c supergeleiders voor toepassing in sterke magneten. Dit wordt in het bijzonder bereikt op de volgende manieren:

- Door het presenteren van een methode die geschikt is om de kritieke stroomdichtheid te voorspellen van spoelen die in achtergrond magneetvelden tot 20 T gebruikt worden.
- Door het presenteren van een efficiënt ontwerp van een spoelenset die bedoeld is om dicht bij de kritieke rekgrens gebruikt te worden, zodat duidelijk onderscheiden kan worden of de rek-toestand van de geleider nauwkeurig voorspeld is of niet.
- Door het verhelderen van de rol die hoekafhankelijkheid speelt in de optimalizatie van een ontwerp.

De toepasbaarheid van het bovenstaande is aangetoond door de ontwikkeling van de eerste succesvolle hoge-T_c spoelenset die, samen met een achtergrond magneet, 25 T bereikt. Het bereiken van dit magneetveld wordt gezien als een mijlpaal door bijvoorbeeld het commitee van de Amerikaanse National Academy of Science voor “Opportunities in High Magnetic Field Science”. Dit resultaat is ten dele verantwoordelijk voor hun aanbeveling aan het NHMFL om 30 T supergeleidende magneten te ontwikkelen.

Vooruitblik voor magneten sterker dan 25 T

Vier van de BSCCO geleiders die beschreven worden in dit proefschrift, zijn geschikt voor toepassing in 25 T magneten, met een achtergrondmagneet die 20 T opwekt. De stroomdichtheid in de geleiders is hoog genoeg opdat, na toevoeging van de benodigde versterking, isolatie en struktuur materialen, een gemiddelde stroomdichtheid van 100 A/mm^2 in de wikkelingen van de spoel mogelijk is. Dat is voldoende om praktische magneten te kunnen ontwerpen. Hieropvolgend komt de mogelijkheid om supergeleidende magneten van tenminste 30 T te ontwikkelen aan de orde, inclusief opmerkingen over hoe de ideale geleider er uit kan zien en bij welke magneetveldsterkte het omslagpunt voor het gebruik van hoge- en lage-T_c geleiders te verwachten is.

30 T supergeleidende magneet

Voor hoge-T_c secties van een redelijk kompakte 30 T magneet is het wenselijk om een gemiddelde stroomdichtheid in de wikkelingen van 200 A/mm^2 te hebben. Dit geldt onder de aanname dat een 20 T achtergrondveld in een magneet beschikbaar is met een vergelijkbare koude boring als die hiervoor gebruikt is en de hoge-T_c sectie een koude boring heeft van ongeveer 4 cm. Dat laatste wordt beschouwd als de kleinste boring die nog nuttig is in magneten voor algemene onderzoeksdoeleinden. De 900 MHz/21.1 T NMR magneet van het NHMFL zou 20 T in een 20 cm boring hebben als de binnenste Nb_3Sn spoel verwijderd zou worden, wat een iets grotere boring oplevert dan de 20 T watergekoelde magneet die voor de 5T spoelenset gebruikt is. Verbeteringen van Nb_3Sn geleiders sinds het ontwerp van de 900 MHz magneet maken het mogelijk een kompaktere achtergrond magneet te creëren, dus er is geen twijfel dat de technologie voor zo'n supergeleidende achtergrond magneet beschikbaar komt.

Tweehonderd A/mm^2 vereist hoge-T_c geleiders met de dubbele stroomdichtheid en 2 tot 2.4 keer de sterkte dan vereist voor hoge-T_c geleiders in 25 T magneten. Alleen ReBCO dunne-film geleiders halen of benaderen op dit moment dergelijke waarden. Als versterking van de geleider nodig mocht zijn is het waarschijnlijk efficiënter om de geleider onder negatieve voorspanning (druk) te brengen dan de wikkelingen als geheel met extra materiaal aan de buitendiameter te versterken. Negatieve voorspanning kan aangebracht worden door de geleider te lamineren met versterkende banden die onder positieve voorspanning aangebracht worden. De methoden die gebruikt zijn om de rektoestand van de geleider en de magneetveld afhankelijkheid van de kritieke stroomdichtheid in BSCCO spoelen te bepalen zijn ook geschikt voor ReBCO spoelen.

Een onderwerp dat waarschijnlijk veel ontwikkeling vereist is bescherming van de spoelen wanneer de kritieke stroomdichtheid overschreden wordt en de temperatuur lokaal sterk stijgt. Deze warme zone verspreidt zich maar langzaam in hoge-T_c geleiders wat tot dermate hoge temperaturen en temperatuurgradiënten kan leiden dat de spoelen onherstelbaar beschadigd raken. Een belangrijke parameter die bepalend is voor de snelheid waarmee de warme zone zich verspreid is de maximaal toelaatbare stroomdichtheid in de koperen stabilisatielaag. Deze waarde is nog onbekend en het is te verwachten dat de waarde van deze parameter een grotere invloed zal hebben op het magneetontwerp en de gemiddelde stroomdichtheid in de wikkelingen dan de hoeveelheid versterkingsmateriaal.

Het ontbreken van een algemeen geaccepteerde waarde voor de maximale stroomdichtheid in de koperlaag maakt het moeilijk om een algemene specificatie te geven hoe de *ideale* hoge-T_c geleider eruit zou moeten zien voor toepassingen in magneten van 30 T of hoger. Desondanks biedt het productieproces van ReBCO geleiders

een mate van flexibiliteit die het toelaat om de geleiderspecificaties te veranderen zonder de meest gevoelige stappen in het produktieproces te beïnvloeden. Een belangrijk nadeel van BSCCO en Nb_3Sn ligt in het feit dat een verandering in de geleiderspecifikaties meestal betekent dat de vele trek-stappen voor de draad, en voor BSCCO ook de wals-stappen, opnieuw geoptimalizeerd moeten worden. Hier staat tegenover dat voor ReBCO dunne-film geleiders het mogelijk is om:

- de absolute waarde van de krtieke stroom aan te passen door de breedte van de geleider te veranderen tijdens het snijden van de strips,
- de geleider sterker te maken door een dikker substraat te gebruiken of de geleider te lamineren met een versterkende strip,
- de geleider stabieler te maken door de dikte van de koper laag te vergroten,

zonder de gevoelige stappen in het productieproces zoals het aanbrengen van de buffer-lagen, de supergeleidende laag, en de zilveren toplaag te beinvloeden. Bovendien bestaat het overgrote deel van de doorsnede van de geleider uit materialen die bijdragen aan de sterkte of stabiliteit van de geleider, terwijl de supergeleidende- en bufferlagen een vrijwel verwaarloosbare hoeveelheid ruimte innemen. Dit zijn bijzonder gunstige factoren voor toepassing van deze dunnefilm geleiders in toekomstige sterke magneten.
Een aantal andere gewenste factoren, zoals hieronder wordt weergegeven, vereisen de nodige ontwikkeling:

- de opdeling van het stroompad in fijne filamenten,
- verkabeling,
- hogere stroomdichtheid,
- lagere kosten en
- geleiderverbindingen met weinig of geen weerstand.

De financiering die beschikbaar is voor het ontwikkelen van ReBCO dunnefilm geleiders voor toepassingen in de energieopwekking en distributie zou het mogelijk moeten maken om op tenminste de eerste drie punten flink vooruitgang te boeken. Hieruit kan worden geconcludeerd dat ReBCO dunne-film geleiders de beste en meest veelbelovende geleiders zijn voor toepassing in magneten van 30 T of hoger.

Omslagpunt van Nb_3Sn naar ReBCO

ReBCO dunne-film geleiders zijn sterker dan Nb_3Sn wat tot gevolg heeft dat ze, bij dezelfde stroomdichtheid, minder versterking nodig hebben wat leidt tot een hogere gemiddelde stroomdichtheid in de wikkelingen. Dit is een argument om de overgang tussen spoelen met Nb_3Sn en ReBCO dunne-film geleiders plaats te laten vinden bij een lager magneetveld dan waarbij de stroomdichtheden in de geleiders gelijk zijn. Een dergelijke overgang ligt waarschijnlijk tenminste enkele tesla onder de 20 T. De hogere stroomdichtheid die nodig is in hoge-T_c spoelen om 30 T magneten mogelijk te maken plus de uitbreiding van hoge-T_c spoelen tot het magneetveld bereik onder de 20 T heeft tot gevolg dat de maximale veldhoek groter zal zijn. De hoekafhankelijkheid in het verband tussen het magneetveld en de kritieke stroomdichtheid zal daarom een sterkere rol spelen in het ontwerpproces van 30 T magneten in vergelijking tot 25 T magneten. De waarschijnlijkheid dat hoge-T_c spoelen beperkt zullen zijn door de maximale veldhoek (dan wel maximale radiele magneet-veld component) is groter in 30 T magneten. Als laatste kan opgemerkt worden dat het in 30 T magneten niet meer toepasselijk zal zijn om de hoge-T_c spoelen als een beperkte toevoeging aan een magneetsysteem te zien, omdat dan ongeveer de helft van het totale magneetveld door hoge-T_c spoelen opgewekt wordt.